Laser Wakefield Accelerated Electron Beams: Optimization, Novel Energy Diagnostic, and Experimental Applications

by

Jason Cardarelli

A dissertation submitted in partial fulfillment
of the requirements for the degree of
Doctor of Philosophy
(Nuclear Engineering and Radiological Sciences)
in the University of Michigan
2024

Doctoral Committee:

Professor Alexander G.R. Thomas, Chair
Professor Karl Krushelnick
Dr. Anatoly Maksimchuk
Professor Louise Willingale

Jason Cardarelli

jcardar@umich.edu

ORCID iD: 0000-0002-2060-494X

© Jason Cardarelli 2024

This work is dedicated to those who supported me most through my PhD: Silvia, Ellis, Walrus, and Sputnik.

ACKNOWLEDGMENTS

I owe a great deal to those who helped me through the past several years toward completing this dissertation. I must first acknowledge my advisor, Professor Alexander Thomas, for his wealth of expertise and patience in guiding me through essential milestones in this work. My committee members, Professor Karl Krushelnick, Professor Louise Willingale, and Dr. Tolya Maksimchuk, have all taught me so much through discussions in the classroom, in the lab, and at annual HFS BBQs. I would be amiss not to mention Dr. Yong Ma, as working closely with him on running several experimental campaigns allowed me to learn from his clever problem-solving and patient teaching style. Similarly, I'd like to thank Dr. Matthew Streeter for being a reliable source of answers to any question that pops up while conducting a laser wakefield acceleration experiment. I am also indebted to Dr. Paul Campbell for his endless time and effort on several of the projects in this thesis and for his humble approach to working with those around him. John Nees was an invaluable source of knowledge and expertise in all things related to ultrashort lasers.

I want to thank Dr. Nick Peskosky for being an encyclopedic source of anything experimental and for choosing the best tunes during homework sessions. Stephen DiIorio's ability to offer advice when asked for and a sense of humor when needed have helped make long days in the office enjoyable. Thanks to Dr. Brandon Russell, who has never hesitated to help work through an interesting physics question. Other students including, but not limited to, André Antoine, Rebecca Fitzgerrald, Qian Qian, Nick Ernst, Tanner Nutting, Dr. Hongmei Tang, Veronica Contreras, Brendan Stassel, and Jon Murphy have made my time in doing (or avoiding) studies and research much more enjoyable.

Finally, I must acknowledge my family for supporting me toward a PhD - the second most challenging and rewarding endeavor I've ever pursued (after parenthood).

TABLE OF CONTENTS

DEDICATION ii

ACKNOWLEDGMENTS iii

LIST OF FIGURES vii

LIST OF TABLES xv

LIST OF APPENDICES xvi

LIST OF ACRONYMS xvii

ABSTRACT xviii

CHAPTER

1 Introduction 1

1.1 Brief history of electron accelerators 1
1.2 Laser wakefield acceleration 4
1.3 Thesis outline 8

2 Theoretical Background 11

2.1 Laser wakefield acceleration 13
2.1.1 Single particle motion in a laser field 13
2.1.2 Laser propagation in a plasma & description of plasma wakefields 15
2.1.3 Trapping & injection 20
2.1.4 Betatron radiation from LWFA electron beams 24
2.2 Relativistic current filamentation instability 26

3 Experimental Methods 29

3.1 High power laser systems 29
3.1.1 Gemini laser system 30
3.1.2 ALEPH laser system 32
3.1.3 ALLS laser system 34
3.2 Laser diagnostics 35
3.2.1 Energy measurement 35

3.2.2 Pulse duration measurement . . . 36
3.2.3 Focal spot measurement . . . 37
3.3 Plasma & beam diagnostics . . . 39
3.3.1 Plasma density measurement: interferometry . . . 39
3.3.2 Beam energy measurement: magnetic spectrometer . . . 41
3.3.3 Beam emittance measurement: emittance mask . . . 45
3.3.4 Betatron emission measurement: transmission filter pack . . . 48
3.4 Gas targets . . . 49
3.5 Particle-in-Cell (PIC) simulations . . . 53

4 Monoenergetic Beams in a Laser Wakefield Accelerator Via Shock Injection . . . 57

4.1 Introduction . . . 57
4.2 Methods . . . 59
4.3 Results and discussion . . . 62
4.4 Conclusions . . . 66

5 Streaked Laser Wakefield Trajectory Producing Angular vs Time Correlation in Wakefield Accelerator . . . 68

5.1 Introduction . . . 68
5.2 Methods . . . 73
5.3 Results and discussion . . . 78
5.4 Conclusions . . . 83

6 Parametric Studies of Current Filamentation Growth in Laser Wakefield Accelerated Beams . . . 84

6.1 Introduction . . . 84
6.2 Methods . . . 86
6.3 Results and discussion . . . 89
6.4 Helium, nitrogen, and argon filamentation gas species . . . 101
6.5 Conclusions . . . 106

7 Laser Wakefield Accelerator Source of Positron Beams Suitable for Injection into a Plasma Accelerator . . . 108

7.1 Introduction . . . 108
7.2 Methods . . . 113
7.3 Results and discussion . . . 115
7.4 Particle-in-Cell simulations . . . 123
7.5 Conclusions . . . 126

8 Conclusions . . . 128

8.1 Summary . . . 128
8.2 Challenges . . . 131
8.3 Future prospects . . . 132

APPENDICES . . . 135

BIBLIOGRAPHY 145

LIST OF FIGURES

FIGURE

1.1 Three-dimensional visualization of a Particle-In-Cell (PIC) simulation of laser wakefield acceleration in the nonlinear bubble regime using a normalized laser intensity a0 = 6, a beam waist of 22 μm, full-width half-maximum (FWHM) beam duration of 27.3 fs, and a plasma density of 3×10^{18} cm^{-3} using the FBPIC PIC code. The purple-to-yellow colormap shows electron density, and the projection of the longitudinal accelerating field is shown in the blue-white-red colormap. Simulation and visualization completed by Dr. Daniel Seipt (Helmholtz-Institut Jena). 5

2.1 Diagram of longitudinal (top) and transverse (bottom) electric fields within a wakefield driven by a laser of the normalized vector potential of a) $a_0 = 0.1$ in the linear regime, and b) $a_0 = 1$ in the nonlinear regime. Regions of accelerating longitudinal and focusing transverse fields are labeled, with the accelerating + focusing regions enclosed with a dotted line. Adapted from Thomas (2020) 17

2.2 One-dimensional demonstration of (top) an $a_0 = 0.1$ laser driver wake potential ϕ, electric field E and density perturbation $\delta\rho$ and (bottom) the resulting phase space orbits allowed for particles at specific longitudinal positions with specific longitudinal velocities. Reprinted from Thomas, arxiv (2020). 21

2.3 Diagram of the two betatron regimes of $K \gg 1$ wiggler regime (left) and $K \ll 1$ undulator regime (right). Reprinted with permission from Corde et al. (2013). 24

3.1 Schematic of the Astra-Gemini laser system. Reprinted from Schumaker (2014) 31

3.2 Schematic of the Advanced Laser for Extreme Photonics (ALEPH) laser line amplification stages. Included at the end of this diagram is the facility's optional second-harmonic generation to the main beam which was not used in the work in this dissertation. The ultimate chamber relevant to this work was a long focal length chamber as opposed to the short focal length shown in this figure. Reprinted with permission from Opt. Lett. 42, 3828 (2017) ©Optical Society of America. 33

3.3 Image of the Advanced Laser Light Source (ALLS) $f/15$ focus experimental chamber used primarily for wakefield light source experiments. Image reproduced from ALLS facility section on LaserNetUS website. 34

3.4 Example of the vacuum focal spot measurement taken at the ALEPH laboratory during the current filamentation instability experiment in this thesis. The spatial scale of the image is ~ 25 pixels/10 μm. 38

3.5 a) Render of 1) an interferometer probe laser, 2) a main accelerator driving laser, and 3) a plasma target utilized in this dissertation for the current filamentation instability experiment in this thesis. b) An example of a raw image from the target shown, and c-e) the flowchart of the process used to retrieve the density for gas targets for experiments in this dissertation. 39
3.6 Horizontal (left) and vertical (right) midplane visualizations of the magnetic fields within the magnetic gap regions of a representative arbitrary magnetic dipole gap. In each midplane visualization, the calculated divergence of the magnetic field is zero throughout the domain. 41
3.7 Example of output from 3D particle stepper code used to generate an energy-to-position dispersion curve correlation for a given spectrometer geometry, field strength (1 Tesla), and beam energy and angular properties. Witness electrons ranging from 50-1500 MeV pass through the dipole field region with on-axis pointing and with 5 mrad pointing angle to the top, left, bottom, and right of the beam's on-axis trajectory to simulate the effect of divergence angle on the measured beams. 42
3.8 Particle trajectories (top) and resulting $E(x)$ dispersion relationship to determine the correlation between electron energy and position on the scintillator screen in the dispersion direction (bottom) for the current filamentation instability experiment at the ALEPH laboratory. Dipoles consisted of central field strength of 0.97 T. 43
3.9 Example of the emittance retrieval process using an emittance mask used in Chapter 7. a) Annotated raw data of positrons landing on the first scintillator screen after being deflected by a dipole magnetic field. b) Data, fitted ideal signal, and retrieved signal from the emittance retrieval process. 47
3.10 Example synthetic positron spectrometer particle distribution. Particles that pass through the grid freely propagate onto the detector plane, and are dispersed according to their energy. Taking a slice along the y-axis mixes some particle energies due to the effect of the beam divergence. Particles labeled 'energy band' have energies within 450-550 MeV. Selected particles have x positions corresponding to the expected position for zero-divergence particles within the same energy range. The signal $S_x(y)$ is generated by making a histogram of selected particle y coordinates. 48
3.11 a) The X-ray filter array design used on the streaked betatron beam experiment in Chapter 5 and b) its corresponding transmission curves over the X-ray energy range relevant to the experiment. c) An example image was taken of the betatron radiation output interacting with the filter pack recorded by an Andor indirect X-ray CCD. . . . 49
3.12 a) Side and b) top-down profile views and c-d) interferometric measurements of the transverse density profile along the length of the accelerator for the gas target used at the ALLS facility. 50
3.13 a) Side and b) top-down profile views of the gas jet and shock-producing blade at the $z_{\mathrm{blade}} = 0$ mm position from a CAD model of the gas jet. 51
3.14 width = 1 51

3.15 Flowchart representation of the sequential categories of calculations in a particle-in-cell simulation. Subscripts $j, k,$ and l represent cardinal unit vectors in a three-dimensional spatial grid, and i represents a property of the $i-$th macroparticle. The user-defined initialized values represented by the blue and red items in the top-left of the figure are added to the simulation only on the first loop of the computational cycle, where the charge is first interpolated to the grid and the resulting fields are added to any external fields defined by the user. 54

4.1 Schematic showing the experimental setup for this work. The results from this work were taken alongside a counter-propagating beam experiment. The counter-propagating tight focal-length laser was not utilized in the data discussed in this chapter; only the long focal-length drive pulse was used. 59
4.2 Example of shock locator code process for three different blade positions' monoenergetic beam results. a) The raw image undergoes a b) Laplace kernel operation, which is Fourier filtered and vignetted to make vertical shocks in the center of the data region more visible. c) This is blurred and thresholded, which is then d) also blurred and thresholded to reduce false selection of small high-frequency contrast features in the image. f) The angularly-summed energy spectrum with colorbars normalized to the highest charge density in the spectrum for each shot. The blade positions of these shots are 1) 1.0 mm, 2) 1.5 mm, and 3) 2.5 mm. 60
4.3 (Top) Relative angularly-integrated and energy-integrated charge on the (Bottom) electron spectra observed in a scan of the razor blade position across the gas jet ordered from left-to-right by increasing shock position. Each spectrum spans the angular range of ± 5 mrad around the beam centroid. 61
4.4 Angularly integrated electron number spectra for the optimised shock position $z_{\mathrm{inj}} = 2$ mm. The values indicated in the inset show the energy, charge, and FWHM energy spread of the high energy peaks in the spectra. 62
4.5 Experimentally extracted average density profile from interferograms for shots with the blade position $z_{\mathrm{blade}} = 1.0$ mm, where monoenergetic GeV electron beams were measured. 63
4.6 Results from 2D fluid simulation of the razor blade placed 2 mm in front of the gas jet's edge 200 μs of flow time after valve opening. a) The density heatmap in the gas jet domain using a logarithmic color bar scale. b) The line-out representation of the density at the height above the jet opening where the laser travels. 64
4.7 Quasi-3D simulations with FBPIC. (a) The density profile from the hydrodynamic simulation that was used in the simulation. (b) and (c) show the plasma wave just before and after the shock transition, showing the trapping of a short and monochromatic bunch. (d-e) the momentum space and spectrum (inset) (d) just after the shock transition and (e) near the end of the simulation. (f) shows the plasma wave's beam profile and longitudinal electric field just after the shock transition. 66

5.1 A theoretical and simulated curved laser trajectory example for an intense laser wakefield driving pulse ($a_0 > 1$) traveling perpendicular to a transverse density gradient (a). Snapshots of the wakefield acceleration along different points in its curved trajectory are also shown (b). Reprinted with permission from Phys. Plasmas 25 (11): 113105 (2018), AIP Publishing. 70
5.2 The target and diagnostic setup of the experiment. Not shown is the transverse interferometer used to measure the on-shot plasma density in the target. 73
5.3 The two cases of target geometry in which shots were taken. In case 1 the density gradient inducing angular streaking is along the x-axis transverse to the initial laser trajectory. Case 2 rotates the target by 25 mrad such that the laser in the acceleration stage of the gas target will travel first up and then back down the steering density gradient. 74
5.4 Results of reconstructed neutral gas density measurements via interferometry of the accelerator stage with the transverse direction in the x-direction. The height above the orifice of the gas jet is labeled on the left y-axis, with density line-outs for selected heights above the target corresponding to the right y-axis. 75
5.5 Top-view diagnostic from the experiment demonstrating measurement of the plasma emission in the cases where the laser was shot in the transverse-center of the accelerator jet (a), and where the laser was shot along the highest density gradient edge of the accelerator jet (b). This is an example of the the target in 'Case 1' configuration. . . . 76
5.6 The transmission as a function of photon energy for the series of materials and material thickness that made up the vertical-grid X-ray filter with the material and the thickness in microns labeled. 77
5.7 The process correlating the angularly-resolved betatron spectra with the temporal measurement of the average energy within the electron beam from the X-ray CCD image of the streaked beam (a). This yields a critical energy to angle-of-emission correlation (b), which, combined with the top-view measurement of the trajectory angle along the longitudinal z position along the accelerator (c), can be used to measure the Z-position evolution of electron energy and angular pointing correlated to the longitudinal position within the accelerator (d). 78
5.8 Measurements of the streaking from various diagnostics for the straight-on transverse gradient case (case 1) and the grazing-incident angle case (case 2) as the transverse $x-$position of the accelerator is scanned. For case 1 results, a dotted line is added to represent the position where the laser enters the transverse density gradient so that points to the right side of the line are interacting with the transverse density gradient in the accelerator. The measurements shown are the difference of positions of the laser center at the entrance and exit of the accelerator (a, e), the angular deviation of the peak of the betatron beam on the X-ray CCD with respect to the central laser axis (b, f), the transverse angular deviation of the electron beams measured on the Electron spectrometer (ESPEC) (c, g), and processed angularly-integrated ESPEC scintillator images (d, h) for each shot at a given x position. 79

5.9 The resulting ESPEC waterfall plots for two target $x-$position scans for the case 1 geometry (top row) and for case 2 geometry (bottom row) when the raw ESPEC images are only median filtered (left column), and where they have been through de-noise image processing and Fourier filtering (right column). These are same ESPEC waterfall plots that are shown in (d) and (h) in Figure 5.8. Each column in these waterfall plots represents an ESPEC image integrated in the angular direction of the scintillator screen. The colorscale in each of the four axes is normalized to the maximum dN/dE within its respective axis. 82

6.1 Experimental setup. The main laser first focuses into the accelerator gas cell which has an interferometer probing its plasma. The beams propagate a distance of 1.7 cm to the next filamentation gas cell, which spans a length range of 0.2 cm to 15 cm and is also probed for an interferometer measurement. This second gas cell was controlled independently from the first, allowing measurement of the electron beams with and without filamentation gas within a data run. The electron beams then traveled to the 45-degree oriented electron profile (EProfile) LANEX scintillating screen, which has an image captured by a CCD oriented 45 degrees with respect to the screen's normal vector. Finally, the electron beam exits the back of the chamber through a 1" Ultem window (not shown) and travels into a 0.97 T dipole system to disperse the electrons onto a LANEX scintillator to measure the energy of the produced beams. 87

6.2 Representative filamentation hydrogen gas on (top row) / off (bottom row) pairs of shots for different lengths and filamentation gas cell plasma density as labeled above every column of images. 90

6.3 Qualitative example of sequential filamentation hydrogen gas on (red) vs. off (blue) shots for the 3 filamentation gas cells used. The color scale for each of the three cell groups is normalized to the maximum integrated dN/dE for the examples in each cell. . 91

6.4 Examples of 1) raw EProfile images and 2) the inferred filamentation parameters of beam area (light blue), filament FWHM charge area (red), and individual filaments (light green) from the image processing algorithm on a) a nonfilamented reference shot with one filament, b) a moderately filamented shot with four filaments, and c) a highly filamented shot with ten filaments. 92

6.5 Weighted 10×10 histogram spanning the length (x-axis) and filamentation plasma density (n_p) parameter space that was scanned in the experiment. Blank spaces in this parameter space represent regions where data was not taken or there were not enough valid shots to provide reliable statistics. 93

6.6 Evolution of the I) total area of the beam on the EProfile screen, II) number of inner-contour filaments that exceed a minimum area threshold, III) the integrated pixel values in the global region (50% of the max contour value or larger) to integrated inner-contour filament pixel values, and IV) The ratio of average energy of the nearest 6 reference shots to the energy of a given data shot, assuming a threshold signal-to-noise ratio on the ESPEC screen. The x-axis is the length of the filamentation gas target interaction times the measured filamentation background plasma frequency divided by the speed of light (number of plasma wavelengths). Each data point is an equally weighted bin of averaged data with the standard deviation of that data shown around the average as error bars. Linear fits are shown to highlight the behavior of these measurements as a function over the scanned parameter space for length and plasma density. 94
6.7 The estimated growth rate multiplied by the elapsed filamentation time of the CFI instability with hydrogen gas in the filamentation gas cell given the average of a filamentation shot's nearest 6 reference shots' energies (yielding γ and β), as well as their inferred average beam density from the measurement of charge and divergence. Instability growth is plotted both in the style of Figure 6.6 (left) and Figure 6.5 (right). 95
6.8 3D OSIRIS simulation of an ~ 360 MeV electron beam propagating through a background plasma with a density of 10^{18} cm^{-3}. Row 1 shows the $p_y - p_z$ phase-space while rows 2-4 show slices taken near the middle of the beam at $x = 0.4$ μm of the beam density and magnitude of the in-plane electric and magnetic fields. 98
6.9 3D OSIRIS simulations of an ~ 360 MeV electron beam propagating through vacuum (row 1 and 2), through a background plasma with a density of 10^{18} cm^{-3} (row 3) and with an energy ~ 100 MeV propagating through the same background (row 4). 99
6.10 2D OSIRIS simulation of an ~ 360 MeV electron beam propagating through a background plasma with a density of 10^{18} cm^{-3}. The beam is seen to rapidly focus due to the partial shielding of the electric field. 100
6.11 The laser intensity (a) and the relative ionization level (b) from the laser power along the radial and longitudinal range of the filamentation gas cell. Longitudinal positions are relative to the front of the acceleration gas cell for hydrogen (top-left), helium (top-right), nitrogen (bottom-left), and argon (bottom-right). 102
6.12 2D histogram (top left) and 1D binned evolution of the measured growth parameters (top right) for helium filamentation gas with axes identical to that of Figure 6.5 and Figure 6.6. Measured estimates of the initial CFI growth rate in these two visualization styles are oriented directly beneath the 2D histogram and 1D binned fit plots. 103
6.13 2D histogram (top left) and 1D binned evolution of the measured growth parameters (top right) for nitrogen filamentation gas with axes identical to that of Figure 6.5 and Figure 6.6. Measured estimates of the initial CFI growth rate in these two visualization styles are oriented directly beneath the 2D histogram and 1D binned fit plots. 104
6.14 2D histogram (top left) and 1D binned evolution of the measured growth parameters (top right) for argon filamentation gas with axes identical to that of Figure 6.5 and Figure 6.6. Measured estimates of the initial CFI growth rate in these two visualization styles are oriented directly beneath the 2D histogram and 1D binned fit plots. 105

7.1 Diagram of the laser, targets, and diagnostic setup used in this campaign. The laser first interacts with the laser wakefield acceleration (LWFA) plasma accelerator target. Then, it is diverted with the tape drive so solely the electrons can propagate from the accelerator to the converter target. After this is an emittance mask followed by a lead wall with a collimation aperture. Electrons (red) and positrons (blue) are separated by Dipole 1 and interact with scintillators for electrons (LE1 & LE2) and positions (LP1 & LP2). Positrons also interact with an energy band selection aperture and are steered back toward the laser axis with Dipole 2. 112
7.2 Typical examples of measurements of the LWFA electron beam source. a) Angularly-resolved and b) angularly-integrated electron spectra from the accelerator (red), along with the average (black) and standard deviation (grey) of example shots. Also shown is a simple analytic approximation used as an input for the spectrum of electron beams in Monte-Carlo positron generation simulations. c) A snapshot of the plasma emission from the accelerator during a shot on this experiment with a description of the gas jet. 116
7.3 Positron spectra measured after energy-selection for different positions of the energy selection slit. The data is background-subtracted and smoothed with a Gaussian filter that spans a 10 MeV bandwidth, as indicated by the shaded RMS scatter error in the data. The central energy and FWHM bandwidth of each spectrum is noted in the legend of the figure. 117
7.4 Example a) positron and b) electron spatial charge density as a function of position on the LE1 and LP1 screens (x_p, y_p, x_e, x_e) for a single shot with a converter thickness of 8.0mm and the emittance mask in the beam-line. The particles corresponding to the given particle energies in MeV are shown as vertical red dashed lines. 118
7.5 Measured electron and positron beam properties as functions of particle energy for different converter thicknesses. The a) spectra (charge per 5% bandwidth), b) source size, c) divergence, and d) geometric emittance are given for each converter length as shown by the color-bars at the side of the figure. For each converter thickness, only the shots resulting in the highest charge of the positron beams were used for the analysis; the lines shown are thus an average of 4, 6, 3, and 8 shots for converter lengths of 1.0, 2.0, 4.0, and 8.0 mm, respectively (rms variation of $\approx 43\%$ in the spectrum and $\approx 20\%$ in emittance). Each line results from a Gaussian weighting of each measurement point using a kernel width of $\sigma E = 25$ MeV. The typical input electron spectrum (black-dashed) is shown in a) for comparison 119
7.6 Positron beam a) spectrum (charge per 5% bandwidth), b) source size, c) divergence, and d) geometric emittance plotted for a 1.0 mm thick lead converter. The experimental data (red) is plotted alongside FLUKA simulations for zero drift distance for the primary electron beam (black); including the drift distance and the primary electron beam divergence and source size (cyan dashed); and including the 12.6 mrad shielding aperture (blue). 121

7.7 a-b) The longitudinal electric fields of the plasma wakefield are generated by the laser pulse (yellow orb) and the witness positron bunch (density in a logarithmic color-scale) at the beginning of the plasma and after 96 mm of propagation. c-d) The positron longitudinal phase space before and after acceleration, with the energy spectra indicated by the red lines. e) The average energy and normalized emittance of the trapped bunch, defined as being comprised of particles that remain within ± 50 μm of the central axis. 123
7.8 Output in same format as Figure 7.7 for the output of a simulation that only includes positrons with energy above 500 MeV from the input FLUKA-generated particles. This demonstrates the chromatic selection that would be present in a magnetic chicane or quadrupole electron transport system. 124

8.1 Example of magnetic focusing experienced by energy-selected positron beams (bottom) diagnosed through numerically stepping particles with parameters consisting of a Gaussian spread of angular distribution from on-axis to 24 mrad through an analytic model of dipole fields similar to those used in the experiment (top). 133

B.1 Sequential filamentation gas cell on / off shots to compare the structured beams due to the filamentation cell compared to local reference shots for the shortest-length filamentation cell. Each image's color scale is normalized minimum and maximum range in pixel intensity values of that image. 141
B.2 Sequential filamentation gas cell on / off shots to compare the structured beams due to the filamentation cell compared to local reference shots for the intermediate-length filamentation cell. Each image's color scale is normalized minimum and maximum range in pixel intensity values of that image. 142
B.3 Sequential filamentation gas cell on / off shots to compare the structured beams due to the filamentation cell compared to local reference shots for the longest-length filamentation cell. Each image's color scale is normalized minimum and maximum range in pixel intensity values of that image. 143

C.1 Physical measurements of the beveled region of the blade that was utilized in the shock injection experiment which produced high-energy ($E > 1$ GeV), monoenergetic ($\Delta E < 10\%$) electron beams from a moderate-power ($P_L < 200$ TW) LWFA driver. The angles between the horizontal bulk blade body and the angled portion that leads to the knife edge are measured to be approximately 172° on the top surface of the blade and 168° on the bottom of the blade. 144

LIST OF TABLES

TABLE

1.1 Comparison of different modern electron accelerators and their documented maximum acceleration gradients and maximum output beam energies. 3

7.1 Summary of measured and inferred positron parameters, compared with sources used for previously reported proof-of-principle positron wakefield acceleration experiments and the modern linear accelerator positron beamline at SLAC's FACET-II. *Note that this value is the RMS of a uniform distribution with a width of 14 μm. 127

LIST OF APPENDICES

A Linear Growth Rate for the Filamentation of Warm Ultrarelativistic Beams 135

B Current Filamentation Instability: Electron Transverse Profile Examples 140

C Characterization of Shock-Front Inducing Razor Blade 144

LIST OF ACRONYMS

ALEPH Advanced Laser for Extreme Photonics

ALLS Advanced Laser Light Source

CFD computational fluid dynamics

CPA chirped pulse amplification

DOE Department of Energy

ESPEC Electron spectrometer

FROG frequency-resolved optical gating

FWHM full-width half-maximum

INRS Institut National de la Recherche Scientifique

linac linear particle accelerator

LWFA laser wakefield acceleration

Nd:Glass neodymium-doped glass

Nd:YAG neodymium-doped yttrium aluminum garnet

OAP off-axis parabola

PIC Particle-In-Cell

RF radio-frequency

SHG second-harmonic generation

Ti:Sapphire titanium-doped sapphire

QED quantum electrodynamics

ABSTRACT

This thesis describes the results of four experiments using Laser Wakefield Acceleration (LWFA) to generate highly relativistic electron beams. These beams were subsequently used to optimize beam energy and relative energy spread, develop a novel spectral diagnostic for these systems, and conduct applied studies into the current filamentation instability and positron generation.

The first experiment described in this thesis demonstrates shock injection of electrons into a laser wakefield accelerator producing high energy ($E > 1$ GeV) and low relative energy spread ($\Delta E/E < 10\%$) electron beams. This shock injection technique was optimized through a scan of the position of the shock-producing blade, and an average increase in charge, an increase in relative energy spread, and a decrease in maximum energy with an increase of the shock position toward the center of the accelerator's length is measured.

The second work detailed in this thesis demonstrates the angular streaking of a laser driver due to transverse plasma density gradients from a supersonic gas jet along the propagation length of a wakefield accelerator to measure the angular dependence of the critical energy of the resulting betatron X-ray beams emitted from the trapped LWFA electron beams. The critical energy of radiation from the betatron oscillations of the electron beam correlates with electron beam energy within the accelerator. This work uses this fact to describe a novel diagnostic technique for measuring temporally resolved on-shot electron beam energy gain.

Beams produced via LWFA were used to study the development of the Weibel-like relativistic current filamentation instability by propagating them into an independently controlled filamentation cell with parametrically scanned length, plasma density, and ionizing gas species. We find a general agreement with the predicted relative amount of growth of the instability, with devia-

tions explainable through statistical fluctuations and nonlinear behavior in the highly developed filamentation parameter space.

The first demonstration of an LWFA electron beam source of positrons with sufficient spectral and spatial quality to be injected into a plasma accelerator is reported in this work. Selection and transport of positron beamlets containing $N_{e+} \geq 10^5$ positrons in a 5% bandwidth around 600 MeV with inherent femtosecond-scale duration and micron-scale normalized emittance is shown. While the ~ 16 fC positron beams have relatively low charge compared to the nC's of charge from conventional accelerator sources, the charge of the beams produced from similar LWFA sources is expected to scale favorably with increasing laser driver power.Numerical simulations show the feasibility of these beams to be injected and further accelerated via LWFA.

The results presented in this thesis should help LWFA experiments to improve the spectral qualities of the electron beams they produce, control the filamentation of these beams due to propagation in plasma media, and provide relativistic positron beams suitable for positron wakefield acceleration.

CHAPTER 1

Introduction

1.1 Brief history of electron accelerators

Acceleration and control of high-quality relativistic particle beams is a crowning achievement of humanity's scientific pursuit which has led to breakthroughs over the past two centuries in many fields, from understanding the structure of the atom and nuclear interactions to the development and confirmation of the Standard Model description of the universe. While large-scale multinational accelerator facilities have been a boon to scientific research into a myriad of fundamental physics questions, accelerator facilities also exist for a variety of applications such as particle radiation sources for medical therapies, industrial material processing, production of medicinal isotopes, or bright light sources with photon energies extending into the hard X-ray regime for use in industrial imaging and crystal diffractometry scattering measurements.

While what constitutes the first particle accelerators can be debated, for the sake of this document studies involving the electrostatic acceleration of electrons in the late 1800s will set the start date for the field. These DC voltage-based accelerators led to the discovery of the electron in 1897, the discovery of X-ray radiation and experimental observation of the photoelectric effect in 1895, the development of the Rutherford model of the atom from experiments in 1906 and 1911, and helped generally kick off the fields of quantum mechanics and the standard model in the early 20th century. The energy-gain limit in this accelerator is directly proportional to the potential difference between the cathode and anodes, typically limited to the range of MV. However, energies could be

increased by adding more electrostatic acceleration stages.

The next major development in electron accelerators came in 1924 when Ernst Ising proposed the concept for radio-frequency (RF) acceleration in a linear accelerator for ions, which was experimentally achieved by Rolf Widerøe in 1928. These devices' acceleration gradients per stage are limited by the cavity material's voltage breakdown limits, which physically is around $100\ \mathrm{MVm}^{-1}$, but with operating limits typically closer to $10\ \mathrm{MVm}^{-1}$. At the largest linear particle accelerator (linac) user facility the Stanford Linear Accelerator (SLAC), for example, the acceleration gradient is $17\ \mathrm{MVm}^{-1}$ [1]; although, acceleration gradients have reached up to $65\ \mathrm{MVm}^{-1}$ at a test linac at the Japan Linear Collider [2], and plans for the future Compact Linear Collider at CERN involve accelerating structures supporting $100\ \mathrm{MVm}^{-1}$ [3]. In theory, the energy gain of the electron beam in a linear accelerator is only limited by the number of acceleration stages and the acceleration gradient per stage - thus making the practical limitation the required economic investment for these facilities.

After the development of the linac, Ernest Lawrence's 1931 cyclotron improved control of the acceleration method using circular motion of charged particles in a magnetic field to control the phase of the particles in a cylindrical accelerator. The invention of this circular-orbit accelerator concept directly led to the adaption of the cyclotron design for lepton accelerators and storage rings with the advent of the first betatron accelerator in 1940. A limitation of circular-orbit accelerators is that they suffer from radiative losses from accelerating radially which is made worse as energies are pushed higher due to a γ^2 scaling to these losses, where $\gamma = \left(1 - \frac{v^2}{c^2}\right)^{-1/2}$ is the relativistic Lorentz factor.

The material and rigid size limits of betatron accelerators were addressed with the construction of the first synchrotron in 1949, which used time-varying magnetic fields to control the orbital phase of electrons at specific energy ranges, linac-like electromagnetic cavities to accelerate particles and dipole magnets to control the steering and energy properties of the particles as they are accelerated. The record for lepton energies from a synchrotron was set by the Large Electron-Positron accelerator in 2009, reaching energies of $E > 104\ \mathrm{GeV}$; which corresponds to

Accelerator	Max Acceleration Gradient (MVm^{-1})	Max e^- Energy (GeV)
Linear Accelerator	65 [2]	50 [1]
Betatron	2.7	0.315 [5]
Synchrotron	7.5 [6]	104.5 [6]

Table 1.1: Comparison of different modern electron accelerators and their documented maximum acceleration gradients and maximum output beam energies.

$E > 209$ GeV in the center-of-mass frame of the electron/positron collisions [4]. As higher energy gains of particles eventually necessitate both an increase in the radius of the synchrotron and an increase in the fields they can produce, they have functionally reached the point where cost is the limit of achieving higher energies. Synchrotron accelerators also suffer γ^2 radiative losses from accelerating electrons in a circular orbit.

These limits to synchrotrons spurred interest in optimizing RF linac facilities and developing hard X-ray radiation sources from their beamlines. To this end, in 2009 SLAC converted 1 km of its total 3 km acceleration length into a light source facility, the Linac Coherent Light Source (LCLS). This facility relies on injecting beams accelerated from the first 2 km of the facility into a long magnetic undulator device to create a novel X-ray free-electron laser (FEL) producing coherent X-ray beams with energies between 0.48–10 keV with temporal duration under 100 fs. This facility demonstrated the injection of high-energy electron beams to generate ultrashort, bright, coherent X-ray beams. Work on a second FEL beamline at SLAC, the LCLS-II, began development in 2016 and is expected to produce X-ray pulses with maximum photon energies higher than that available from LCLS and at a much higher repetition rate.

A comparison of the maximum acceleration gradients that various modern accelerators have produced is shown in Table 1.1. The maximum energy gain in these accelerators going forward is mainly limited today by the cost and size of the accelerators themselves, as the acceleration gradients have material limits that cannot be exceeded without inducing plasma breakdown of the accelerator's cavities. Given the limits of conventional lepton accelerators and the desire to increase electron beam energies further to push the boundaries of high-energy physics, there is a motivation

to develop alternative accelerator technologies that allow for larger acceleration gradients to serve as compact high-energy injector sources for conventional accelerators, or to one day potentially replace large linac and synchrotron facilities altogether with compact accelerator facilities. The field operating limits of conventional RF accelerators are due to material breakdown into a plasma if excessive voltage is applied to drive acceleration. This damage can also be caused by the material interacting with wakefields that follow relativistic particle beams. Thus, the natural question arises as to what material can sustain a significantly increased accelerating gradient without inducing a transition into a breakdown of the accelerating structure into a plasma. There is an obvious answer: plasma. Over the past half-century, scientists have developed a promising alternative accelerator concept in the plasma wakefield accelerator. The question of how one could set up an acceleration gradient within a plasma medium is addressed in the following section.

1.2 Laser wakefield acceleration

Laser wakefield acceleration (LWFA) is a method of accelerating charged particle beams in the wake driven by an intense laser pulse with a longitudinal duration of less than the plasma wavelength. LWFA is achieved by focusing an ultrashort laser pulse into a neutral gas to both ionize the gas and force plasma electrons away from the laser's propagation axis, which sets up a strong acceleration gradient that follows the laser pulse. The longitudinal acceleration gradients found in these plasma wakefields typically exceed 100000 MVm^{-1}, which is nearly four orders of magnitude higher than the operational acceleration gradients of 10's of MVm^{-1} seen in conventional accelerators. These large acceleration gradients offer an alternative particle acceleration mechanism that can produce electron beams in a few centimeters of acceleration on energy scales similar to those seen in hundreds of meters of RF accelerating fields. LWFA falls under the broader category of plasma wakefield accelerators, which can alternatively be driven by highly relativistic particle beams with a technique known as plasma wakefield acceleration (PWFA) [7], or by a self-modulated laser or charged particle beam in self-modulated laser wakefield acceleration [8] and

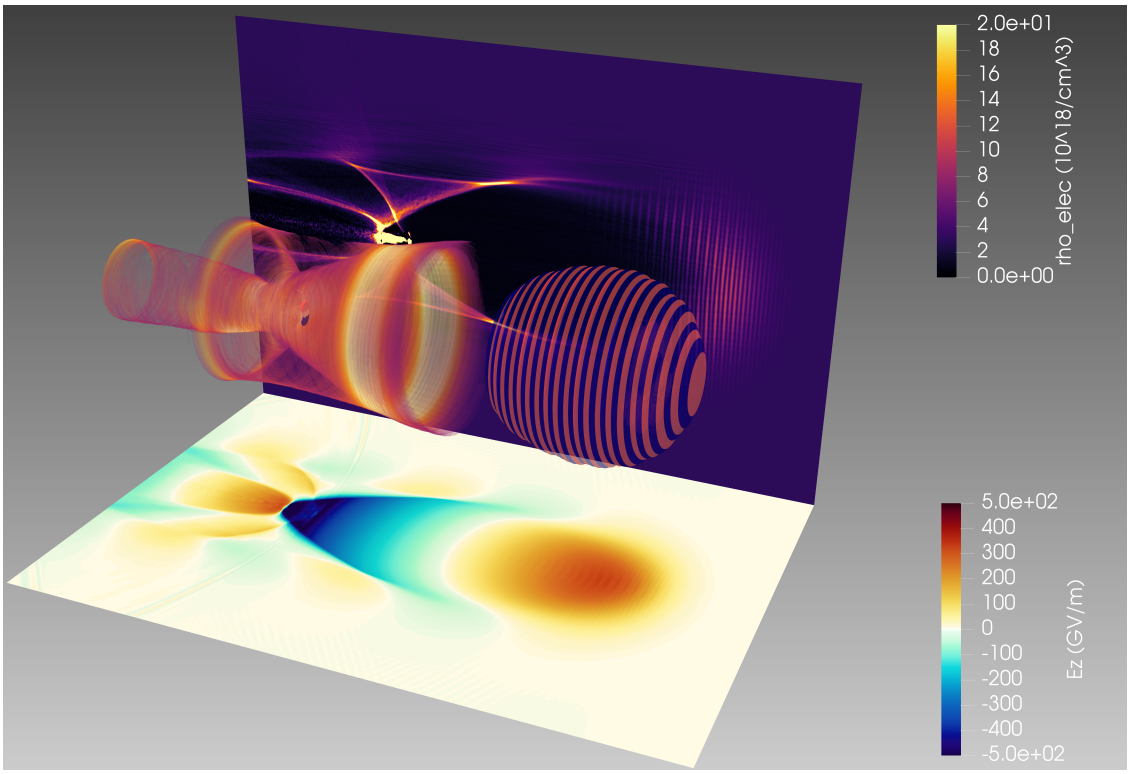


Figure 1.1: Three-dimensional visualization of a PIC simulation of laser wakefield acceleration in the nonlinear bubble regime using a normalized laser intensity a0 = 6, a beam waist of 22 μm, FWHM beam duration of 27.3 fs, and a plasma density of 3×10^{18} cm^{-3} using the FBPIC PIC code. The purple-to-yellow colormap shows electron density, and the projection of the longitudinal accelerating field is shown in the blue-white-red colormap. Simulation and visualization completed by Dr. Daniel Seipt (Helmholtz-Institut Jena).

seeded self-modulated plasma wakefield acceleration [9].

The laser-driven acceleration technique was first conceived by Toshiki Tajima and John Dawson in 1979 [10]. The timing of this publication shows impressive foresight to anticipate laser driver intensities, which were not realizable at the time, as it took a Nobel prize-worthy advancement to ultrashort laser technology in 1985, chirped pulse amplification (CPA) [11], and then further development of ultrashort laser technologies to bring driving lasers both short and energetic enough to be capable of testing the concept. It was, in fact, 25 years that separated Tajima and Dawson's original publication and the publication of the first successful demonstrations of electron beams with monoenergetic peaks in their spectra via LWFA in 2004 by three separate experimental campaigns [12–14]. The field rapidly developed in tandem with high-power ultrafast laser capabilities

worldwide stemming from improved laser facilities and refined engineering techniques to produce higher energy, more monoenergetic, and higher charge electron beams from these accelerators. Advances in laser facilities are ongoing with, for example, the construction of the ZEUS laser facility, which will be the most powerful laser system in the United States when completed [15]. The rapid increase in laser powers available around the world has made possible not only wakefield acceleration experiments but also led to a boon in the production of laser-driven ion beams [16, 17], high-harmonic generation in the interactions between intense lasers and plasmas [18, 19], and laser-driven indirect-drive inertial confinement fusion [20], among many other fields.

There have also been advances in refining the wakefield accelerator mechanisms, with a significant focus in recent years being put toward studying, to name one example, 'dephasingless' laser wakefield accelerators, which overcome the dephasing limit in accelerators by controlling the phase velocity of the focal point of a laser to either be superluminal or subluminal by exploiting either radially-dependant phase delay on the pulse before focusing [21] or by exploiting chromatic separation of the pulse via temporal chirping and chromatic-dependant focusing [22].

Because the energy gain of the electron beams produced via non-linear LWFA scales proportionally with the normalized strength parameter $a_0 = \frac{e|A|}{m_e c} \approx 8.55 \times 10^{-10} \lambda[\mu\mathrm{m}] \sqrt{I_0[\mathrm{W/cm^2}]}$ of the laser driver [23, 24], resources have been devoted to developing increasingly high-power lasers on the Petawatt scale in many parts of the world [15, 25]. With the global investment into LWFA systems, there have been ample opportunities to study both the physics and optimization of LWFA itself [26, 27]; as well as opportunities to use accelerated beams, for example, in high-energy astrophysics and strong-field QED experiments [28, 29].

One question that has been studied since the early experiments into laser wakefield acceleration is how exactly the electrons that get accelerated in the wakes traveling through a plasma with relativistic phase velocity find their way into the wakefield structure in the first place. This process is called injection by the LWFA community. Given the potential profiles in the wakefield and the phase velocity in which the structure is moving, one can derive the phase space trajectories from the Hamiltonian of electrons in the frame of reference co-moving with the laser driver. An example

of the phase space trajectories from a laser driver with $a_0 = 0.1$ can be found in Figure 2.2. A consequence of these trapped orbits existing within wakefields suggests that electrons must meet a combination of position and longitudinal velocity conditions for them to find themselves on one of these trapped trajectories.

There are several methods by which electrons fall within the requisite parameters for injection. The simplest of these methods is self-injection: electrons from the background plasma can gain longitudinal energy both from the direct interaction of the laser pulse and from the strong space charge field set up by the laser expelling electrons radially via the ponderomotive force. A detrimental quality of this injection technique is the continuous nature of this injection, leading to an electron beam consisting of particles that have undergone different amounts of acceleration lengths, yielding a wide energy spread. Other injection techniques such as ionization injection [30] and density downramp injection [31] seek to localize the longitudinal position of charge injection into the accelerator to ensure equal-acceleration length (and therefore equal energy gain) for all of the injected charge to produce monoenergetic beams. Shock injection, which is the extension of down-ramp injection where the density down-ramp is on a longitudinal scale similar to the plasma wavelength, has been shown to most-reliably produce low-energy spread electron bunches compared to other injection mechanisms [32]. Historically, the downside of shock injection has been that it has not efficiently accelerated the injected electron bunch to as high energies as beams produced via self-injection and ionization injection.

The improved fidelity of laser wakefield accelerators over the past several decades has allowed researchers to apply beams produced via LWFA to study astrophysical phenomena relevant to high energy density plasma experiments. One subject that has garnered attention from facilities that produce on-axis highly relativistic electron beams is the current filamentation instability. This is a beam-plasma instability akin to the general Weibel instability, with the restriction that the beam species is highly relativistic and has a transverse size greater than the cold, stationary background plasma's skin depth. Observation of the growth rate of these instabilities is achievable in laboratory scale lengths with commonly used plasma and beam parameters produced in both alternative

and conventional accelerator facilities [28, 33]. These previous experiments studying the relativistic current filamentation instability scanned only a somewhat limited parameter space to track the statistical growth of the instability, and a prior study with a LWFA electron source had the electrons transition directly into a background plasma through transitioning past the pump depletion length of the accelerator, therefore not isolating the plasma conditions in the accelerator and the filamentation plasma.

As alternative accelerator technologies have evolved, attention has been given to the potential to use plasma-based accelerators to achieve phenomena only available to a few accelerator facilities. An example of such a phenomenon is the production of positrons suitable for injection into an accelerator, which in recent history has been dominated by the SLAC accelerator facility FACET-II [34–36]. The positron beams for this application must have %-level energy spreads, femtosecond-scale duration, and micron-scale normalized emittance [37]. A contemporary literature review from Cao et.al [38] details the history and results of experimental studies of positron acceleration in plasmas. Studies have demonstrated the ability of LWFA electron beams to produce electron/positron pair beams through the collision with a high-Z target [39]; however, prior results of LWFA-based sources of positron beams have not had all of the required qualities for injection into a wakefield accelerator.

1.3 Thesis outline

This thesis details results from four LWFA-based experimental campaigns. Two of these experiments focus on laser wakefield accelerators as an electron accelerator technology, with one study optimizing electron beam energy qualities through shock injection, and another developing a novel LWFA diagnostic to take temporally-resolved measurements of electron energy gain. The remaining experiments focused on applying LWFA electron beams in studies on current filamentation instability and laser-accelerator-based generation of positrons suitable for injection into a plasma accelerator. These experiments are introduced as the main chapters in this dissertation:

- **Monoenergetic beams from a laser wakefield accelerator via shock injection** Electron beams with energies $E >$ GeV levels with low relative energy spread were produced in a laser-driven wakefield accelerator utilizing a sharp-density downramp injection technique known as shock injection. This experiment shows the electron beams' chromatic dependence on the longitudinal position of the shock-producing blade in the accelerator target. In particular, the dual goal of minimizing the relative energy spread and maximizing the electron beams' peak energy by changing the shock's position concerning the driving laser's focal position is measured and discussed.

- **Streaked laser wakefield trajectory producing pointing vs time correlation in wakefield accelerator** Here, results are discussed from an experiment that used controlled transverse density gradients in the LWFA gas target to angularly streak the laser driver as it propagates through the target. The resulting electron beams and betatron photon beams produced from the accelerator were measured with an electron spectrometer and an indirect detection X-ray CCD, respectively. The scattered light from a top view of the accelerator allowed for verification of the curved trajectory of the laser through the accelerator. A technique for single-shot electron energy growth measurement is provided for the first time. The correlation between the angular pointing of the electron beam in a longitudinal position along its acceleration path and the instantaneous angle of betatron emission onto the X-ray camera can be exploited by measuring the growth in X-ray energy along the streaked path on the X-ray CCD. The results from this experiment present a novel way to control the trajectory of a laser through a gaseous target and a novel diagnostic technique for measuring the energy growth of beams from wakefield accelerators.

- **Parametric studies of the current filamentation instability with laser wakefield accelerated beams** This experiment aimed to study filamentation growth in relativistic electron beams produced via LWFA by measuring filamentation modes in the transverse profiles of the beams. This experiment utilized two separated gas targets: an accelerator gas cell and

a filamentation gas. The acceleration of the electron beams and the plasma in which the filamentation was allowed to grow were independently controlled. The length and plasma density of the filamentation cell were scanned to measure the growth of the filaments in the beam. The expected relative growth of the instability based on a theoretical growth rate model is compared to experimental results, finding a general agreement with theory with statistical deviations and saturation effects in the longest lengths and highest background plasma density regime of the scans.

- **Laser-wakefield accelerator source of positron beams suitable for injection into a plasma accelerator** The result discussed in this chapter presents measurements of a laser wakefield accelerator-based source of positron beams with femtosecond-scale duration, micron-scale normalized emittance, and an energy-selected band around 600 MeV. Measured positron beams agree with results from Monte-Carlo simulations of the simulated electron beams interacting with a high-Z target used in the experiment. PIC simulations of the positron beams produced in this experiment being externally injected into a quasi-linear wakefield to experience subsequent acceleration are presented. These results demonstrate the possibility of using LWFA facilities to conduct positron acceleration experiments in a plasma wakefield.

CHAPTER 2

Theoretical Background

Presented here is the theoretical background for the major topics covered in this thesis. These broadly include the topics of wakefield acceleration, injection theory, and Weibel and relativistic current filamentation instability growth rate derivations. A brief introduction of fundamental expressions relevant to the physics of lasers/plasma interactions will first be presented, supporting topics that follow in subsections. Physics specific to an individual chapter in this thesis may be described in those chapters. Still, this chapter should provide enough background on the physics involved in the thesis to understand the topic of the following chapters. Most derivation steps are not explicitly included where citations to source materials deriving expressions are given. Unless otherwise stated, the expressions in this thesis are in SI units.

Plasmas are often defined in terms of a particular regime of three fundamental plasma parameters: the particle number density of each species n, the temperature of each particle species T, and the steady state magnetic field in the plasma B. The discussion of the physics of the laser/plasma interactions touched on in this dissertation generally focuses on plasma that has an underdense electron density, $n_e < n_c$ where n_c is the critical density (the electron density at which electromagnetic waves reflect instead of transmit through a plasma), which has a background electron plasma temperature that can be generally assumed to be cold, $T_e \approx 0$, and which is non-magnetized, $B = 0$. Typically, the phenomena focused on in this dissertation occur within a short duration compared to the characteristic ion motion time scale in the field strengths presented, but on the time scale to resolve electron response to electromagnetic fields; therefore, ions are assumed to be

at rest unless otherwise stated.

For a cold, non-magnetized plasma, the fundamental plasma frequency for electrons can be expressed as

$$\omega_p = \sqrt{\frac{n_e q_e^2}{\varepsilon_0 m_e}}, \tag{2.1}$$

where q_e and m_e are the charge and mass of an electron, and ε_0 is the vacuum permittivity constant. The critical density n_c describes when the laser frequency ω_0 equals the plasma electron frequency ω_p. By substituting ω_0 into Equation 2.1, one can solve for the critical density: $n_c = \frac{\varepsilon_0 m_e \omega_0^2}{q_e^2}$.

Through a process of linearizing the wave equation in a cold, collisionless, and nonmagnetic plasma, the dispersion relation of electromagnetic radiation in a plasma can be derived as

$$\omega_0^2 = \omega_p^2 + c^2 k^2, \tag{2.2}$$

which describes the relationship between the frequency of the electromagnetic wave and the resulting phase velocity, $v_\phi = \frac{\omega}{k}$, and group velocity, $v_g = \frac{d\omega}{dk}$. The index of refraction $\eta = \frac{v_g}{v_\phi} = \frac{ck}{\omega}$ of electromagnetic radiation in the plasma medium can be found from this dispersion relation, resulting in the formula,

$$\eta = \sqrt{1 - \frac{\omega_p^2}{\omega_0^2}} = \sqrt{1 - \frac{n_e}{n_c}}. \tag{2.3}$$

While the foundational relationships between electromagnetic radiation and plasmas are commonly derived assuming cold, collisionless, and nonmagnetized plasmas, amendments and higher-order effects can lead to adjustments to the expressions for the dispersion relation, index of refraction, and resulting derived terms. In particular, as is relevant to the work in this thesis, an intense laser pulse moving plasma particles to relativistic energies can give an energy dependence to, for example, the plasma frequency which is written as $\omega_p = \sqrt{\frac{n_e q_e}{\gamma m_e \varepsilon_0}}$, where $\gamma = \left(1 - \frac{v^2}{c^2}\right)^{-1/2}$ is the relativistic Lorentz factor. This relativistic energy consideration comes from the direct interaction between the laser pulse and particle species in the plasma, where the strength of the fields in the light is proportional to the square root of the pulse's intensity, which can be large enough to drive

relativistic motion. Adjustments to plasma theory from the cold, collisionless, and nonmagnetized plasma assumption to account for high-intensity laser pulse interactions have been studied previously, and as such, higher-order effects can be considered where necessary [40].

2.1 Laser wakefield acceleration

2.1.1 Single particle motion in a laser field

The basic single-particle motion of an electron in a laser field can be derived from a few simple sets of equations, including Maxwell's equations,

$$\nabla \cdot \boldsymbol{E} = \frac{\rho}{\epsilon_0} \tag{2.4a}$$

$$\nabla \cdot \boldsymbol{B} = 0 \tag{2.4b}$$

$$\nabla \times \boldsymbol{E} = -\frac{\partial \boldsymbol{B}}{\partial t} \tag{2.4c}$$

$$\nabla \times \boldsymbol{B} = \mu_0 \boldsymbol{J} + \mu_0 \epsilon_0 \frac{\partial \boldsymbol{E}}{\partial t}, \tag{2.4d}$$

as well as the planar description for an electromagnetic wave,

$$\boldsymbol{E}(\boldsymbol{x}) = E_0 e^{i(\boldsymbol{k}\cdot\boldsymbol{x}-\omega t)} \tag{2.5a}$$

$$\boldsymbol{B}(\boldsymbol{x}) = B_0 e^{i(\boldsymbol{k}\cdot\boldsymbol{x}-\omega t)}, \tag{2.5b}$$

and the relativistic Lorentz equation,

$$\frac{d\boldsymbol{p}}{dt} = q_e(\boldsymbol{E} + \boldsymbol{v} \times \boldsymbol{B}), \tag{2.6}$$

where $\boldsymbol{E}$ is the electric field vector, $\boldsymbol{B}$ is the magnetic field vector, μ_0 is the vacuum permeability term, and $\boldsymbol{p} = \gamma m \boldsymbol{v}$ is the momentum of a particle. The characteristic electron motion in an

intense planar electromagnetic field follows a figure-eight pattern due to the electric fields pushing the electrons away from the wave's propagation axis, while the magnetic fields impart longitudinal momentum to the electrons proportional to the electron's velocity (and mass). As the field strength in a laser field increases, the electron's γ magnitude in the influence of the laser field also increases due to Equation 2.6. Through a linearization of Equation 2.6 into fast and slow components, one can derive the time-averaged slow transverse motion of the electron due to what is referred to as the relativistic ponderomotive force [41],

$$F_{\mathrm{p}} = -\frac{e^2}{2\langle\gamma\rangle m_e}\nabla\langle \boldsymbol{A}^2\rangle, \tag{2.7}$$

where $\boldsymbol{A}$ is defined as the vector potential given by the relation $\boldsymbol{B}(\boldsymbol{x}) = \nabla \times \boldsymbol{A}(\boldsymbol{x})$ and terms enclosed by the angled brackets indicate cycle-averaged values over the laser phase. A useful term to describe the magnitude of this force for a given particle species is been defined as the normalized vector potential [42–44],

$$a_0 = \frac{e|A|}{m_e c} = \frac{e|E_0|}{m_e\omega_0 c} \approx 0.85\lambda_0[\mu\mathrm{m}]\sqrt{I_0[10^{18}\mathrm{Wcm}^{-3}]}. \tag{2.8}$$

This term describes a threshold in which the case that $a_0 > 1$ implies that electron motion in the transverse direction in the laser field is well in the relativistic regime, while if $a_0 \ll 1$, the interaction between the pulse and particles is considered to be non-relativistic. The ponderomotive force can thus be rewritten in terms of the normalized vector potential as

$$F_p = -\frac{m_e c^2}{\langle\gamma\rangle}\nabla\frac{a_0^2}{2}. \tag{2.9}$$

The relativistic ponderomotive force describes a net force in the radial direction away from the axis of a finite electromagnetic wave that acts to move mobile electrons away from the laser axis, proportionally scaling with the laser intensity. We note that while the ponderomotive force does not depend on the species charge, so both ions and electrons are pushed away from the central axis, we

are not concerned in the context of this thesis with the motion of the ions due to the time scales of the interactions with ultrashort pulses with a duration on the scale of 10's of femtoseconds interacting with plasma and a_0 scales inversely with the mass of the particle it is interacting with. Thus, for the pulses with normalized laser vector potentials for electrons used in this work are on the order of $1 \leq a_0 \leq 5$, the interactions with hydrogen ions would be on the order of $0.0002 \leq a_0 \leq 0.001$. Thus, the relativistic ponderomotive force in the regime of the laser drivers employed in this thesis describes the phenomenon of an intense laser expelling electrons away from its path. This sets up a charge separation between the electrons and the stationary ions, which pull the electrons back to the axis via an electrostatic plasma wave that travels behind the driving laser.

2.1.2 Laser propagation in a plasma & description of plasma wakefields

For the sake of this discussion, the description of the transverse and longitudinal envelopes of a laser driver will be assumed to follow a Gaussian profile unless otherwise stated. As a laser focuses over its propagation axis $\hat{z}$, to first-order the transverse beam waist defined as [45]

$$w(z) = w_0 \sqrt{1 + \frac{\lambda_L^2 z^2}{\pi^2 w_0^4}}, \tag{2.10}$$

where w_0 is defined as the minimum beam waist at the laser's focal plane. Generally in a uniform media, the beam remains roughly collimated with a tightly focused beam waist over a longitudinal distance known as the Rayleigh range $z_R = \pi w_0^2 / \lambda_L$, which is enclosed by the points around the focal plane where the beam waist is $\sqrt{2}$ times larger than w_0, and after which the edge of the transverse envelope of the beam linearly diverges away from the focal plane. In a plasma accelerator, maximizing the amount of time (i.e., propagation length) in which an electron beam experiences the acceleration gradient within a plasma wakefield results in higher maximum energies the accelerator can achieve. This motivates the apparent need for a long Rayleigh length, which could be achieved directly, for example, by using a large F-number focal optic. However, this would increase the focal plane waist of the beam, leading to a less intense beam along the focal length of

the laser pulse and a reduction in the a_0 parameter of the driving pulse.

Conveniently, there is a nonlinear intensity-dependant increase in the index of refraction of plasma due to the relativistic mass increase of electrons if they, through the ponderomotive force, reach relativistic velocities under the influence of the laser pulse. This increases the index of refraction toward the higher-intensity center of a highly-intense Gaussian laser pulse, leading to a focusing of the pulse. The onset of nonlinear self-focusing of a laser in a plasma medium can be triggered by the laser power crossing a critical power threshold [46, 47],

$$P_{\text{crit}} \simeq 17.5 \frac{\omega_0^2}{\omega_p^2} [\text{GW}]. \tag{2.11}$$

As the laser intensity due to this self-focusing increases, the a_0 parameter at the center of the pulse increases, further increasing this self-focusing instability. This intensity-dependant relativistic focusing effect is a waveguide-like phenomenon from the ponderomotive force: the pulse front pushes on-axis electrons off-axis, creating a radial density profile of higher-density plasma electrons surrounding the laser axis. This effect counters the natural diffraction of the focused laser for the duration that the pulse remains intense enough in the plasma to drive relativistic plasma waves, allowing for tightly focused laser pulses to be guided at a specified focal size at lengths longer than the Rayleigh length would limit [48]. At a matched spot size condition, these focusing and diffraction effects can be in equilibrium to have a collimated pulse at the diffraction-limited spot-size waist [23],

$$w_{\text{matched}} \simeq 2\sqrt{a_0} c/\omega_p. \tag{2.12}$$

As for longitudinal effects on the laser pulse, as it travels through a plasma, the longitudinal index of refraction gradients that the pulse interacts with creates a red-shift in areas where the pulse experiences positive plasma density gradients (typically at the front of a laser driving a plasma wave), and blue-shifts in regions of negative plasma density gradients. If the laser pulse's duration is more than that of half of the plasma wavelength, $L_{\text{laser}} < \lambda_p/2$, then the back of the pulse is expected to blue-shifted. This phenomenon is known as self-phase modulation and can lead to pulse

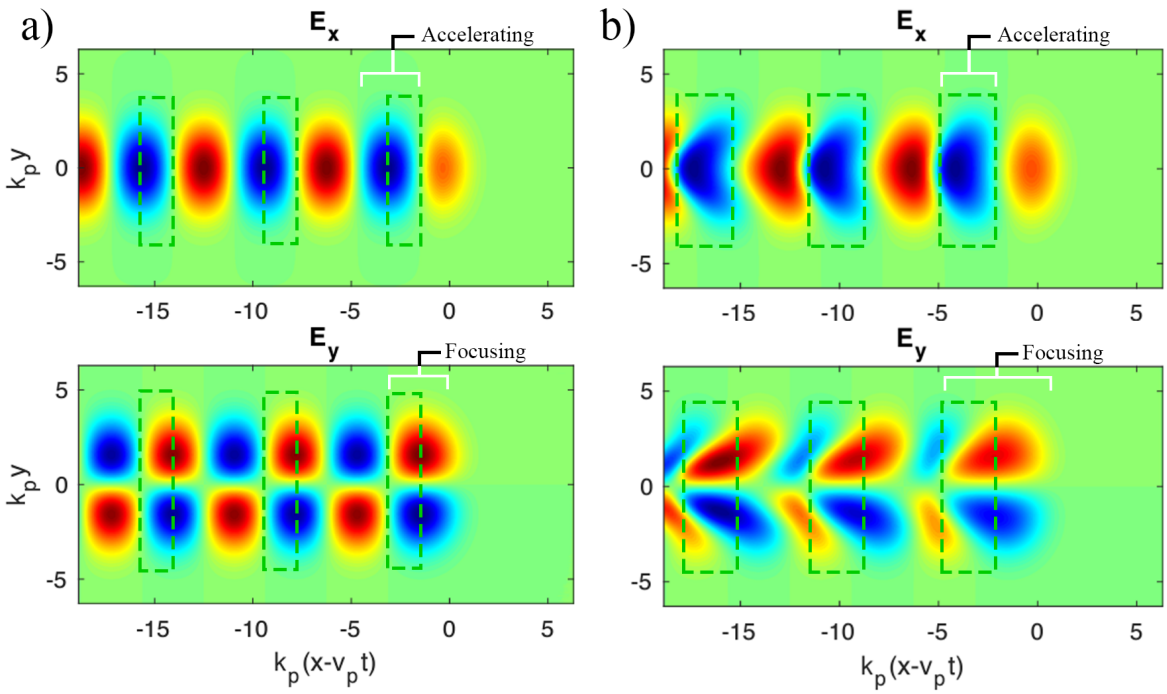


Figure 2.1: Diagram of longitudinal (top) and transverse (bottom) electric fields within a wakefield driven by a laser of the normalized vector potential of a) $a_0 = 0.1$ in the linear regime, and b) $a_0 = 1$ in the nonlinear regime. Regions of accelerating longitudinal and focusing transverse fields for electrons are labeled, with the accelerating + focusing regions enclosed with a dotted line. Adapted from [51].

compression in a plasma [49], or can be exploited to achieve bulk photon acceleration in specially tailored plasma density profiles [50]. It should be noted that the intensity-dependent phenomena of self-focusing and self-phase modulation-induced pulse compression are both instabilities that cause the pulse to become increasingly intense as it propagates through an underdense plasma.

As described in Section 2.1.1, a plasma wave is set up behind an intense laser pulse propagating through a plasma via the relativistic ponderomotive force. As the laser pulse moves with a group velocity near (but notably under) the speed of light in vacuum, this plasma wave's phase velocity through the plasma matches the driving pulse. The electric field within this plasma wave structure, as it travels in the wake of the driving laser pulse, is appropriately termed a laser-driven plasma wakefield. The radial expulsion force of the ponderomotive force is contrasted by the implosive force of the charge separation between the quasi-stationary ions that the electrons are pushed away from by the laser.

The balance between these two forces describes the regime of the plasma wave propagating behind the laser driver: the linear wakefield regime or the nonlinear blowout (or 'bubble') wakefield regime. In the linear regime, a linear sinusoidal-profile plasma wave is driven in the density profile of the plasma, with a sinusoidal profile of similar frequency describing the shape of the longitudinal accelerating/decelerating and, with a $\pi/2$ phase shift with respect to the plasma wavelength, transverse focusing/defocusing regions in the wakefield for an electron [24]. In the linear regime, the accelerating field E_z, focusing field E_r, and electron density profiles in the wakefield are given by [52]

$$\frac{E_z}{E_{p,0}} = -\frac{1}{k_p}\frac{\partial \phi}{\partial \xi} \tag{2.13a}$$

$$\frac{E_r}{E_{p,0}} = -\frac{1}{k_p}\frac{\partial \phi}{\partial r} \tag{2.13b}$$

$$\frac{\delta n_e}{n_{e,0}} = \frac{1}{k_p^2}\frac{\partial^2 \phi}{\partial \xi^2}, \tag{2.13c}$$

where $\phi(r,\xi) = -f(r)\sin(k_p\xi)$, $f(r) = a_0^2\sqrt{\frac{\pi}{2}}\frac{k_p}{4}\exp\left(\frac{-2r^2}{w_0^2}\right)\exp\left(-\frac{(k_p c\tau_0)^2}{8}\right)$, is the analytic solution for the (normalized) electric potential in the plasma wave in the linear regime with a gaussian ponderomotive driver, δn_e denotes the density change from an unperturbed plasma ($n_{e,0}$), and $E_{p,0} = \frac{m_e c\omega_p}{e}$ is the wavebreaking field. $\xi = z - v_p t$ is a term to denote the longitudinal coordinate in the frame of reference that is co-moving with the plasma wakefield. An example of the field structure from a linear wakefield can be found in Figure 2.1a.

In the nonlinear 'bubble' regime, wavebreaking is reached and the electrons are expelled completely around a region surrounding the laser axis, leaving a bare ion channel center. This regime has no analytical solution for nonlinear fields in 3D; however phenomenological scalings have been made to give approximations of the field structure in this regime [23], and 1D approximation for the field structure has also been derived in literature [24]. By assuming that the electron sheath surrounding the plasma wakefield is a perfect sphere, one can derive an approximation for

the accelerating and focusing fields [53],

$$\phi = \frac{k_p^2}{4}(r^2 - r_b^2) \tag{2.14a}$$

$$\frac{E_z}{E_{p,0}} = \frac{k_p}{2}\xi \tag{2.14b}$$

$$\frac{E_\perp}{E_{p,0}} = \frac{k_p}{4}r_\perp, \tag{2.14c}$$

where $r_b \simeq 2\sqrt{a_0}/k_p$ is an approximation of the plasma wakefield spherical radius, $r^2 = \xi^2 + r_\perp^2$ is the radius from the cavity center. A laser pulse most efficiently drives the nonlinear wakefield regime with a duration of at most half of a plasma wavelength, or $c\tau_{\text{laser}} \leq \lambda_p/2$ [10]. Note that these approximations for the fields scale linearly with ξ and $r_\perp$, with an acceleration gradient for electrons pointing toward the center of the wakefield, and thus in the regions far enough away from the electron sheath around the bubble, electrons are focused toward the central axis and accelerate if they are behind the longitudinal center of the bubble. This thus makes the nonlinear bubble regime of wakefield acceleration advantageous for electron acceleration, as nearly half of the plasma wavelength from the rear of the plasma wakefield bubble to the center is both accelerating and focusing. In the linear regime, in contrast, only a phase region spanning $\frac{\pi}{2}$ of the plasma wavelength's phase is accelerating and focusing. A numerical example of the 3D field structure in the nonlinear bubble regime can be found in Figure 1.1. An example of the field structure in a nonlinear wakefield can be found in Figure 2.1b.

In the case of positrons, the charge being opposite to that of an electron has the consequence that the regions that were favorably accelerating and focusing for electrons are decelerating and defocusing for positrons, and vice versa. Where the bubble regime is optimal for maximizing the favorable acceleration and focusing regions for electrons, it is suboptimal for accelerating positron beams. It is thus the quasi-linear regime for a normal Gaussian-pulse driver which increases the area that would be favorable for positron acceleration while maintaining enough intensity in the driver to achieve high acceleration gradients.

The regime of a given laser driver may conveniently be determined by knowing the laser driver's normalized vector potential a_0, where $a_0 \ll 1$ is strongly linear and $a_0 \gg 1$ is strongly nonlinear, with a quasi-linear transition region with $a_0 \sim 1$. The laser drivers used in this thesis all generated plasma wakefields in the nonlinear regime.

Within the field structures of the 3D nonlinear regime, scalings for electron beam qualities given laser and plasma properties have been derived [23]. These scalings suggest maximum energy gains $\Delta\gamma_{||}$ depending on the limiting factor of the accelerator: the dephasing length over which an electron beam reaches a velocity that surpasses the group velocity of the laser driver, $L_{\mathrm{deph}} \propto \frac{c}{\omega_p}\frac{4\sqrt{a_0}}{3}\frac{\omega_0^2}{\omega_p^2}$, or the pump depletion length over which the energy in the laser pulse is depleted to the point where the pulse can no longer generate the wakefields trailing the pulse, $L_{\mathrm{pd}} \propto ca_0\frac{\omega_0^2}{\omega_p^2}\tau$, where τ is the pulse duration. The derivations that arrive from these scalings suggest that electrons in a LWFA accelerator have a dephasing-limited maximum energy gain of $\Delta\gamma_{||} = \frac{2}{3}a_0\frac{\omega_0^2}{\omega_p^2}$, and a depletion-limited maximum energy gain of $\Delta\gamma_{||} = a_0^{2/3}\frac{\omega_0^2}{\omega_p^2}\omega_p\tau$. These scalings imply that the maximum achievable energy increases with pulse intensity, laser frequency, and decreasing plasma density.

2.1.3 Trapping & injection

Given the field structures in plasma wakefields noted in Section 2.1.2, one can derive the equation for the Hamiltonian of the wake given electromagnetic potentials ϕ and $\boldsymbol{A}$,

$$H = \sqrt{(mc^2)^2 + (\boldsymbol{P} - e\boldsymbol{A})^2c^2} - e\phi, \tag{2.15}$$

where $\boldsymbol{P} = \gamma mv + e\boldsymbol{A}$ is the canonical momentum, and γ can be written in terms of the canonical momentum as $\gamma = \sqrt{1 + (\boldsymbol{P} - e\boldsymbol{A})^2/m^2c^2}$. One can rewrite this expression in the wake's co-moving frame coordinate $\xi = z - v_\phi t$ to give the so-called wake Hamiltonian [51],

$$H_W = \sqrt{(mc^2)^2 + (\boldsymbol{P} - e\boldsymbol{A})^2c^2} - e\psi - v_\phi P_z, \tag{2.16}$$

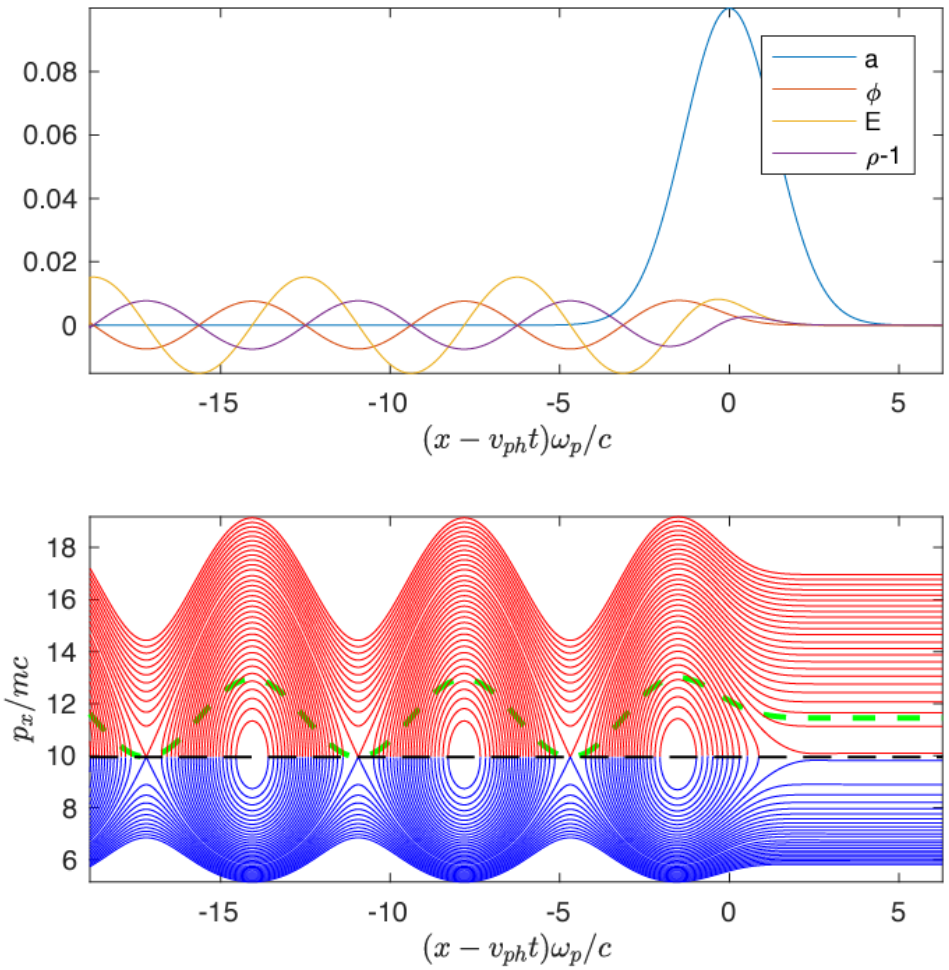


Figure 2.2: One-dimensional demonstration of (top) an $a_0 = 0.1$ laser driver wake potential ϕ, electric field E and density perturbation $\delta\rho$ and (bottom) the resulting phase space orbits allowed for particles at specific longitudinal positions with specific longitudinal velocities. The green dotted line represents the electric potential profile at different longitudinal positions. Reprinted from [51].

where $\psi = \phi - v_p A_z$. Assuming no temporal evolution of the wake, the Hamiltonian is conserved. The normalized wake Hamiltonian is given as a constant of motion,

$$\frac{H_W}{mc^2} = h_0 = \gamma - \beta_\phi u_z - \Psi, \tag{2.17}$$

where $\Psi = e\psi/mc^2$, $\beta_\phi = v_\phi/c$, and $u_z = P_z/mc$. This conserved Hamiltonian expression determines the trajectories of electrons interacting with a wakefield. Figure 2.2 displays an example of the determined electron trajectories plotted in the longitudinal momentum vs longitudinal position

phase space.

The Hamiltonian of the plasma wakefield system suggests that there are positions in the longitudinal phase space within the wakefield in which a particle's trajectory appears to be a loop, where the longitudinal velocity increases toward the center of the wake, it decreases as it overshoots the center position of the wake, and so on. These orbits in the phase space indicate a longitudinal position and momentum range in which electrons are 'trapped' within the wakefield structure. Given the orbital trajectory in phase space, to produce monoenergetic electron beams from a wakefield accelerator, one must have a narrow injection region within the wakefield (on the scale $\lesssim \lambda_p/4$). This single-particle trajectory approximation of particle trajectories is made more complex when assuming effects like dynamic evolution of the laser driver and/or wakefields via effects such as the field profiles in the wakefield plasma wave changing due to the electric fields from charge trapped in the wakefield, known as beam loading [54, 55]. Common properties of beams injected into an LWFA accelerator via self-injection include relatively high charge and moderate-to-high relative energy spread.

The process of charge being trapped on a loop trajectory in the wake Hamiltonian is called injection. There are several proven methods to inject charge into a laser-driven wakefield, some of which are detailed here. Self-injection can occur from electrons gaining adequate longitudinal energy through interactions in the high charge density sheath surrounding the wakefield bubble such that when the charge chaotically pushes far enough into the wakefield region, it becomes trapped [56, 57]. The threshold for self-injection to occur abundantly is typically around a laser wavelength times intensity value greater than $I\lambda > 10^{18}$ Wcm$^{-2}\mu$m^2.

Ionization injection is another injection technique in which the laser is focused into a gas species that has an inner-shell electron ionization potential near that of the peak potential of the laser field [58–60]. An approximation for the ionization intensity to ionize a given inner-shell ionization level-Z electron from an atom with ionization potential I_p can be written as,

$$I_{\text{thresh}} = \frac{cI_p^2}{128\pi Z^2 e^6}. \tag{2.18}$$

This technique can be combined with gas target shaping techniques to localize the ionization injection gas species region so that the injected charge undergoes uniform acceleration length [61]. Ionization injection has been shown to reliably control injection, showing tunability with electron energy and beam charge by balancing laser power, gas density, gas species, and localization of ionization gas species in the accelerator.

A final injection technique covered in this document is sharp density transition injection, otherwise known as shock injection. This injection technique is characterized by significantly reducing the plasma density in the target over a spatial scale on the order of a single plasma wavelength λ_p [62, 63]. The reduction of the plasma density grows the plasma wavelength, which increases the ion cavity radius for a wakefield in the bubble regime. When this transition occurs over a propagation distance similar to a plasma wavelength, the high charge density sheath surrounding the wakefield is suddenly placed in the accelerating field structure before the sheath charge has time to react. In the language of the Hamiltonian description of injection, if the geometry of the wakefield bubble changes at a specific rate, then the Hamiltonian will change at a given rate $\partial H_W/\partial t$. All particles far away from the wake are not trapped and have potentials $A = 0$, $\phi = 0$, thus $H_{W,\text{untrapped}} = \sqrt{1 + P^2c^2} - v_0 P_z > 0$. This implies a minimum condition for trapping of charge to be $H_W < 0$. It has been suggested, then, that the condition for sufficient electron trapping if the bubble is expanding fast enough, trapped electrons would meet the condition [64]:

$$\Delta H = \int \frac{\partial H_W}{\partial t} dt = \int \frac{d\xi}{v_\phi - v_z} \frac{\partial H_W}{\partial t} < -1, \tag{2.19}$$

where, as a reminder, v_ϕ is the phase velocity of the wake and $\xi = z - v_{\phi t}$. Several experimental studies have looked into this technique for producing electron beams this way. The extreme locality (small spatial scale) of the injection mechanism has proven to produce low-relative energy spread ($\Delta E/E < 10\%$) electron beams [32, 65, 66].

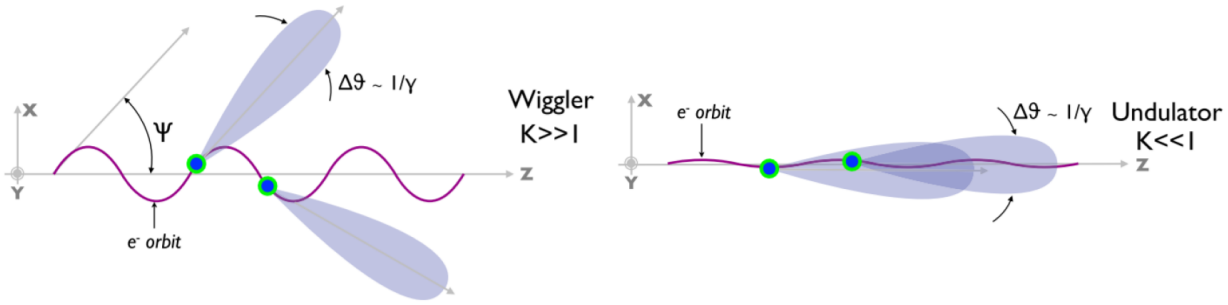


Figure 2.3: Diagram of the two betatron regimes of $K \gg 1$ wiggler regime (left) and $K \ll 1$ undulator regime (right). Reprinted with permission from [67].

2.1.4 Betatron radiation from LWFA electron beams

While a large focus of the previous discussion of electrons accelerated via LWFA concerned their longitudinal momentum, there are also important consequences from their transverse momentum in the wakefield. Electrons with any finite initial transverse momentum or initial off-axis trapped position will oscillate about and through the longitudinal axis of the wakefield. As electrons undergo these oscillations, broadband X-rays, known as betatron radiation, are produced.

A description of the transverse electron motion in the wakefield can be determined by the transverse fields in a wakefield, listed in Equation 2.14. Due to the oscillatory nature of electrons in the wakefield about the longitudinal axis, these oscillations can be described with a characteristic frequency called the betatron frequency,

$$\omega_{e,\beta} = \frac{\omega_p}{\sqrt{2p_z}}, \tag{2.20}$$

where the longitudinal momentum normalized to $m_e c\, p_z \simeq \gamma_\phi a_0 m_e c(1 - \xi^2/r_b^2)$ is assumed to be slowly varying.

A dimensionless parameter, K, is often used to describe the regime of X-ray radiation from the LWFA accelerator. $K = \gamma k_{e,\beta} r_{e,\beta}$ is a measure of the ratio of the oscillation amplitude to the wavelength which spans from a "wiggler" regime of large-scale oscillations compared to the betatron wavelength ($K \gg 1$) to an "undulator" regime of small-scale oscillations ($K \ll 1$), where

$k_{e,\beta} \simeq 1/\lambda_p\sqrt{2\gamma}$ is the angular wavenunmber for the betatron motion, λ_p is the plasma wavelength, and $r_{e,\beta}$ is the radius of the betatron oscillation about the central wakefield axis. In a case typical of LWFA experiments today, if a laser driver of $a_0 = 5$ is focused into a target with plasma density $n_e = 1 \times 10^{18}$ cm^{-3}, this would lead to a wakefield bubble radius of $r_b \approx 2\sqrt{a_0}c/\omega_p = 23.8$ μm. Electrons injected into this wakefield with energies of 1 GeV have $K > 1$ for all radii of betatron orbits down to an oscillation radius of 0.17 microns, corresponding to 0.7% of the wakefield bubble radius. If we assume an average oscillation radius of $\bar{r_\beta} = \frac{r_b}{4}$, this yields an average $K \approx 35$; well in the wiggler regime. Examples of these two regimes of betatron motion with exaggerated emission cones are found in Figure 2.3.

The radiation emission of electrons undergoing betatron motion largely depends on the dimensionless K parameter. For example, at the extreme limit where $K \ll 1$, the wavelength of the produced radiation from an electron undergoing betatron motion is [67],

$$\lambda_\beta = \frac{\lambda_u}{2\gamma^2}\left(1 + \frac{K^2}{2} + \gamma^2\theta^2\right), \tag{2.21}$$

where θ is the emission angle with respect to the longitudinal axis, and λ_u is the wavelength of the oscillation in the rest frame of the electron. In this regime, the transverse momentum of the electrons is much less than that of the longitudinal momentum such that $\beta_z \simeq \beta$, and $\gamma_z = \sqrt{1-\beta_z^2} \simeq \gamma$. The electron acts like an oscillating dipole emitting a single wavelength on-axis emission derived from Equation 2.21, which is Doppler-upshifted due to the relativistic velocity of the emitting electrons [68],

$$\omega_\beta = 2\gamma^2\omega_u. \tag{2.22}$$

In the opposite limit where $K \gg 1$, the oscillating dipole approximation is no longer appropriate due to the transverse oscillatory motion being a significant percentage of the electron's motion. It is for this type of radiation from an electron's motion that an analysis technique from Jackson

[69] may be employed to solve for the radiated power per unit frequency,

$$\frac{dP}{d\omega} = \frac{P_\gamma}{\omega_\beta} S(\omega/\omega_\beta), \tag{2.23}$$

where

$$S(x) = \frac{9\sqrt{3}}{8\pi} \int_x^\infty K_{5/3}(\xi) d\xi,$$

$$P_\gamma = \frac{e^2 c \gamma^4}{6\pi\epsilon_0 r_{e,\beta}^2},$$

and,

$$\omega_\beta = \frac{3}{2}\gamma^3 \frac{c}{\gamma}.$$

$K_{5/3}$ is a modified Bessel function of the second kind, P_γ is the radiated power, and ω_β is the critical frequency of the synchrotron-like spectrum. If the motion of the emitting electrons is sufficiently relativistic, then the synchrotron spectrum is measured to be more continuous, akin to a synchrotron's radiation spectrum.

2.2 Relativistic current filamentation instability

Theoretical derivations of plasma instabilities typically involve linearizing a system of equations relevant to the parameters involved in an instability and arranging the resulting linearized equations to yield a dispersion relation of the interaction. Complex roots of the dispersion relation describe unstable modes predicted by this result. Previous studies have used these general techniques to derive the general growth rate for the Weibel-like current filamentation instability [70–72]. A derivation for the general growth rate of the filamentation of warm ultrarelativistic beams can be found in Appendix A. The initial description of the equations used in this derivation and the final result are presented in this section.

Through the assumption that the beam species is ultrarelativistic propagating into a general second plasma species, a paraxial approximation is taken that yields the following linearized fluid

equations for electron species s,

$$\frac{\partial \delta n_s}{\partial t} + n_s \nabla_\perp \cdot \delta \mathbf{v}_{s\perp} = 0,$$

$$\frac{\partial \delta \mathbf{v}_{s\perp}}{\partial t} \simeq -\frac{q_s}{\gamma_s m_s} \nabla_\perp \psi_s - \frac{1}{2} \gamma_s v_{th,s\perp}^2 \nabla_\perp \delta n_s,$$

as well as the conservation of longitudinal canonical momentum,

$$\delta v_{s\parallel} \simeq -\frac{q_s \delta A_z}{\gamma_s m_s},$$

where $\perp$ and $\parallel$ indicate components perpendicular or parallel to z, respectively, n_s is the initial (unperturbed) density of the species s, the pseudopotential $\psi_s = \phi - A_z v_{s\parallel}$ with ϕ and A_z the scalar and z-component of the vector potentials expressed in the Lorenz gauge, respectively, which may be combined into a single wave equation for ψ_s

$$-\left(\frac{\partial^2}{\partial t^2} - c^2 \nabla_\perp^2\right) \psi_s = \frac{c^2}{\varepsilon_0} \left[\sum_{s'} q_{s'}(n_{s'} + \delta n_{s'}) - \rho_n - \frac{v_{s\parallel}}{c^2} \sum_{s'} j_{s'\parallel}\right] ,$$

where ρ_n is a background (partially) neutralizing charge density. $\delta A_z = A_z - A_{z0}$ where A_{z0} is the initial z component of the vector potential. Through several substitutions and a series of assumptions (Appendix A), the growth rate of the instability for two colliding plasma species with equivalent densities, velocities, and transverse temperatures is given by

$$\Gamma = \beta_b \omega_b, \tag{2.24}$$

which agrees with literature [70].

Alternatively, a relativistic electron beam traveling into a plasma with a differing density and a fast enough response time to shield charge and magnetic fields from the beam produces a growth

rate found to be,

$$\Gamma \simeq \sqrt{\frac{\beta_b^2 \omega_b^2}{1 + \frac{\omega_p^2}{k_\perp^2 c^2}} - \frac{1}{2}\gamma_b k_\perp^2 v_{th\perp}^2} \,, \tag{2.25}$$

which for $v_{th\perp}^2 \to 0$, this expression reduces to the growth rate for a cold, weak beam [72]. In the nonlinear and inhomogenous regimes the behavior becomes less easy to model analytically and we must resort to numerical simulations.

CHAPTER 3

Experimental Methods

The experiments outlined in this dissertation required high-power ultrashort laser pulses to drive the wakefield acceleration of the particle beams as the subjects of study. The laser systems that create these driving pulses require a complex system of optics and electronics, which requires specialized staff and facilities to maintain. These labs and the characteristic parameters of their laser pulses that were utilized in the experimental campaigns detailed in this thesis will be discussed. The experimental gas targets and diagnostics that were installed into these laser systems' experimental areas are detailed. PIC simulations were performed as a method to simulate the physics of the LWFA experiments in this thesis. As such, the PIC method is also mentioned.

3.1 High power laser systems

Each of the experiments outlined in this work was performed on one of three different laser systems: the Gemini laser system at the Central Laser Facility in the Rutherford Appleton Laboratory, the Advanced Laser for Extreme Photonics (ALEPH) at Colorado State University, and the Advanced Laser Light Source (ALLS) at the Institut National de la Recherche Scientifique (INRS). This section describes the common features of these laser systems, while the following three subsections discuss each laser's unique qualities. All of these laser facilities are high-power titanium-doped sapphire (Ti:Sapphire) ultrashort laser systems, and as such the main pulse produced at the end of the amplification and compression chain is centered at a wavelength of 800 nm with a pulse

duration between 20 fs and 70 fs. The laser front-ends all operate mode-locked Ti:Sapphire oscillators outputting ultrashort pulses from the laser cavity at a MHz-scale repetition rate, typically with energies on the scale of nano-Joules. Programmable acousto-optic dispersive filters are used after the front-ends in these systems to control the spectral phase and temporal shape of the output pulse. There is also a pulse-picker system comprised of electro-optics, such as a Pockels cell paired with a polarizer, to control the acceptance timing of the pulse in the high-frequency front-end pulse train that is allowed to enter the amplifying stages of the laser chain. These systems utilize CPA to enable amplification of the pulse's energy past the front-end of the systems and thus stretch the pulses from the front end of the system before interacting with the energy gain amplification stages in the laser chain. All pump amplification stages use frequency-doubled infrared light from either neodymium-doped yttrium aluminum garnet (Nd:YAG) or neodymium-doped glass (Nd:Glass) lasers to excite the Ti:Sapphire amplification medium. Amplification of the pulses is achieved in stages of multi-pass amplification stages, where the number of passes is determined by the saturation threshold of each amplifying crystal and how much energy the pulse gains with each pass. After appropriate amplification, the pulse travels to a compressor usually made up of four optical gratings to compress the pulse to as close as possible to its bandwidth Fourier-limited pulse length.

Measurement techniques of the compressed pulse length and spectral phase may vary from facility to facility. A non-exhaustive but typical list of compressed-laser diagnostics includes a frequency-resolved optical gating (FROG) to measure spectral phase and intensity vs delay, a calorimeter to measure the integrated pulse energy, and a wavefront measurement and imaging of the far-field at the focal plane to determine the Strehl ratio and wavefront uniformity. These laser diagnostics will be discussed in more detail in Section 3.2. The following subsections will discuss in turn each of the three laser facilities that the work in this dissertation was completed on.

3.1.1 Gemini laser system

The experiment concerning monoenergetic beams in an LWFA accelerator via shock injection in this thesis was conducted using the Gemini laser at the Central Laser Facility [74]. The Gem-

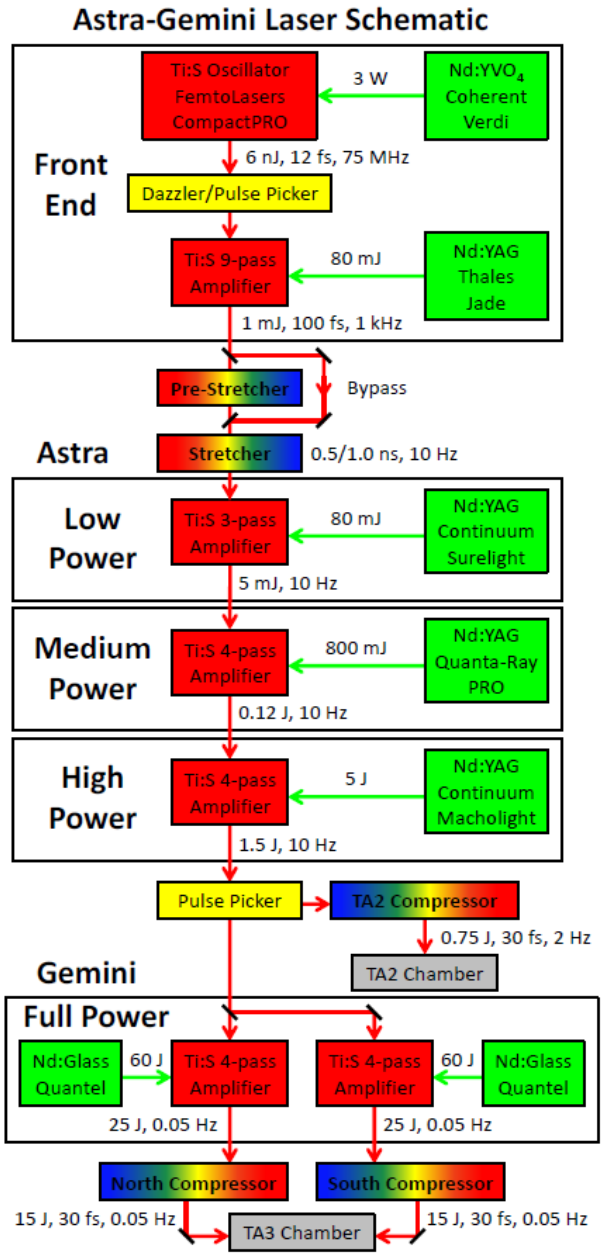


Figure 3.1: Schematic of the Astra-Gemini laser system and target area end stations. Reprinted from [73]

ini laser system is located within the Central Laser Facility at the Rutherford Appleton Laboratory Harwell Campus in Didcot, United Kingdom. Gemini is the ultimate stage in the laser system Astra-Gemini. Gemini has two separate target areas with different power and repetition rate regimes: a moderate-energy high-repetition rate target area target area 2, and a high-energy moderate-repetition rate target area target area 3. The work discussed in this dissertation was conducted using target area 3. The laser system is a two-beam high-power ultrashort pulse system as advertises being able to deliver two 15 J, 30 fs FWHM pulses, yielding 500 TW pulses at a repetition rate of 3 shots per minute.

The experimental campaign that utilized Gemini in this dissertation used a laser pulse containing 12.5 ± 0.2 J focused with an $f/40$ parabolic mirror into a gas jet inside a vacuum chamber. The laser pulses were slightly positively chirped to a duration of 61 fs FWHM, giving a peak power of 195 TW. An adaptive optic was used to flatten the phase front and create an approximately Airy focal sport distribution with a spot width of 48.6×39.2 μm FWHM, an average peak intensity of 75 GWμm^{-2} and a peak normalized vector potential of $a_0 = 1.88$ in vacuum.

3.1.2 ALEPH laser system

The experiment in this thesis probing the current filamentation instability in LWFA-produced beams was conducted using the ALEPH laser at Colorado State University's Advanced Beam Laboratory in Fort Collins, Colorado. This facility is a host facility in the Department of Energy (DOE)-funded LaserNetUS, a network of high-intensity laser user facilities at the time of the experiment. Work done at this facility was made possible through official LaserNetUS support. This facility's 30 fs laser undergoes five stages of amplification before entering the vacuum compressor in the facility, as shown in the laser chain schematic in Figure 3.2. The ALEPH system has two modes of operation: at the Ti:Sapphire fundamental frequency at a maximum of 26 J on target, or in a frequency-doubled high-contrast mode with up to 10 J on target [75]. There are also two primary experimental target chambers at the ALEPH facility: a short-focal length ($f/2$) primarily solid target chamber and a long-focal length ($f/25$) primarily gas target chamber. The

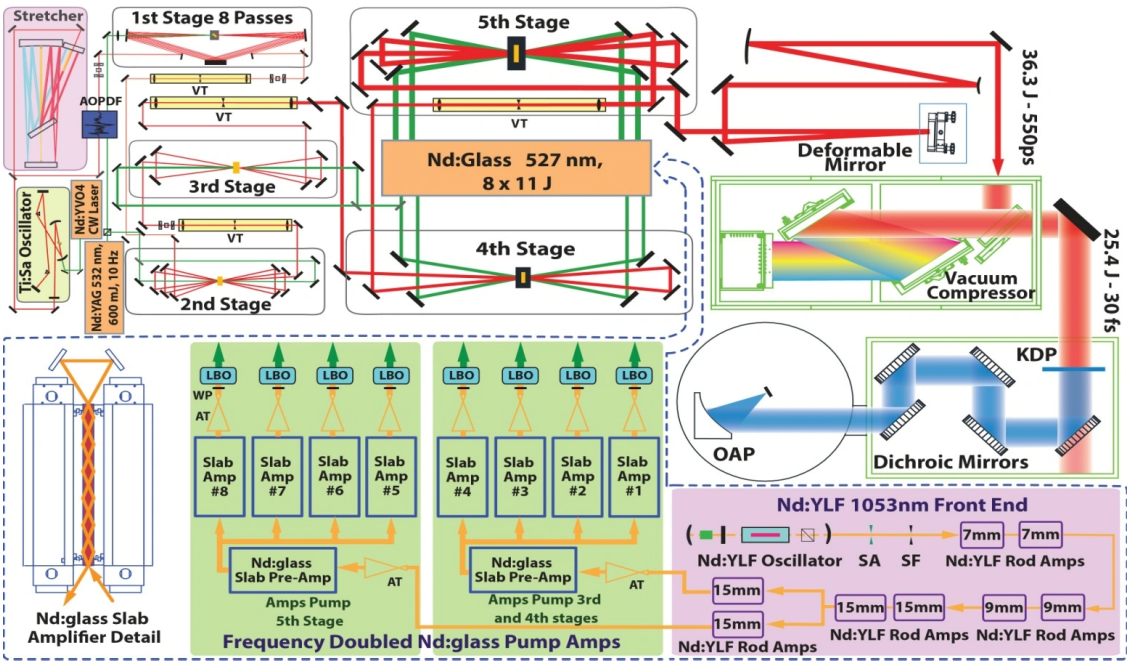


Figure 3.2: Schematic of the ALEPH laser line amplification stages. Included at the end of this diagram is the facility's optional second-harmonic generation to the main beam which was not used in the work in this dissertation. The ultimate chamber relevant to this work was a long focal length chamber as opposed to the short focal length shown in this figure. Reprinted with permission from [75] ©Optical Society of America.

short-focal length and long-focal length experimental areas can produce a 2.4 μm intensity FWHM and a 40 μm intensity FWHM at focus, respectively.

The on-shot energy of each pulse was measured by a calibrated calorimeter measurement from light leak-through of a mirror directly before the vacuum compressor and takes into account a 60% throughput of the compressor and a 10% loss from a protective pellicle placed directly in front of the $f/25$ off-axis parabola (OAP). In the experimental campaign discussed in this dissertation, the average energy on target was 15.7 J with a standard deviation of 3.0 J. The laser's measured pulse length during this thesis experiment was 45 fs. The repetition rate of the system is 3.3 Hz, but the gas load in the vacuum chamber for this experiment limited the repetition rate to 1 shot per minute in single-shot mode.

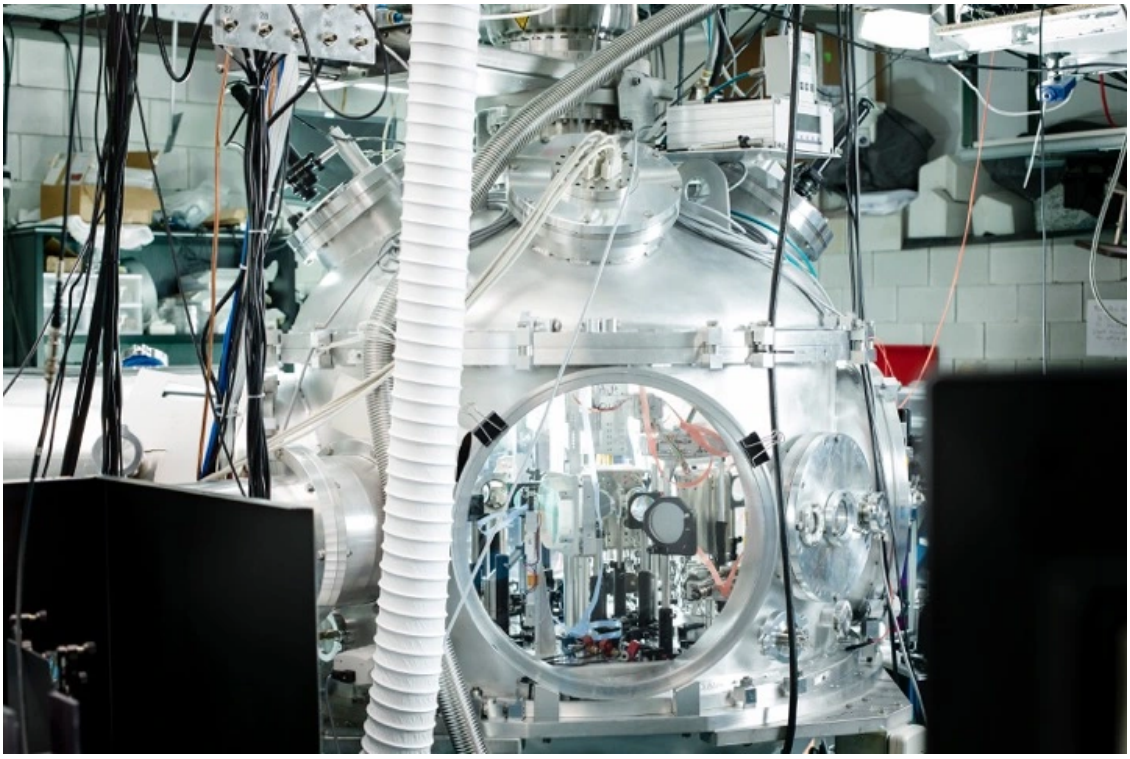


Figure 3.3: Image of the ALLS $f/15$ focus experimental chamber used primarily for wakefield light source experiments. Reproduced from ALLS facility section on LaserNetUS website [76].

3.1.3 ALLS laser system

The betatron streaking experiment detailed in this thesis was conducted on the ALLS laser system located in the INRS campus in Varennes, Quebec, Canada. This facility is a host facility in the DOE-funded LaserNetUS at the time of the experiment, and work done at this facility was made possible through official LaserNetUS support. The facility's advertised laser quality to users includes a FWHM pulse length of 22 fs, an on-target energy of 3.2 J, a FWHM spot size of 15 μm at focus. These advertised qualities match the qualities of the beam used in the campaign in this thesis. The Strehl ratio of the beam measured in the experiment was 0.8. The system can shoot at a repetition rate of 2.5 Hz, but the operational mode used for this thesis was single-shot on-demand mode due to limits to repetition rate due to radiation safety, diagnostic data collection, and vacuum chamber gas loads.

3.2 Laser diagnostics

This section describes various laser diagnostics and metrology methods which are common across ultrashort laser facilities to measure the energy, pulse duration, spectral phase, and wavefront qualities of the laser pulses used in this thesis. These measurements characterize the laser pulse to primarily be able to calculate laser intensity I_L, simply given by the relationship

$$E_L = \int_{-\infty}^{\infty} dt \iint_{\mathbf{S}} I_L dA \ , \tag{3.1}$$

where E_L is the energy in the laser pulse and dA is a differential area defined on a surface $\mathbf{S}$ normal to the laser Poynting vector. For a pulse that is gaussian in time and space with FWHM duration τ_L and minimum waist w_0 the intensity is $I_L = 2\sqrt{\ln 16/\pi^3} E_L/(w_0^2 \tau_L) \simeq 2E_L/(\pi w_0^2 \tau_L)$.

3.2.1 Energy measurement

A measurement of the energy of the pulse in these laser facilities is essential in the design of their use in the experiment, as the intensity of a focused LWFA laser pulse will determine much of the physics of the LWFA interaction. Laser energy measurements are typically done using a combination of photodiodes measuring leak-through from various optics in the laser chain calibrated by calorimeter readings throughout stages of the laser chain. This method involves the placement of a photodiode behind a highly reflective dielectric mirror (usually with characterized reflectance over 99%) to measure the small amount of transmitted light through the dielectric optic. The photodiode measuring this light sends a proportionate voltage signal to an oscilloscope where the voltage trace is recorded. This voltage level is correlated with the amount of light in the laser pulse, or otherwise the energy in the laser pulse for a pulse of similar wavelength bandwidth. The integrated energy for a pulse can be measured by a calibrated power meter. An example of such a power meter is a calorimeter which measures the energy in an incident laser pulse by the heat it produces on its sensing surface. The photodiode voltage level is then correlated to the calorimeter measurements to produce an on-shot output of laser energy. This method of energy metrology relies on two main

assumptions: that the pulse bandwidth remains stable so the transmission percentage of the pulse on the leak-through mirror remains constant, and that there is a linear scaling of the photodiode signal with the laser energy. These assumptions may be confirmed with measurements of the laser spectrum, and by ensuring the photodiode remains in a linear regime of input vs output signal. This method can also be done by replacing the photodiode with a calorimeter and calibrating it in a similar way with a second calorimeter directly in the laser chain.

3.2.2 Pulse duration measurement

A variable needed to calculate laser intensity is pulse duration. As femtosecond-scale pulses are among the quickest events ever engineered, technologies that are typically used to measure temporal qualities of light with longer pulses such as photodetectors (with fastest impulse response times at tens of picoseconds) or fast oscilloscopes (with quickest analog response times down to about ten picoseconds) are not adequate to resolve these ultrashort pulses. Temporal measurement techniques have been produced that utilize the overlap of the pulse with a reference copy of itself at a known delay to achieve an autocorrelation measurement from nonlinear optical effects to measure the duration of the pulse. Two typical setups for these measurements which are common to ultrashort laser pulse laboratories are discussed here: autocorrelation and frequency-resolved optical gating (FROG).

An intensity autocorrelator operates by using a beam splitter to split the pulse into two copies. One copy enters a delay stage to vary the relative timing between the two pulses. They are sent with a symmetric crossing trajectory into a thin second-harmonic generation (SHG) crystal. The produced second-harmonic signal is on-axis due to the symmetry of the crossing k-vectors in the crystal and is recorded with an on-axis camera [77]. By scanning the delay and taking measurements of the SHG energy level, translating to integrated pixel values on the slow detector collecting the light, one can retrieve the temporal autocorrelation of the pulse signal with itself. That evolution of the autocorrelation signal can then be used to calculate the temporal intensity envelope of the input pulse, assuming a temporal envelope shape of the input pulse, which is usually assumed

to follow a sech^2 envelope shape according to ultrafast laser theory.

While autocorrelation is the standard way to measure ultrashort pulse temporal envelopes, it only measures the intensity envelope as a function of delay, and does not measure the phase of the pulse which is also important to characterize. Advancements to the autocorrelation measurement to measure the spectral phase of the laser pulse have been made by way of the development of the FROG technique first described in [78] be utilizing self-diffraction of overlapping pulses in a nonlinear sample. Although self-diffraction was the first nonlinear mechanism used to demonstrate FROG, the use of an SHG crystal to use the generated on-axis SHG to create a frequency vs time delay FROG trace is also possible [79]. The SHG-FROG is nearly identical to the setup of a SHG autocorrelator with the replacement of the intensity sensor with an optical spectrometer following the second-harmonic generating crystal. The expression, for the intensity of the signal on the FROG detector using SHG to generate autocorrelation signal is

$$I_{FROG}^{SHG}(\omega,\tau) = \left| \int_{-\infty}^{\infty} E(t)E(t-\tau)e^{-i\omega t}dt \right|^2, \tag{3.2}$$

where ω is the frequency of the input light, τ is the delay in the delay stage. An iterative algorithm to solve for the instantaneous spectral phase is designed to quickly converge on the solution of the spectral phase and intensity that satisfies both the nonlinear interaction signal strength criteria and the intensity relation in Equation 3.2. The resulting trace yields an intensity heatmap in ω, τ space of the pulse once solution convergence has been reached.

3.2.3 Focal spot measurement

A measurement of the focal spot is essential to understand the peak intensity of the focused pulse and measure the uniformity of that energy distribution and wavefront quality at the LWFA interaction point. The simplest way to measure this is to image the focal spot onto a camera with the laser operating at low energy; however, it is not uncommon to measure the focal spot or with the laser operating at full energy to include thermal lensing effects in the measurement, and to attenuate the

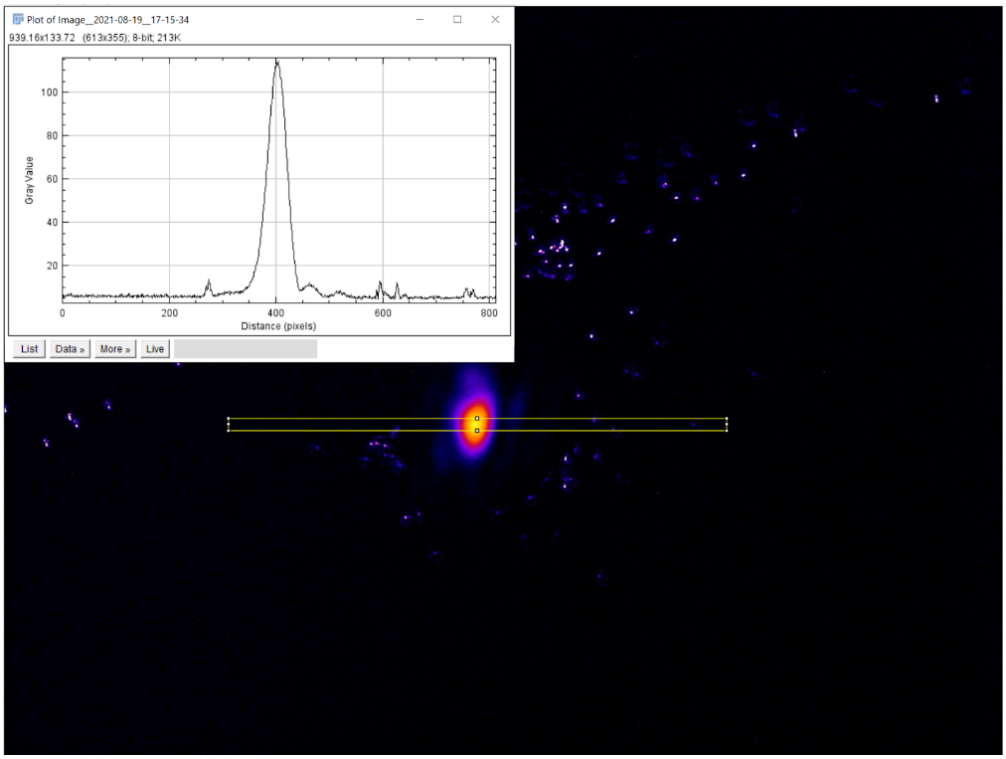


Figure 3.4: Example of the vacuum focal spot measurement taken at the ALEPH laboratory during the current filamentation instability experiment in this thesis. The spatial scale of the image is ~ 25 pixels/10 μm.

beam so to not damage the CCD detectors. This method assumes that further amplification of the laser does not significantly change the far-field wavefront of the pulse. The camera is spatially calibrated so that the pixel$/\Delta x$ is known such that the number of pixels of the focal intensity on the camera chip can be used to calculate the radius of the focal spot. By assuming an ideal focal spot transverse envelope, which is often either a Gaussian envelope or an Airy disk profile, the average deviation away from an ideal focal spot for a given wavelength and focusing optic can be determined by the Strehl ratio of the pulse, given by:

$$S.R. = e^{-(2\pi\sigma/\lambda)^2}, \tag{3.3}$$

where σ is a measure of the RMS wavefront error. X- and Y- rotation axis adjustments to the alignment of the focusing optics in these laser systems are made to maximize the Strehl ratio and

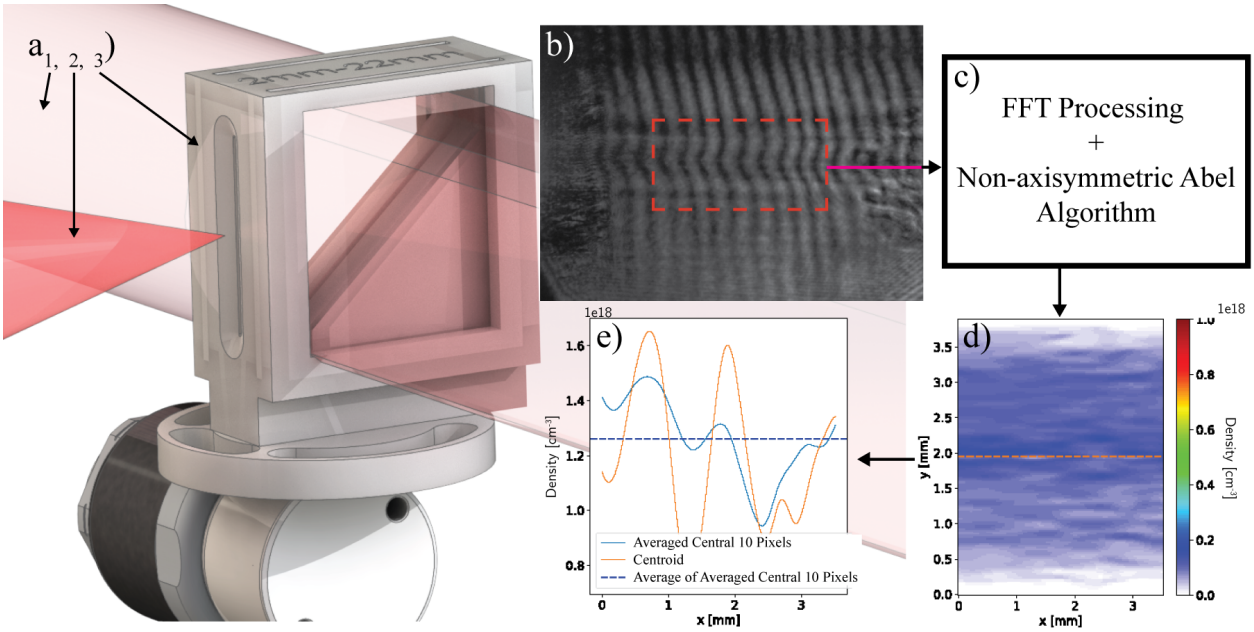


Figure 3.5: a) Render of 1) an interferometer probe laser, 2) a main accelerator driving laser, and 3) a plasma target utilized in this dissertation for the current filamentation instability experiment in this thesis. b) An example of a raw image from the target shown, and c-e) the flowchart of the process used to retrieve the density for gas targets for experiments in this dissertation. The dotted line in e) represents the average value of the longitudinal array of the mean density value about the center of the channel by n-pixels (10 in this case), and is quoted plasma density for a plasma unless stated otherwise.

achieve as uniform a Gaussian or Airy disk focal spot shape as possible. Figure 3.4 shows the raw measurement of the imaged focal spot taken during the campaign at the ALEPH laser system measuring the current filamentation instability.

3.3 Plasma & beam diagnostics

3.3.1 Plasma density measurement: interferometry

Electron plasma density, being one of the three primary variables that describe plasma and a variable that is significant to the LWFA interaction, is important to diagnose on-shot in the plasma targets used in the experiments outlined in this thesis is important. Optical interferometry is a technique that can used to measure plasma density in such a manner. In this thesis' experiments,

a probe beam that has a large transverse diameter compared to the interaction plasma traverses through the interaction with the plasma region vertically off-center of the large pulse. A Michelson interferometer is used post-interaction, with one arm of the interferometer containing a roof prism to flip the beam vertically, so that the region of the beam that interacted with the plasma (called the 'subject' probe) interferes with the region of the beam that did not travel through the plasma (called the 'reference' probe) and creates fringes that are recorded by a CCD camera. One of the arms in the interferometer has its optics installed on a micrometer-controlled delay stage to control the temporal overlap between the two arms. The delay is adjusted until fringe contrast is maximized.

The fringes in the overlapped reference and subject regions of the probe beam are generated from a phase difference of the probe laser in those two regions due to traversing through regions of different integrated indices of refraction, η. This two-dimensional phase shift map may be expressed as,

$$\Delta\phi = \frac{2\pi}{\lambda_0}\int_{-\infty}^{\infty}\Delta\eta dx\ , \tag{3.4}$$

where x is the distance along the optical path, λ_0 is the wavelength of the probe beam, $\eta = \sqrt{1-\frac{\omega_{pe}^2}{\omega^2}}$ is the index of refraction of the plasma, and $\omega_{pe} = \sqrt{\frac{n_e e^2}{\varepsilon_0 m_e}}$. This can be expressed in terms of the plasma density:

$$\Delta\phi(x,r) = \frac{2\pi}{\lambda_0}\int_{-\infty}^{\infty}\left(\sqrt{1-\frac{n_e(x,r)}{n_c}}-1\right)dx\ , \tag{3.5}$$

which can be simplified for a uniform plasma slab of thickness L with a Taylor expansion for small n_e/n_c as

$$\Delta\phi(x,r) \approx \frac{\pi}{\lambda_0}\left(\frac{n_e(x,r)}{n_c}\right)L. \tag{3.6}$$

This phase shift array can be inserted into a generalized non-axisymmetric Abel inversion method to reconstruct the map of the electron density [80]. Unless otherwise stated, any quoted plasma densities reconstructed using this method represent the average density around the center

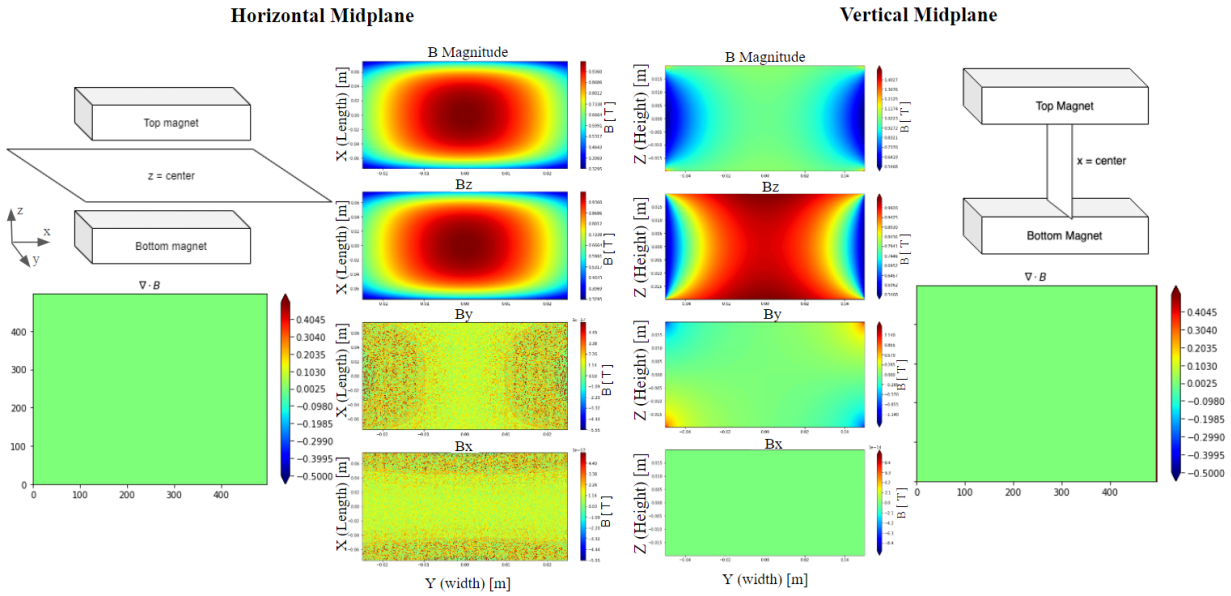


Figure 3.6: Horizontal (left) and vertical (right) midplane visualizations of the magnetic fields within the magnetic gap regions of a representative arbitrary magnetic dipole gap. In each midplane visualization, the calculated divergence of the magnetic field is zero throughout the domain.

and along the length of the fringe shift region.

3.3.2 Beam energy measurement: magnetic spectrometer

After beams have been accelerated via LWFA, the energy spectrum and angular divergence of the particles often need to be measured in an on-shot basis. In LWFA systems, this measurement is made with a magnetic spectrometer system. A magnetic spectrometer consists of a dipole magnetic field in the path of the charged particle beam which disperses particles to different trajectory angles based primarily on the energy of the individual particles and the transverse magnetic field strength according to the relativistic Lorentz force of the magnetic field in the dipole region. Other factors that influence the output of trajectories of the particles from the dipole region are the pointing angle of the beam into the dipole gap region, the distance between the source of the beam to the entrance of the dipole gap, the length and width of the magnetic dipole faces, the uniformity of the dipole field, the fringe-fields around the dipole, and the acceptance-angle of particles into the dipole gap region. The dispersed particles are measured by a detector screen, which is typically either an

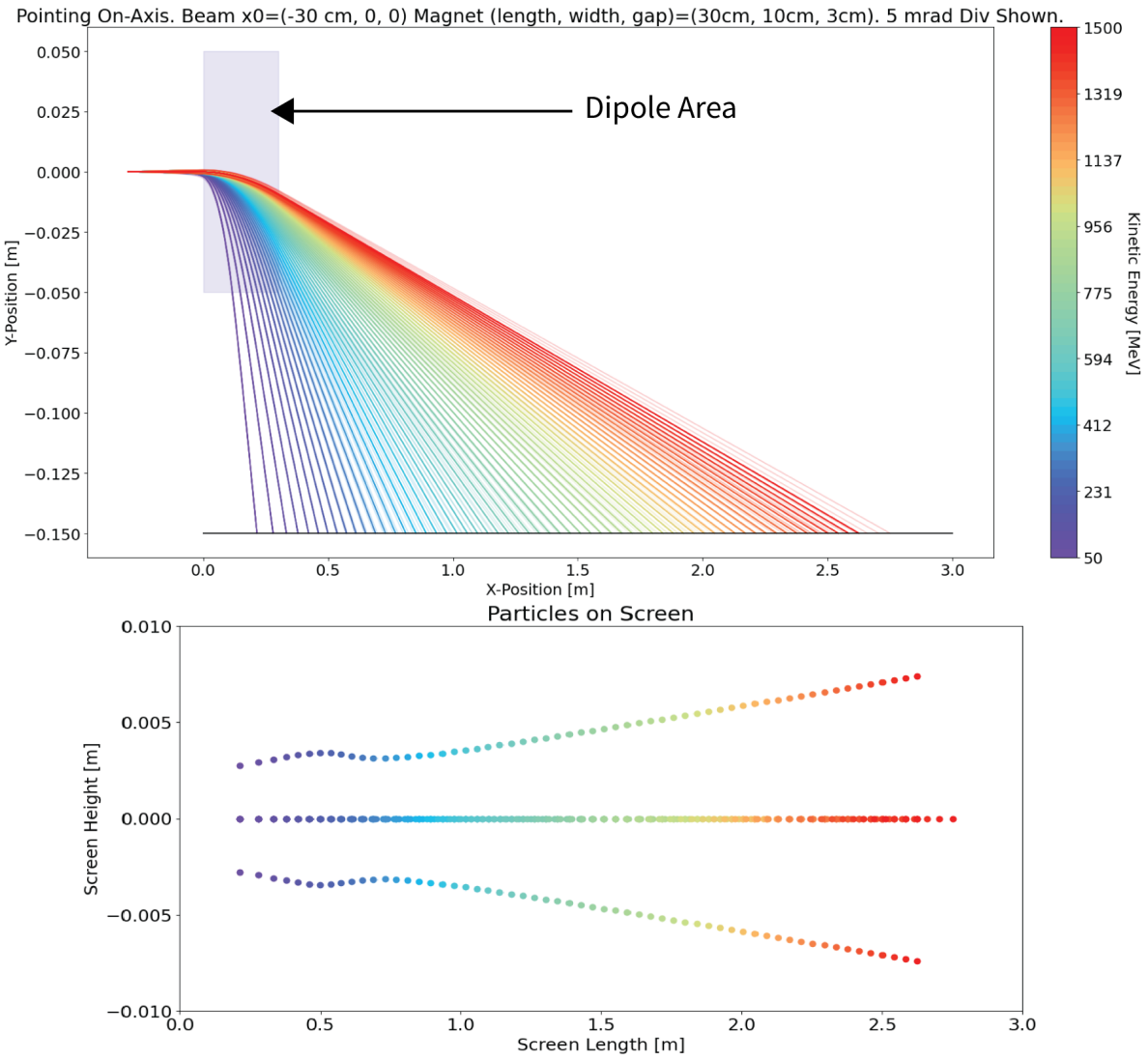


Figure 3.7: Example of output from 3D particle stepper code used to generate an energy-to-position dispersion curve correlation for a given spectrometer geometry, field strength (1 Tesla), and beam energy and angular properties. Witness electrons ranging from 50-1500 MeV pass through the dipole field region with on-axis pointing and with 5 mrad pointing angle to the top, left, bottom, and right of the beam's on-axis trajectory to simulate the effect of divergence angle on the measured beams.

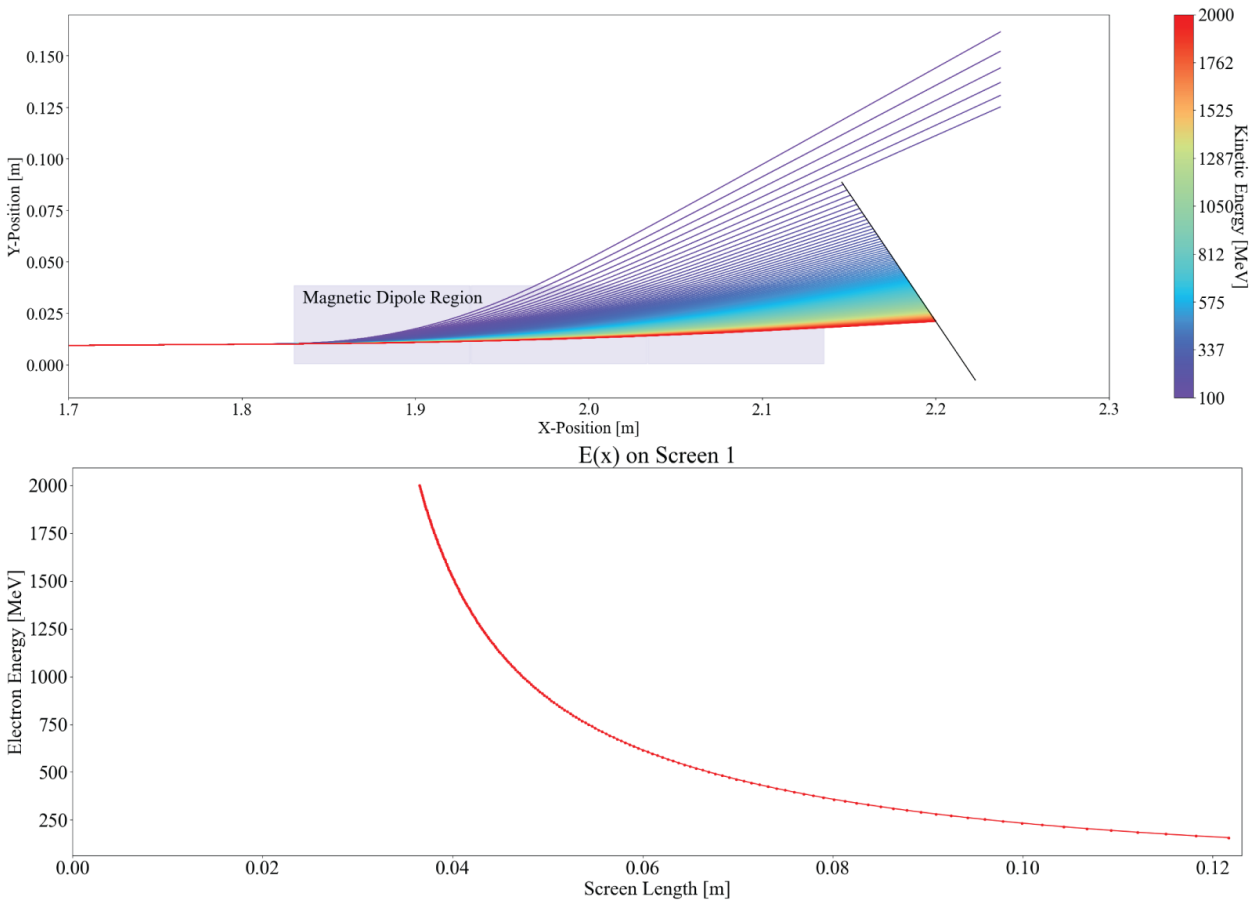


Figure 3.8: Particle trajectories (top) and resulting $E(x)$ dispersion relationship to determine the correlation between electron energy and position on the scintillator screen in the dispersion direction (bottom) for the current filamentation instability experiment at the ALEPH laboratory. Dipoles consisted of central field strength of 0.97 T.

image plate or a scintillator that is sensitive to high-energy leptons. Positions along the detector screen are correlated to the energy of the particles landing on that position given a relation known as the dispersion curve of the spectrometer. Angular divergence can also be determined from this diagnostic, as the spatial profile of the beam transverse to the direction of dispersion is largely unperturbed by the dispersion in the magnetic spectrometer. The consequence is that the size of the beam in the non-dispersed direction on the detector screen may be used in combination with the electron-trajectory distance between the screen and the particle source or angular acceptance aperture (if there is one present) to determine the divergence angle of the beam.

To determine the energy dispersion curves of the magnetic spectrometer system, typically a

computational particle-stepper is used to simulate particles of different energies traveling through the geometry of the magnetic spectrometer system. A custom three-dimensional particle tracking code designed to model electron spectrometers is employed. This uses a relativistic Boris algorithm [81] particle pusher to calculate the particle trajectories through an analytic dipole field produced from overlapping analytic fields from rectangular parallelepiped block magnets [82] with the same gap-height, width and length measurements of the dipole used in the experiment. A tall parallelepiped block assumption has the effect of straightening and making more uniform the fields in the overlapping field region, much like the yoke effect in the dipoles used in the lab. The qualitative shape of the field structure within the dipole gap produced by this model can be found in Figure 3.6.

Often, these systems are calibrated by assuming a perfectly uniform field confined perfectly within the volume of the magnetic dipole gap. While this approximation is relatively safe to make for particles traveling on-axis in the center of the dipole gap region, it does not capture the off-axis magnetic-field components to electron trajectories, the magnetic field gradients in and around the dipole, nor the bent fringe fields around the dipole volume region. These fields contribute to particle focusing/defocusing effects in the beam being measured by the spectrometer, as shown in Figure 3.7. In this example, an hourglass-like angular profile appears along the 5 mrad divergence trajectories for different energies of electrons going through a single 1 Tesla central field-strength dipole spectrometer with the particular setup shown. This particular hourglass profile is due to the lowest energy particles being dispersed enough to exit the side plane of the magnetic dipole gap, where high enough energy particles transition into exiting the rear exit plane of the gap, changing the profile of the transverse focusing fields that the particles experience in their trajectories. This is a motivation to simulate magnetic fields as close to the fields as the dipole magnets used in the lab. The influence of the dipole field on the particles' trajectories was tracked starting within a region inside and around the volume of the space defined by the gap between the magnets in the dipole.

The particle tracking results for the reference beam pointing in the current filamentation instability experiment used to determine the campaign's reference electron energy vs. screen position

correlation are found in Figure 3.8. Due to electron beam pointing jitter issues in this experiment, a narrow angular discriminating aperture was not included in front of the ESPEC dipoles. To compensate for this, on-shot $E(x)$ dispersion curves were generated using the measured pointing angle of the electron beams to model electrons with matching angular pointing entering the ESPEC system.

For the betatron beam streaking experiment conducted at the ALLS laser system, the facility provided calibrations for their electron spectrometer that yielded the $E(x)$ dispersion relation for electrons measured in that experiment. Examples of ESPEC measurements from this campaign can be found in Figure 5.9. The electron spectrometers in both experiments conducted at the Gemini laser facility were calibrated in the positron generation via a similar method to that shown in Figure 3.8.

3.3.3 Beam emittance measurement: emittance mask

Beam emittance measurements were made by analyzing the profile of a beam after passing through a high-Z emittance mask and being dispersed by a magnetic dipole via the following method, also summarized in the publication detailing the results from Chapter 7 [83]. First, we assume that the beam is angularly selected using a circular aperture, as was the case in this thesis, at an aperture plane z_{ap} with radius R_{ap}. The beam profile was modeled as an azimuthally symmetric clipped Gaussian distribution such that only particles with $R_{\mathrm{ap}}^2 \geq x_{i,\mathrm{ap}}^2 + y_{i,\mathrm{ap}}^2$ are transmitted, where $x_{i,\mathrm{ap}}$ and $y_{i,\mathrm{ap}}$ are the transverse coordinates of the i-th particle at the aperture plane. This profile is dispersed according to the individual particle energies onto a spectrometer screen. The particle distribution $S_y'(x)$ is measured at the detector plane z_{det} where x and y are transverse coordinates perpendicular and parallel to the dispersion plane of the spectrometer respectively. Due to the combination of energy spread and divergence, the profile $S_y'(x)$ is due to particles over a range of different energies where their initial propagation angle $\theta_{i,y}$ and energy E_i result in the particle intersecting the detector plane at the position y. With the assumption that the spectrum $N(E)$ is slowly varying, then each slice measurement $S_y'(x)$ represents the integral of the beam profile over

y, i.e.,

$$S'_y(x) = 2A_{y,0} \int_0^{\sqrt{R^2-x^2}} \exp\left[-\frac{x^2+y^2}{2\sigma_x^2}\right] \mathrm{d}y$$
$$S'_y(x) = \sqrt{2\pi} A_{y,0} \sigma_x \left(\sqrt{\frac{R^2-x^2}{2\sigma_x^2}}\right) \exp\left[-\frac{x^2}{2\sigma_x^2}\right] \tag{3.7}$$

where $A_{y,0}$ is the amplitude of the particle distribution, $R = R_{\mathrm{ap}} z_{\mathrm{det}}/z_{\mathrm{ap}}$ is the projected size of the aperture at the detector plane and $x \leq R$. The functional form of equation 3.7 is used to fit the amplitude of the modulated signal $S_y(x)$ when retrieving the apertured beam properties as described below.

Several steps were followed to extract the particle emittance from the spectrometer signals in Chapter 7 in which this measurement was taken. First, a variable threshold filter was used to remove hard hits caused by stray photons hitting the CCD directly. Second, the defocusing of the effect of the magnetic dipole fringe fields was removed by re-scaling the measured signal in the non-dispersion direction such that the spatial frequency of the grid pattern was made constant for all energies. Vertical slices were taken through the resultant image, averaging over 4 mm in the dispersion direction to produce the signal modulation $S_y(x)$ as a function of x at a given $y-$position. The scattered particles from the grid formed a smooth background on the detector, which was removed by fitting a Gaussian to the values at the minimum of the observed modulations. The signal envelope was similarly found by fitting the beam profile function, Equation 3.7, to the signal maxima. The RMS width of the fitted envelope was then divided by the source-to-screen distance to obtain the beam divergence σ_θ.

An ideal zero source size beam would produce a sharp step-function within the bounds of the scattering signal and the beam envelope, with the spatial period of the magnified grid size. The blurring of this pattern was observed due to contributions of the finite spatial resolution of the diagnostic (215 μm) and the source size σ_x of the beam, which was found by iterative minimization of the mean squared error between the measured signal and the calculated signal for a given source size. The geometric emittance was calculated as the product of the measured divergence and source

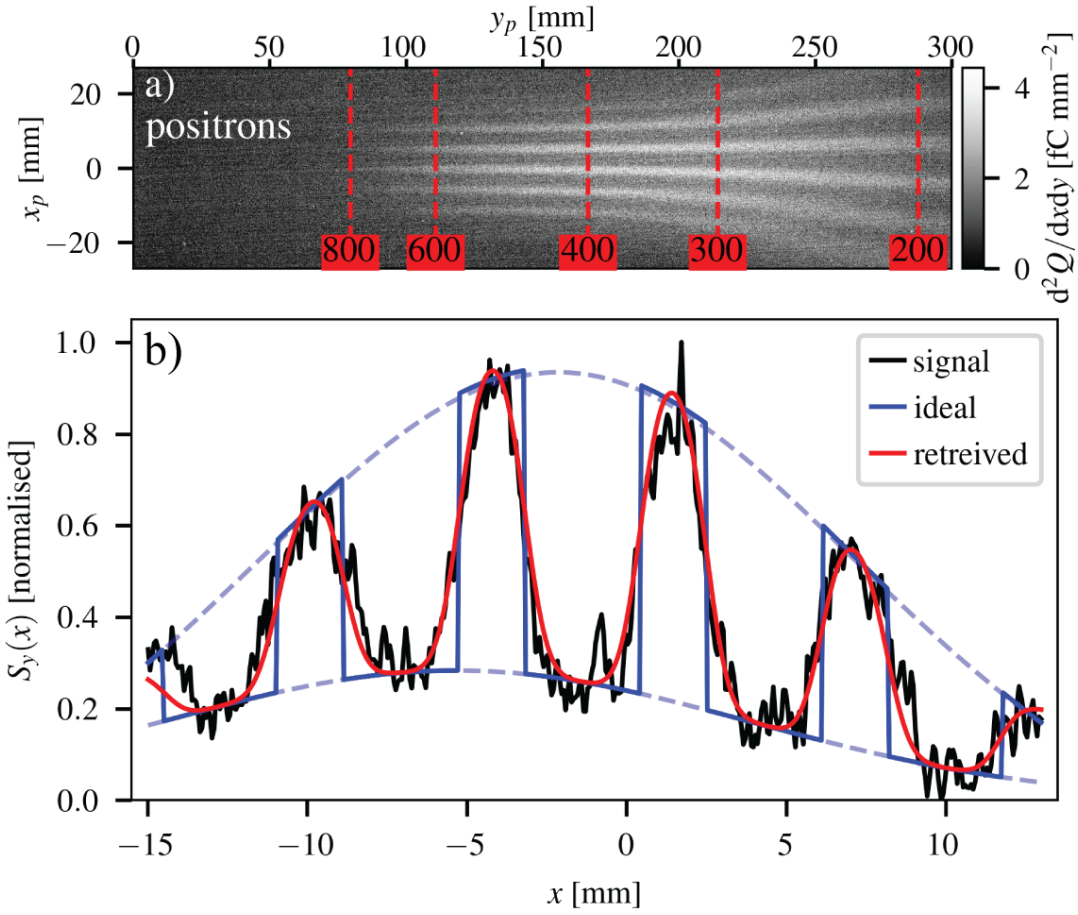


Figure 3.9: Example of the emittance retrieval process using an emittance mask used in Chapter 7. a) Annotated raw data of positrons landing on the first scintillator screen after being deflected by a dipole magnetic field. b) Data, fitted ideal signal, and retrieved signal from the emittance retrieval process.

size, i.e. $\epsilon = \sigma_x \sigma_\theta$. An example of a measured signal and retrieved modulation signal is shown in Figure 3.9.

Synthetic data can be created to benchmark the retrieval process by numerically propagating results from a Monte-Carlo simulation and removing particles that would hit the solid bars of the emittance measurement grid. The dispersion of the magnet was added by shifting the particles transversely according to their energy using the same dispersion function as for the experimental spectrometer. The particles are selected according to their position on the spectrometer to create the modulated signal $S_x(y)$ for a given energy band. Due to the significant beam divergence, there

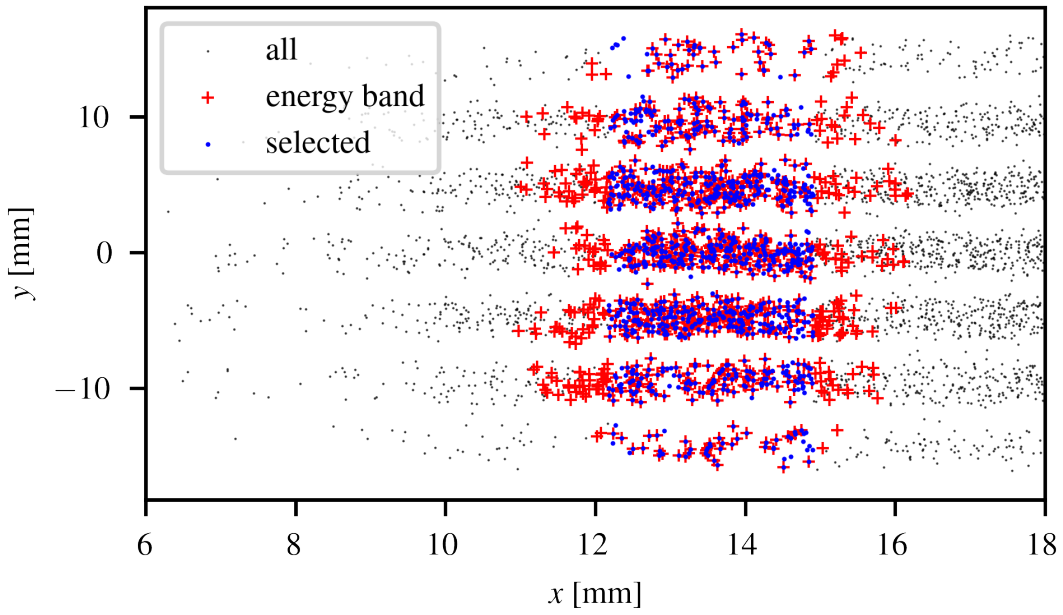


Figure 3.10: Example synthetic positron spectrometer particle distribution. Particles that pass through the grid freely propagate onto the detector plane, and are dispersed according to their energy. Taking a slice along the y-axis mixes some particle energies due to the effect of the beam divergence. Particles labeled 'energy band' have energies within 450-550 MeV. Selected particles have x positions corresponding to the expected position for zero-divergence particles within the same energy range. The signal $S_x(y)$ is generated by making a histogram of selected particle y coordinates.

is some trajectory crossing such that some particles of different energies are selected, and some of the correct energy is omitted, as illustrated in figure 3.10.

3.3.4 Betatron emission measurement: transmission filter pack

In the experimental campaign concerning the temporally-resolved measurement of the energy gain of a LWFA electron beam via its betatron radiation, the measurement of the spatially-resolved betatron X-ray critical energy spectra was required. For this experiment, the betatron radiation propagated out of the vacuum chamber through a Beryllium window, the X-ray filter pack (see Figure 3.11a), and a fixed distance of air before being incident on a Princeton Instruments SCX 4300 X-ray CCD coupled to a Gd_2O_2S : Tb phosphor screen. All of the integrated materials were considered to determine the X-ray transmission, as seen in Figure 3.11b. Figure 3.11c shows a

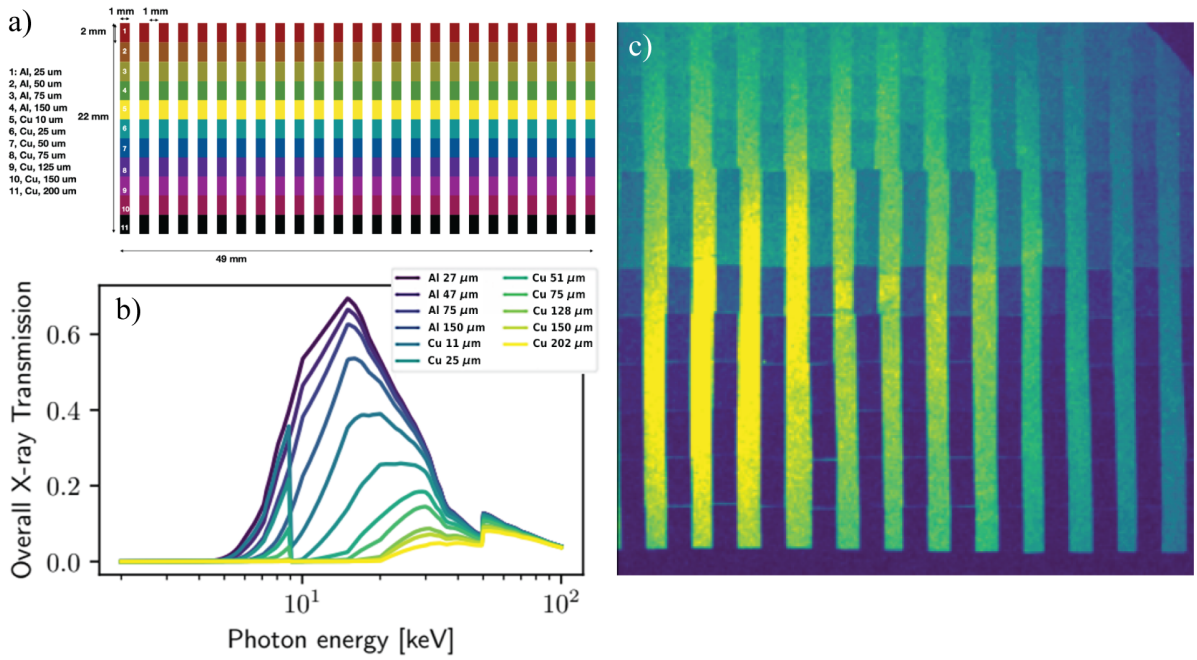


Figure 3.11: a) The X-ray filter array design used on the streaked betatron beam experiment in Chapter 5 and b) its corresponding transmission curves over the X-ray energy range relevant to the experiment. c) An example image was taken of the betatron radiation output interacting with the filter pack recorded by an Andor indirect X-ray CCD.

data shot taken by the X-ray CCD with the filter in the beam line. The spectral reconstruction procedure involves interpolating from the unfiltered regions to reconstruct the X-ray beam profile. After normalizing the filtered regions using the measured X-ray beam profile, the spectrum can be retrieved through an iterative algorithm starting from a guessed critical energy E_c of an assumed synchrotron-like spectrum and obtaining the best fit to the transmission of the filter column elements [84, 85].

3.4 Gas targets

As laser-driven wakefield acceleration involves the interaction with intense ultrafast laser pulses with underdense plasma and the most common laser wavelength for high-power ultrafast laser systems is typically $\lambda_l = 800$ nm, a plasma density suitable for LWFA can be derived. Firstly, the plasma must be below the critical density $n_c = \frac{\varepsilon_0 m_e}{e^2}\omega_p^2$ for the laser to propagate through the

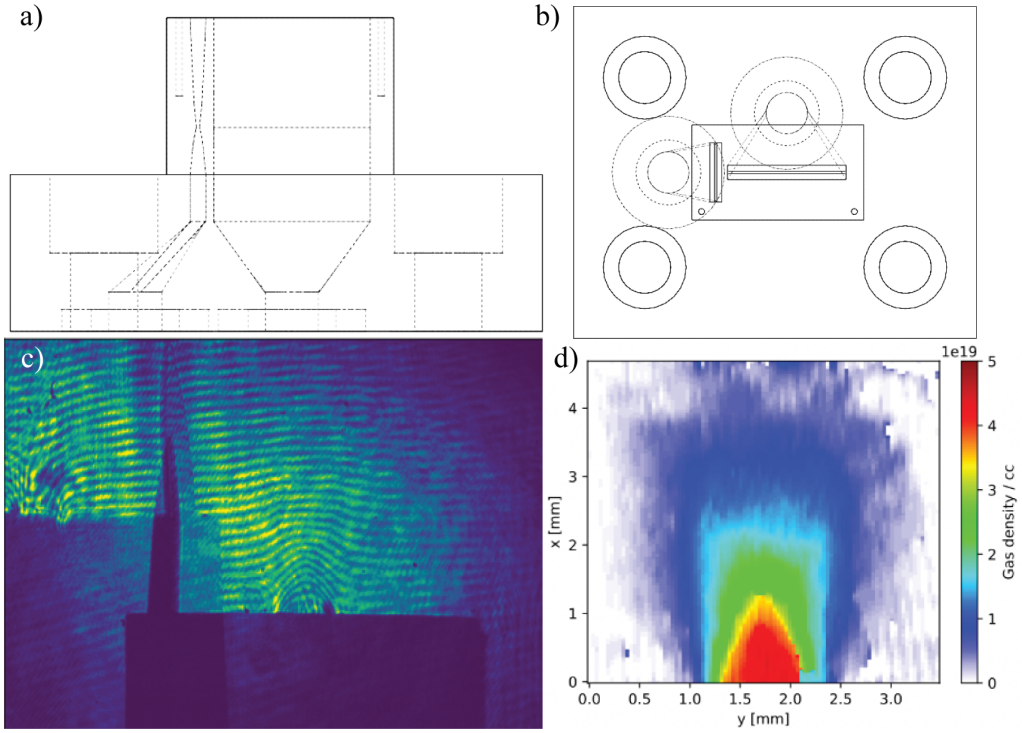


Figure 3.12: a) Side and b) top-down profile views and c-d) interferometric measurements of the transverse density profile along the length of the accelerator for the gas target used at the ALLS facility.

length of the accelerator. Secondly, the plasma density in the accelerator must be within a range that favorably agrees with the LWFA laser/plasma parameter to allow for efficient acceleration [23]. This can be achieved via gas jet or enclosed gas cell targets produced via fast and inexpensive additive manufacturing, or by high-precision machining of steel or aluminum. Once the driving laser pulse ionizes the gas, the gas species and backing pressure can be controlled to yield a desired plasma electron density.

An additive manufacturing process advantage allows highly customizable gas target shapes to produce tailored density profiles to fit an experiment's needs. In gas jets, this can be done by changing any intricate internal shape of the inlet nozzle, for example, potentially leading to a change in the Mach number and profile of the gas exiting a supersonic flow jet [86]. One could use a gas cell instead of a gas jet in LWFA experiments, which improves beam stability, divergence, and energy spread of the resulting beams [61]. In the case of a gas cell, customization from additive

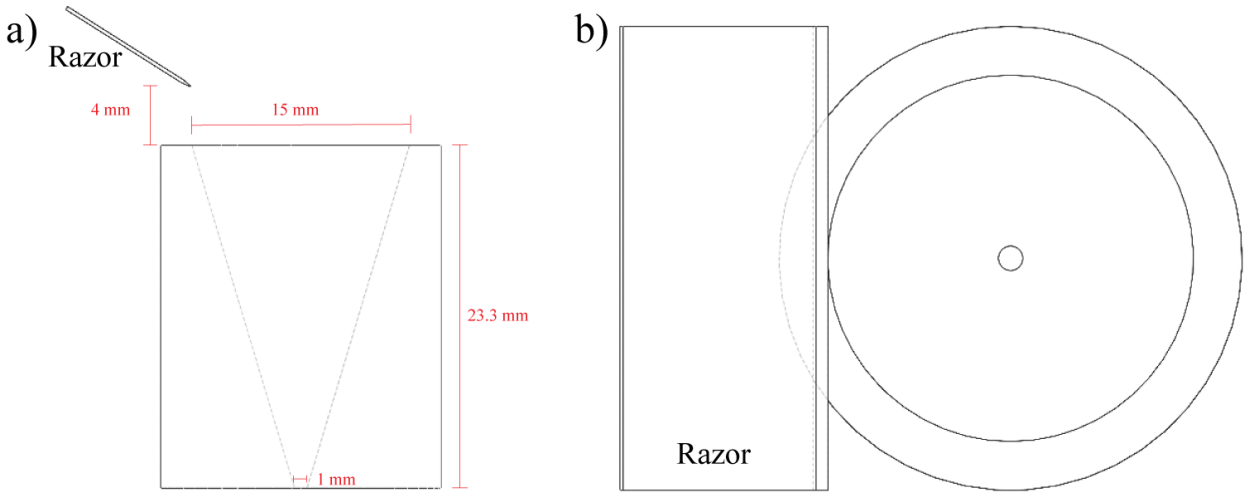


Figure 3.13: a) Side and b) top-down profile views of the gas jet and shock-producing blade at the $z_{\text{blade}} = 0$ mm position from a CAD model of the gas jet.

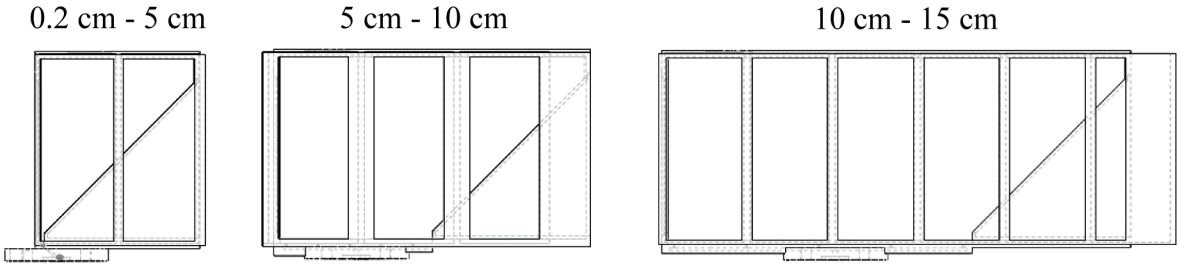


Figure 3.14: Side profiles of the three filamentation gas cells used in the current filamentation instability experiment in this thesis. The open windows in the gas cells had optical-grade glass microscope slides fit into them to allow probe light to propagate through them.

manufacturing can yield a variable acceleration length and/or localize a region in the accelerator's length to, for example, contain an ionization injection gas species [85].

Several examples of gas target designs from the experimental campaigns are included for reference. Figure 3.12 shows the side and top profile of the CAD file for the supersonic gas jet target used in the experiment, which measured angularly-streaked betatron beams. This figure also shows neutral gas interferometric measurements taken during the experiment to confirm the density gradient at the edge of the supersonic gas flow, which agreed with measurements taken before the experiment. This gas target had two stages: first, the laser interacts with a 1 mm$\times$5 mm (length$\times$width) injector stage with a mixed gas (99.5% Helium + 0.5% Nitrogen) controlled by a

Parker solenoid valve with a backing pressure of 30 PSI with the laser either 2.0 mm or 2.5 mm vertically offset from the gas nozzle exit face. After this injector stage, the accelerator transitions to the narrower 10 mm$\times$1.2 mm (length$\times$width) pure-helium gas acceleration stage, which had a typical backing pressure of 300 PSI fed to its solenoid valve. The two stages' nozzle openings were separated by 0.5 mm in the longitudinal direction. The interior of the nozzle was designed with a parabolic cross-section to achieve supersonic flow based on a supersonic gas nozzle design for laser wakefield application [87]. The throat of the nozzle was 200 μm wide. Each stage had an independent gas valve triggered by the timing signal of the ALLS laser system.

The experimental study of acceleration of shock-injected electron beams was performed at the Gemini facility using a gas jet designed to generate a sharp shock feature along the longitudinal propagation length of the laser in the gas profile. This was achieved using a razor blade oriented with a pitch-angle of $-32.4 \pm 0.3^{\circ}$ to the horizontal plane and placing its edge 4 mm above the gas nozzle's exit plane. The blade was attached to a motorized stage that allowed movement in the longitudinal direction independent from the gas jet's positioning system. The supersonic jet had an inlet throat of 1 mm diameter that expanded conically to a diameter of 15 mm over a vertical distance of 23.3 mm. Pure helium gas at 100 bar backing pressure was controllably injected into the jet with a pulsed solenoid valve. The LWFA driving laser was focused 14 mm above the exit face of the gas cell. It propagated a gas distance that did vary due to the blade position over the gas jet. However, it maintained a distance ~ 15 mm for the most optimal high-energy monoenergetic beams. The blade geometry was measured in order to be included as accurately as possible in CFD simulations due to the sensitivity of shock-producing features in shock front formation in supersonic fluid flows. The results of these measurements can be found in Appendix C.1.

The gas jet used in the positron generation experiment had the same dimensions as the target used in the shock injecting experiment, except without the razor blade present, and instead used a gas mixture of 2% nitrogen and 98% helium in order to increase electron beam charge.

In the campaign to measure the current filamentation instability, gas cells were chosen instead of gas jets to maintain a gas density that was as uniform across the target as possible. The accelerator

gas cell was a 3D-printed 2 – 22 mm variable-length gas cell and the filamentation cell length range was split across three 3D-printed variable-length gas cells as seen in Figure 3.14: a 0.2 – 5 cm cell, a 5 – 10 cm cell, and a 10 – 15 cm cell. The gas species used in the filamentation cells was iterated between hydrogen, helium, nitrogen, and argon for each cell, and the backing pressure was scanned as a primary variable in the experimental campaign.

3.5 Particle-in-Cell (PIC) simulations

Particle-In-Cell (PIC) refers to a computational method to simulate the interactions between charged particles and electromagnetic fields. This section will briefly introduce the main concepts and computational loop in this method and detail the specific codes used in this dissertation. For a more detailed explanation of PIC principles please refer to Birdsall & Langdon's textbook on computational plasma physics [88]; or to any of several contemporary papers that summarize the method and describe modern amendments and additions to solvers in PIC codes [89–91].

The PIC algorithm simulates individual particles that possess characteristic charge and mass for a given species, as well as position and momentum values that are defined at the continuous-space location of each particle. The number of particle objects is specified by the user. Separately defined by the user are the initial charge density and momentum distributions of the particles. Defining both the number of particle objects for a given species with a characteristic charge as well as the charge density distribution separately is allowed by weighting the charge and mass into each particle object given the initial distribution of charge density on the grid. These weighted particle objects are referred to as macroparticles, and they represent local distributions of a particle species as a point object while maintaining the charge-to-mass ratio of that species. By weighting the charge and mass of macroparticles, we can simulate the total charge and mass of particles in a plasma without the need to model every single particle in that plasma computationally.

The simulation domain is comprised of a spatial grid of points at which the electric and magnetic fields are defined. The particle positions and momenta are defined in free space while the

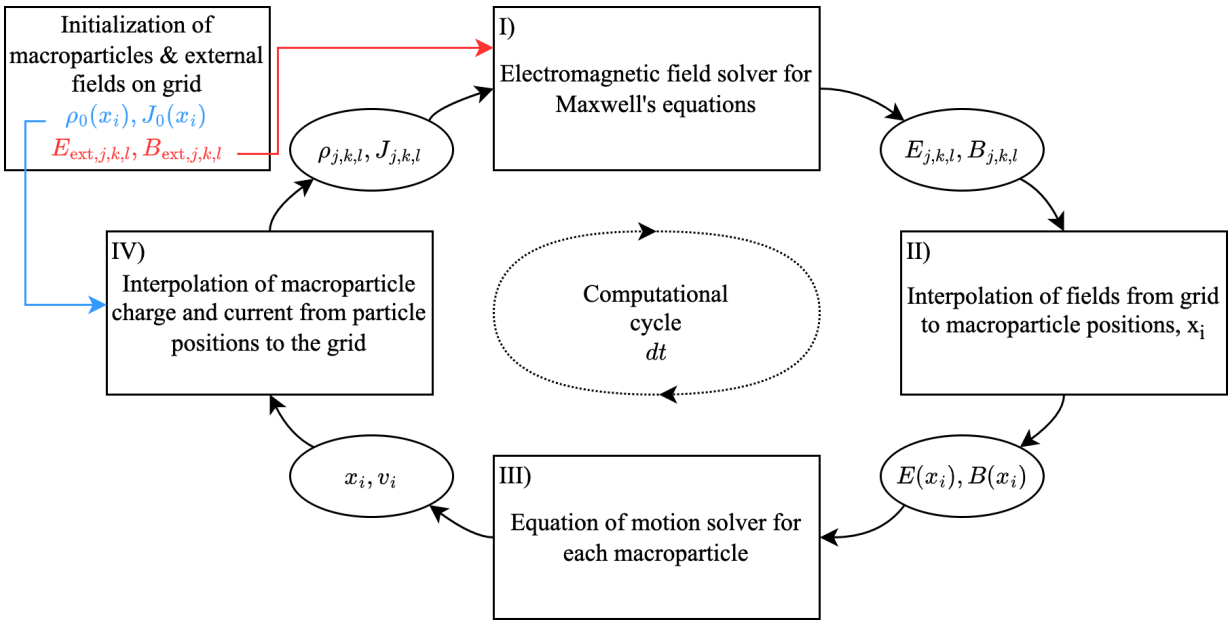


Figure 3.15: Flowchart representation of the sequential categories of calculations in a particle-in-cell simulation. Subscripts j, k, and l represent cardinal unit vectors in a three-dimensional spatial grid, and i represents a property of the $i-$th macroparticle. The user-defined initialized values represented by the blue and red items in the top-left of the figure are added to the simulation only on the first loop of the computational cycle, where the charge is first interpolated to the grid and the resulting fields are added to any external fields defined by the user.

electromagnetic fields are defined at discrete points on a grid; this raises the question of how the interactions between fields and particles take place if they are not necessarily defined at the same spatial locations. The general answer is to interpolate values on the grid to particle points and to then also interpolate values from particle points onto the grid. That is the PIC algorithm in its most basic form: interpolation of free-space charge density and currents from individual macroparticles to a grid to update electromagnetic fields and then interpolation of those fields back onto the particles to update their positions and momenta. A flowchart representation of this computation loop is found in Figure 3.15.

After a user defines initialization parameters such as initial plasma species' charge and current distributions and any initial electrostatic or electromagnetic fields in the simulation domain, the PIC computational process can be broken down into 4 categories of calculations: I) calculating electric and magnetic fields using Maxwell's equations, II) interpolating fields from the grid to

particles, III) updating macroparticle momenta and updating their position using their momenta, and IV) interpolating the resulting updated charge and current densities from the particles to the grid. These sections correspond to the Roman numeral labels in Figure 3.15. In part I) of the PIC algorithm, Maxwell's equations (Equation 2.4) are solved on the simulation grid. To get field values on the simulation grid, one must either discretize Maxwell's equations like is done in the standard Yee algorithm [92], or calculate the fields in spectral space [93]. In part IV) of the computational cycle, the Lorentz force (Equation 2.6) on each macroparticle is solved using the field values interpolated to the particle positions. This force is used to update the particles' positions and momenta. These steps are usually done using a computational leap-frog scheme.

The interpolation methods used by the solvers in parts II) and IV) of the computational cycle can vary in interpolation degree (linear, cubic, bicubic, quadratic, etc). While interpolation allows for the efficient PIC method to interact discrete fields with particles on a continuous plane, the approximation of field, charge, and current values leads to nonphysical noise in the simulation, which can have the effect of adding energy to the simulation via a phenomenon known as grid heating. A higher-order interpolation method will mitigate these adverse effects at a higher computation cost.

Another theoretical consideration is whether the time step size and the grid spatial size in each direction can adequately resolve the physics in each dimension. A general condition that must be met when considering the velocities of the objects being modeled comes from fluid dynamics and is known as the Courant–Friedrichs–Lewy condition for explicit time step solvers. This equation states that the time step Δt and grid size in each coordinate direction, Δx, Δy, Δz, given a characteristic velocity, say c, should be set such that

$$c\Delta t\sqrt{\frac{1}{\Delta x^2}+\frac{1}{\Delta y^2}+\frac{1}{\Delta z^2}} \leq 1. \tag{3.8}$$

Further constraints on the spatial and time step sizes can be imposed by the physics being modeled, such as high-density plasmas requiring fine enough spatial resolution to resolve the Deybe length of the plasma, simulations with lasers requiring a sufficient number of grid cells per wavelength to

properly resolve the electromagnetic waves, or simulations with long time-scale dynamics like ion diffusion to not have a time step so low to be impossibly computationally expensive to run.

When deciding to run a PIC code there are several options for different codes, both commercial and open-license, to choose from. Although all PIC codes operate with the same computational cycle, some offer auxiliary solvers to solve advanced physics interactions such as general relativity effects in extreme astrophysical plasmas [94] or quantum electrodynamics effects like pair-production from high-field interactions [95] as examples. Beyond auxiliary physics solvers, other codes are optimized to efficiently calculate particular geometries of interactions [96], or to manipulate the structure of the grid to load-balance calculations as the simulation progresses [97]. Nearly all PIC can simulate particles from 1 to 3 spatial dimensions while maintaining fully 3-dimensional momentum spaces. Within the scope of the simulations done in this dissertation, there were two PIC codes that were relied on depending on the modeling requirements: the OSIRIS 4.0 code [98] and the FBPIC code [93].

CHAPTER 4

Monoenergetic Beams in a Laser Wakefield Accelerator Via Shock Injection

4.1 Introduction

Although the development of LWFA as an alternative accelerator technology has been quite an active field in the past several decades, there are a few beam fidelity requirements for the applications of the beams from accelerators that currently hinder the technology as a replacement of conventional RF accelerators. Many potential applications of beams accelerated via LWFA necessitate, for example, reduced relative energy spreads compared to what most of the published results in the past two decades report (ranging from $\Delta E/E \sim 5\%$–100%, heavily dependant on the injection mechanism) while maintaining central energies in the $E >$ GeV range. For example, experiments measuring radiation reaction between an electron beam and an intense laser pulse benefit from having electron beams with energy spreads $\Delta E/E < 10\%$, where it has been shown that approximately 10 shots would be needed with a beam energy of 1 GeV and laser pulse of $a_0 = 5$ to discriminate between semi-classical and quantum radiation reaction models; which, for an electron with energy spread of 50% would take over 100 shots [99].

Longitudinal phase space trajectories in a plasma wakefield's Hamiltonian for electrons suggest that localizing the spatial region in which injection occurs in the accelerator's co-moving frame of reference $\xi = z - v_\phi t$, the resulting energy spread of the accelerated beam will be minimized. As such, one may localize to as small a $\Delta\xi$ region as possible the region of injection in the accelerator

to limit the amount of time injection occurs. There are several possible ways to achieve this, including localized ionization injection, cross-beam injection schemes, and rapid density-downramp injection, otherwise known as shock injection. The latter of these is the focus of this chapter.

The general criteria for shock injection are that the plasma density must decrease significantly on the spatial scale of the plasma wavelength, $\lambda_p = \frac{v_\phi \omega_p}{2\pi}$, where v_ϕ is the phase velocity of the plasma bubble. If the density transition occurs on the scale of the plasma frequency, the high-density electron bunch at the back of the wakefield's sheath suddenly transition from the 'untrapped' region of the original plasma bubble's Hamiltonian to the 'trapped' area of the new plasma bubble's Hamiltonian. The analysis of this interpretation below is drawn from previous work on the topic [62, 64].

In this work, we demonstrate the generation of low-energy spread beams at centroid energies in the range 1.2–1.3 GeV using shock injection with a 195 TW laser pulse driver. Similar experiments have previously shown electron beams with up to 2 GeV monoenergetic electron beams but on laser systems with higher peak power than the facility where this experiment was conducted [100]. A notable prior result on a 200 TW laser system validates the results found in this work, producing 8.5–23.6 pC beams injected via shock injection with energies exceeding 800 MeV and energy spreads (2.4%–4.1%) over an acceleration length of approximately 6 mm [101]. The shock in this work was created by placing a blade in the flow of a supersonic gas jet to make a sharp-density transition. The electron beam properties were shown to be sensitive to the longitudinal position of the shock.

The experimental results and numerical modeling detailed in this chapter are a part of an in-progress manuscript. The project was led by Stuart Mangles and Matthew Streeter. The team consisted of Nicholas Bourgeois, Jason Cole, Cary Colgan, Elias Gerstmayer, Brenden Kettle, Eva Los, Zulfikar Najmudin, Rajeev Pattathil, Gianluca Sarri, Guillermo Marrero Samarin, Aaron Alejo, Matt Zepf, Christian Roedel, Dominik Hollatz, Harsh, Felipe Salgado, Chris Murphy, Christopher Baird, Chris Underwood, Chris Ridgers, Chris Arran, Dan Symes, Mario Balcazar, Alexander Thomas, Mattias Marklund, and Tom Blackburn. My contribution included assisting

with experiment setup and running numerical CFD simulations alongside Matthew Streeter and Alexander Thomas to simulate the gas target's shock-front profile.

4.2 Methods

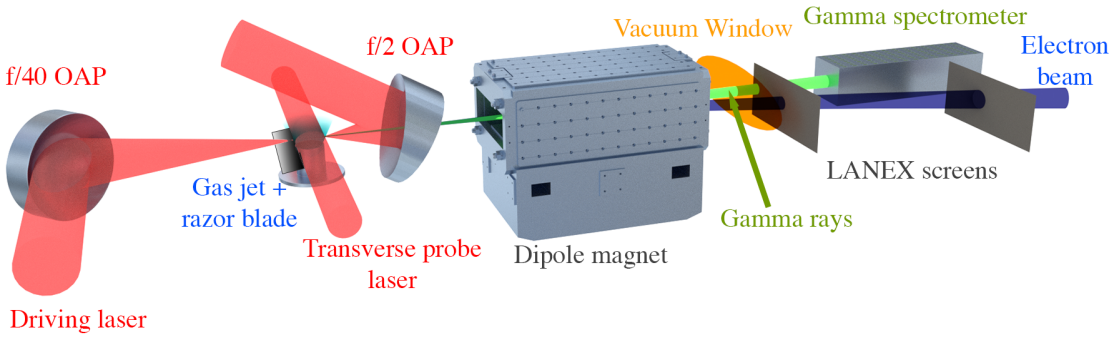


Figure 4.1: Schematic showing the experimental setup for this work. The results from this work were taken alongside a counter-propagating beam experiment. The counter-propagating tight focal-length laser was not utilized in the data discussed in this chapter; only the long focal-length drive pulse was used.

An experiment was conducted using the Gemini laser at the Central Laser Facility. Laser pulses containing 12.5 ± 0.2 J were focused with an $f/40$ parabolic mirror into a gas jet inside a vacuum chamber, as shown in Figure 4.1. The laser pulses were slightly positively chirped to a duration of 61 fs FWHM, giving a peak power of 195 TW. An adaptive optic was used to flatten the phase front and create an approximately Airy focal spot distribution with a spot width of $48.6 \times 39.2 \mu$m FWHM, a peak intensity of 75 GWμm^{-2} and a peak normalized vector potential of $a_0 = 1.88$ in vacuum.

A pulsed solenoid valve pressurized to 100 bar was coupled to a conical nozzle to create the supersonic gas jet. The conical nozzle had an exit diameter of 15 mm positioned 14 mm below the laser beam height. A steel blade was mounted perpendicular to the laser axis 4 mm above the nozzle exit at a fixed angle of $-32.4 \pm 0.3\,^\circ$ to the horizontal plane. Due to the gas jet's supersonic flow, a shock front was generated in the gas flow above the blade. In this, a density modulation was introduced along the path of the laser wakefield interaction. The position of this shock z_{inj} was

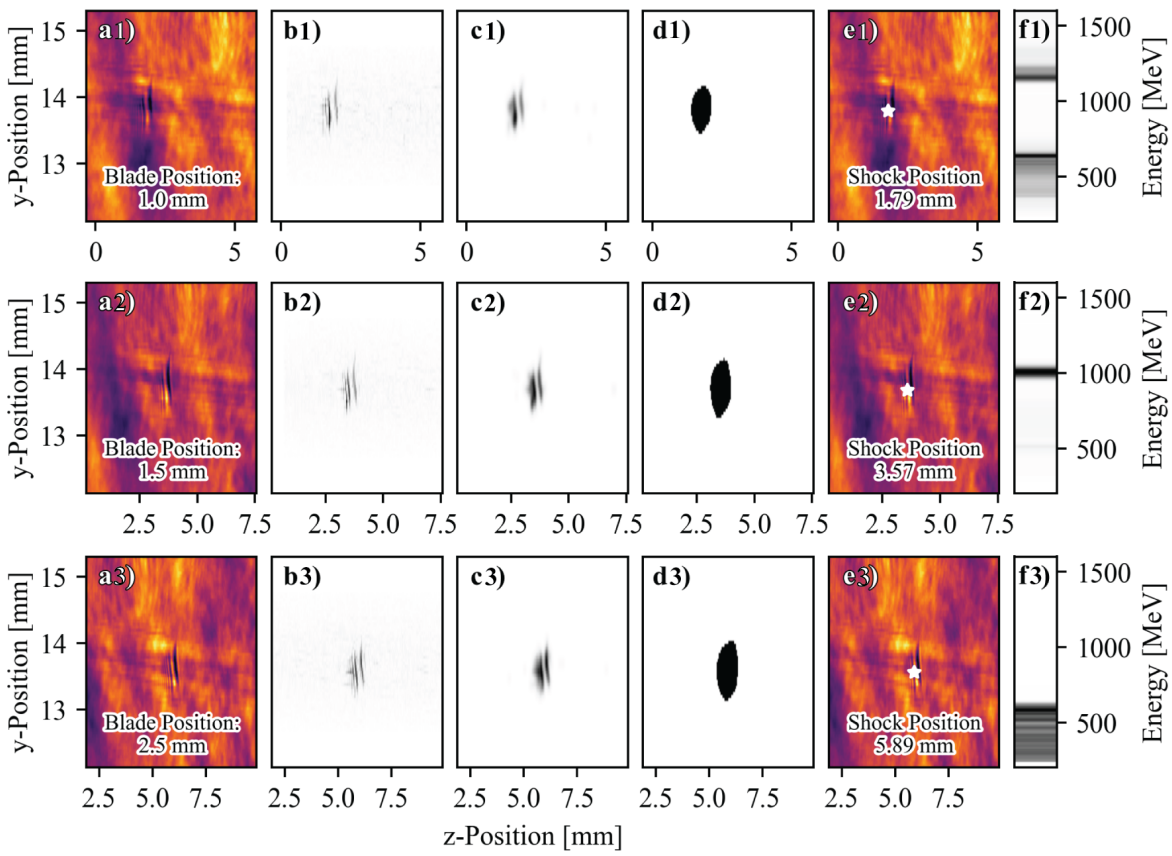


Figure 4.2: Example of shock locator code process for three different blade positions' monoenergetic beam results. a) The raw image undergoes a b) Laplace kernel operation, which is Fourier filtered and vignetted to make vertical shocks in the center of the data region more visible. c) This is blurred and thresholded, which is then d) also blurred and thresholded to reduce false selection of small high-frequency contrast features in the image. f) The angularly-summed energy spectrum with colorbars normalized to the highest charge density in the spectrum for each shot. The blade positions of these shots are 1) 1.0 mm, 2) 1.5 mm, and 3) 2.5 mm.

varied by translating the blade along in the laser propagation direction. A transverse probe beam was used to measure the on-shot channel structure and electron density through shadowgraphy and interferometry. A magnetic dipole was used to disperse the electron beams in the horizontal plane onto two Lanex scintillator screens. The signals on these two screens were recorded with optical CCDs (Andor Neo), which were used to determine the angularly resolved spectra of the generated electron beams. The signal on each screen was used to determine the pointing of the electron beam in the plane of dispersion to allow for retrieval of electron spectra in the energy range 200–2500 MeV.

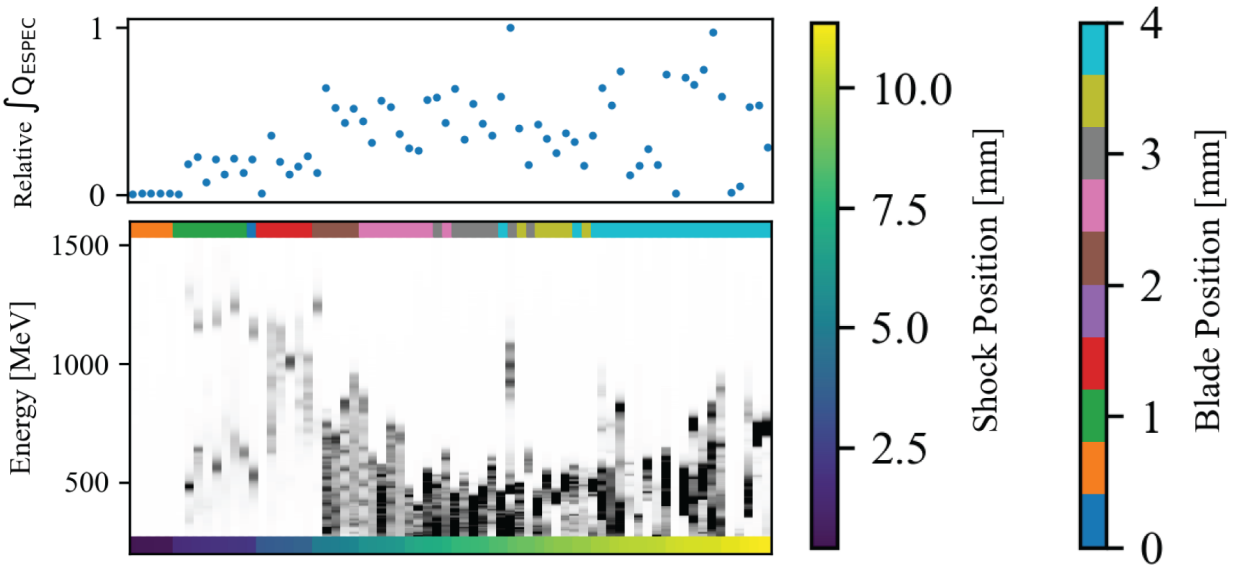


Figure 4.3: (Top) Relative angularly-integrated and energy-integrated charge on the (Bottom) electron spectra observed in a scan of the razor blade position across the gas jet ordered from left-to-right by increasing shock position. Each spectrum spans the angular range of ± 5 mrad around the beam centroid.

To determine the effect of the shock, the blade position was scanned, moving the shock position from $z_{\text{inj}} = 0$ mm to $z_{\text{inj}} = 6.9$ mm, as measured by the transverse probe shadowgraphy. Between five to nine repeat shots were taken at each blade position, in which the shock position fluctuated randomly with a standard deviation of ± 0.12 mm due to fluctuations in the gas flow. The shock location was determined through a process of taking the Laplacian of the shadowgraphy images to detect the high-contrast edges of the shock front. These Laplace images were Fourier-filtered to remove predominately horizontally-oriented features in the images, and were also vignetted to make the pixels in the region of the laser's path most dominant in the image. To determine the central position of the shock feature, these Laplace images were blurred using a Gaussian filter and thresholded twice to blend the edges of the shocks and remove minor high-contrast artifacts in the images. The centroid of any remaining features was recorded as the position of a shock in the image. Three examples of this shock location process for different blade positions are found in Figure 4.2. These highlight a general decrease in peak energy and a broadening of energy spread as the shock progresses toward the back of the gas jet. Figure 4.3 shows the angularly-integrated

electron spectra for each shock position, for which these trends can also be observed. The shock position changes faster than the blade position due to the fluid flow angle in the supersonic gas target and the flow distance between the shock-producing blade and the laser height above the gas jet.

4.3 Results and discussion

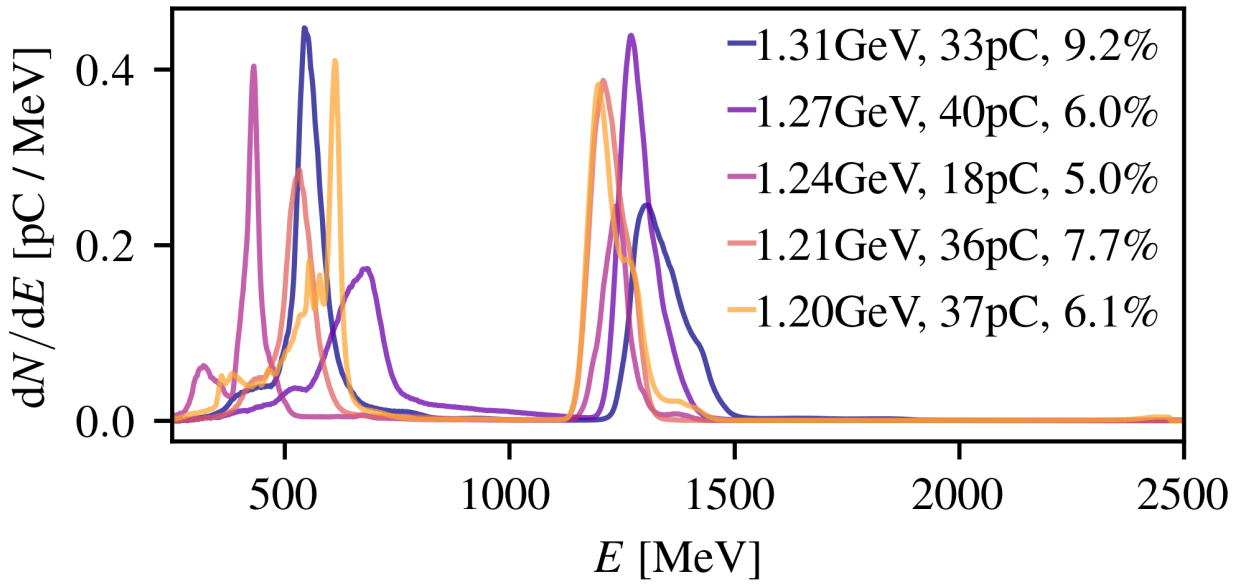


Figure 4.4: Angularly integrated electron number spectra for the optimised shock position $z_{\mathrm{inj}} = 2$ mm. The values indicated in the inset show the energy, charge, and FWHM energy spread of the high energy peaks in the spectra.

Low-charge (8 ± 4 pC) electron beams with charge extending up to 2 GeV were observed for $z_{inj} = 0$, consistent with self-injection in the unperturbed gas flow. A clear threshold is visible at $z_{\mathrm{inj}} = 2.0$ mm, where the shock front triggered significant injection. At this point, the total measured charge increased to 120 ± 30 pC, with an isolated spectral peak at 1.2-1.4 GeV appearing for 7 out of 8 shots. For 5 of those shots, the charge in the high energy peak exceeded 18 pC, while the others were much lower. Moving the shock position further into the gas flow resulted in increased total charge and energy spread. In addition, the maximum electron energy is reduced with increasing z_{inj}, consistent with the reduced acceleration length in the remaining plasma.

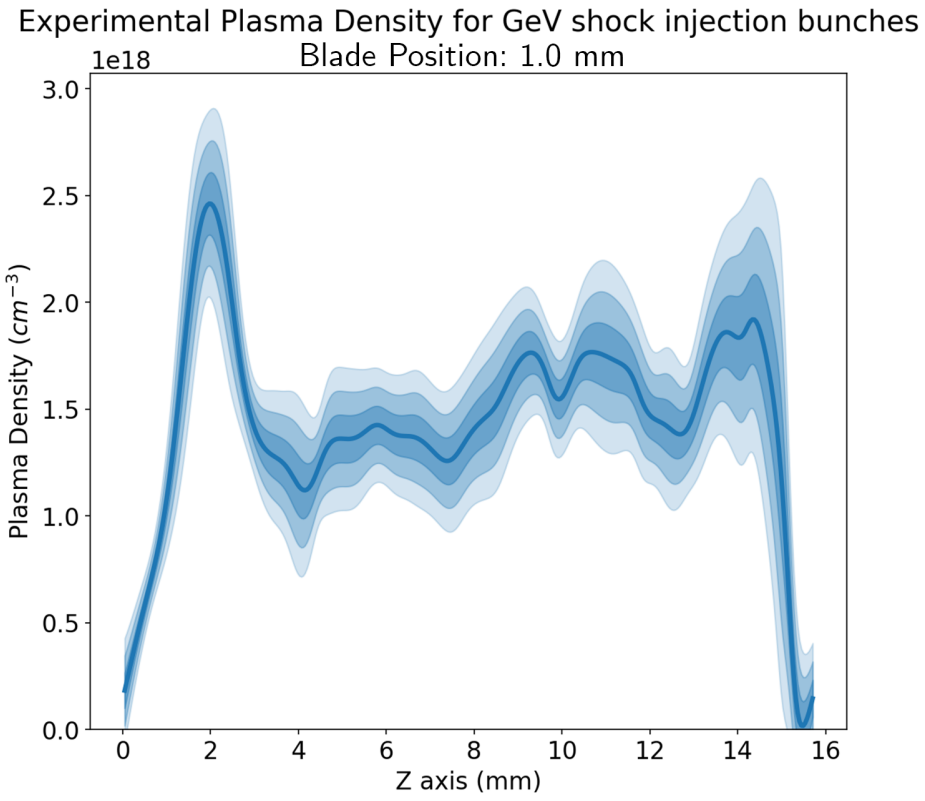


Figure 4.5: Experimentally extracted average density profile from interferograms for shots with the blade position $z_{\text{blade}} = 1.0$ mm, where monoenergetic GeV electron beams were measured.

The number spectra for the five optimal electron beams observed at $z_{\text{inj}} = 2$ mm, integrated over ± 2 mrad are shown in Figure 4.4. The high energy peaks of these beams contained 33 ± 8 pC at an energy of 1.24 ± 0.04 GeV. The measured percentage energy spread values were 5-9%, although these values were convolved with the divergence spread of the electron beams, and so are lower in reality. For each beam, a second lower energy peak was observed, consistent with injection into the second period of the plasma wakefield.

The longitudinal electron density profiles were determined by measurements of the accumulated phase of the transverse probe. This was corroborated with 2D fluid simulations performed using Ansys Fluent, the results for which after 2×10^{-4} s of flow time shown in Figure 4.6. These simulations used 3734008 nodes to resolve the gas flow from a 2D midplane cutout of the gas jet

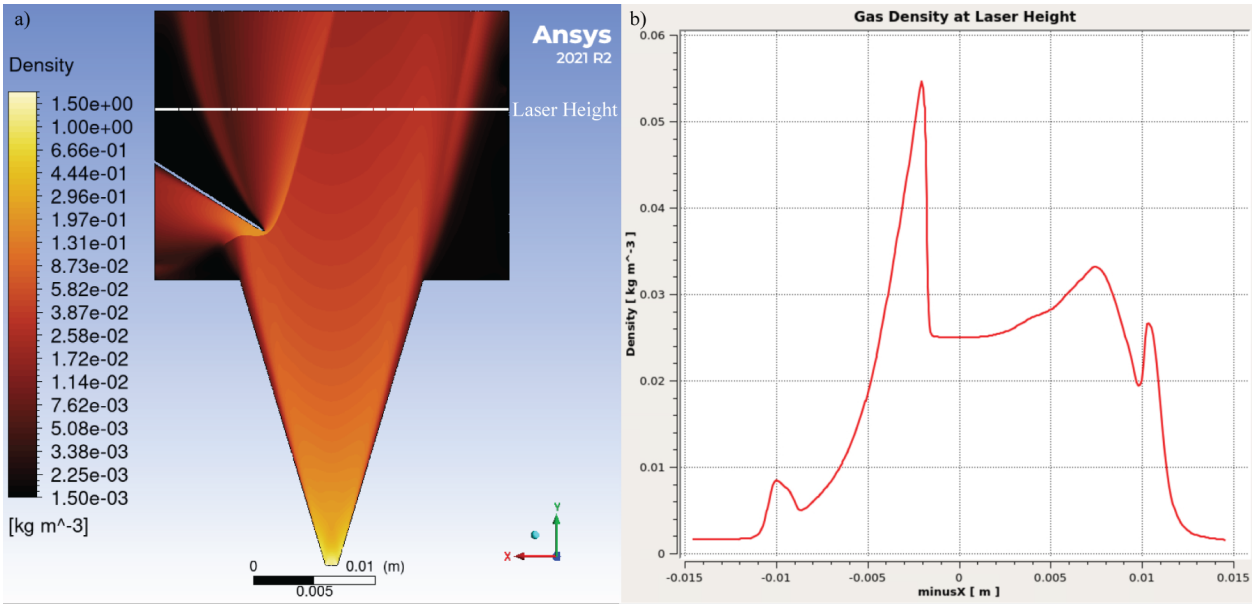


Figure 4.6: Results from 2D fluid simulation of the razor blade placed 2 mm in front of the gas jet's edge 200 μs of flow time after valve opening. a) The density heatmap in the gas jet domain using a logarithmic color bar scale. b) The line-out representation of the density at the height above the jet opening where the laser travels.

used in the experiment, with a pressure inlet set to constant pressure of 100 bar into a vacuum environment set to 1% of atmospheric pressure (0.001 bar) for the sake of the fluid simulation's stability. The razor blade was modeled after the angle and dimensions of the blade used in the experiment as best as could be reproduced via measurement of the blade. The Spalart-Allmaras turbulence model was chosen to improve the convergence of the simulation while also capturing turbulence effects in the fluid evolution. The simulation had an explicit time step size of 1×10^{-8} s with an adaptive refinement operation on the mesh to dynamically resolve sharp gradients in the density profile as they evolve over time. A 1 cm-long straight reservoir region with a width of 1 mm was added to the bottom of the jet's entrance to initialize the pressure gradient of the inlet pressure at the bottom of the reservoir to the ambient pressure at the top. This also helps improve the inlet conditions by moving the inlet away from the entrance of the conical jet opening, as supersonic flow quickly establishes at that point. The vertical simulation domain boundaries above the gas jet exit and the top boundary were defined as pressure outlets with a pressure set to the vacuum pressure in the simulation. Due to the nature of 2D fluid simulations not being able to capture the

full 3D expansion of the gas propagating through the nozzle, the density magnitude for the plateau following the shock was scaled from these fluid simulations to correlate with the measured plasma density for this region, as seen in Figure 4.5.

In order to explore the injection dynamics and demonstrate the injection of a low energy spread beam, relativistic particle-in-cell simulations were performed using the quasi-cylindrical particle-in-cell code FBPIC [93]. The simulation region was 100×160 μm^2 in the propagation (z) and radial r directions respectively. The fields were calculated on a grid of 2000×200 ($z \times r$) points, with two azimuthal θ modes. The plasma was simulated with $2 \times 2 \times 4$ ($z \times r \times \theta$) macro-electrons per cell and an immobile ion background. The probe measurements determined the initial plasma profile and compared to the hydrodynamic simulations shown above. The hydrodynamic simulated profile was linearly interpolated to define the simulated plasma profile, as shown in Fig. 4.7a. As defined in the experimental section, the laser was initialized with the measured temporal and spatial profile, assuming these are separable functions.

The simulations show the formation of a plasma wake, Fig. 4.7b, which, on crossing the shock boundary, expands to trap a well-defined beam of electrons, Fig. 4.7c. This beam has a small energy spread and temporal duration, as shown in the momentum space diagnostic in Fig. 4.7d, along with the spectrum shown in an inset panel. The trapping is highly sensitive to the global density, magnitude, and steepness of the shock, as well as the laser conditions and evolution, representing a multidimensional parameter space to search. In the simulation here, a large charge is trapped, which overloads the wake, leading to a substantial gain in energy spread, Fig. 4.7e. This is because the feedback of the beam charge on the plasma wake is so strong it strongly modifies the longitudinal electric field, Fig. 4.7f, leading to the growth in energy spread. When the injected charge is properly optimized, as in the experiment, the resulting flattened fields are well known to maintain the beam energy spread [55].

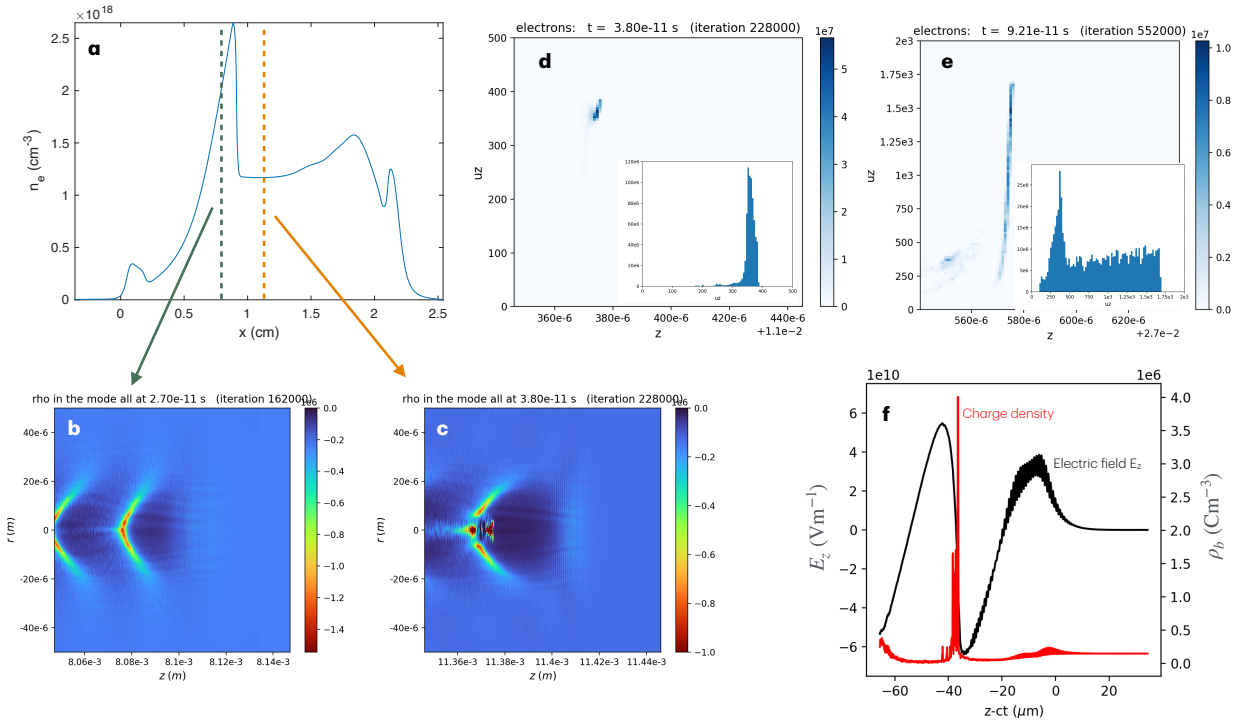


Figure 4.7: Quasi-3D simulations with FBPIC. (a) The density profile from the hydrodynamic simulation that was used in the simulation. (b) and (c) show the plasma wave just before and after the shock transition, showing the trapping of a short and monochromatic bunch. (d-e) the momentum space and spectrum (inset) (d) just after the shock transition and (e) near the end of the simulation. (f) shows the plasma wave's beam profile and longitudinal electric field just after the shock transition.

4.4 Conclusions

This campaign has demonstrated a method for generating narrow energy spread electron beams at 1.2 GeV. These electron beams are ideal for applications such as studying strong-field radiation reaction [29, 102]. Compared to previous LWFA-based radiation reaction experiments, using electron beams such as those generated in this work would allow for a much higher degree of discrimination between semi-classical and quantum-based models due to the ability to observe a reduction in the electron beam energy and the increase in energy spread that would result from the stochastic photon emission process [99]. When the position of the shock front in the accelerator was scanned further into the length of the accelerator, the resulting average electron beam energy decreased, charge increased, and relative energy spread increased.

The generated electron beams were shown to be particularly sensitive to the longitudinal density profile, which varied considerably due to the chaotic dynamics of the supersonic gas flow. High current and high spectral brightness beams would be expected to be generated consistently by harnessing this technique with a more stable gas target. The consistent production of high-energy monoenergetic electron beams could be a potential route to LWFA-based free-electron lasers and other accelerator applications.

CHAPTER 5

Streaked Laser Wakefield Trajectory Producing Angular vs Time Correlation in Wakefield Accelerator

5.1 Introduction

As the total energy gain achievable via LWFA is limited by a mixture of diffraction, depletion, and dephasing of the driving laser, the endeavor of optimizing the design of the accelerator to maximize the quality of the beams would benefit from on-shot measurements of these phenomena in an accelerator. Typically dephasing, which is the phenomenon that occurs as electrons gain energy and outrun the phase velocity of the wake in the plasma to the point where they leave the accelerating-field region of the plasma bubble and begin to decelerate, is the limiting factor for energy gain at high-power LWFA facilities. There has been recent work to mitigate dephasing in laser-driven plasma accelerators with so-called 'dephasingless' acceleration schemes [21]. These types of acceleration schemes extend the dephasing length of the laser in a controlled manner, potentially to the point that diffraction or pump depletion limits energy gain; however, recent work has also addressed mitigating diffraction by using plasma channel profiles as guiding structures for the laser driver [26, 103].

On-shot measurements of the temporally resolved energy growth of the beams are needed to be able to measure phenomena such as dephasing occurring in an accelerator so that parameters could

be tuned in real-time to optimize the output of an LWFA accelerator. Previous works have used invasive multi-shot methods to take such a measurement of dephasing, involving either scanning the effective length of the accelerator to track the energy of the electrons produced at each length [65, 104–107] or by colliding the beam with a probe pulse to induce Thompson scattering and measuring the output from that interaction [108]. These methods depend on a high level of stability in the accelerator system as averages of several shots (ranging from 3 to 10, for example, in prior experiments [65, 104]) at each location are used to determine the mean energy gain at that location, and the probing location must be scanned over multiple points along the accelerator to achieve an energy-growth measurement along the length of the gas target. As such, they do not capture the energy gain vs time for any one shot, but as an average over many shots.

This work presents an experimental verification of a method for measuring the on-shot energy growth of an electron beam by exploiting an approximately quadratic correlation in the X-ray critical energy of a betatron beam to the electron beam energy that produced it. On-shot measurement of streaked betatron signal as a tool to diagnose wakefield-accelerated electron beams' energy growth was first proposed by Yong Ma et. al. (2018) [109], who showed through theory and simulation that a pulse-front tilt can be induced in a driving laser pulse with a controlled transverse plasma density gradient in the accelerator gas target. First, the transverse trajectory for a laser in the linear regime can be derived, and then effects from intense laser propagation through nonlinear plasma media are considered. The plasma density gradient, described by $n_p(x)$, where x is the transverse direction, drives a transverse gradient in the laser phase velocity according to the plasma dispersion relation for light. This spatially varying density gradient gives the phase velocity of

$$v_\phi = c/\sqrt{1 - \frac{n_p(x)}{n_c}}, \tag{5.1}$$

where c is the speed of light in vacuum, and n_c is the critical density for the laser pulse. The pulse front tilt results in the beam steering toward the low-density side of the transverse density gradient as a result of refraction. For a known longitudinally-constant density gradient in the transverse

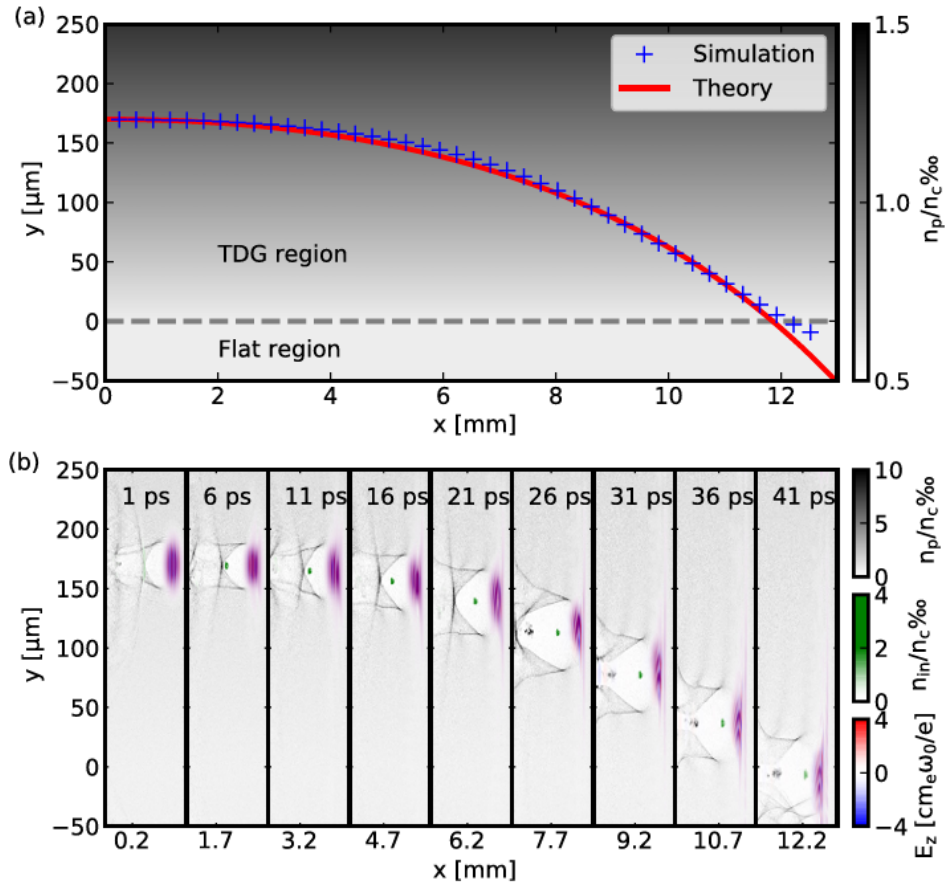


Figure 5.1: A theoretical and simulated curved laser trajectory example for an intense laser wakefield driving pulse ($a_0 > 1$) traveling perpendicular to a transverse density gradient (a). Snapshots of the wakefield acceleration along different points in its curved trajectory are also shown (b). Reprinted with permission from [109], AIP Publishing.

x-direction the theoretical trajectory can be determined from Snell's law:

$$\frac{d}{dx}\nu(x)\cos\alpha = 0, \tag{5.2}$$

where $\nu = \frac{c}{v_\phi}$ is the refractive index in the plasma and α is the grazing angle of the laser with respect to the longitudinal z-axis. If we assume a linear transverse density gradient of the form of $n_e(y) = n_0 + y\frac{n_0}{L}$, we are left with a theoretical parabolic trajectory,

$$y(z) = \Phi(z^2 - zz_s), \tag{5.3}$$

where $\Phi = n_p/\left(4Ln_{cr}\cos^2\alpha_0\right)$ and $z_s = \frac{\tan\alpha_0}{2\Phi}$, where n_p and α_0 refer to the plasma density and the initial grazing angle of the laser at the point $x = y = 0$.

This can be made more accurate for the case of a driving laser pulse in the nonlinear plasma wakefield regime, where nonlinear evolution of the pulse causes a spatially variable red-shift in the pulse described by the expression $d\lambda/dx = \sigma a_0 \left(n_p/n_{cr}\right)^{3/2}$, where σ is a scale factor relating the steepness of the gradient and the distance from the rising front of the laser pulse. A variable red-shift results in a variable critical density, leading to a variable parabolic path in the pulse. This process is discussed in Ma et al. [109], where σ is fit to agree with 2D PIC simulations of the curved trajectory along a wakefield accelerator in a transverse density gradient such that $\sigma = 0.17$. An example of a curved trajectory from the theoretical framework discussed above compared to a 2D PIC simulation of a driving pulse of $a_0 > 1$ is in Figure 5.1 showing quite good agreement between simulation and theory.

The physics of electron energy gain and betatron emission is included in Chapter 2; however, it is helpful to the understanding of the discussion in this chapter to highlight the correlation between properties of the betatron X-ray emission with the properties of the electron beams in the wakefield. The critical energy E_c and the divergence angles parallel to an electron's plane of oscillation $\theta_{||}$ and transverse to the direction of oscillation $\theta_\perp$ of the betatron X-rays can be related to the electron beam via the following equations [67]:

$$\begin{aligned} E_c(z) &= \frac{3}{2}\hbar\omega_\beta(z)K(z)\gamma(z)^2 \\ &= \left[\frac{3\hbar e^2}{4\epsilon_0 m_e c} r_{\beta 0}(n_0\gamma_0)^{1/4}\right] n_p(z)^{3/4}\gamma(z)^{7/4}. \end{aligned} \tag{5.4}$$

$$\theta_{||}(z) = \frac{K(z)}{\gamma(z)} = \frac{\omega_p(z)r_\beta(z)}{c\sqrt{2\gamma(z)}} \tag{5.5}$$

$$\theta_\perp(z) = \frac{1}{\gamma(z)}, \tag{5.6}$$

where γ is the relativistic Lorentz factor, $K = \frac{\gamma\omega_\beta r_\beta}{c}$ is the characteristic betatron oscillation

strength parameter, $\omega_\beta = \frac{\omega_p}{\sqrt{2\gamma}}$ is the betatron frequency, and $r_\beta \simeq r_{\beta 0}\left(\frac{n_0\gamma_0}{n_p\gamma}\right)^{1/4}$ is the betatron oscillation amplitude dependant on the initial betatron amplitude r_0, the initial plasma density n_0, and the initial normalized particle energy γ_0. We note that the term within the square brackets of the ultimate expression for E_c is independent of the temporal evolution in the accelerator and is a constant determined by the initial $r_{\beta 0}$, n_0, and γ_0 terms. The betatron critical energy and divergence characteristics are therefore determined by the the energy of the electrons and the plasma density in the accelerator. It is this relationship that this experiment exploits in order to measure the temporally-resolved energy growth of the electron beam in the accelerator: as the electrons gain energy, the critical energy of the betatron photons increases. By transversely sweeping the electrons as they are accelerated the instantaneous pointing of the electron beam changes, and thus the angular emission of the betatron beam yields a measurement of the growth of the critical energy of the betatron beam with respect to angle.

If all terms except for $\gamma(z)$ in Equation 5.4 are known, then the $z-$ resolved energy of the electron beam can be solved for as $\gamma(z) = \left(E_c(z)/\left[\frac{3\hbar e^2}{4\epsilon_0 m_e c} r_{\beta 0}(n_0\gamma_0)^{1/4}\right]\right)^{4/7} n_p(z)^{-3/7}$. It should be noted that the initial betatron parameters $r_{\beta 0}$ and γ_0 are quite difficult to measure experimentally; however, since we do measure the final energy of the electron beams γ_f, the corresponding final betatron critical energy E_{cf} and the corresponding plasma density in the accelerator n_{pf}, we can fit the value of $r_{\beta 0}$ to scale with these values assuming an electron beam at position z with energy $\gamma(z)$ and an uncorrelated betatron oscillation width $r_{\beta 0}$. This results in an expression for the longitudinally-resolved energy of the electron beam from the betatron critical energy emitted at angle $\theta(z)$:

$$\gamma(z) = \left[\frac{E_c(\theta(z))}{E_{cf}}\right]^{4/7} \left[\frac{n_{pf}}{n_p(z)}\right]^{3/7} \gamma_f. \tag{5.7}$$

The work outlined in this chapter resulted in a paper that has been accepted for publication at the time of submitting this thesis: *Single-shot diagnosis of electron energy evolution via streaked betatron x-rays in a curved laser wakefield accelerator,* Y. Ma, J.A. Cardarelli, P.T. Campbell, et al. *Physical Review Letters* (2024). My role in this work was to provide in-person support for

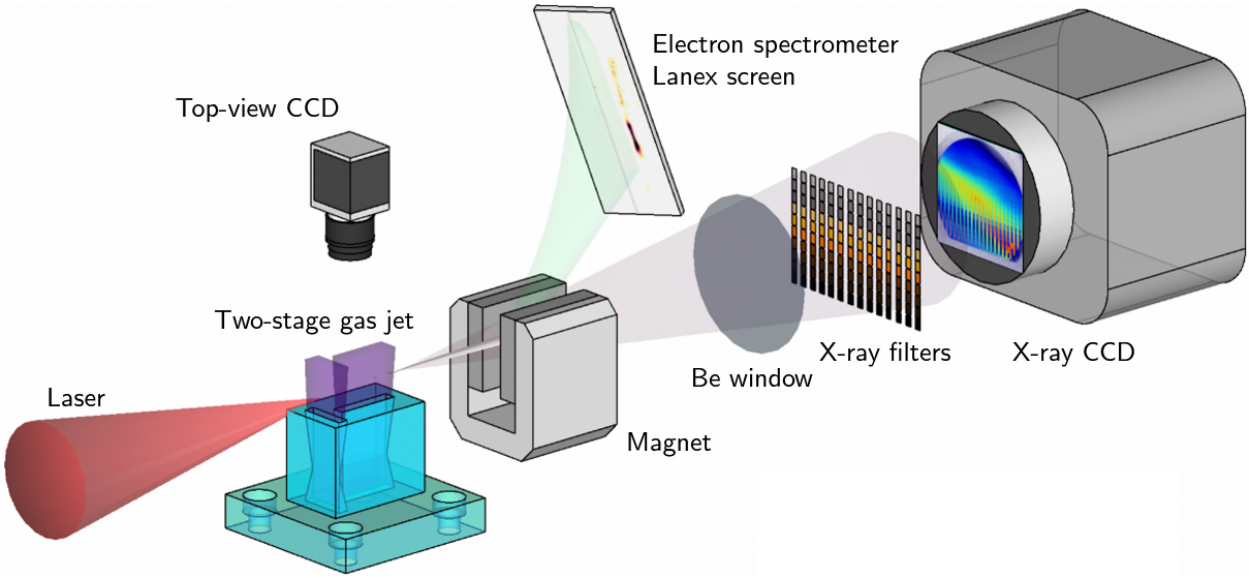


Figure 5.2: The target and diagnostic setup of the experiment. Not shown is the transverse interferometer used to measure the on-shot plasma density in the target.

the experiment throughout the campaign and to contribute data analysis of the ESPEC diagnostic. Yong Ma and Alexander Thomas contributed to the project's conceptualization and experimental advising. In-person experimental support was provided by Nicholas Beier, Paul Campbell, André Antoine, Mario Balcazar, Rebecca Fitzgarrald, and myself; as well as from the research faculty and staff at the Advanced Laser Light Source (ALLS) laboratory: François Légaré, Sylvain Fourmaux, Joël Maltais, Stéphane Payur, and Claude Sirois. Yi Fei Li assisted with gas target design, and Yong Ma did the bulk of precursory experimental planning and data analysis shown in this chapter. This experiment was made possible by support from the DOE Office of Science, Fusion Energy Sciences under Contract No. DE-SC0021246: the LaserNetUS initiative at Advanced Laser Light Source; DOE grant DE-SC0022109, NSF grant 2108075, and DOE grant DE-SC0020237.

5.2 Methods

This experiment took place at the Advanced Laser Light Source (ALLS) laboratory at the Institut National de la Recherche Scientifique (INRS) in Quebec, Canada as a sponsored campaign within the LaserNetUS program. The setup of the experiment can be found in Figure 5.2. The laser's

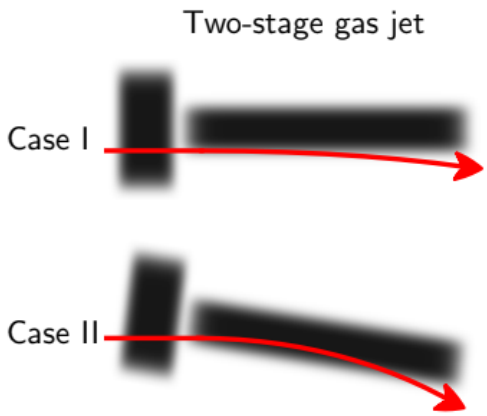


Figure 5.3: The two cases of target geometry in which shots were taken. In case 1 the density gradient inducing angular streaking is along the x-axis transverse to the initial laser trajectory. Case 2 rotates the target by 25 mrad such that the laser in the acceleration stage of the gas target will travel first up and then back down the steering density gradient.

characteristics measured at the time of this experiment include an energy of 3.2 J, a FWHM duration of 22 fs, a spot size of 15 μm, a Strehl ratio of 0.8, and a pointing stability of 2.6 μm. The pointing of the laser was measured as an on-shot diagnostic using leak-through light from the final dielectric turning mirror before the focusing optic. The gas target used in this campaign was a 3D-printed two-stage "T"-shaped supersonic gas jet made of stereolithographed Acurra 60. The first injector stage had a longitudinal length of 1 mm and a transverse length of 5 mm and expelled a gas mixture of 99.5% helium + 0.5% nitrogen. This gas mixture is intended to utilize ionization injection at the front of the accelerator to inject charge locally and maximize acceleration length for the bulk of the injected charge. The second accelerator stage was 10 mm long and 1.2 mm wide with pure helium gas.

The two stages' nozzle openings were separated by 0.5 mm in the longitudinal direction. The interior of the nozzle was designed with a parabolic cross-section to achieve supersonic flow based on a supersonic gas nozzle design for laser wakefield application [87]. The throat of the nozzle was 200 μm wide. Each stage had an independent gas valve triggered by the timing signal of the ALLS laser system. Before the experiment, the longitudinal and transverse density profiles were characterized using neutral density gas and a CW diode laser via interferometry using a fast-gated

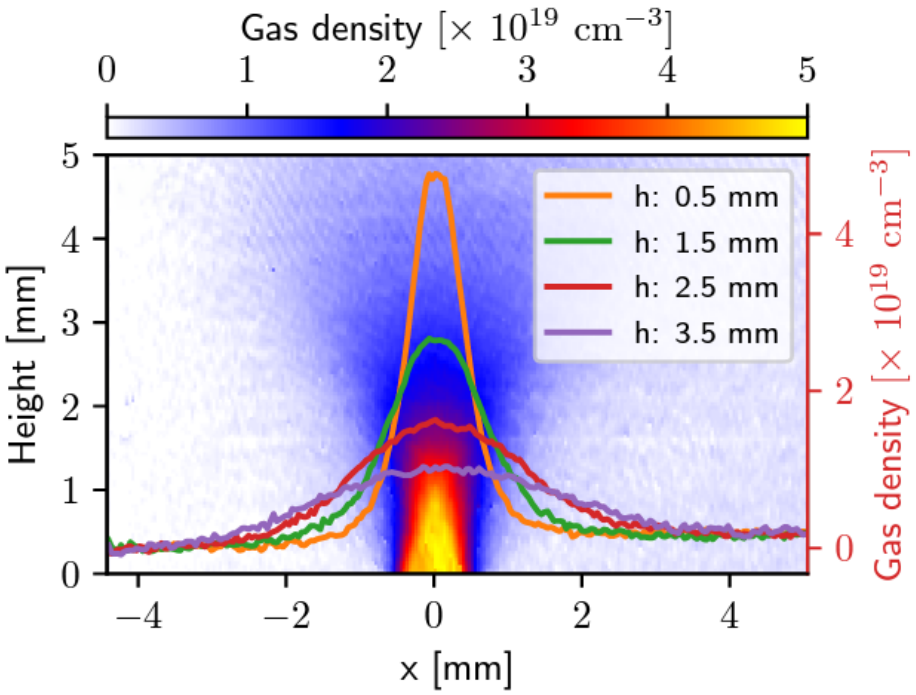


Figure 5.4: Results of reconstructed neutral gas density measurements via interferometry of the accelerator stage with the transverse direction in the x-direction. The height above the orifice of the gas jet is labeled on the left y-axis, with density line-outs for selected heights above the target corresponding to the right y-axis.

CCD, akin to previously published methods [110]. Results for the transverse density profile for the accelerator stage with 600 PSI backing pressure can be found in Figure 5.4, where notably the density gradient at the transverse edges of the high-density gas profile at different heights is characterized.

In the setup were on-shot diagnostics measuring the laser pulse trajectory, the electron beams' energy, divergence, and pointing, and the betatron photons' critical energy and angle of emission. The laser pulse trajectory in the accelerator was measured with a top-view CCD collecting scattered light emission from the ionization front along the laser's path in the accelerator. An example of this diagnostic measuring both a straight and a curved trajectory is shown in Figure 5.5. The electron beams were dispersed in the direction transverse to the streaking direction by two removable $10\ cm$ long dipoles of strengths 1.12 T and 0.83 T, and measured by scintillating LANEX screen in the electron spectrometer system. The energy range of the spectrometer was $0.1 \leq E \leq 1$ GeV.

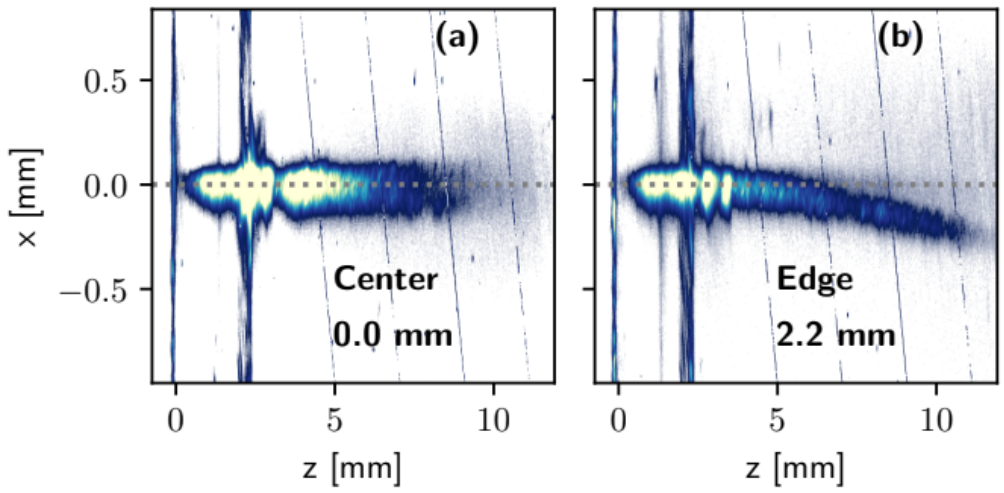


Figure 5.5: Top-view diagnostic from the experiment demonstrating measurement of the plasma emission in the cases where the laser was shot in the transverse-center of the accelerator jet (a), and where the laser was shot along the highest density gradient edge of the accelerator jet (b). This is an example of the the target in 'Case 1' configuration.

The direction of the dispersion in the y-axis (as opposed to the transverse x-axis that the streaking takes place) so that the angular dispersion due to the electron spectrometer does not severely influence the measurement of the pointing of the electron beams in the streaking direction, and also that the streaking would not affect the energy dispersion relation relating position and energy on the LANEX screen. The betatron spectrum and emission angle was measured by a Princeton Instruments SCX 4300 CCD with a Gd_2O_2S : Tb phosphor screen in front of the chip placed 1.35 m away from the source outside of the vacuum chamber with only a Be window and air outside the chamber between the source and the CCD. The phosphor screen emits at a constant wavelength, so the CCD's chromatic quantum efficiency need not be taken into account while the phosphor screen's absorption vs photon energy is well calibrated. This CCD has a chip size of 50 mm x 50 mm, and a pixel size of 24 μm x 24 μm, which means the acceptance angle from the source to the chip was 37 mrad. The position on the chip is correlated to the angular emission from the source. This CCD thus serves as a measurement of the angular streaking of the emission of the X-rays.

The angularly-resolved spectrum of the X-rays incident on the CCD is measured using a transversely-periodic X-ray filter pack. This filter pack consists of 11 different materials and thick-

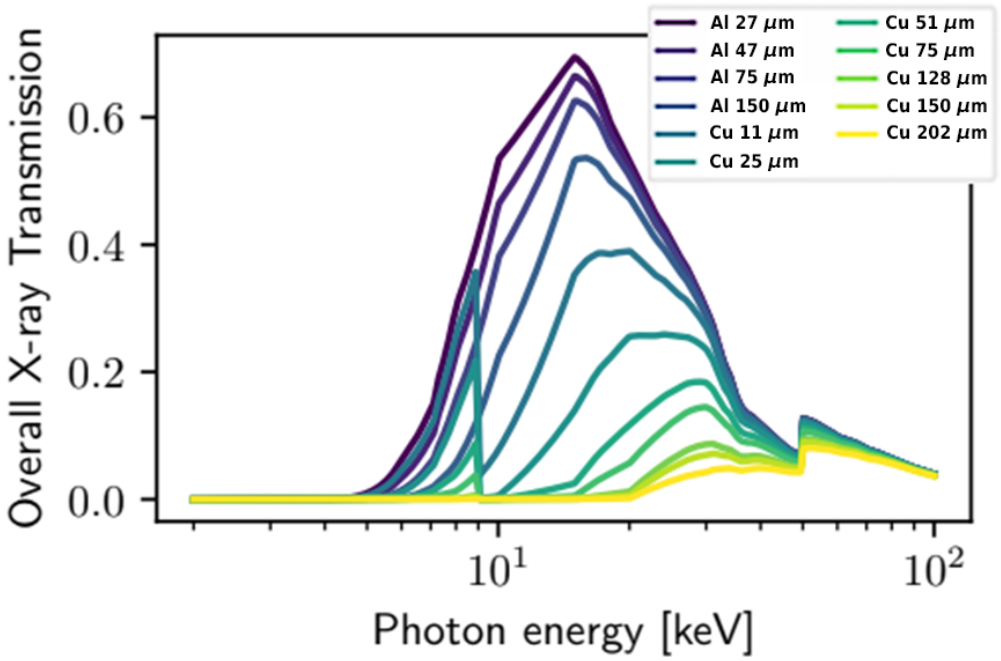


Figure 5.6: The transmission as a function of photon energy for the series of materials and material thickness that made up the vertical-grid X-ray filter with the material and the thickness in microns labeled.

nesses stacked along the y-axis, repeated 25 times in the x-axis (the direction of angular streaking) with a spacing of 1 mm between each repeated column to give a measurement of background and local betatron beam profile in the region of each column. Each material and thickness has a characteristic X-ray transmission for different energy X-ray energies. The transmission of each combination of material and thickness for the filter used in this campaign is shown in Figure 5.6. The mean spectrum at each filter location is retrieved with a forward least-squares fit of the transmission through each filter element normalized to the background profile given by the unfiltered regions of the X-ray image. A solution for the critical energy E_c at each column along the x-axis is obtained iteratively from an initial guess assuming a synchrotron-like spectrum from the wakefield source to find the best-fit from the transmission of every filter in each column, as is routine to reconstruct X-ray energies from wakefield-produced betatron beams [84, 85]. The width of each column represents an angular resolution of 1.7 mrad for each energy measurement along the x-axis. As Equation 5.7 suggests, this limit in the resolution of angle $\theta(z)$ in the measurement of E_c

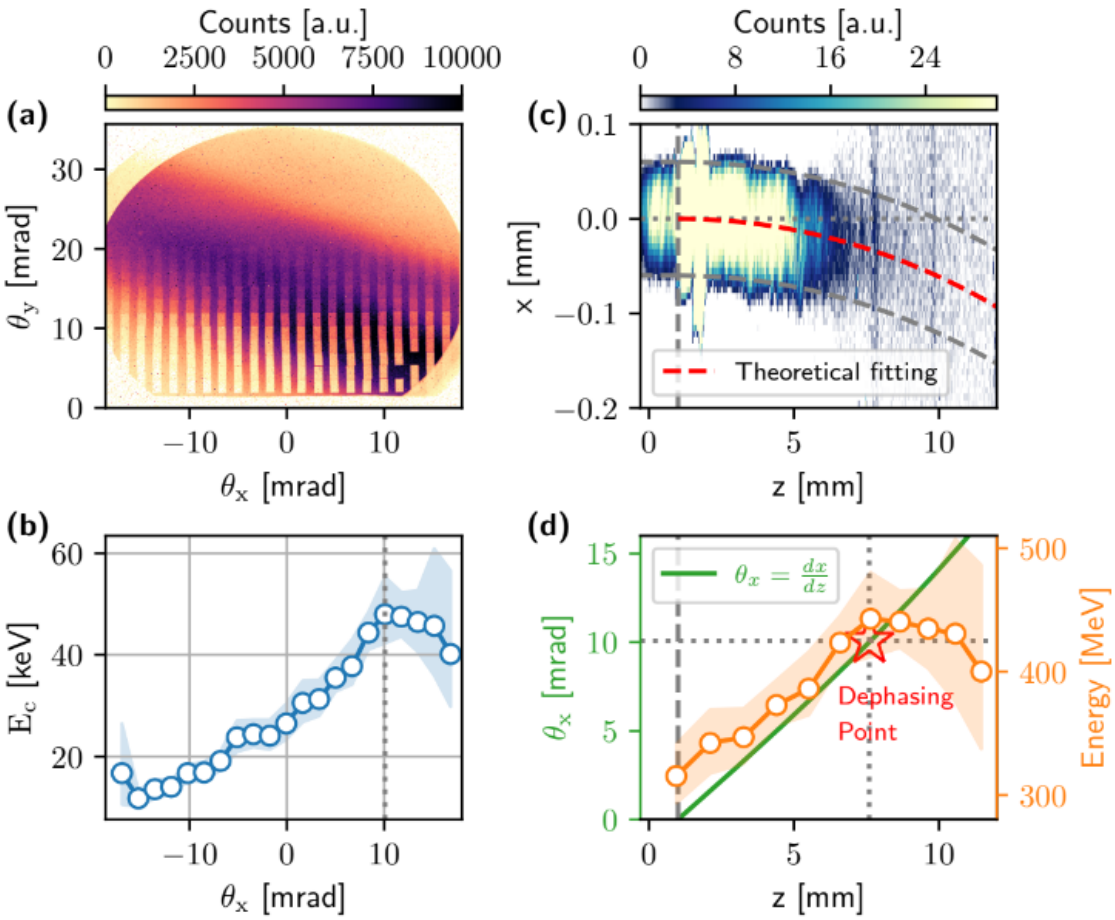


Figure 5.7: The process correlating the angularly-resolved betatron spectra with the temporal measurement of the average energy within the electron beam from the X-ray CCD image of the streaked beam (a). This yields a critical energy to angle-of-emission correlation (b), which, combined with the top-view measurement of the trajectory angle along the longitudinal z position along the accelerator (c), can be used to measure the Z-position evolution of electron energy and angular pointing correlated to the longitudinal position within the accelerator (d).

leads to a limited resolution of the longitudinal points measured along the accelerator. Specifically, a 1.7 mrad angular resolution corresponds to a $\delta z = 1.1$ mm longitudinal resolution in the energy gain of the electron beams.

5.3 Results and discussion

An example of the measurement of the energy gain as a function of longitudinal position in the accelerator is shown in Figure 5.7. The process of this reconstruction of the electron temporal

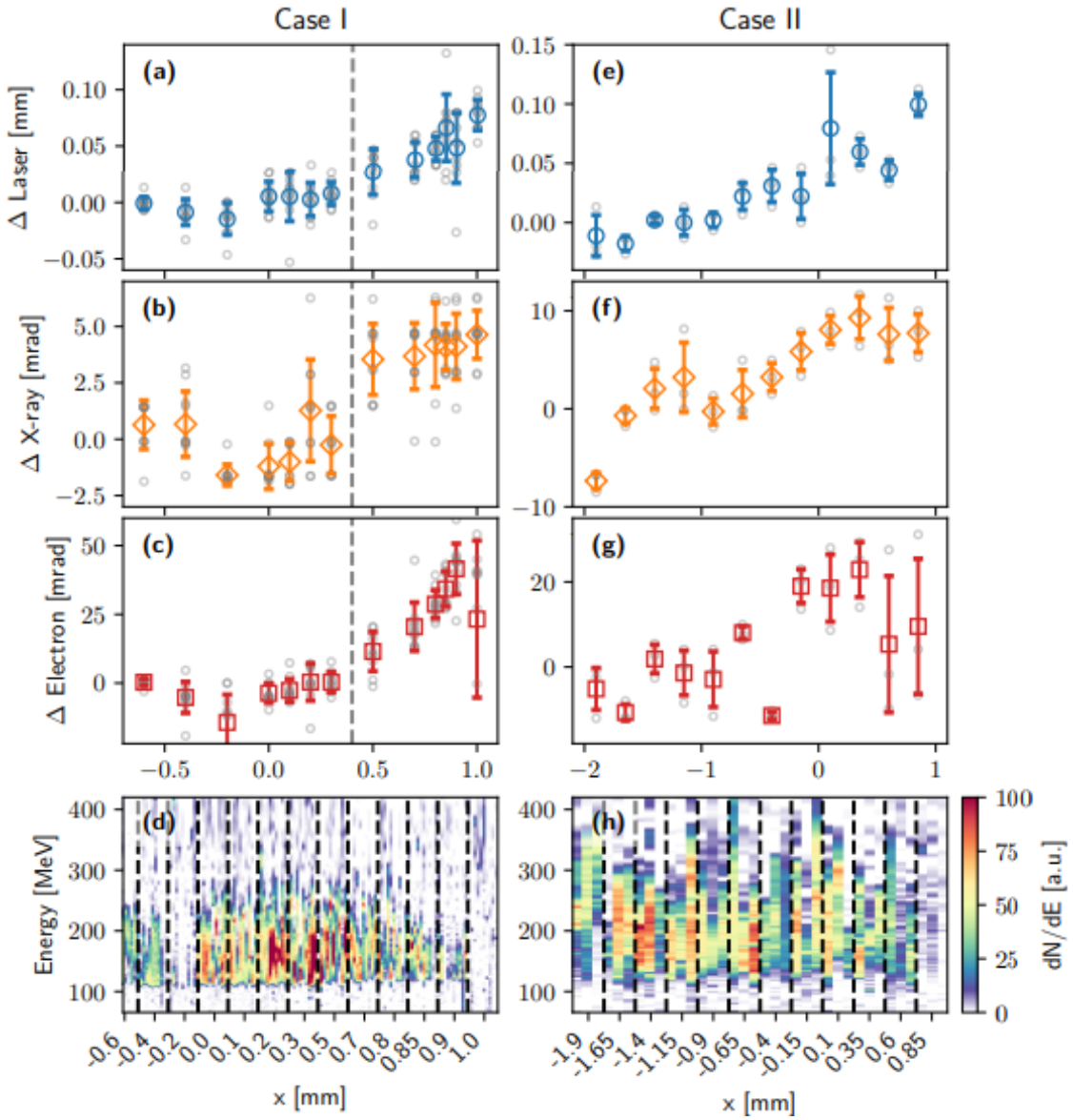


Figure 5.8: Measurements of the streaking from various diagnostics for the straight-on transverse gradient case (case 1) and the grazing-incident angle case (case 2) as the transverse $x-$position of the accelerator is scanned. For case 1 results, a dotted line is added to represent the position where the laser enters the transverse density gradient so that points to the right side of the line are interacting with the transverse density gradient in the accelerator. The measurements shown are the difference of positions of the laser center at the entrance and exit of the accelerator (a, e), the angular deviation of the peak of the betatron beam on the X-ray CCD with respect to the central laser axis (b, f), the transverse angular deviation of the electron beams measured on the ESPEC (c, g), and processed angularly-integrated ESPEC scintillator images (d, h) for each shot at a given x position.

energy gain from a streaked LWFA shot is as follows. First, the X-ray CCD image of the betatron interacting with the X-ray filter pack is analyzed to give the on-shot angular pointing vs betatron critical energy correlation. Then the top-view measurement of the laser ionization front is used to determine the on-shot correlation between the longitudinal position along the z-axis and the pointing angle between the x- and z-axes made by the trajectory. Finally, the pointing angle of the electron beam is correlated to the pointing of the betatron beam to give the pointing angle of the critical energy vs the longitudinal position of the electron beam correlation. Thus, from the relations in Equation 5.7, the average electron energy per z-position in the accelerator is determined. It is worth noting that while the electron energy first increases with the longitudinal position in the accelerator, there is a measured decrease in the beam's energy in the rear of the accelerator. This decrease in energy can be explained by the electrons reaching the dephasing length in the accelerator and beginning to decelerate.

In both target case geometries shown in Figure 5.3, the transverse x-position of the target was scanned to either gradually transition the transverse position of the laser in the accelerator from the approximately constant high-density region in the middle of the gas jet to the density gradient at the edge of the accelerator jet in case 1, or to scan the total curvature obtained by the laser in case 2. The results of these scans for the change in the transverse x-position of the laser from the back to the front of the accelerator, the change in X-ray peak pointing angle, the electron pointing angle, and electron spectra for these position scans can be found in Figure 5.3. In case 1 geometry, this scan showed a clear dependence on the curvature of the trajectory on the position of the laser entering the accelerator with respect to the position of the quasi-linear density gradient at the edge of the density profile. When the laser entered the center of the acceleration density plateau region, no net curvature in the profile was measured in the top-view diagnostic. However, when the laser was incident on the density profile in the accelerator starting at around $x = 0.4$ mm in Figure 5.8, a curvature was observed resulting in a maximum laser $x-$position deviation of 300 μm between the front and back of the accelerator. It is worth mentioning that this trajectory curvature is in good agreement with PIC simulations performed with similar plasma and laser

parameters as was performed in Ma et. al. [109]. The streaking of betatron X-rays was also observed in the X-ray CCD diagnostic, and the critical energy of the X-rays was measured to vary along the angularly streaked axis. The electron spectra had a roughly consistent profile for x-positions within the density gradient as those measured within the plateau of the accelerator, with a decrease in maximum energy reached as the average plasma density in the accelerator density decreases due to the transverse gradient, which agrees with known energy-gain scaling of LWFA acceleration [23].

In case 2 geometry, on the other hand, the scanning of the $x-$position of the target changed the total curvature of the streaking, but the streaking was present at all $x-$positions. The electron spectra in the case 2 geometry were measured to have maximum energies greater than those measured in the case 1 geometry, which suggests that rephrasing of the electrons in the wakefield occurs due to the density up-ramp which allows the electrons to gain further energy beyond the dephasing length limit in a constant-density gas target [109, 111–115]. This increase in maximum electron energy was also observed as an increase in maximum betatron X-ray critical energy.

A systemic issue with the ESPEC diagnostic during the experiment was a poor signal-to-noise ratio in the captured signal and the presence of high-frequency noise due to difficulty with shielding the CCD from radiation. The plan to develop a script to identify both the mean transverse position of the electron beam on the ESPEC screen and the electron beam spectra was made difficult by these issues, and thus required image processing techniques to make the electron beam data more prominent in the collected images. First a small square kernel (3 x 3 pixel kernel) median filter was used on the image, and then a low-pass Hamming window Fourier filter was applied to the images. While this filtering did improve the signal-to-noise issue in the dataset, the algorithm used to find the maximum integrated angular position of the electron beam on the LANEX screens was prone to misidentifying the transverse positions of the beam due to the integrated influence of large amounts of radiation snow-like noise on the images as high-energy single photons saturate an appreciable percentage of the pixels on the CCD. While these 'snow' features vary in size, shape, and intensity, they were, on average, smaller and more circular than the elongated electron beam

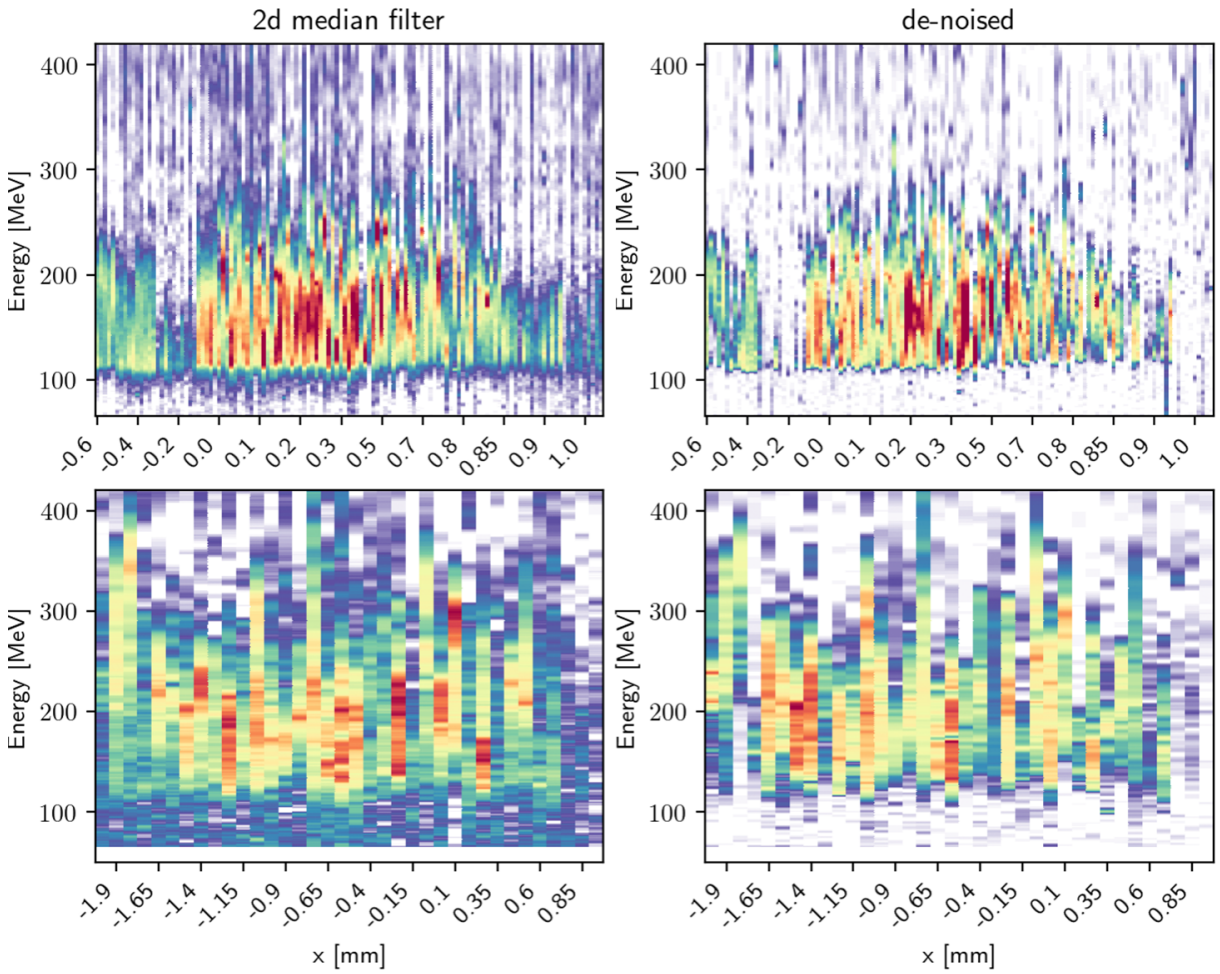


Figure 5.9: The resulting ESPEC waterfall plots for two target $x-$position scans for the case 1 geometry (top row) and for case 2 geometry (bottom row) when the raw ESPEC images are only median filtered (left column), and where they have been through de-noise image processing and Fourier filtering (right column). These are same ESPEC waterfall plots that are shown in (d) and (h) in Figure 5.8. Each column in these waterfall plots represents an ESPEC image integrated in the angular direction of the scintillator screen. The colorscale in each of the four axes is normalized to the maximum dN/dE within its respective axis.

distribution on the ESPEC screens. Thus, the idea to identify features with a minimum circularity below a maximum area in the pixel space of the images was employed to identify the boundaries around these radiation 'snow' features and interpolate the background values from the boundaries to the inside of each 'snow' hard hit. This effectively removes the majority of the snow noise from the images. When combined with the median and Fourier filtering, it greatly enhances the signal-to-noise ratio in the images and improves the accuracy of the algorithm finding the maximum

integrated pixel row to retrieve the transverse position of the electron beam on the LANEX screen. The influence of this image filtering process as compared to simple median filtering of the images on the ESPEC measurements can be seen in Figure 5.9.

5.4 Conclusions

This experiment successfully demonstrated angular streaking of a laser driver due to transverse plasma density gradients from a supersonic gas jet along the propagation length of a wakefield accelerator to measure the angular dependence of the critical energy of the resulting betatron beams. The critical energy of betatrons from a LWFA accelerator correlates with the growth of electron beam energy within the accelerator. This is a demonstration of a novel diagnostic technique to measure on-shot electron beam energy gain. On-shot measurements of electron beam dephasing and rephasing were observed, proving that energy gain limits can be measured on-shot allowing, as an example, to optimize the energy gain of the accelerator by dynamically changing the acceleration length. This streaking technique can be used for various applications as well, such as generation of a controlled curved plasma channel [116] for guiding pulses in LWFA [117], for coupling of staged LWFA facilities [118], or for guiding pulses and beams for compact synchrotron sources [119].

CHAPTER 6

Parametric Studies of Current Filamentation Growth in Laser Wakefield Accelerated Beams

6.1 Introduction

Understanding the physics of Weibel [120] or current filamentation [72, 121] instability in plasma is of great interest and importance in many contexts. For example, suppression of this instability is crucial for the stopping and depositing energy of the fast electrons in the fast ignition concept of inertial confinement fusion [122, 123]. This instability is also one of the leading mechanisms of shock formation in space, which can explain the observation of energetic particles and is a contributing explanation for measured astronomical gamma-ray bursts [124]; it has been thought to contribute to gamma-ray radiation generation mechanisms [125]; it can impact laser-ion acceleration mechanisms [126].

Weibel first identified a class of transverse electromagnetic instabilities arising in a plasma with velocity space anisotropy [120]. In the extreme case of counter-streaming electron flows, a Weibel-like instability can occur, with the beam breaking up into a series of current filaments [70, 72, 121, 127]. For the current filamentation instability the primary mechanism in linear theory for initially homogeneous beams is as follows. In equilibrium, there is no net-current owing to the counter-streaming beams and charge neutrality. Inhomogeneity in the plasmas' current density profiles leads to transverse magnetic modes, which feedback on the regions of higher current density in the beam, leading to an exponential increase in these current density filaments inside the beam.

A simple analysis of the linearized fluid equations for ultrarelativistic, collimated beams yields a growth rate [70, 72],

$$\Gamma = \omega_p \beta_b \sqrt{\frac{n_b}{\gamma n_p}} = \beta_b \sqrt{\frac{n_b e^2}{\gamma_0 m_e \epsilon_0}}, \tag{6.1}$$

where Γ is the exponential growth rate term, ω_p is the electron plasma frequency of the background plasma, $\beta_b = \frac{v_b}{c}$ is the normalized velocity of the relativistic beam, n_b is the plasma density of the beam species, γ is the Lorentz factor for the relativistic beam $\gamma = (1 - \beta_b)^{-1/2}$, and n_p is the density of the background plasma electrons. This arises from highly simplified linear theory, and it is important to understand the behavior of filamentation in the presence of other instability modes [128, 129], short beams [130], nonlinear behavior and inhomogeneity [70, 121, 131], or quantum effects [132], to mention a few examples.

There have been recent experiments to probe the current filamentation instability with relativistic electron beams using a traditional accelerator facility [33]. In these experiments, similar to this Chapter's work, the electron beam is unneutralized and propagates into plasma, so the physics of the filamentation is different from the idealized current and charge-neutral case considered in previous theoretical studies. A single-mode analysis can be shown to yield approximately the same growth rate for a single beam propagating in plasma as colliding beams provided the return current and screening effects of the plasma mitigate the bare charge and current of the beam (see Appendix A).

There has been a previous study to use electron beams generated via LWFA to study the current filamentation instability for a single beam [28]. A limitation of this previous experiment was that the acceleration and filamentation processes took place in the same gas target, making it difficult to separate laser-plasma interaction and filamentation instability effects. Further, the data repetition rate was low, which limited the parameter space that could be investigated. In the studies here, by using a higher repetition rate system and separating out the acceleration and filamentation processes with two gas targets, we can study a wider parameter space, including different gas species and a continuous scan in plasma density and length. We can provide a controlled experiment by alternating between gas on and off shots.

This chapter is detailed in an in-progress manuscript, *Parametric Studies of Current Filamentation Growth in Laser Wakefield Accelerated Beams* by Jason Cardarelli, Yong Ma, Paul Campbell, Brandon Russell, et al. In-person experimental support was provided by Paul Campbell, Yong Ma, Rebecca Fitzgarrald, myself, and the research staff and faculty at Jorge Rocca's ALEPH laboratory including Shoujun Wang, Huanyu Song, John Morrison, Ryan Nedbailo, and Reed Hollinger. Remote support and contribution toward project conceptualization was provided by Stuart Mangles, Gianluca Sarri, Brenden Kettle, Matthew Streeter, Daniel Seipt, and Meriame Berboucha. Brandon Russell, Paul Campbell, Yong Ma, and Alec Thomas helped set up and run supporting numerical simulations. Sophie Carlson assisted in testing image thresholding algorithms. I conducted the bulk of the data analysis with support from Yong Ma. Acknowledgment to NSF (Grant # 1804463) and the DOE Fusion Energy Sciences Lasernet US (Grant # DE-SC0021246).

6.2 Methods

An experimental campaign at the Advanced Laser for Extreme Photonics at the Colorado State University took place to probe the behavior of the current filamentation instability in electron beams produced via LWFA. Figure 6.1 shows a diagram of the experimental setup. A laser pulse with FWHM duration 30 fs and a central wavelength of 800 nm was focused using an f/25 focusing optic to a FWHM spot size of 40μ m (yielding a laser strength parameter $a_0 = 2.16$) to drive wakefield acceleration of relativistic electron beams in the accelerator gas cell. The gas target for the wakefield acceleration was a 3D-printed 2 – 22 mm variable length gas cell which produced electron beams of mean charge $3.2 \times 10^{-10} \pm 1.0 \times 10^{-11}$ C with a standard deviation of 1.7×10^{-10} C with centroid energies in the range 200 – 600 MeV via self-injection. These statistics were taken for shots with only the accelerator gas cell plasma present, accounting for 283 shots over 3 data runs. The electron beam and residual laser pulse were allowed to exit the rear of the acceleration cell and traverse a distance in the range of 1.7 – 2 cm to the entrance face of a second 3D-printed variable-height gas cell, where the interaction between the electron beam

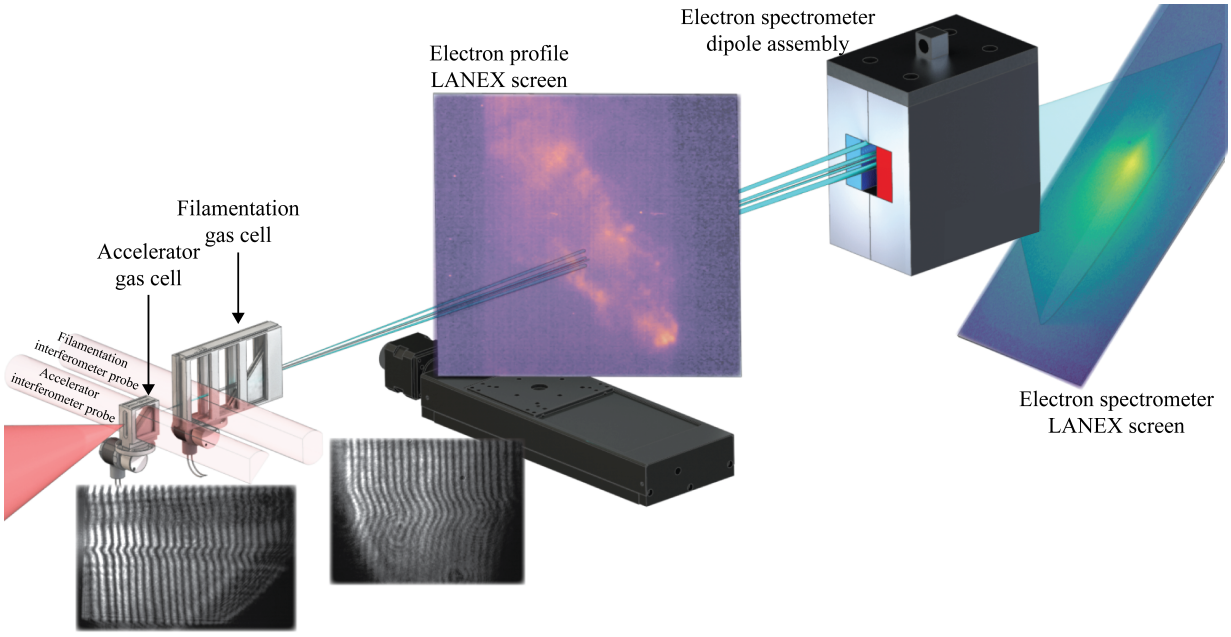


Figure 6.1: Experimental setup. The main laser first focuses into the accelerator gas cell which has an interferometer probing its plasma. The beams propagate a distance of 1.7 cm to the next filamentation gas cell, which spans a length range of 0.2 cm to 15 cm and is also probed for an interferometer measurement. This second gas cell was controlled independently from the first, allowing measurement of the electron beams with and without filamentation gas within a data run. The electron beams then traveled to the 45-degree oriented electron profile (EProfile) LANEX scintillating screen, which has an image captured by a CCD oriented 45 degrees with respect to the screen's normal vector. Finally, the electron beam exits the back of the chamber through a 1" Ultem window (not shown) and travels into a 0.97 T dipole system to disperse the electrons onto a LANEX scintillator to measure the energy of the produced beams.

and the background plasma ionized by the post-acceleration, diverging laser pulse occurred. This second cell was one of three unique cells consisting of different length ranges: a 'short' length filamentation cell ranging from 0.2 cm – 5 cm, a 'medium' length filamentation cell ranging from 5 cm – 10 cm, and a 'long' length filamentation cell ranging from 10 cm – 15 cm. The total parametrically scanned filamentation plasma interaction length was covered by the three cells due to spatial constraints of the experimental chamber. By separating the two gas cells, the filamentation plasma was isolated from the wakefield accelerator plasma and the two gas targets' lengths and densities could be controlled independently.

The plasma density in the gas cells was measured via interferometry using a probe pulse picked off from the driving pulse. The electron beams propagated a distance of 1.08 m from the LWFA

source to a scintillating LANEX screen, referred to as the 'EProfile' screen in this work, in the beam path oriented 45 degrees from orthogonal to the laser propagation direction through the chamber in the horizontal plane. The light was collected with a camera oriented on the opposite side of the screen also with a 45-degree perspective offsetting horizontal-skew in the image of the beam on the screen due to perspective skew. Qualitative examples of this diagnostic over a range of filamentation cell lengths and gas backing pressures may be found in Figure 6.2, with many more examples provided in Appendix B where qualitative trends of the filamentation structure at different lengths and pressures can be observed.

The electron beam then propagated out of the chamber through a 1" diameter 635 ± 50 μm thick Ultem window to an electron spectrometer consisting of a series of three connected dipoles of central field strength 0.92 T with a magnetic gap of dimensions 4" long by 1.5" tall and a gap width of 0.75". A scintillating LANEX screen was oriented at the back of the magnet with an angle of 38.7 degrees with respect to the exit plane of the dipoles to collect the electrons dispersed by the dipoles. For all runs with hydrogen gas in the filamentation stage, the total distance from the LWFA source to the entrance plane of the spectrometer system was 1.83 m. Qualitative angularly-integrated examples of this diagnostic displaying sequences of shots turning on and off the gas supply to the filamentation gas cell may be found in Figure 6.3. As opposed to a typical electron spectrometer setup in a LWFA experiment, a slit to discriminate the angle of propagation from the source to the spectrometer was not included due to the coupled facts that pointing fluctuation of the electron beams in the system was appreciable and that there was a relatively large longitudinal distance between the source and the dipoles. This led to the amount of charge consistently going through the spectrometer system to be of a signal level difficult for our imaging system to distinguish from the background signal if a slit was in place. To compensate for this fact, when analyzing spectrometer data a weighted centroid of charge on the EProfile screen within the angular window that allows charge to enter the dipole entrance gap was used to retrieve a centroid pointing angle of charge entering the spectrometer.

This pointing angle was then used to create shot-to-shot spectrometer energy dispersion rela-

tions, taking into account the pointing of the particles to the spectrometer by using a relativistic Boris particle pusher [81] to model an energy spectrum of particles traversing through an analytic 3D dipole magnetic field produced in the gap of two rectangular parallelepiped magnetic dipoles [82] with the same transverse and longitudinal dimensions and central magnetic field strength as the ones used in the experiment. Not including a pointing discrimination slit or aperture did produce a measurement error in our ESPEC proportional to the divergence spread of the particles entering the spectrometer. The geometry of the dipole system also introduced measurement error of the beam energy. Given the length of the square-yoke dipole system, there is a pointing angle dependent on shot characteristic cutoff energy where the particles are swept into the yoke of the magnet and are heavily attenuated before reaching the ESPEC scintillator. This causes a lower resolvable energy limit that can be measured by the ESPEC system. Since the pointing angle is given by the weighted centroid of the charge on the EProfile screen, if this centroid feature on the EProfile screen is not more energetic than the cutoff energy, then those particles will not be measured by the ESPEC diagnostic, leading to an artificially high energy measurement for those shots. Charge in the electron beams was calibrated by overlapping an MS image plate with the ESPEC LANEX screen and correlating the charge within the ESPEC angular aperture on the EProfile screen and the PSL value retrieved from the image plate measurements.

6.3 Results and discussion

The data was analyzed to measure the characteristics of the electron beams after interacting with the filamentation plasma. On the EProfile screen, the longitudinally-integrated transverse charge distribution of the beam was measured. From this distribution, post-filamentation beam qualities are retrieved, including the area of the beam signal on the EProfile screen, the number of filament features within the beam, and the ratio of the signal located within filaments vs the entire beam. A definition of what qualifies as a filament and what qualifies as a beam signal on the screen may be made for quantitative measurements of these EProfile images. Before the images are analyzed, the

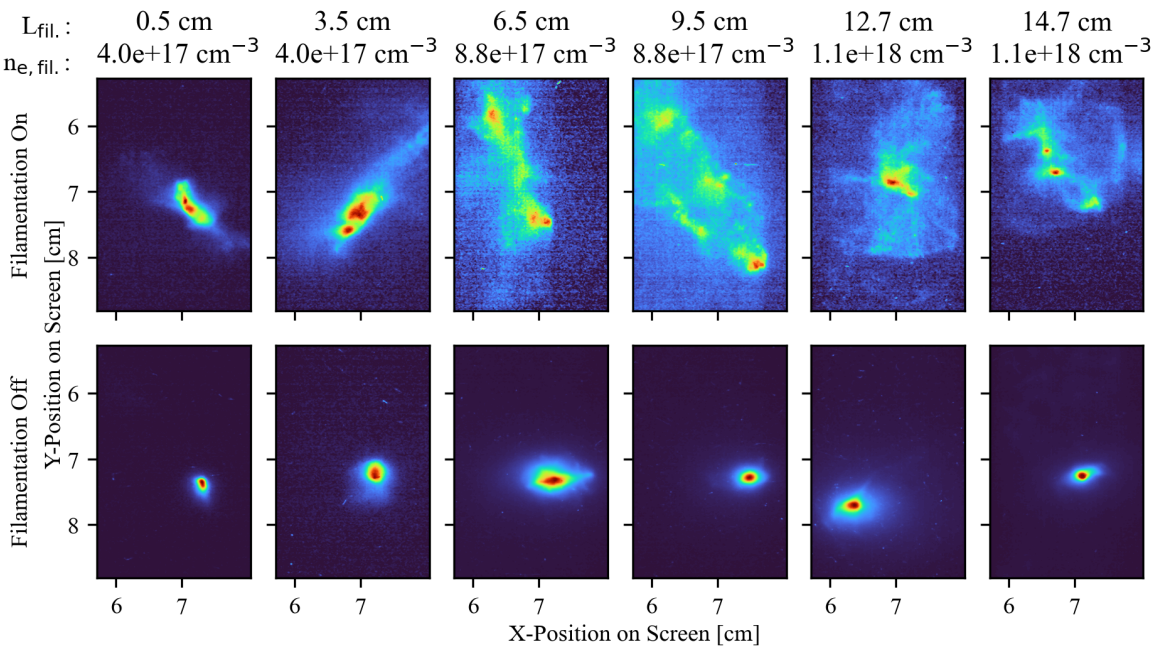


Figure 6.2: Representative filamentation hydrogen gas on (top row) / off (bottom row) pairs of shots for different lengths and filamentation gas cell plasma density as labeled above every column of images.

background signal is subtracted using a reference image, and a median filter of kernel size 3×3 is applied to reduce the influence of hot pixels. The dynamic range of the signal collected from the EProfile diagnostic was reduced to unsigned-integer base 2^5, leading to pixel intensity values ranging from 0 to 31. The coarsening of the dynamic range smooths the local fluctuation of pixel values and yields contours for regions of similar pixel intensities. The images were cropped to an identical region for all shots, which subtends the angular width of particles allowed to exit the rear of the longest gas cell. Three filamentation parameters were measured on the EProfile screen: the total beam area, the filament-to-global charge ratio, and the number of inner filaments in the transverse profile of the beam.

A beam area of the charge signal on the EProfile screen was defined as the area subtended in these images of all pixels with at least a pixel value of 3 ($\sim$ 10% of the image's maximum). Given the relatively large distance between the filamentation target and the EProfile screen and the nature of the CFI fields to increase the transverse momentum spread of the electron beam,

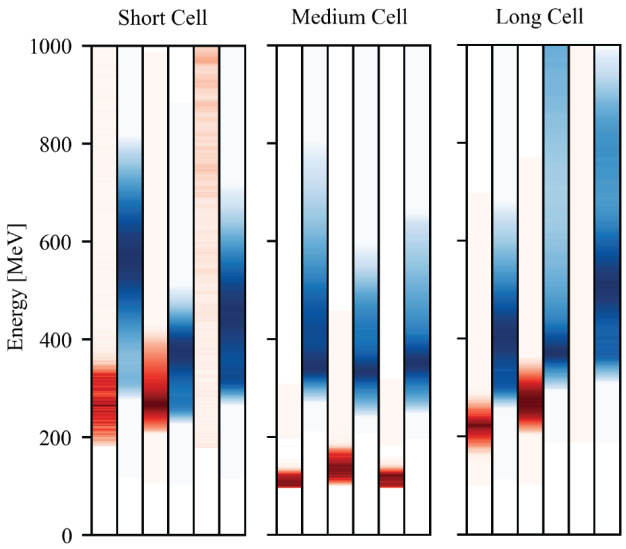


Figure 6.3: Qualitative example of sequential filamentation hydrogen gas on (red) vs. off (blue) shots for the 3 filamentation gas cells used. The color scale for each of the three cell groups is normalized to the maximum integrated dN/dE for the examples in each cell.

one should expect to see an increase in beam area as filamentation increases. Filaments in the beam profiles are then defined as follows: any inner-most contour with at least a pixel intensity value of 6 (approximately 20% of the maximum signal level in the image), which encloses a local maximum and has at least a minimum area equivalent to a circle with a radius of 5 pixels. The global beam signal is simply an integration of the pixel values on a background-subtracted EProfile image. The local signal around the beam filaments was found by taking half the local maximum value at each filament and integrating the pixel values within the surrounding contour values at that half-maximum level. For an ideal transverse Gaussian profile, this corresponds to the FWHM of the distribution. The charge ratio may be used by creating a mask for the image using all of the contours within the image that define filaments and summing the pixel intensity in the $Image \times Filament\ Mask$ product; the global charge is done similarly by using the mask produced from the global charge contour. As the filamentation instability causes strong fields to form around current density peaks in the beam profile that cause the filamentation to grow, this also pushes charge in the area surrounding the beam filaments away from the filament region into the global distribution around the beam. This can be seen as a halo-like feature or large-wavelength structure

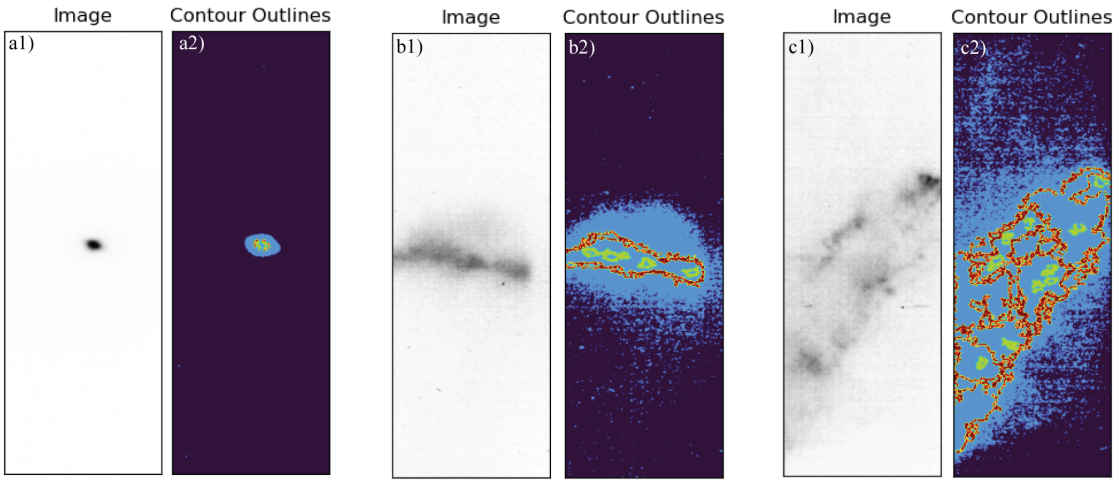


Figure 6.4: Examples of 1) raw EProfile images and 2) the inferred filamentation parameters of beam area (light blue), filament FWHM charge area (red), and individual filaments (light green) from the image processing algorithm on a) a nonfilamented reference shot with one filament, b) a moderately filamented shot with four filaments, and c) a highly filamented shot with ten filaments.

around filamented beam profiles, as seen in Figure 6.2. One final signature of CFI measured in this campaign was the relative energy loss between shots with the filamentation gas cell turned on versus it being turned off, as there is expected to be a transfer of energy from the relativistic electron beams to the energy in the strong fields around the beam filaments. In addition to the previously mentioned disclaimers, it should be noted that due to an observed lower average pointing angle of the beams in the angular window to enter the electron spectrometer system with the filamentation gas cell turned on, these shots have, on average, an error biasing higher measured centroid energy in the beams compared to the shots without the filamentation cell turned on. Thus, if energy loss is observed at all, it is of a great enough magnitude to overcome these measurement limitations.

The results of these measurements with the parameter space of the length and plasma density are visually separated in Figure 6.5 and combined as the length normalized to the skin depth of the filamentation cell in Figure 6.6. All of the filamentation shots are binned together to allow statistics of several shots in a similar area of the parameter space to give a better measurement of the instability growth in that region of the parameter space. In Figure 6.6, a red line and shaded region are added to the plots to represent the linear fits of the raw data. This is not included to suggest that the data behaves linearly but rather is included to show the average trend of the data over the

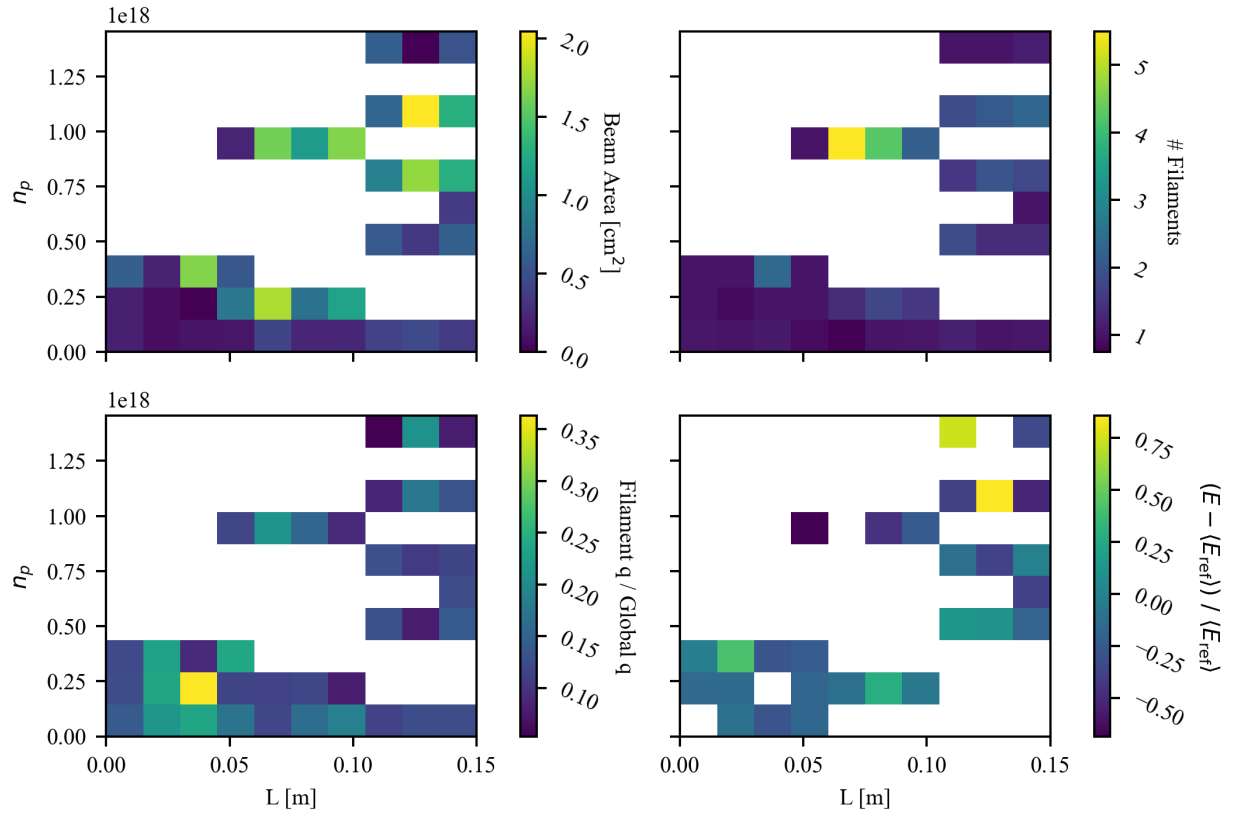


Figure 6.5: Weighted 10 × 10 histogram spanning the length (x-axis) and filamentation plasma density (n_p) parameter space that was scanned in the experiment. Blank spaces in this parameter space represent regions where data was not taken or there were not enough valid shots to provide reliable statistics.

$L\omega_p/c$ space that the plasma density and length scan cover — whether these values are overall increasing or decreasing over this parameter space. The general trends shown by these linear fits begin to show an expected trend suggesting growth of the filamentation instability: increasing beam area, increasing number of filaments, decreasing filament over global charge ratio, and decreasing relative energy between filamentation on shots compared to local filamentation off reference shots.

Equation 6.1 suggests that the theoretical growth rate of the instability only depends on the variables of a beam's density and energy. On-shot beam charge can be retrieved from charge calibrations in the EProfile system and energy measurements are given by the electron spectrometer. To retrieve an estimate for the on-shot beam density in the filamentation gas cell, a few assumptions can be made regarding the volume of the beam in the filamentation plasma. The beam can

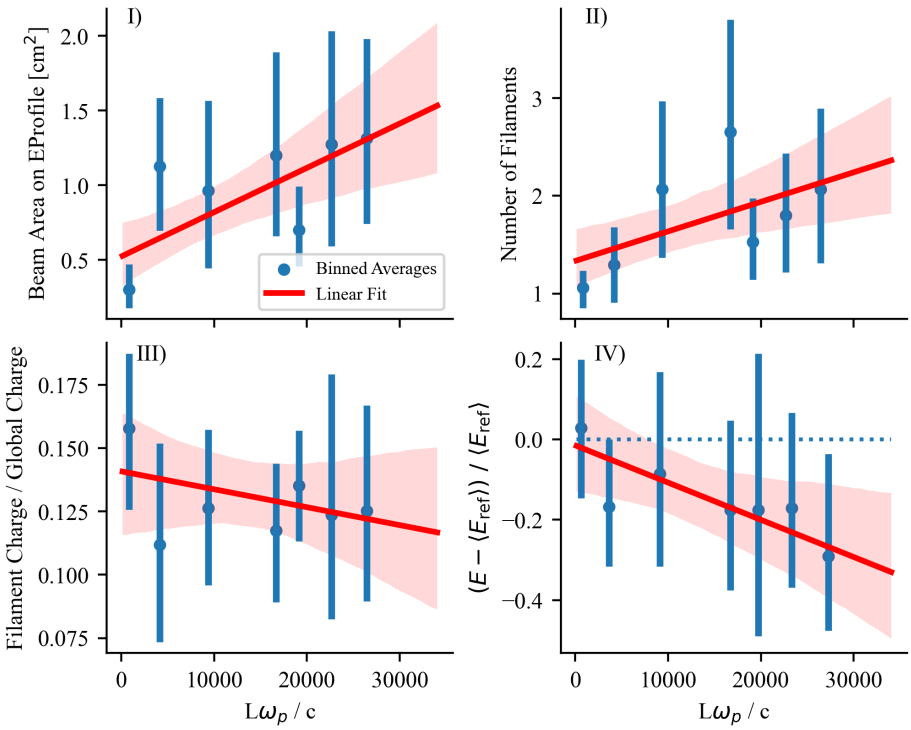


Figure 6.6: Evolution of the I) total area of the beam on the EProfile screen, II) number of inner-contour filaments that exceed a minimum area threshold, III) the integrated pixel values in the global region (50% of the max contour value or larger) to integrated inner-contour filament pixel values, and IV) The ratio of average energy of the nearest 6 reference shots to the energy of a given data shot, assuming a threshold signal-to-noise ratio on the ESPEC screen. The x-axis is the length of the filamentation gas target interaction times the measured filamentation background plasma frequency divided by the speed of light (number of plasma wavelengths). Each data point is an equally weighted bin of averaged data with the standard deviation of that data shown around the average as error bars. Linear fits are shown to highlight the behavior of these measurements as a function over the scanned parameter space for length and plasma density.

be assumed to be roughly a cylindrical distribution of charge with a radius at the entrance of the filamentation gas cell given by the distance between the two gas cells L_0 and the divergence angle of the beam θ_{div}: $r_{b,0} \approx L_0 \tan\theta_{div}$. The longitudinal duration of the beam, ξ_b, can be assumed to span about 10 μm; as a measurement of the beam duration could not be made with the diagnostics in this experiment and this assumed length is around a quarter-to-half of the plasma wavelength for the regime of plasma density from this experiment. The quarter-to-half of the accelerator plasma wavelength duration estimate comes from this being within the length of the favorably accelerating and focusing region of a laser-driven wakefield in the nonlinear bubble regime [23]. This method

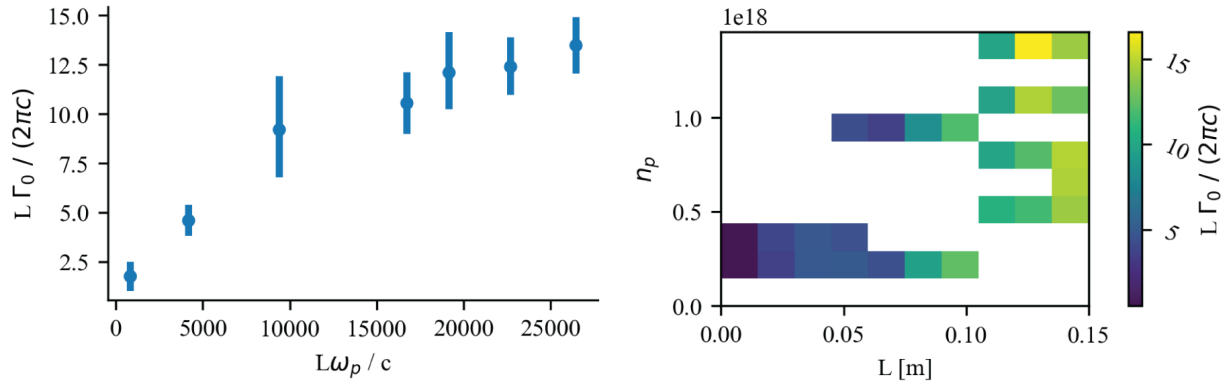


Figure 6.7: The estimated growth rate multiplied by the elapsed filamentation time of the CFI instability with hydrogen gas in the filamentation gas cell given the average of a filamentation shot's nearest 6 reference shots' energies (yielding γ and β), as well as their inferred average beam density from the measurement of charge and divergence. Instability growth is plotted both in the style of Figure 6.6 (left) and Figure 6.5 (right).

reliably calculates the initial expected growth rate of the instability as the beam travels with an initial divergence angle, and its charge density dynamically increases as the filamentation grows. The initial growth rate multiplied by the time the beam travels through the plasma should be a first-order estimate for the amount of filamentation the beam undergoes.

The effect of the beam traveling through the filamentation cell plasma can affect the beam's measured divergence, energy, and total charge; thus, only local shots with filamentation gas turned off can be used to give an estimate of the CFI growth rate for filamented shots. This all gives an expression for the measured initial CFI growth rate based on reference shots around a given filamentation data shot:

$$\Gamma_0 = \beta_b \sqrt{\frac{n_b e^2}{\gamma_0 m_e \epsilon_0}} = \beta_b \sqrt{\frac{\left[\left(\frac{q_b}{e}\right)/(\pi(L_0 \tan\theta_{div})^2 \xi_b)\right] e^2}{\gamma_0 m_e \epsilon_0}}. \tag{6.2}$$

We can multiply this by the filamentation length over the speed of light to give the estimated e-foldings of the instability based on the initial growth rate for different regions of our scanned parameter space. The results of this calculation can be found in Figure 6.7. These estimates can be used to qualitatively compare the results from Figure 6.5 and Figure 6.6, and any deviation

from the trends in these plots to the trends in Figure 6.7 could be explained by a deviation of the filamentation behavior from the 1D growth rate model.

A trend of the expected initial filamentation rates suggests an increase in filamentation instability with increasing $L\omega_p/c$ and with increasing filamentation length and background plasma density. It should be noted that the 2D histogram plots are more susceptible to local statistical fluctuations compared to the $L\omega_p/c$ scatter plots due to the smaller density of contributing binned at each point in its parameter space. If the trends in the magnitude of the growth rate observed in the 1D $L\omega_p/c$ plots and the 2D histograms for the hydrogen filamentation parameters in Figure 6.5, this could support the growth rate theory's postulate that the instability does not depend on the background plasma density. For the longest length gas cell's points in Figure 6.5, for example, Figure 6.7 suggests a noticeable decrease in filamentation across the jump from plasma density of $n_p \approx 0.8 \times 10^{18}$ cm^{-3} to $n_p \approx 1.15 \times 10^{18}$ cm^{-3}. Interestingly, in our measurements for beam area, number of filaments, and the ratio of local to global charge for the filaments, there is hardly any difference in the average values measured between those two data regions. One could point to this as evidence that the increase in plasma density increased the degree of filamentation instability compared to the decrease expected solely from the measurement of the input beam charge and energy parameters. An alternative explanation for this could be that within this large-length parameter space, the interaction between the beams and the filamentation plasma may be within the saturation limit of the current filamentation instability, where filamentation parameters are more or less constant, with the beams potentially susceptible to highly nonlinear behavior.

To gain insight into the growth of the instability, simplified 3D simulations were performed using the PIC code OSIRIS [98]. These simulations were set up to represent a beam with a short-duration top-hat longitudinal profile, similar to that expected for an LWFA electron beam, as it propagates through the plasma in the second gas cell. To do this, a box with dimensions 5.7 μm $\times$ 714 μm $\times$ 714 μm and resolutions $\Delta x = 0.7$ μm and $\Delta y = \Delta z = 1.08$ μm were used. The transverse resolution provides 5 cells per skin-depth (c/ω_p) in the background plasma at the peak density that we simulate, 1×10^{18} cm^{-3}. A moving window was used, therefore the beam prop-

agated through the background plasma as would be the case in the experiment. The background plasma, representing the ionized gas in the second gas cell, was initialized as electrons with a stationary neutralizing background. This was done because we did not expect the ions to move significantly over the length of the electron beam. Open boundary conditions were used for particles and fields. The background plasma was, therefore, tapered linearly toward the boundaries, and a vacuum gap was included to reduce boundary effects. This background was initialized at rest with a temperature of ∼51 eV. The electron beam was initialized as a population of electrons with a Gaussian transverse spatial profile and a top-hat profile in the longitudinal (x-direction). This beam propagated in the positive x-direction with an energy ∼360 MeV. A longitudinal thermal velocity gave an energy spread $\Delta E/E = 20\%$. The beam's divergence was set by initializing a spatially varying transverse velocity that varied linearly with y and z. This is what would be expected for a point source. A full-angle divergence of 5 mrad was used. Additionally, a transverse temperature of ~ 1.3 keV was used. The background and beam were initialized with 8 and 27 particles per cell respectively. The beam was initialized with electric and magnetic fields calculated using the potential form of Maxwell's equations in cylindrical coordinates using the Lorenz gauge and assuming negligible transverse velocities and ultrarelativistic beam energy such that the wave equation reduces to a two-dimensional Poisson equation. For a Gaussian beam of the form,

$$n_e(y,z) = n_0 \exp\left(-\frac{(y-y_0)^2 + (z-z_0)^2}{2\sigma^2}\right), \tag{6.3}$$

the fields may be derived,

$$E_y = \frac{e}{\epsilon_0}\frac{-n_0\sigma^2}{(y-y_0)^2+(z-z_0)^2}\left[1-\exp\left(-\frac{(y-y_0)^2+(z-z_0)^2}{2\sigma^2}\right)\right](y-y_0)u(l-|x|), \tag{6.4}$$

$$E_z = \frac{e}{\epsilon_0}\frac{-n_0\sigma^2}{(y-y_0)^2+(z-z_0)^2}\left[1-\exp\left(-\frac{(y-y_0)^2+(z-z_0)^2}{2\sigma^2}\right)\right](z-z_0)u(l-|x|), \tag{6.5}$$

$$B_y = -E_z/v_x, \tag{6.6}$$

$$B_z = E_y/v_x. \tag{6.7}$$

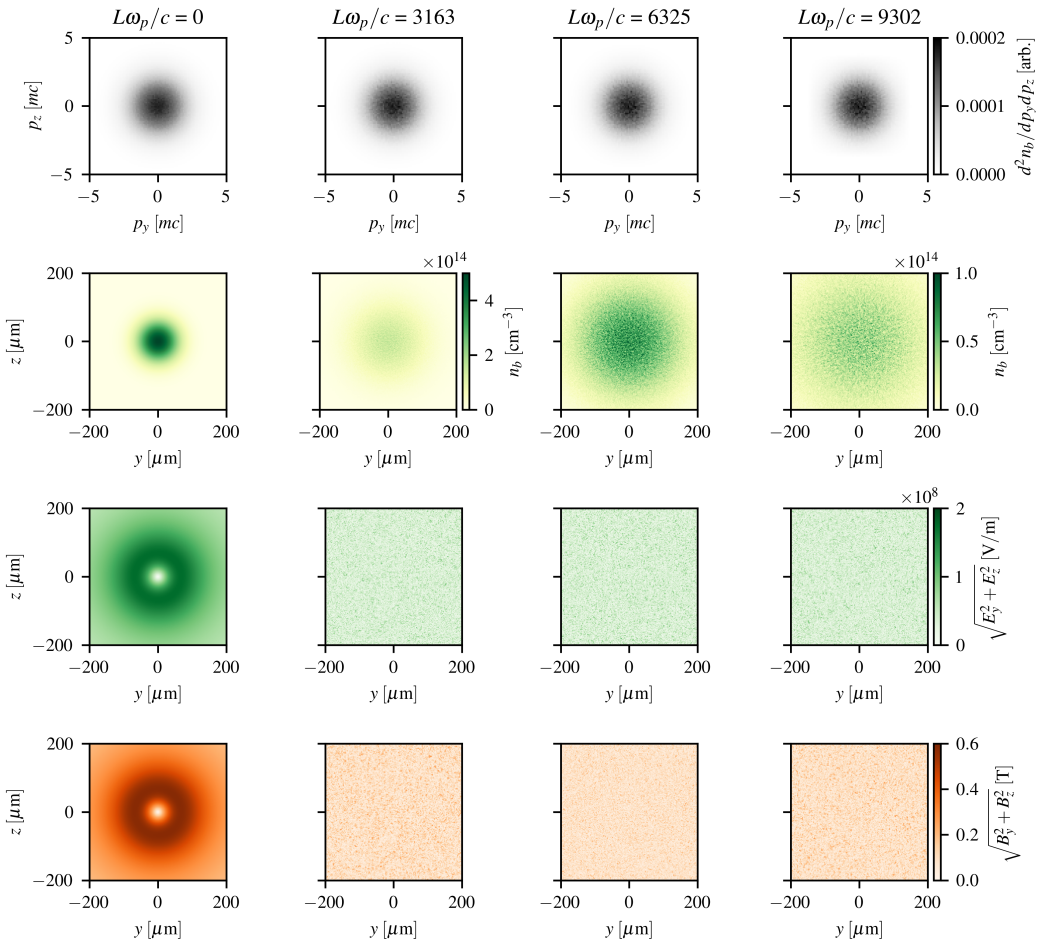


Figure 6.8: 3D OSIRIS simulation of an $\sim$ 360 MeV electron beam propagating through a background plasma with a density of 10^{18} cm^{-3}. Row 1 shows the $p_y - p_z$ phase-space while rows 2-4 show slices taken near the middle of the beam at $x = 0.4$ μm of the beam density and magnitude of the in-plane electric and magnetic fields.

Here, $u(x)$ represents the unit step and acts to truncate the fields to the extent of the beam, which has a length of $2l$. Due to the relatively small transverse velocities and highly relativistic longitudinal velocities, these fields were found to be accurate.

Fig. 6.8 demonstrates the evolution of a beam in a slice taken at $x = 0.4$ μm. At $t = 0$, the beam is initialized in a background that is 2000 times denser than the beam with the fields given by the equations written previously. Due to the dense background's small Debye length, the beam's electric fields are rapidly shielded. Additionally, because the background is very dense relative to the beam, although the beam is highly relativistic, a return current is formed within the background

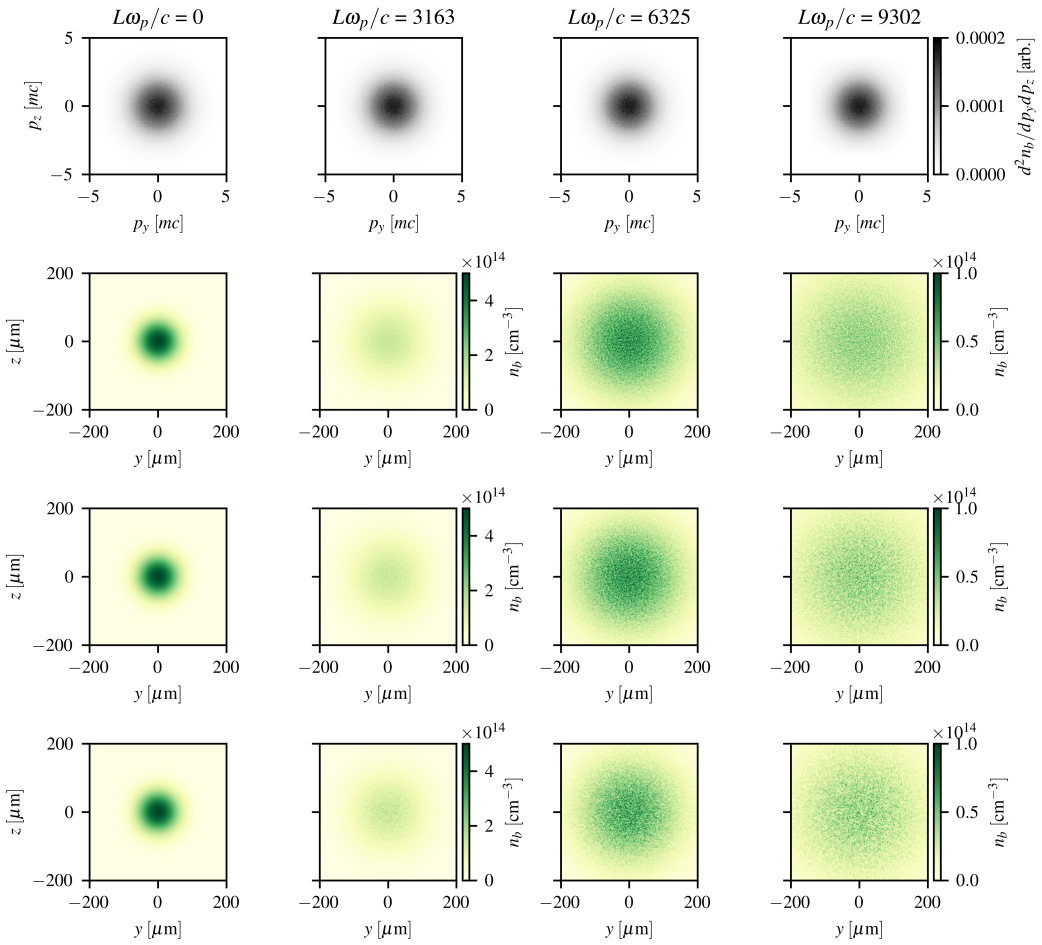


Figure 6.9: 3D OSIRIS simulations of an ~ 360 MeV electron beam propagating through vacuum (row 1 and 2), through a background plasma with a density of 10^{18} cm^{-3} (row 3) and with an energy ~ 100 MeV propagating through the same background (row 4).

that is sufficient to shield the magnetic field. This overall shielding results in the beam's ability to propagate with its initial divergence angle. As the beam continues to propagate through the plasma we observe the formation of high-frequency filaments in the transverse density profile of the beam. These filaments also appear in the $p_y - p_z$ phase-space; however, the shape of the phase-space is approximately constant.

Similar simulations were performed at lower background densities and showed slightly different dynamics. At a background density twice that of the beam both the electric and magnetic field of the beam were not shielded. While this is different from the high density case, the result is the same, the beam is allowed to propagate maintaining its initial divergence. However, with a low

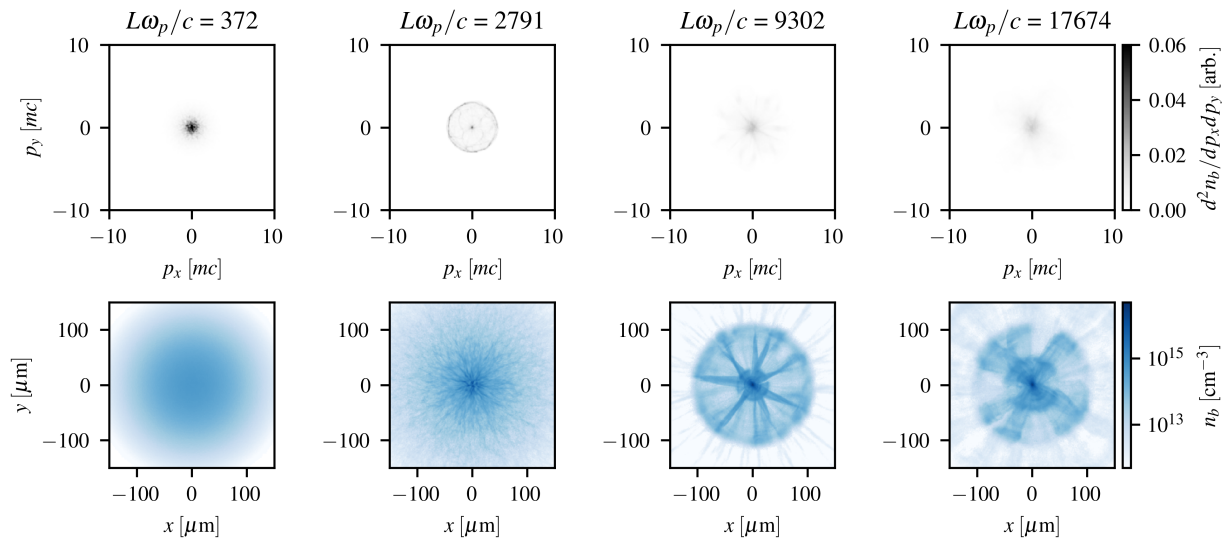


Figure 6.10: 2D OSIRIS simulation of an ~ 360 MeV electron beam propagating through a background plasma with a density of 10^{18} cm^{-3}. The beam is seen to rapidly focus due to the partial shielding of the electric field.

density background we also do no observe the formation of filaments.

In Figure 6.9 row 1 and 2 the propagation of the beam through vacuum is shown which demonstrates that the density profile is noisy even without a background plasma to generate filaments however the phase-space is smooth. In row 3 the propagation through the 2000 times more dense background is shown where radial filaments form in the density profile. The growth of these filaments is increased with a reduced beam energy as is shown in row 4 where a ~ 100 MeV beam with a 20% energy spread was propagated through the same background density. The type of filaments we observe in these simulations is qualitatively different from what was observed in the experiment (Figure 6.2). However, these simulations are only preliminary. The more pronounced filaments may appear with different background plasma temperatures where the electric field may be more strongly suppressed compared to the magnetic field. Additionally, in the experiment after propagating 1.83 m to the detector, structure in the phase-space should dominate the image observed on the detector screen. Comparing Figure 6.8 row 1 to Figure 6.9, we do see significant structure that does not appear in the phase-space of the beam propagating through vacuum. Further simulations are necessary to obtain a better agreement with the experimental data.

Note that these results are very different from what would be observed if a simulation was run in 2D. For example, Fig. 6.10 shows a 2D simulation representing a slice of a beam propagating through a 2000 times more dense background. In this case the background tries to shield the fields, but overcompensates, resulting in oscillating longitudinal electric fields. This does not happen in 3D because the beam continuously propagates into unperturbed plasma. The partial shielding of the fields allows the beam to focus rapidly. The 3D effects are therefore important and necessitate the use of the more computationally intensive 3D simulations.

6.4 Helium, nitrogen, and argon filamentation gas species

In addition to scanning length and plasma density in the filamentation gas cell, filamentation gas species were also scanned to probe the effect on the ion species in the filamentation plasma. The results for hydrogen were shown in the prior discussion of this chapter. Included here are results from replacing hydrogen with helium, nitrogen, or argon. Although these scans were completed similarly to that of Hydrogen, the results are presented with the caveat that there is a question as to whether the gas maintained a uniform ionization state (and therefore uniform plasma density) the entire probed length in the experiment. An estimate of the gas ionization level as a function of longitudinal propagation in the filamentation gas cell assuming laser energy and f-number used in the experiment can be found in Figure 6.11. As is shown clearly in this Figure, a fully ionized plasma is maintained through the duration of the plasma in the filamentation cell. The helium gas undergoes a transition from fully ionized to single-level ionization after about 2 cm of filamentation gas length within a 10 mrad region about the laser axis. Likewise, it is estimated that nitrogen and argon have two ionization level transitions in the longitudinal duration of the filamentation cell. The effect of these density transitions between distinct plasma densities on the growth of the instability is not well-defined, so the following results are presented separately from the results of the measurements using hydrogen gas in the filamentation cell from this experiment. As the filamentation cell's interferometer probe had a width of 1.8 cm and was centered approximately

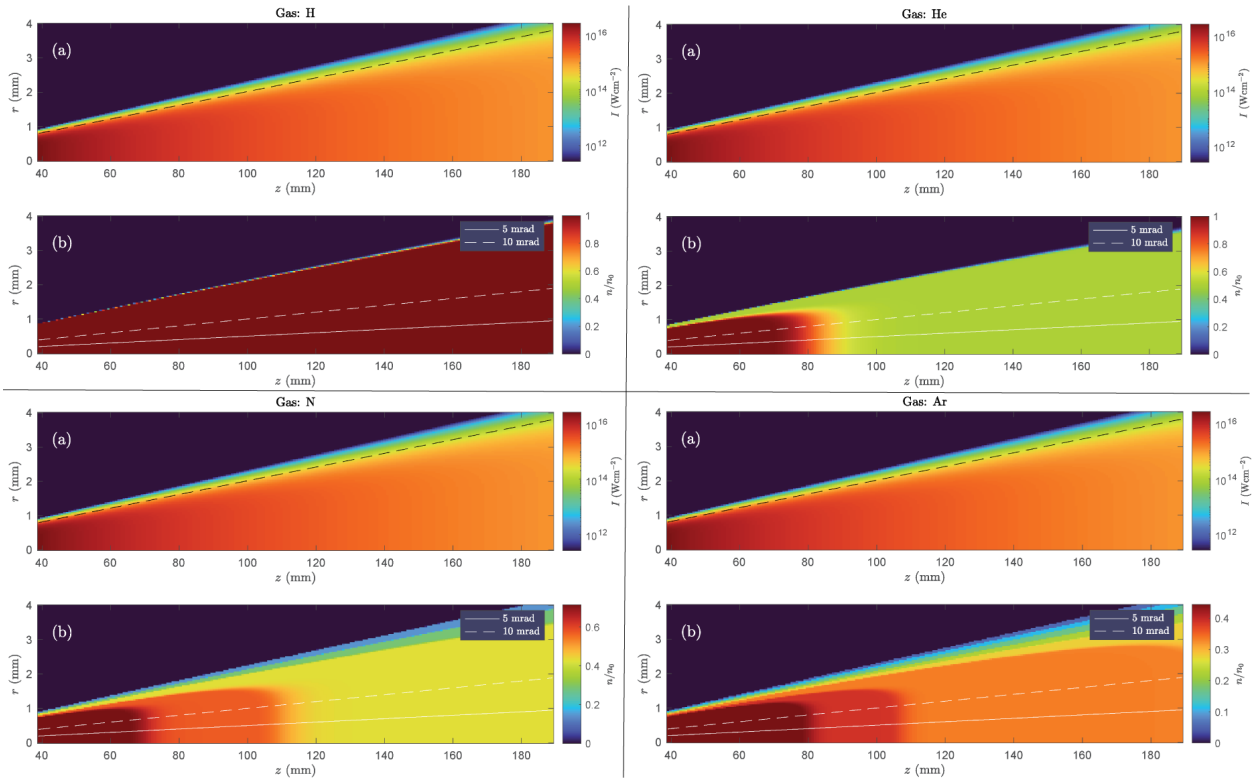


Figure 6.11: The laser intensity (a) and the relative ionization level (b) from the laser power along the radial and longitudinal range of the filamentation gas cell. Longitudinal positions are relative to the front of the acceleration gas cell for hydrogen (top-left), helium (top-right), nitrogen (bottom-left), and argon (bottom-right).

1 cm in front of the entrance of the filamentation cell, the filamentation probe was not in an ideal location to capture the density shift predicted by the model used to produce Figure 6.11. This ionization level transition should be kept in mind in interpreting results.

Figures 6.12, 6.13, and 6.14 show the measured results for filamentation in the form of 10x10 2D histograms (axes in the same orientation as in Figure 6.5), 1D binned data over the scanned $L\omega_p/c$ space (axes in the same orientation as in Figure 6.6), and the estimated filamentation growth magnitude based on initial conditions of the beams for filamentation gas species of helium, nitrogen, and argon respectively. These figures will be discussed in turn, and trends from these plots will be compared to the results from measurements taken with hydrogen as the filamentation gas species. The density vs length parameter space covers a fairly different distribution for these gases when compared to hydrogen due to different backing pressures and gas cell-fill fluid dynamics.

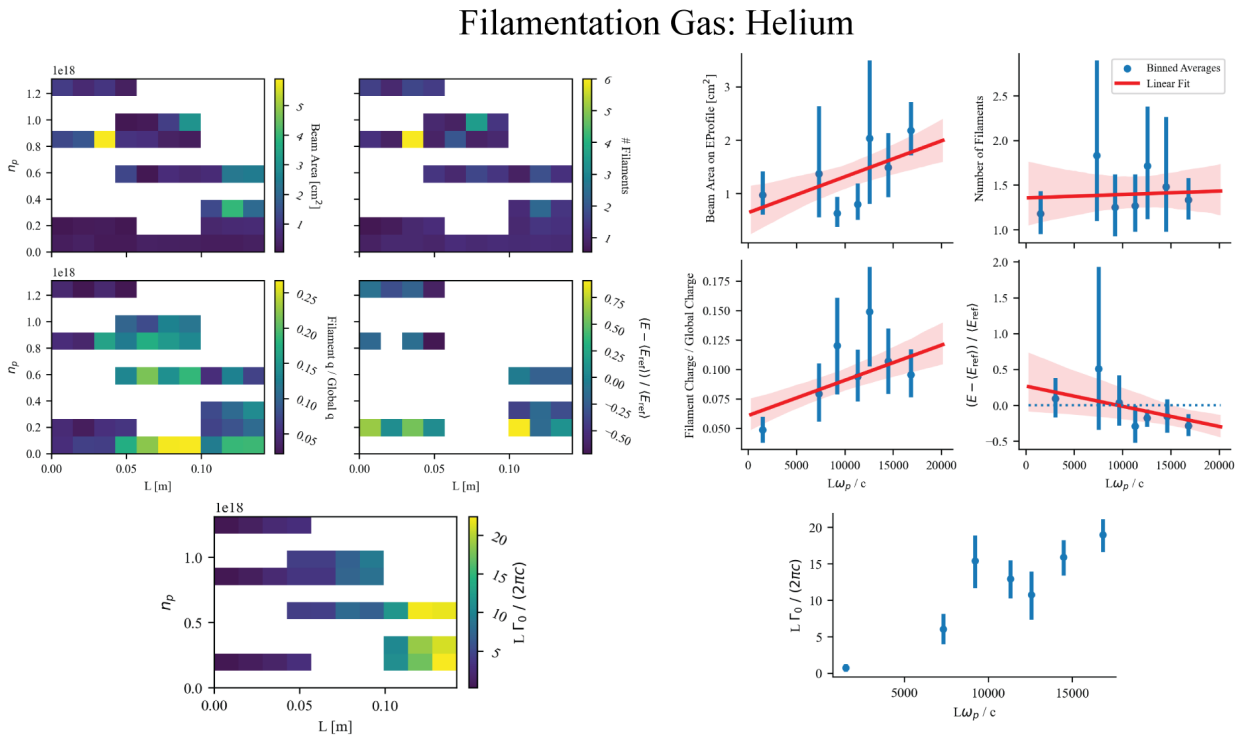


Figure 6.12: 2D histogram (top left) and 1D binned evolution of the measured growth parameters (top right) for helium filamentation gas with axes identical to that of Figure 6.5 and Figure 6.6. Measured estimates of the initial CFI growth rate in these two visualization styles are oriented directly beneath the 2D histogram and 1D binned fit plots.

The results using helium as a filamentation gas species are shown in Figure 6.12. When looking at the 1D binned data on the right-hand side of the plots, one notices a few different and more uneven trends than those measured in hydrogen. While there is an increase in beam area and a weak increase in the average number of filaments that does agree with hydrogen's behavior, there is also, however, an increase in the filament charge over the global charge ratio. The measured filamentation based on the initial growth rate in the cell, as seen in the bottom row on the right-hand side of the figure, first increases and then dips down before increasing again, which is a general trend that differs from the trends seen in the hydrogen dataset. This is due in large part to the short cell, consisting of shorter lengths, having the widest ranges of plasma densities, and notably having the lowest lengths as well as the highest densities. The distribution of growth of the filamentation is better visualized in the 2D histogram plots. Comparing the trends in the beam area and number of filaments, which are expected to increase with increasing filamentation, and filament charge to

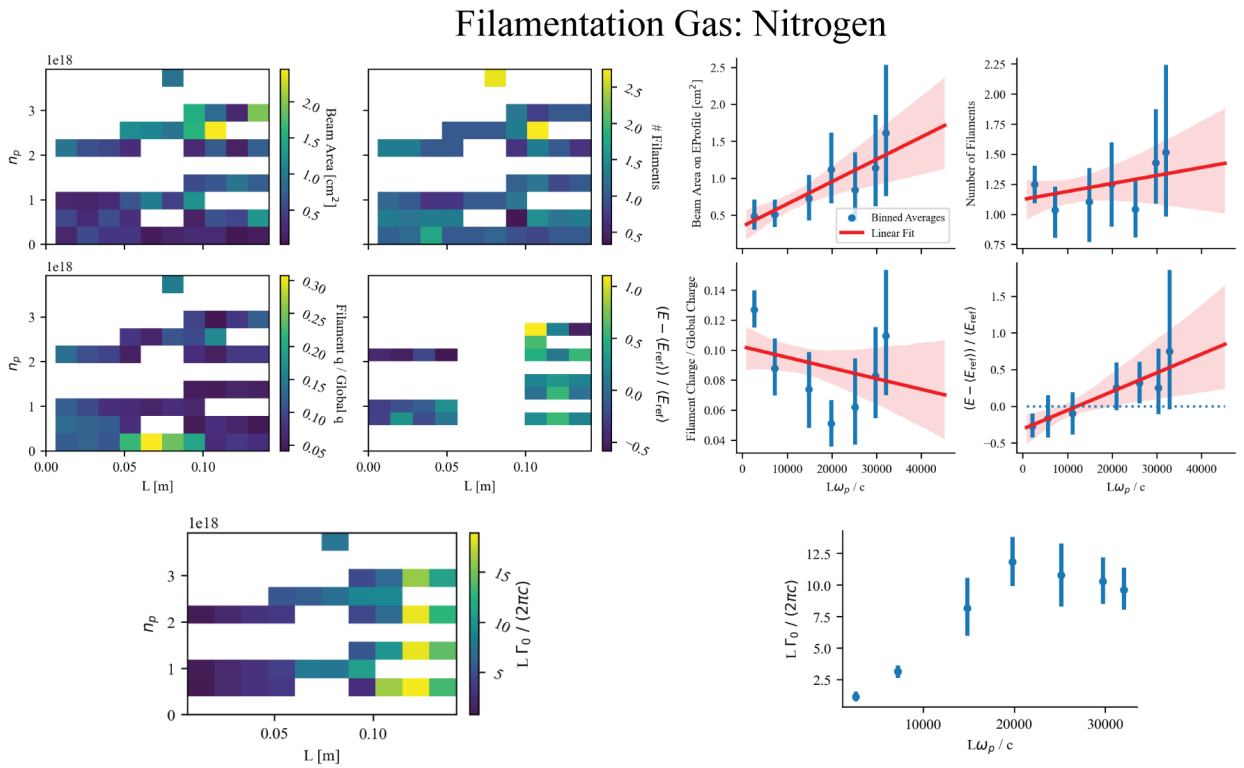


Figure 6.13: 2D histogram (top left) and 1D binned evolution of the measured growth parameters (top right) for nitrogen filamentation gas with axes identical to that of Figure 6.5 and Figure 6.6. Measured estimates of the initial CFI growth rate in these two visualization styles are oriented directly beneath the 2D histogram and 1D binned fit plots.

global charge ratio and relative energy loss, which should decrease with increasing filamentation, a weakly varying parameter space washed out by a outlier in beam area and number of filaments at around a filamentation gas length of 4 cm and plasma density of 0.85×10^{18} cm^{-3}. While the trends in these plots are not in obvious disagreement with the trends suggested by the estimated entry filamentation growth rate, they do not agree with these trends either.

The same figure structure is applied to data taken by using nitrogen gas in the filamentation cell, which is found in Figure 6.13. Interestingly, the maximums and minimums of the beam area, number of filaments, and filament charge to global charge ratio do not correlate well with the trends shown in the measured growth estimates shown in the bottom left plot. The length at which a global maximum in growth rate estimate occurs is a local minimum in the beam area and number of filaments parameters. This may be due to several density down-ramps within the filamentation

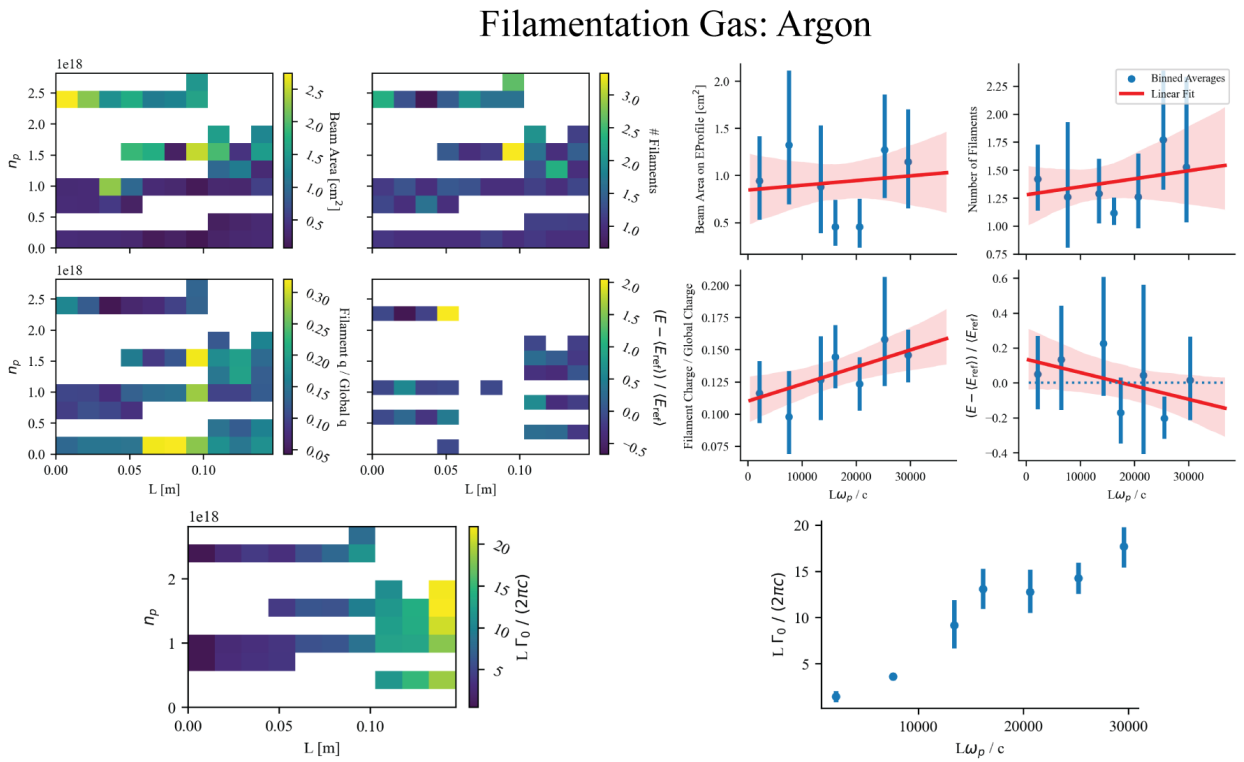


Figure 6.14: 2D histogram (top left) and 1D binned evolution of the measured growth parameters (top right) for argon filamentation gas with axes identical to that of Figure 6.5 and Figure 6.6. Measured estimates of the initial CFI growth rate in these two visualization styles are oriented directly beneath the 2D histogram and 1D binned fit plots.

cell causing dynamics during the filamentation process that would affect the growth rate of the instability such that the final filamentation parameters do not align well with an estimate based on the entry conditions of the electron beams into the filamentation gas cell.

Finally, the results for argon are presented in Figure 6.14. By looking at the 2D histogram plots on the left-hand side of the figure, one can notice a fairly clear trend that the beam area and filament charge to global charge ratio happen to suggest the opposite trends in the measured filamentation parameters than the initial filamentation rate estimate would suggest - in particular, this suggests that at the shortest lengths and higher plasma densities, there is a maximum in the filamentation parameters measured. While the number of filaments is a more varied result, there is also a trend in the 2D histogram that suggests that the region of pixels in the short lengths and higher densities are brighter on average than those at the highest lengths and lowest densities, which disagrees with

the predicted growth rate plots; however, there are some high-filament local outliers in the regions predicted to have high-growth, as well. By looking at the 1D binned data plots, the trends that pop out are that beam area, number of filaments, and filament charge over global charge all increase with respect to $L\omega_p/c$.

One may notice that while all filamentation gas species displayed an overall increase in the number of filaments and beam area as a function of $L\omega_p/c$, two gases (hydrogen and nitrogen) showed an overall linear-fit decrease in filament charge to global charge ratio. The other two gases (helium and argon) displayed the opposite trend with an overall fit increase in this ratio. Nitrogen, to be fair, did have a uniquely parabolic shape to the fitted distribution of data points in $L\omega_p/c$ space, but preserved a negative linear fit. This work does not explore the exact reason for these gases to produce seemingly opposite trends in the charge distribution of beams that undergo CFI in their ionized plasmas. An interesting commonality between these groups of gases is that hydrogen and nitrogen are diatomic gases as opposed to the monatomic gases of helium and argon. An exploration of this particular effect is suggested as a future area of study to focus on, where a similar experiment could be conducted ensuring that the level of ionization of each different gas species is kept uniform over the length of filamentation.

6.5 Conclusions

We measured the relativistic current filamentation instability in the case of an ultrarelativistic electron beam with femtosecond-scale duration traveling through an independently controlled background plasma from ionized hydrogen. These measurements were parametrically scanned over a wide range of background plasma densities in the filamentation cell and filamentation plasma length. Properties of the electron beams, which served as indirect measurements of the degree of filamentation growth, were derived and agreed with theoretic growth rates within a reasonable degree, considering statistical fluctuations within the data. At the limit where the highest number of e-foldings for the instability were expected, the instability parameters expected by the theo-

retical models were deviated from in some portion of the parameter space; however, future work would need to be done to discriminate the effect of the saturation of the instability for these shots. Similar parametric scans were taken using helium, nitrogen, and argon in the filamentation cell, but are presented with the caveat that the degree of ionization, which was not measured in the experiment, was likely non-uniform along the length of the plasma. This likely led to transitions between plasma densities at different portions of the species lengths, the effect of which is not explained by current theoretical models. 3D PIC simulations were run of the beam traveling approximately $1/3$ of the longest filamentation cell distance from the experiment to help explain the measured filamentation dynamics. Although more work is actively being done to improve these simulations, there is evidence that the filamentation in phase-space — which is what was measured in the experiment — depends somewhat on the plasma density. Future simulations will show the filamentation along the entire filamentation cell length and plasma density range as was performed in the experiment.

CHAPTER 7

Laser Wakefield Accelerator Source of Positron Beams Suitable for Injection into a Plasma Accelerator

7.1 Introduction

While the topic of plasma-based acceleration of electron beams at high-power laser facilities has been widely explored, experimental studies of plasma-based acceleration of positrons have been limited in large part due to the scarcity of positron sources that have sufficient energy and emittance qualities to be injected into a wakefield accelerator. The main positron source for these experiments has been the SLAC facility [34–36, 133]. This is largely due to the prohibitive fidelity requirements that positrons must possess to be injected efficiently into a wakefield accelerator. As an example, the required transverse and longitudinal size properties of positron beams to be injected into a plasma wakefield accelerator with a plasma density of $n_p = 10^{17}\mathrm{cm}^{-3}$ based on baseline studies for laser-plasma linear colliders would be σ_x, $\sigma_z \lesssim 10$ μm [134]. The required amount of charge for favorable beam-loading conditions in the wakefield would be in the range of 10's of pC [55], while plans for future lepton colliders call for positron beams with charge $Q_+ \gtrsim 10$ nC with energy $E_+ > 10$ GeV [135].

Positron sources typically consist of ultra-relativistic low-emittance electron beams colliding with a high-Z target to generate high-energy photons via bremsstrahlung in the solid, which then

interact with the solid to generate electron-positron pairs in a QED cascade shower. This process, which is summarized here, is detailed in a publication from Sarri et al on the topic of generating collimated positron beams from a wakefield accelerator source [136]. If we assume that the incident relativistic electron beams are collimated along the normal vector of the solid's surface, any resulting particle cascades should be expected to travel on the same axis as the incident electron beam [137]. This ensures that the distribution of positron output from the interaction between the high-energy beam and the high-Z target depends on the distribution function of the incident electron beam with a given mean energy, and the thickness of the high-Z target. At high enough energies, the energy loss of particles due to scattering within the high-Z material can be neglected as it is much less a factor compared to energy loss due to photon emission via bremsstrahlung, and then subsequent bremsstrahlung-induced or direct Trident process electron-positron pair production. The radiation length of the material can be estimated by assuming these interactions are predominately in the total screening regime. This is true when an electron with energy E emits a photon with energy ω, producing a value of $S \gg 1$, where $S = \alpha Z^{1/3} E(E-\omega)/(\omega m)$. α is the fine structure constant, m is the rest-mass of an electron and a Thomas-Fermi model of the atom is assumed [138]. These assumptions can yield an approximate radiation length of $L_{\mathrm{rad}} \approx 1/\left(4\alpha(Z\alpha)^2 n \lambda_C^2 L_0\right)$, where n is the number density in a unit volume of the solid, $\lambda_C = 3.9 \times 10^{-11}$ cm is the Compton wavelength, and $L_0 = \log\left(183 Z^{-1/3}\right) - f(Z\alpha)$ with $f(x) = \sum_{l=1}^{\infty} x^2/l(l^2+x^2)$. With a given target thickness in units of radiation length δ, an approximation of the kinetic equations for produced electrons and positrons ($f_{\pm}$) and gammas (f_{γ}) is given as [137]

$$\frac{\partial f_{\pm}}{\partial \delta} = -\int_0^1 \psi_{\mathrm{rad}}(\nu)\left[f_{\pm}(E,\delta) - \frac{1}{1-\nu} f_{\pm}\left(\frac{E}{1-\nu},\delta\right)\right] d\nu + \int_0^1 \psi_{\mathrm{pair}} f_{\gamma}\left(\frac{E}{\nu},\delta\right)\frac{d\nu}{\nu}, \quad (7.1)$$

$$\frac{\partial f_{\gamma}}{\partial \delta} = \int_0^1 \psi_{\mathrm{rad}}(\nu)\left[f_{-}\left(\frac{E}{\nu},\delta\right) + f_{+}\left(\frac{E}{\nu},\delta\right)\right]\frac{d\nu}{\nu} - \mu_0 f_{\gamma}(E,\delta), \quad (7.2)$$

where the expressions

$$\psi_{\mathrm{rad}}(\nu) = \frac{1}{\nu}\left[1 + (1-\nu)^2 - (1-\nu)(\frac{2}{3} - 2b)\right], \tag{7.3}$$

$$\psi_{\mathrm{pair}}(\nu) = \nu^2 + (1-\nu)^2 + \nu(1-\nu)(\frac{2}{3} - 2b), \tag{7.4}$$

$$\mu_0 = \frac{7}{9} - \frac{b}{3}, \tag{7.5}$$

$$b = 1/18 \log\left(183/Z^{1/3}\right), \tag{7.6}$$

relate to an electron's cross section for the QED bremstrahlung and pair production processes in the presence of an atom with ionization state Z. The description of the distribution function for electron/positron pairs yields an ideal target thickness for a given beam energy E to produce maximum positron yield, as a thinner target would reduce the flux of relativistic positrons produced via the initial electron beam bremsstrahlung interaction, and a thicker target would reduce the flux of relativistic positrons due to energy loss and scattering.

The divergence angle of the emitted radiation is approximately proportional to the divergence angular cone of the incident electron beam as it interacts with the high-Z target. For a target with a thickness less than or equal to the radiation length of that material, the divergence angle of highly relativistic electron beams (and thus the produced positrons) is described as $\sqrt{\langle\theta_{e^+}^2\rangle} \approx 1/\gamma^2$ [138]. If the target is thicker such that a cascade is likely triggered, the angular divergence cone can be related to $\delta = d = L_{\mathrm{rad}}$ the thickness of the target in units of radiation length: $\sqrt{\langle\theta_{e^+}^2\rangle} \approx \frac{19.2\mathrm{MeV}/c}{p}\sqrt{\delta}$, where p is the momentum of a given particle [139]. This suggests that in thick targets, an increase in energy of the incident positrons will also favorably reduce the divergence angle to produce a more collimated positron beam - although the effect is balanced by the divergence increasing proportionally with the square root of the target thickness.

As the quality of electron beams produced via LWFA continues to increase, the feasibility of using these accelerators as an alternative source of electron beams to generate high-quality positron beams is becoming closer to being a reality. These accelerators have demonstrated being able to

femtosecond duration micron-scale source size electron beams with ultralow emittance to the GeV level [140]. Importantly, modern developments in laser and target control in these accelerators have demonstrated stable, consistent electron beam output for continued pulses over long periods [141], demonstrating the feasibility of these sorts of accelerators to be used to produce consistent positron beams. The femtosecond duration of the electron beams produced via LWFA is a significant quality in the context of generating positrons that can be injected into a plasma wakefield accelerator due to the sub-10 micron longitudinal size requirement paired with the fact that the produced positron beams approximately preserve the spatial qualities of the incident electron beam. These facilities have thus proven capable of producing the electron beams required to generate positron beams, with several studies separately producing relativistic positron beams with energy in the 100's of MeV [136, 142, 143], high density and quasi-neutral electron-positron beams [39], and even observations of pair-plasma dynamics [144]. In order to realize acceleration of positrons in a plasma accelerator, however, the high-energy, low energy-spread, and micron-scale normalized emittance is required.

In this chapter, the results from an experimental campaign are presented which demonstrates that high-fidelity positron beams that meet the requirements for injection into a wakefield accelerator may be generated with LWFA accelerated electron beams from a 150 TW laser system. This experiment presents positron beams consisting of $N_+ \geq 10^5$ positrons measured after successfully being energy-selected to a 5% energy bandwidth with energies $E_+ > 500$ MeV. Emittance measurements of these energy-selected beams are presented, which show micron-scale normalized emittance values. This low emittance combined with the inherent ultrashort duration of the beams suggests that these beams possess adequate angular and temporal properties for injection into a plasma wakefield accelerator. The measurements of the positron beams are comparable to Monte-Carlo simulations of a representative electron beam from an LWFA accelerator interacting with the high-Z target in the experiment. Outputs of the particles from these Monte-Carlo simulations were used as input beams into PIC simulations of these positrons being efficiently injected as a witness beam into a plasma wakefield. These results from this experiment at a moderately

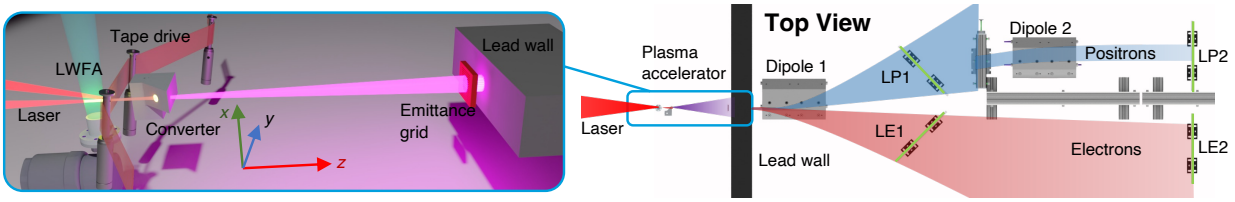


Figure 7.1: Diagram of the laser, targets, and diagnostic setup used in this campaign. The laser first interacts with the LWFA plasma accelerator target. Then, it is diverted with the tape drive so solely the electrons can propagate from the accelerator to the converter target. After this is an emittance mask followed by a lead wall with a collimation aperture. Electrons (red) and positrons (blue) are separated by Dipole 1 and interact with scintillators for electrons (LE1 & LE2) and positions (LP1 & LP2). Positrons also interact with an energy band selection aperture and are steered back toward the laser axis with Dipole 2.

high-power laser facility are encouraging for the prospect of high-power laser facilities serving as an alternative accelerator source of high energy, high fidelity positron beams due to the favorable scaling in beam and spatial characteristics of beams that can be produced from laser systems with higher peak power [145, 146].

The work presented in this chapter culminated in a 2024 paper by Matthew Streeter, Cary Colgan, Jason Cardarelli, Yong Ma, et al. published in Scientific Reports [83]. Gianluca Sarri and Matthew Streeter led the campaign. Thomas Audet, Luke Calvin, Matt Streeter, Yong Ma, and I worked on supporting numerical simulations. The experimental team consisted of Cary Colgan, Nicholas Cavanagh, Eva Los, Hamad Ahmed, Brenden Kettle, Dan Symes, and Rajeev Pattathil, coordinated by Matthew Streeter, Cary Colgan, Stuart Mangles, Zulfikar Najmudin, and Gianluca Sarri. I also contributed to the numerical modeling of the electron spectrometer diagnostic and, in particular, the transverse focusing effects of the two-dipole system. Matthew Streeter conducted most of the data analysis. Support for this project came from EPSRC (EP/V044397/1, EP/N027175/1, EP/V049577/1), STFC (ST/V001639/1), the NSF (grant #2108075), and from the staff of the Central Laser Facility.

7.2 Methods

This experimental campaign was conducted on the Gemini laser at the Central Laser Facility [74]. The setup for this experiment can be found in Figure 7.1. The 800 nm Gemini laser parameters at the time of the experiment include an energy of 7.9 ± 0.5 J, and a FWHM pulse duration of 48 ± 7 fs yielding a peak power of 156 ± 9 TW. The driving pulses were focused into a 15-mm exit diameter LWFA gas jet from an $f/40$ OAP at a facility-limited repetition rate of $\frac{1}{3}$ Hz. The gas jet provided a gaseous mixture of 2% nitrogen and 98% helium which yielded a measured electron density of $n_e = (1.5 \pm 0.2) \times 10^{18}$ cm^{-3}. The focal spot from the OAP had a $1/e^2$ transverse radius in the x and y directions of 37 ± 3 and 52 ± 4 μm, respectively. Dividing the peak power by the spot size gives a peak intensity of $I_0 = (3.1 \pm 0.3)10^{18}$ Wcm^{-2}.

Given the fact that there are converter materials and particle diagnostics on-axis after the accelerator that the electrons produced via LWFA were meant to interact with, the remaining laser pulse energy after the accelerator had to be removed from the axis. This was achieved by using a 125μm polyimide tape as a plasma mirror to reflect the pulse off-axis. The plasma mirror target was regenerated by installing the spool of the tape in a motorized tape drive, allowing it to be used in every shot in this project. The lead positron-generating 45-degree wedge-shaped converter target is placed 50 mm away from the LWFA exit plane of the gas jet nozzle and placed on a motorized stage to control the effective length of the converter target L that the LWFA electrons interact with within a range of $1 \leq L \leq 25$ mm. The positrons are produced within this lead converter target through a two-step bremsstrahlung-induced Bethe-Heitler process [136].

290 mm behind the rear face of the converter target a 5.0 mm thick tungsten mask composed of slits with a regular period of 1.1 mm (550 μm gaps). This mask was put in the path of the electron-positron beams to perform energy-resolved emittance measurements of the beams. The method of these emittance retrieval measurements will be briefly described here and is expanded on in more detail in the Methods chapter in this dissertation, Chapter 3 Section 3.3.3. To summarize the method, an impression of the emittance mask is left in the profile of the beams that pass through it, which show up as shadow-like stripes in the beam profiles when scintillating screens measure

them. Focusing effects on the particle beams in the non-dispersive direction from the dipoles are remedied in the analysis of the mask patterns on the scintillators by transforming the images such that the spatial frequency of the stripes in the images of the LANEX screens are constant throughout the length of the screen. 4 mm slices in the images of the scintillators along the length of the screen's energy dispersion axis are taken to retrieve signal modulation as a function of x, the position along the axis transverse to the dispersion direction, at a given dispersion axis y position on the screen. By fitting a Gaussian function to the values at the filtered portions of the image of the mask in the beam, the background signal at the minimum value in the profile can be removed. The envelope of the resulting profiles at given y positions is retrieved by fitting an analytic function of the mask's shape to the observed profile in the image, yielding an RMS width in the fitted mask features in the beam profile that gives a measure of the beam's divergence angle by dividing this RMS width by the distance between the screen to the source of the particles (the converter target). A source size of the beam, σ_x, is determined by minimizing the error between the measured transition-of-signal at the edges between the filtered signal and non-filtered signal regions beam profile and numerically calculated synthetic images of particles with varying source size with the measured divergence angle from the previous step in the process. This results in a measurement of the geometric emittance of the beam, which is defined for a beam with little correlation between source position and transverse velocity as the product of a beam's divergence and its source size, $\epsilon = \sigma_x \sigma_\theta$.

A lead shielding wall with an on-axis 10 mm diameter aperture followed this converter target, only allowing particles emitted from the converter target with less than a 12.6 mrad half-angle trajectory from the central axis to travel onward to the energy and emittance diagnostics. A magnetic dipole with an integrated field strength $B_x z = 0.3$ Tm was placed after the exit of the lead wall to disperse electrons and positrons in opposite directions, which were measured by LANEX scintillating screens referred to by the names LE1 and LP1 in Figure 7.1 respectively. The correlation between 3D particle dispersion trajectory and energy was calculated numerically using the Boris-pusher within an analytic dipole field as described in the Methods chapter of this thesis, Section

3.3.2, in order to give a calibration of particle energy to position on the scintillator screens. These screens recorded the spectra of these particles with kinetic energy $\gamma m_e c^2$ greater than 200 MeV and less than 2500 MeV and vertical divergence angles $-15 \leq \theta_y \leq 15$ mrad.

The two screens were placed at different yaw angles and distances from Dipole 1 due to experimental limitations: a yaw (angle from the laser axis) of -41.1° with a distance of 134 cm for LP1, and a yaw of 45.4° with a distance of 137 cm for LE1. The electrons were allowed to travel through LE1 and then propagate 1 m to a second scintillating screen LE2 to increase the measurement accuracy of particularly high-energy electrons. In the path of the dispersed positron beam was placed a 25 mm wide slit to allow a selected energy bandwidth from Dipole 1, and then a magnetic dipole, Dipole 2, which is identical to Dipole 1. Dipole 2 acts to put the positrons back toward the z-axis in a dog-leg configuration. After energy selection and being swept back to the longitudinal axis from Dipole 2, the positrons were measured by a second scintillating screen, LP2.

Benchmarks of the emittance retrieval process are done by using synthetic data generated from a particle physics Monte-Carlo package, FLUKA. An analytic copy of the emittance mask is used to filter away particles at the emittance mask plane in these simulations. The dispersion effects of Dipole 1 are included to determine the dispersed trajectories for each particle determined by its longitudinal velocity, which leads to these synthetic images including trajectory crossing in the spectrometer system due to uniformly distributed energy spread in the beam and a finite divergence angle of the beam. This generated synthetic images of particle beams on the scintillators which interacted with the emittance mask on the particle screens. These synthetic images were analyzed via the same methodology as the experimental data.

7.3 Results and discussion

The electron beams from the LWFA accelerator were optimized to produce as many positrons in the converter target as possible. As the spectrum of the positron/electron pairs produced via the bremsstrahlung-induced Bethe-Heitler pair production process is expected to be broadband

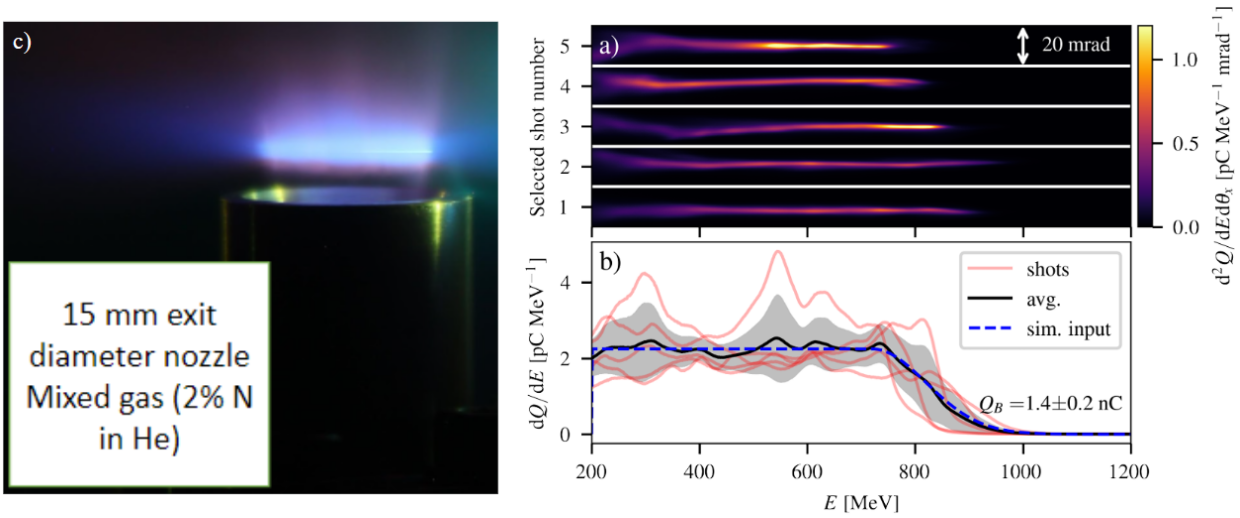


Figure 7.2: Typical examples of measurements of the LWFA electron beam source. a) Angularly-resolved and b) angularly-integrated electron spectra from the accelerator (red), along with the average (black) and standard deviation (grey) of example shots. Also shown is a simple analytic approximation used as an input for the spectrum of electron beams in Monte-Carlo positron generation simulations. c) A snapshot of the plasma emission from the accelerator during a shot on this experiment with a description of the gas jet.

irrespective of the spectrum of the input electron beams, the optimization meant producing electron beams with high charge to maximize the electrons inducing the pair production conversion process.

In order to characterize the electron beams that will interact with the converter target, the spectra and angular measurements of the electron beams from the accelerator were taken with the plasma mirror tape drive after the gas target, but without the lead converter target in the beam line. Out of ten reference shots without the converter target in this data collection run, there was a 30% rms variation in total charge due to shot-to-shot variations in laser and plasma conditions. The five shots with the highest beam energy are shown in Figure 7.2a, with Figure 7.2b showing the angularly-integrated spectra with statistics regarding the variation in energy shot-to-shot. The average shown in Figure 7.2b is taken as the expected LWFA spectrum when interpreting results with the lead converter target placed in the beam line. The mean charge of electrons with sufficient energy to land on the electron spectrometer (with energies > 200 MeV) was measured to be 1.4 ± 0.2 nC. The lowest half of the shots' charge taken in the reference shot run that was not included in the consideration of the mean energy still consisted of a relatively high charge for wakefield accelera-

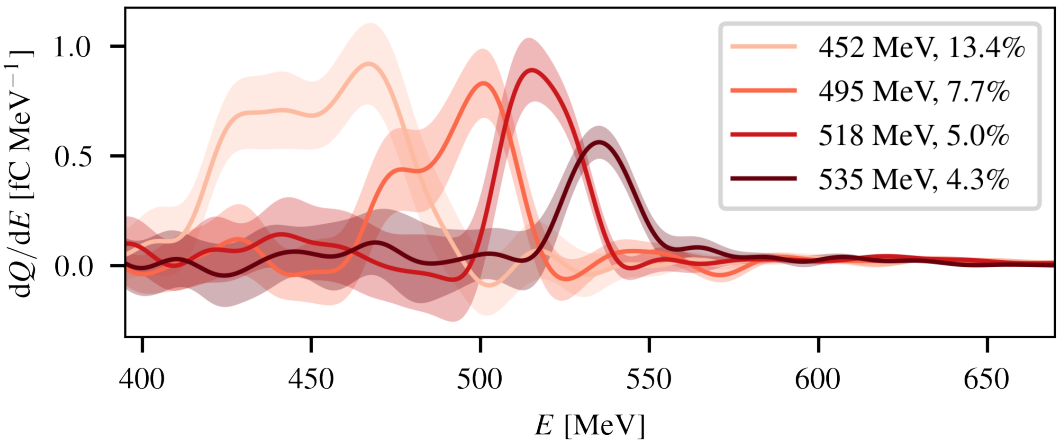


Figure 7.3: Positron spectra measured after energy-selection for different positions of the energy selection slit. The data is background-subtracted and smoothed with a Gaussian filter that spans a 10 MeV bandwidth, as indicated by the shaded RMS scatter error in the data. The central energy and FWHM bandwidth of each spectrum is noted in the legend of the figure.

tors, with an average beam charge of 0.9 ± 0.3 nC. The recorded angular of the beams after they have interacted with the tape drive was estimated to fit a square of a Lorentzian distribution with a FWHM of $\theta = 3.8 \pm 0.4$ mrad.

To demonstrate the energy selection process for positrons produced via the interaction of high-charge electron beams with the high-Z converter target, the transverse position of the selection slit was scanned using a converter thickness equal to approximately 0.9 radiation lengths (5.0 mm). The energy spectra after the second dipole as measured on LP2 are shown in Figure 7.3. When selecting beams with central energy $E > 500$ MeV, more than 10^5 positrons per shot were recorded within a FWHM bandwidth of $\Delta E/E \leq 5\%$. This demonstration of successful energy selection of positrons output from a LWFA accelerator electron source suggests this RF accelerator technique can be utilized in laser/plasma accelerator facilities to capture a selected energy band of positrons. This energy selection was successfully performed over several target thicknesses.

Energy-resolved emittance values for electrons and positrons were measured on the LANEX screens following the emittance mask, the lead shielding wall, and the magnetic dipole. The emittance mask modulated the distribution profile of particles on the LANEX screens, as can be seen in Figure 7.4. The spatial frequency of the modulated profile is energy dependent due to defocusing

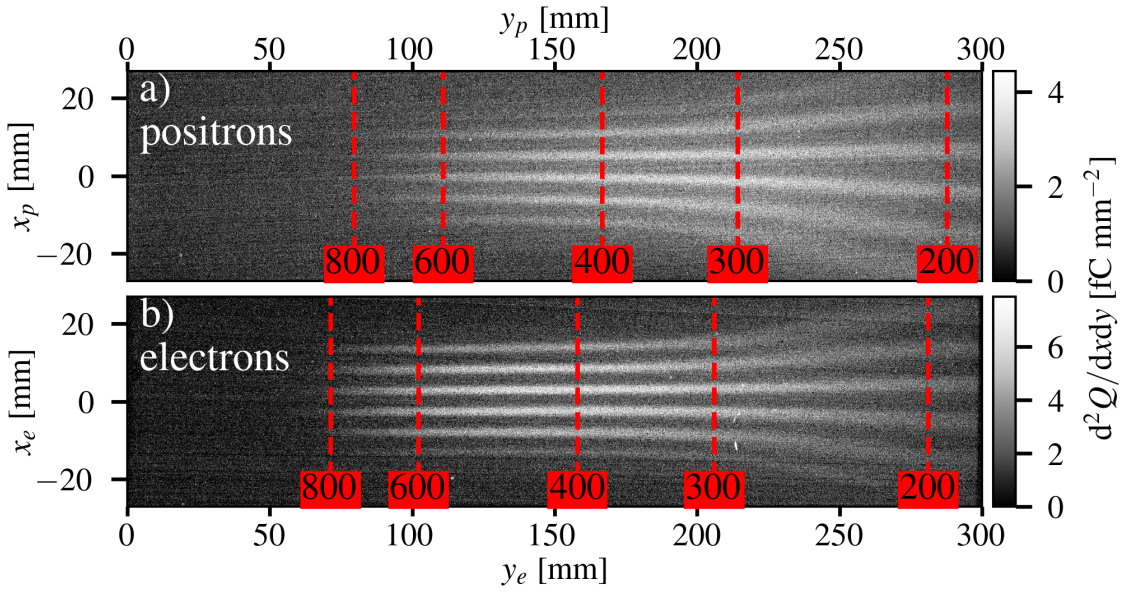


Figure 7.4: Example a) positron and b) electron spatial charge density as a function of position on the LE1 and LP1 screens (x_p, y_p, x_e, x_e) for a single shot with a converter thickness of 8.0mm and the emittance mask in the beam-line. The particles corresponding to the given particle energies in MeV are shown as vertical red dashed lines.

of particularly lower energy particles exiting the side fringe fields of the magnetic dipole where their longitudinal momentum on their dispersed trajectories induced greater magnetic defocusing on the angular axis, as is evident in the example profiles as the 'bending' of the modulation stripes. In analyzing these images to reconstruct the on-shot emittance values, images were rescaled so that the intensity modulation in the beam profile is straightened out and the modulation width is constant along the length of the LANEX screen. For lower energies, this adds error to the emittance measurement that results in an overestimation of the source size by about 5% for particles with energies $E < 300$ MeV. In addition to this source of error, the spatial resolution of the spectrometer blurred the modulation pattern in the beam profile where the magnetic defocusing was greatest, leading to a total uncertainty of about 30% in the source size measurement for particles with energy $E < 350$ MeV. For particles with energy above this 350 MeV threshold, the error in the measurement is reduced.

As mentioned in the methods section, we need the divergence ($\sigma_\theta = \sqrt{\langle x'^2 \rangle}$) and rms source size ($\sigma_x = \sqrt{\langle x^2 \rangle}$) to retrieve the emittance for a beam with a negligible angle-position correlation

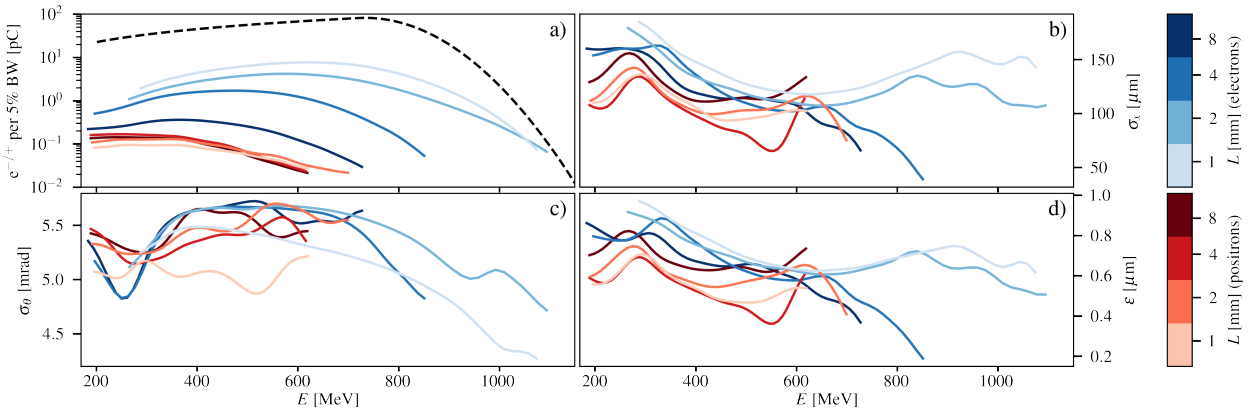


Figure 7.5: Measured electron and positron beam properties as functions of particle energy for different converter thicknesses. The a) spectra (charge per 5% bandwidth), b) source size, c) divergence, and d) geometric emittance are given for each converter length as shown by the color-bars at the side of the figure. For each converter thickness, only the shots resulting in the highest charge of the positron beams were used for the analysis; the lines shown are thus an average of 4, 6, 3, and 8 shots for converter lengths of 1.0, 2.0, 4.0, and 8.0 mm, respectively (rms variation of $\approx$ 43% in the spectrum and $\approx$ 20% in emittance). Each line results from a Gaussian weighting of each measurement point using a kernel width of $\sigma E = 25$ MeV. The typical input electron spectrum (black-dashed) is shown in a) for comparison

($\langle xx' \rangle$), such that $\epsilon = \sqrt{\langle x^2 \rangle \langle x'^2 \rangle - \langle xx' \rangle} \approx \sigma_x \sigma_\theta$. It is assumed that $\langle xx' \rangle$ is negligible in this instance because the large scattering angles in the high-Z target largely randomize the position-to-transverse velocity distribution at the high-Z target plane. By following the method of retrieving the beam divergence by fitting the envelope of the signal on the screen to the source-to-screen distance; and retrieving the beam source size by fitting a Gaussian distribution to the edge of the modulation grid pattern and reconstructing the source size with an iterative deconvolution, we have enough information to solve for the approximation of the emittance of the beams. Monte-Carlo simulations indicate that the small level of remaining correlation implies that the positron beam is equivalent to an uncorrelated beam originating from 100 – 200 μm inside the rear surface of the converter. Therefore, the correlation term was neglected and the geometric emittance was calculated as the product of the measured divergence and source size.

Figure 7.5 shows the spectra, source size, divergence, and geometric emittance of the produced electron and positron beams separately for converter thicknesses of $L = 1.0,\ 2.0,\ 4.0$, and 8.0 mm, corresponding to radiation lengths of $0.2,\ 0.4,\ 0.7$, and 1.4, respectively. While the number of

electrons consistently decreases with converter thickness, a converter length of 4.0 mm was found to maximize the positron yield from the target. While the radiation length of the converter target is in the $\lesssim 1$ regime, pair production observed should be expected to be dominated by an initial interaction between electron beam particles and the high-Z target - ie before many pair-production cascade events are triggered. If we were to increase the converter target thickness to 4-5 radiation lengths, it should be expected that the incident electron beam has undergone several large-angle scattering events converting energy into electron-positron pairs; however, this would be undesirable as the net yield and positron energy would decrease due to the produced positrons scattering and triggering further cascades in the lead converter. Both electron and positron source size weakly decreases with energy: from 140 ± 10 μm at 300 MeV to 110 ± 10 μm at 600 MeV with fluctuations between 200 and 300 MeV. The rms divergence was nearly constant for electrons and positrons at $\sigma_\theta = 5.3 \pm 0.3$ mrad - however, it is noted that this is limited by the acceptance angular range from the aperture in the lead shielding wall in the experiment. Because of the fixed angular divergence of the beams from the converter, the measured source size of the beam determined variations in measured emittance. The positron geometric emittance exhibited a gradual linear decrease as a function of energy with values of $\epsilon = 640$ nm at $E = 200$ MeV and $\epsilon = 480$ nm at $E = 600$ MeV for a 1.0 mm converter. As previously predicted [142], the geometric emittance of the positrons was consistently lower than that of the scattered electrons. There was a measured rms variation of 43% in the spectrum and 20% in emittance due to the shot-to-shot variations of electron beams from the LWFA accelerator.

Simulations using the particle physics Monte-Carlo code FLUKA [147] were run by Matthew Streeter to simulate the generation of the produced positron beams from the interaction between the primary electron beam and the lead converter target, as discussed in the paper describing this experimental work [83] and summarized here. 10^6 electrons were initialized within a distribution of energies following the LWFA electron spectrum approximation shown in Figure 7.6. The number of particles output from the simulation was then scaled up by 8738 to match the charge of the experimental electron beam. A lead converter of variable thickness L was placed in the path of

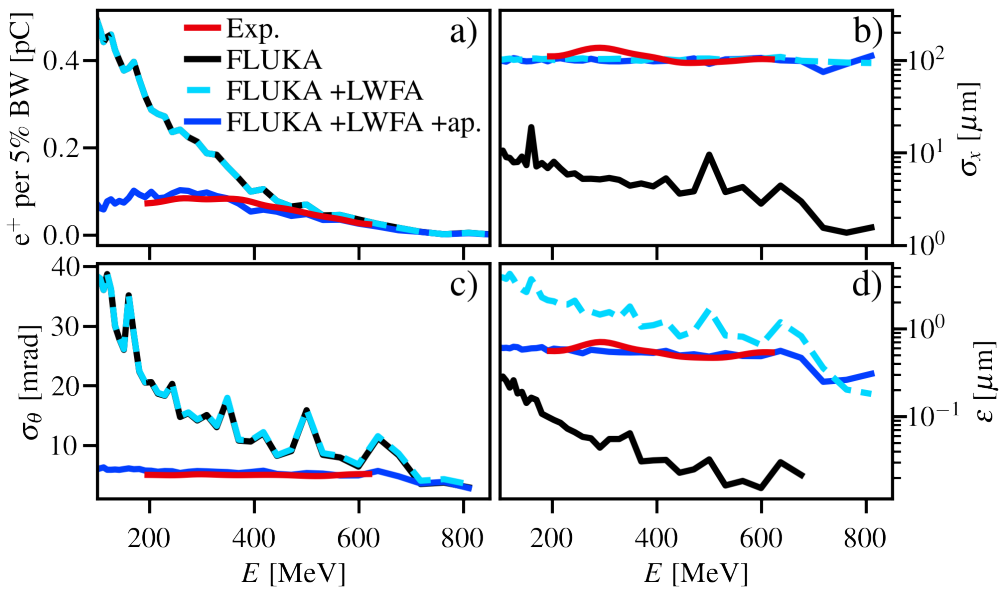


Figure 7.6: Positron beam a) spectrum (charge per 5% bandwidth), b) source size, c) divergence, and d) geometric emittance plotted for a 1.0 mm thick lead converter. The experimental data (red) is plotted alongside FLUKA simulations for zero drift distance for the primary electron beam (black); including the drift distance and the primary electron beam divergence and source size (cyan dashed); and including the 12.6 mrad shielding aperture (blue).

the electrons, and the momenta and position of all electrons, positrons, and photons were recorded as they exited the rear surface of the converter. To simulate the effects of the finite divergence of the electron beam, each particle was assigned random angular shifts ($\Delta x_i'$ and $\Delta y_i'$) from the probability density function $f(x') = f_0[(x'/\theta_w)^2 + 1)]^{-2}$, which approximated the measured transverse profile of the primary electron beam with $\theta_w = 2.9 \pm 0.3$ mrad, where f_0 is a normalization constant. The momenta and positions of the particles were altered according to these shifts, and using the length between the LWFA exit and the converter rear face of 50 mm to allow the electron beam to diverge before entering the converter target. The transverse particle positions were also modified according to the expected LWFA electron source size of 1 μm [148–150], although this contribution was negligible. Particle distributions were then calculated at the longitudinal plane for which the correlation term $\langle xx' \rangle$ was minimized to reflect the stochastic relation between transverse position and angular distribution within the converter target. The results of the numerical simulation for a converter thickness of L = 1.0 mm show good agreement with the experimental

data (blue and red lines in Figure 7.6, respectively) with an rms average difference for all converter lengths of 15%, 3.5%, 2.8% and 0.5% for the spectrum, emittance, source size and divergence, respectively.

The measured spectrum of the particles in this experiment was affected by the 5.3 mrad aperture in the beamline, as lower-energy positrons from the pair-production cascade process have, on average, a higher divergence angle than the higher-energy positrons from the source. This is shown in Figure 7.6, where the numerical results that most closely match the experimental measurements for the properties of the produced positron and electron beams are the ones that consider this limiting aperture. The agreement between simulation and experiment for the source size and emittance of the positron beams also depends on considering the divergence and drift distance between the LWFA primary beam source and the converter target.

The source size of the positron beams can be scaled down from the results presented in this work by reducing the travel distance between the exit of the LWFA accelerator and the entrance plane of the converter target. For the measured LWFA electron beam with FWHM divergence of 3.8 mrad, a typical beam waist at the LWFA source of 1 μm, and a converter thickness of 1 mm, the positron source size at 600 MeV could be reduced to 2.7 μm by having the primary electron beam directly enter the converter target from the LWFA source. This case is discussed in the publication which resulted from this experimental campaign [83] and showed this positron beam would have a divergence $\sigma_\theta = 5.5$ mrad, a geometric emittance $\epsilon = 15$ nm, and a normalized emittance $\bar{\epsilon} = \gamma\beta_z\epsilon = 18$ μm at 600 MeV. Scaling laws can be used to calculate positron yield, spectrum, and emittance parameters for different target thicknesses and primary beam source size [145, 146]. When the converter target is placed directly after the primary electron beam source, simulations indicate that differences in electron source size or divergence will have a small effect on the positron beam characteristics, which can be taken into account by adding it in quadrature. For example, doubling the electron source size only increases the positron source size by approximately 10%. The simulations also show a spreading in the duration of the positron beam of 0.1 fs for positrons within a 5% bandwidth of 600 MeV implying that the positron beam duration will be similar to that

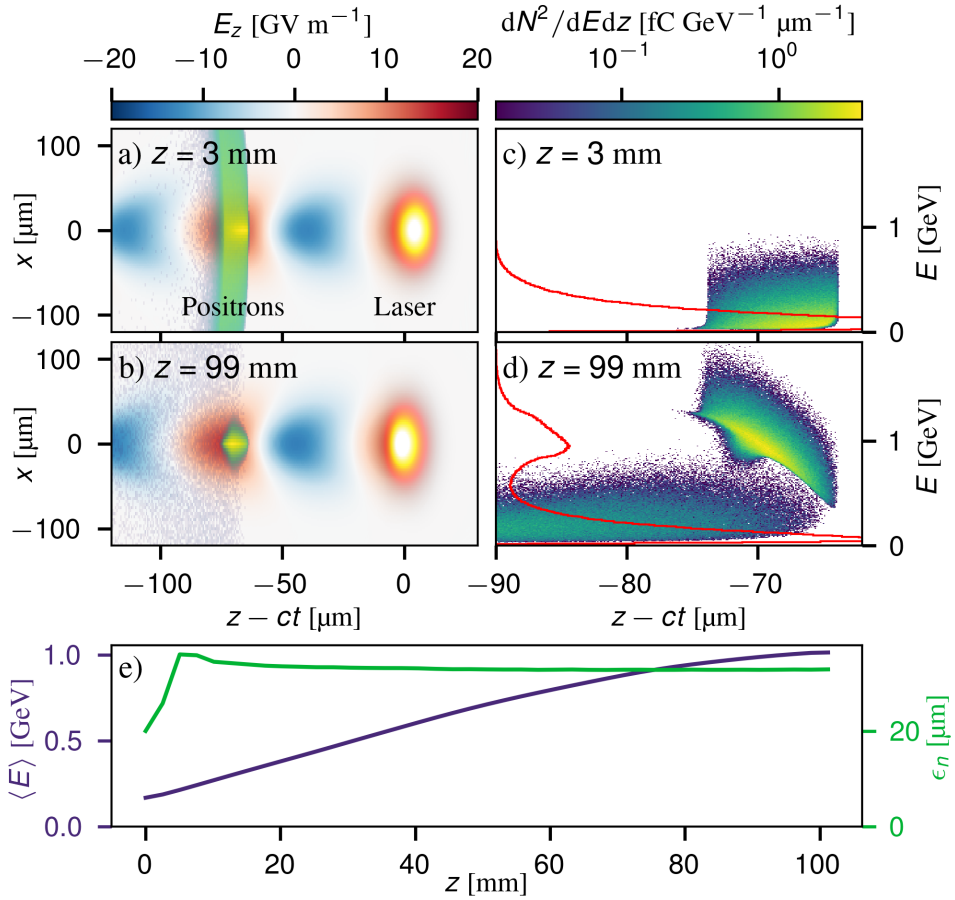


Figure 7.7: a-b) The longitudinal electric fields of the plasma wakefield are generated by the laser pulse (yellow orb) and the witness positron bunch (density in a logarithmic color-scale) at the beginning of the plasma and after 96 mm of propagation. c-d) The positron longitudinal phase space before and after acceleration, with the energy spectra indicated by the red lines. e) The average energy and normalized emittance of the trapped bunch, defined as being comprised of particles that remain within ± 50 μm of the central axis.

of the primary electron beam (i.e., $\sigma_z \lesssim \lambda_p/2 = 14$ μm for $n_e = 1.5 \times 10^{18}$ cm^{-3}, corresponding to $\tau \lesssim 50$ fs).

7.4 Particle-in-Cell simulations

Simulations were performed using the particle-in-cell code FBPIC [93] to assess the suitability of the generated positron beams for post-acceleration in a plasma wakefield. As an example following a baseline study on plasma accelerators [134], the laser wakefields were produced by the interaction

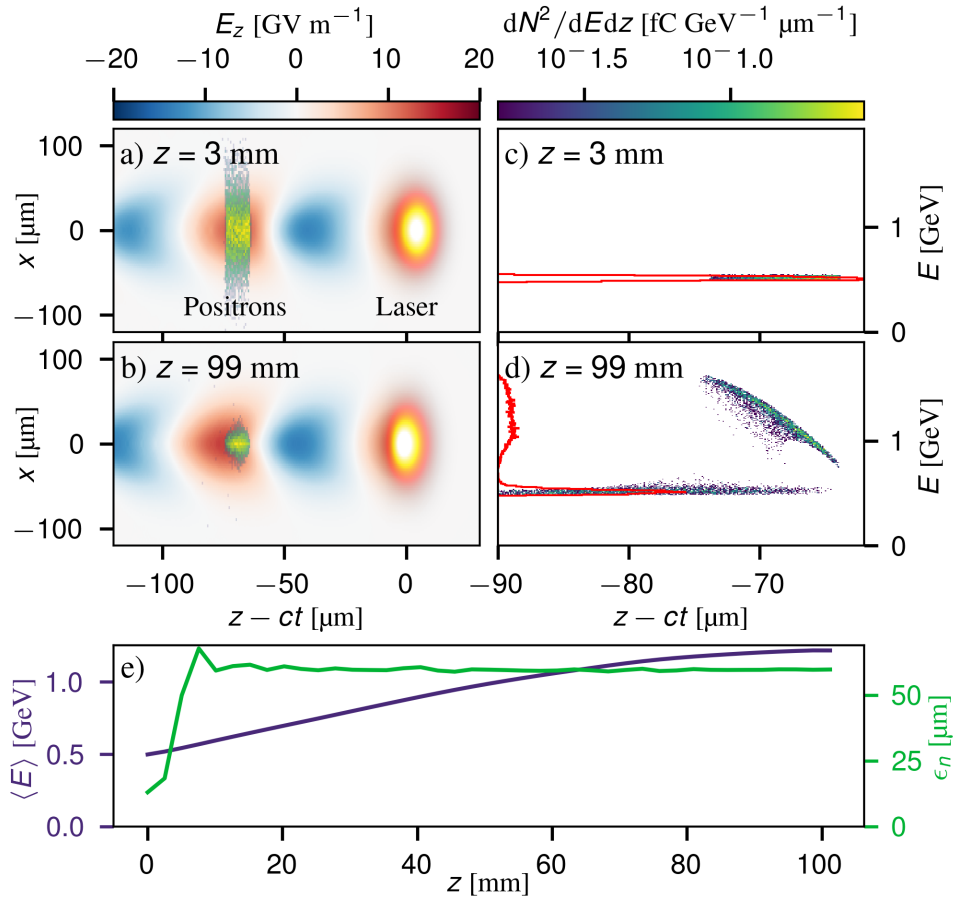


Figure 7.8: Output in same format as Figure 7.7 for the output of a simulation that only includes positrons with energy above 500 MeV from the input FLUKA-generated particles. This demonstrates the chromatic selection that would be present in a magnetic chicane or quadrupole electron transport system.

of a Gaussian laser pulse with radius $r_L = 70$ μm, pulse length $\tau_L = 56$ fs, pulse wavelength of $\lambda_L = 1000$ nm, and normalized vector potential of $a_0 = 1.5$. The accelerator target consisted of a pure helium plasma with an electron density of 2×10^{17} cm^{-3} and a length of 10 cm enclosed by two 0.5 mm-long linear ramps.

As FBPIC employs a cylindrical grid with azimuthal decomposition, two cylindrical modes were used to capture the physics of the wakefield formation and acceleration. The simulation was performed in the Lorentz boosted frame with a Lorentz factor of $\gamma = 10$. The number of particles per cell set for each coordinate direction was 2 along $\hat{z}$, 2 along $\hat{r}$, and 6 along $\hat{\theta}$. The simulation box lengths were $z_{length} = \left(\frac{6c}{\omega_{p0}} + 2\lambda_{p0}\right) \approx 220.6$ μm and $r_{length} = 2 \times r_{max} = 2 \times \frac{15c}{\omega_{p0}} \approx$

2×178.2 μm for $\hat{z}$ and $\hat{r}$ respectively, where $\omega_{p0} = \sqrt{\frac{e^2 n_{e0}}{\epsilon_0 m_e}}$ is the plasma frequency of the peak initial density in the accelerator, and $\lambda_{p0} = \frac{2\pi c}{\omega_{p0}}$ is the plasma wavelength. The number of cells in the $\hat{z}$-direction was $N_z = \lfloor \frac{z_{length}}{\Delta z} \rfloor = 1764$, where $\Delta z = \lambda_L/8$. In the $\hat{r}$-direction this number of cells was defined as $N_r = \lfloor \frac{r_{max}}{\Delta r} \rfloor = 89$, where $\Delta r = 2 \times \lambda_L$. The time step size of the simulation was set to be $\Delta t = r_{max}/(2 \times \gamma \times N_r)/c \approx 0.334$ fs.

The initial positron particle distribution was obtained from FLUKA simulations of the interaction of the LWFA electron beam with a 1 mm converter. A random shift of ± 5 μm taken from a uniform probability distribution was added to the longitudinal position of each positron to approximate the effect of the primary electron bunch duration. This longitudinal spread is consistent with an upper limit of 14 μm estimated for the positron beams obtained in the experiment. The positron bunch was initialized at the peak of the positive accelerating field of the plasma wakefield.

Figure 7.7 shows a summary of the main results of the simulation. For these laser and plasma conditions, a quasi-linear wakefield is generated behind the laser pulse with a peak accelerating field of 13 GVm^{-1} and a period of 75 μm. After 96 mm of propagation in the plasma, 31% of the charge remains in a focused positron beam which is accelerated to an average of 1.0 GeV with a relative rms energy spread of 20%. The beam is chirped, however, and so the energy spread could be reduced further using a plasma dechirper [151]. After an initial increase mainly due to a mismatch between the bunch emittance and the plasma focusing forces, the normalized emittance of the trapped positron beam remains approximately constant throughout the acceleration, at $\bar{\epsilon} = 33.0 \pm 0.2$ μm.

The conditions to inject a positron beam directly after the converter source, as simulated and shown in Figure 7.7, could be achieved in the lab by employing a thin plasma mirror directly following the converter target in the positron beam path, where a laser wakefield driving laser pulse could be reflected by this plasma mirror and focused into an LWFA accelerator gas target close to the plasma mirror. Alternatively, positron beam transport magnets can be used for both energy selection, transport, and transverse focusing into a plasma wakefield a given distance away from the converter target. Magnetic transport systems like this are employed at conventional acceler-

ator facilities and are part of the design process for the future plasma-based accelerator facility EuPRAXIA, for example [152]. As an example of this capability, we performed FBPIC simulations of wakefield acceleration of the energy-selected positron bunch energy centered at 500 MeV with a 5% energy spread in the same conditions as those discussed above, the results for which can be found in Figure 7.8. In this case, approximately 50% of the positron bunch is trapped and accelerated up to an energy of 1.2 ± 0.3 GeV with a normalized emittance of 57 μm.

7.5 Conclusions

It is shown in this work through a process of putting the converter source relatively close to the LWFA source of primary electrons that the resulting positron beams are of suitable energy and emittance for external injection into a plasma wakefield accelerator. The optimized positron beams from this experiment are energy selected using a magnetic chicane, where $N_+ \geq 10^5$ positrons within a 5% bandwidth around 500 MeV were measured. A limited number of previous experiments studying wakefield acceleration of positrons externally injected witness positron beams with similar geometric emittance to our inferred beam properties into plasma wakefields, though at higher energy [34–36, 153]. Properties of these previous studies' post-accelerated positron beams, as well as the properties of the witness positron beam source at SLAC that they used as their injection source, are compared to the positron beams produced in this experiment in Table 7.1. These previous studies demonstrate this work's positron source suitability to provide witness beams for wakefield acceleration studies. The inherent short duration of the positron beam produced from a short-duration primary electron beam is naturally suited for injection in a positron-accelerating wakefield structure without the need for complex beam manipulation, as confirmed by the proof-of-principle simulations reported in this article.

From Table 7.1, it can be seen that the energy of the energy-selected position beams was less than that of those produced at SLAC's FACET-II positron source. Also, the charge measured in the energy-selected positron beams from this campaign, around 16 fC, was smaller than those

	Measured	Inferred	[153]	[34]	[35]	FACET-II [145, 154]
E (GeV)	0.6	0.6	28.5	20.3	20.3	10
σ_x (μ m)	100	2.7	25	< 100	50	4
σ_z (μ m)	-	$\lesssim 4^*$	730	30 - 50	35	6.4
ϵ (nm)	480	15	14×3	5×1	7	-
$\bar{\epsilon}$ (μm)	560	18	390×80	200×50	300	7000×3000
N_+	$\gtrsim 10^5$	-	1.9×10^{10}	1.3×10^9	5.3×10^9	3.1×10^9

Table 7.1: Summary of measured and inferred positron parameters, compared with sources used for previously reported proof-of-principle positron wakefield acceleration experiments and the modern linear accelerator positron beamline at SLAC's FACET-II. *Note that this value is the RMS of a uniform distribution with a width of 14 μm.

produced at SLAC's source, producing beam charge on the order of $\gtrsim$ nC. With higher primary electron beam energies like, for example, the E >5 GeV beams produced at high-power laser facilities [155], and minimized drift distance between the LWFA source and the converter target, positron beams with nm-scale geometric emittance, 10 μm-scale normalized emittance, and $E_+ \sim$ 1 GeV-scale positron beams [145, 146]. Increasing primary electron energy would enable higher-charge positron beams from an LWFA positron source like the one described by this experiment [146].

For LWFA facilities to provide adequate alternative positron sources for future plasma wakefield experiments, the stability and positron fluxes of the positron beams should ideally be improved from the results of this proof-of-concept experiment. Modern laser systems have demonstrated improved LWFA output stability [141], which could be used to address the stability requirements for these facilities. Positron beam flux, as well, can be increased by using a high repetition rate laser system. Components utilized in this chapter's experimental setup that could limit accelerator repetition rates, such as the tape drive plasma mirror, have been demonstrated to be operable on kHz laser rates [156]. The laser system's rate limited this experimental campaign to a repetition rate of $1/20$ Hz. There is no fundamental limitation to the accelerator or converter design that would impede pushing repetition rates of this positron source into the kHz-regime.

CHAPTER 8

Conclusions

8.1 Summary

This thesis comprises work from four experiments based on laser wakefield acceleration of electron beams on high peak-power laser systems. Two of these projects focused on optimizing laser wakefield accelerators as an accelerator technology and their associated diagnostics. Chapter 4 discussed work to minimize the relative energy spread to $\Delta E/E < 10\%$ for $E >$ GeV LWFA electron beams from a sub-200 TW laser system through the use of shock-front induced density transition injection. The demonstration of high-energy, low-relative energy spread beams is becoming increasingly relevant as the development of PW-level laser ultrashort laser systems across the world [15, 157], granting access to laser fields and electron energies suitable for high-field quantum electrodynamics (QED) experiments [99, 158]. This injection mechanism had been shown to reliably generate low relative energy-spread beams before this experimental campaign [65, 66]. Still, it had not at the time of the experiment been shown to produce beams greater than 1 GeV using this injection mechanism without using laser powers greater than 500 TW [100, 159]. Since this experiment, a publication has shown near-GeV electron beams using shock injection and an acceleration distance of 6 mm [101]. This work had the unique quality of scanning the position of the shock front across the length of the accelerator, which led to observations of a decrease in beam energy, an increase in relative energy spread, and an increase in beam charge as the shock front progressed toward the center of the gas jet. The effect of the decrease in energy as the shock propagates fur-

ther into the length of the accelerator can be explained by a reduction in acceleration length due to the charge-injecting shock front moving closer to the rear of the accelerator. The increase in charge and relative energy spread of the beams may be explained by beam loading effects due to higher-density gas flows in the shock front as the blade interacts with more central bulk flows of the accelerator. However, the driving pulse's evolution into the accelerator, as the shock front is moving longitudinally with respect to the laser's focal plane, may also influence this. Explaining the increase in charge and relative energy spread would benefit from work to investigate pulse evolution effects in this accelerator system via PIC simulations.

Another experiment in Chapter 5 focused on developing laser wakefield acceleration as an alternative accelerator technology measured the betatron radiation output from an LWFA beam as the accelerator's driver pulse propagated across a controlled transverse density profile to reconstruct the energy growth of the accelerated beam. This novel diagnostic technique to measure temporally-resolved energies of electron beams from a LWFA accelerator is the first of its kind to resolve on-shot energy growth of these beams from their betatron emission. The diagnostic mechanism is summarized: a transverse density gradient in the profile of the gas target induced a pulse-front tilt on the driving beam, which resulted in the driving pulse 'turning' toward the low-density side of the gradient. This parabolic transverse trajectory generated an angular pointing-to-longitudinal position correlation in the accelerator. This was taken advantage of by measuring the spectrum of the betatron radiation, which is emitted on-axis and has a photon critical energy that depends on the electrons' energy. A combination of an X-ray CCD and a stack filter resolved the angularly resolved betatron beam critical energy, yielding a longitudinally resolved measurement of electron energies in the accelerator. This diagnostic technique may be important for future LWFA facilities, which are increasingly moving toward using on-shot diagnostics as feedback controls of the laser and targets to optimize experimental parameters similar to automated controls which have already begun to be implemented in laser systems [160]. The method is presented as a general diagnostic to experiments where on-shot energy growth measurements would be helpful to, for example, optimize the acceleration length for a given accelerator target to maximize the energy gain and have

electrons exit the accelerator before dephasing takes place, reducing the energy in charge within the LWFA beam.

This thesis also presented the application of electron beams from a LWFA accelerator in studies of interactions of relativistic electron beams with matter. Chapter 6 focuses on measurements of the current filamentation instability. This experiment scanned a wide space of length and background plasma in an independently controlled filamentation plasma species. This naturally occurring astrophysical instability results in high-current-density filaments forming in relativistic beams traveling through a background plasma. Beyond the academic interest in studying this phenomenon in the context of astrophysical plasmas as the origin of gamma-ray bursts [124, 125], this instability is also important to understand as a mechanism for energy absorption and transport in the high-density, high-temperature compressed plasmas of inertial confinement fusion experiments [122, 123]. We observed filamentation that, by and large, followed expected trends in the instability via several indirect measurements of the beam after filamentation occurred. There was a notable statistical fluctuation, particularly in the high expected growth-rate extreme of the dataset. PIC simulations were conducted to show the growth of filamentation using beam and plasma parameters similar to those used in the experiment.

Chapter 7 discusses an experiment that produced low-emittance, relativistic positron beams through the interaction of LWFA accelerated electron beams and a high-Z target. The thickness of the converter target was scanned, and the production of electron/positron beams was measured in agreement with the theory for the two-step bremsstrahlung-induced Bethe Heitler process. Measurements of the emittance of the positrons after angular discrimination and energy selection showed a population of $N_+ > 10^5$ positrons in a 5% bandwidth around 500 MeV which had a measured normalized emittance inferred from Monte Carlo simulations to be 18 μm at the converter target. While this is relatively little charge in these beams compared to the $\sim$nC-scale positron beams produced at, for example, SLAC's FACET-II beamline, the charge of the positron beams should scale favorably from an LWFA source by both minimizing the source size & drift distance of the primary electron beam into the high-Z converter target, and also with increasing laser driver

energy, as can be reached at many modern high-intensity laser facilities. PIC simulations showed a successful injection of positron beams similar to those measured in this campaign being successfully injected into a wakefield accelerator. This work is significant, as the need for more sources of high-fidelity positron beams suitable for injection into a plasma accelerator has hampered the progress of experimental campaigns on the topic. This experiment demonstrates the ability of high-power laser facilities to operate as positron sources in the future.

In conclusion, experiments were conducted that demonstrated optimization and developments in laser wakefield acceleration as an alternative accelerator technology for electron beams. As this technology matures, the prospect of using it to answer fundamental questions regarding interactions involving high-energy electron beams becomes increasingly feasible for a wide range of studies, such as those presented on the current filamentation instability's growth in relativistic electron beams or the generation of low-emittance energy-selectable positron beams.

8.2 Challenges

Anyone who has spent time conducting research in a laboratory (particularly one utilizing high-power lasers to study plasmas) can attest that no experiment is without its challenges. Regarding the shock injection project, setting up a CFD fluid simulation that was stable enough to simulate the shock formation from a supersonic jet injecting gas into a vacuum environment with a blade object in the fluid's path was a particular challenge. This is a mixture of several difficult aspects for fluid simulations to resolve: high-pressure inlet in a vacuum with supersonic flows consisting of shock fronts. This was overcome by reducing the complexity of the turbulence model used in the simulations, employing dynamic load balancing to the simulation grid, and running the simulations with fine temporal resolution.

The current filamentation instability experiment experienced consistency issues with the laser accelerator source, resulting in an appreciable pointing jitter. This made collecting a measurable signal in the electron spectrometer with a narrow angular aperture extremely inconsistent. We

removed the aperture from the magnets for most of the data runs. While this increased the consistency of charge landing on the ESPEC screen, it also increased the error of the energy measurement due to the beam's angular divergence. A shot-to-shot pointing correlation was used to generate an energy dispersion curve for particles landing on the spectrometer screen for each shot. As well for this project there was the issue that for the 4 gasses scanned in the filamentation cell, 3 were likely not uniformly ionized for the extent of the length scans of those gasses. A future similar experiment could take place with a combination of an increase in laser power and a reduction in distance between the accelerator gas cell and filamentation gas cell to ensure maximized laser power propagating through the filamentation gas cell to ensure uniform ionization of the filamentation gas species.

The positron generation project produced interesting magnetic focusing artifacts in the electron beam profiles, as shown in Figure 7.4. In the end, the analysis of the emittance diagnostic was simple enough to transform the images for LE1 and LP1. However, there was an interesting 'bow-tie'-like focusing feature on the screen that captured positrons after the energy electron process. Figure 8.1 shows the results from numerical simulations which confirmed the suspicions that these beam structures were due to focusing from the dipole fields in the post-energy selection chicane. The focusing properties of dipole arrangements should be carefully considered in future experiments, with 3D particle tracking necessary to understand these artifacts, as developed as part of this dissertation work.

8.3 Future prospects

The future of laser wakefield acceleration as an accelerator technology is exciting, especially in the setting in which this work is being written at the University of Michigan as the ZEUS laser prepares for commissioning shots on its high-power target area [15]. Optimizations in the energy and emittance qualities of this technology bring us closer to the use of laser wakefield accelerators to be used, for example, as injection sources of particles to FEL light sources [161, 162], or

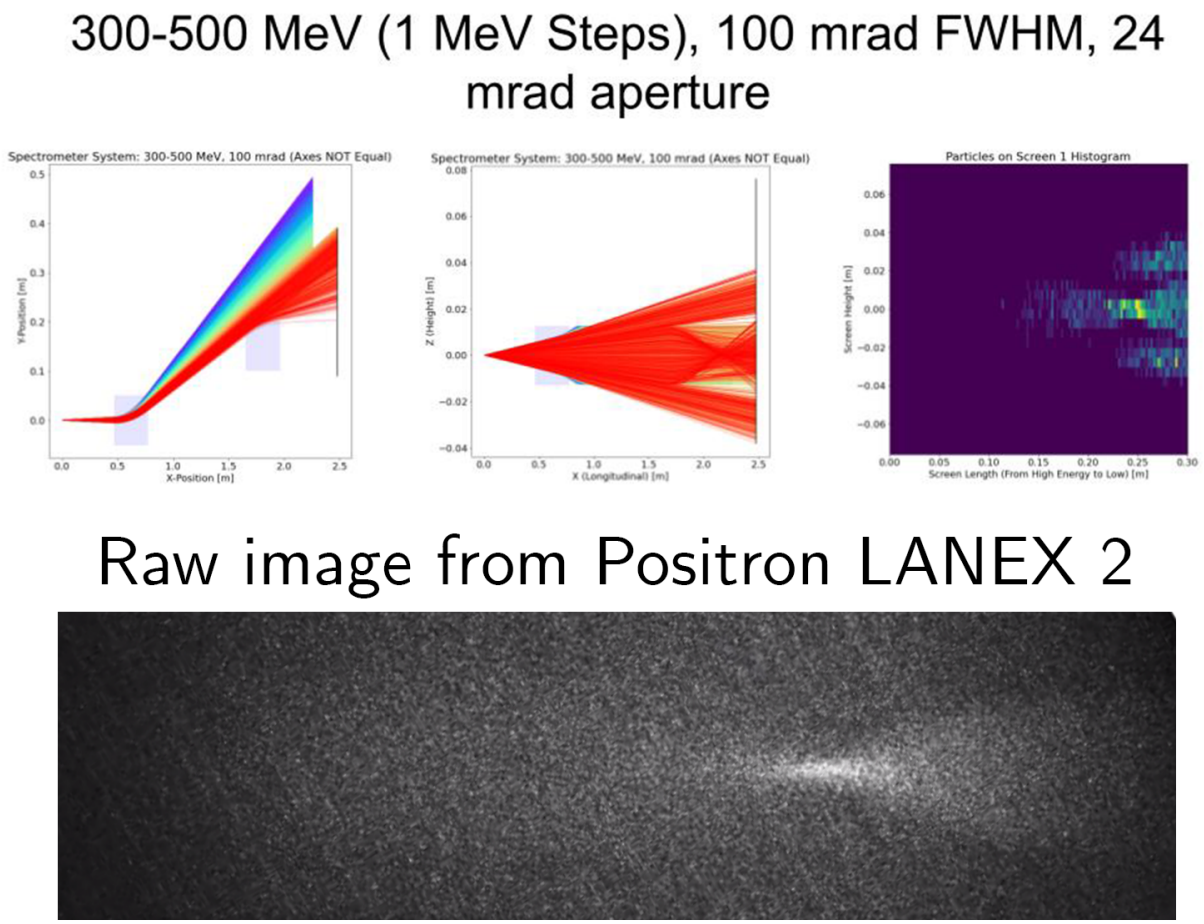


Figure 8.1: Example of magnetic focusing experienced by energy-selected positron beams (bottom) diagnosed through numerically stepping particles with parameters consisting of a Gaussian spread of angular distribution from on-axis to 24 mrad through an analytic model of dipole fields similar to those used in the experiment (top).

for synchrotron storage rings [163–165]. Extensions of using these sources of relativistic electron beams have been suggested for generating muons via interactions with a high-Z target in a manner similar to that which the positron generation project in this thesis described; however, the energies desired for that application extend into the $E > 10$ GeV [166, 167]. This energy level is conveniently in the range of the expected design parameters of electron beams that can be produced at the ZEUS facility's high-peak power target area. As these high-power LWFA facilities turn their attention increasingly towards experiments measuring QED effects in relativistic electron beams, these types of experiments generally benefit from the increases in spectral quality (high energy

with low relative energy spreads), in understanding the effects of beam profile uniformity and, potentially, low-divergence relativistic positron beams that are discussed in this thesis.

With the rejuvenated interest in internal confinement in general from the modern breakthroughs in reaching record-breaking yields of greater than unity [20], there may be an increased interest in "fast ignition" schemes, which involve relativistic electron currents to heat the compressed fuel. Instabilities such as current filamentation and other Weibel-like instabilities have been known for decades to be a source of energy loss [122, 123, 168]. Experiments extending on the work in this dissertation making use of LWFA and the ability to isolate the instability, for example, at higher density should be of interest.

APPENDIX A

Linear Growth Rate for the Filamentation of Warm Ultrarelativistic Beams

We consider the case of an infinite length, ultrarelativistic ($\gamma_b \gg 1$) charged particle beam of charge q_s and mass m_s propagating in the $\hat{\mathbf{z}}$ direction (i.e. no gradients in z) through either a second, counterstreaming beam with a neutralizing ion background (the idealized current filamentation case) or a uniform plasma of initial number density n_0, similar to the experimental case. To generalize this situation, we consider two species labeled s, having an isothermal transverse pressure $\frac{1}{2}m_s n_s \gamma_s^2 v_{th,s\perp}^2$. The ultrarelativistic beam allows us to make the paraxial approximation that the transverse motion is non-relativistic ($d(\gamma_s \mathbf{v}_{s\perp})/dt \simeq \gamma d\mathbf{v}_{s\perp}/dt$), and we assume the plasma motion is nonrelativistic, yielding the following system of linearized fluid equations for the electron species s,

$$\frac{\partial \delta n_s}{\partial t} + n_s \nabla_\perp \cdot \delta \mathbf{v}_{s\perp} = 0 \ , \tag{A.1}$$

$$\frac{\partial \delta \mathbf{v}_{s\perp}}{\partial t} \simeq -\frac{q_s}{\gamma_s m_s} \nabla_\perp \psi_s - \frac{1}{2}\gamma_s v_{th,s\perp}^2 \nabla_\perp \delta n_s \ , \tag{A.2}$$

and conservation of longitudinal canonical momentum

$$\delta v_{s\parallel} \simeq -\frac{q_s \delta A_z}{\gamma_s m_s} \ , \tag{A.3}$$

where $\perp$ and $\parallel$ indicate components perpendicular or parallel to z, respectively, n_s is the initial (unperturbed) density of the species s, the pseudopotential $\psi_s = \phi - A_z v_{s\parallel}$ with ϕ and A_z the

scalar and z-component of the vector potentials expressed in the Lorenz gauge, respectively, which may be combined into a single wave equation for ψ_s

$$-\left(\frac{\partial^2}{\partial t^2}-c^2\nabla_\perp^2\right)\psi_s=\frac{c^2}{\varepsilon_0}\left[\sum_{s'}q_{s'}(n_{s'}+\delta n_{s'})-\rho_n-\frac{v_{s\parallel}}{c^2}\sum_{s'}j_{s'\parallel}\right]\ ,$$

where ρ_n is a background (partially) neutralizing charge density. $\delta A_z=A_z-A_{z0}$ where A_{z0} is the initial z component of the vector potential. Using $j_{s\parallel}=q_s(n_s v_{s\parallel}+n_s\delta v_{s\parallel}+\delta n_s v_{s\parallel})$, we obtain

$$\left(\frac{\partial^2}{\partial(ct)^2}-\nabla_\perp^2\right)\psi_s=\frac{1}{\varepsilon_0}\left[\rho_0+\frac{j_0 v_{s\parallel}}{c^2}-\sum_{s'}q_{s'}\delta n_{s'}\left(1-\beta_{s\parallel}\beta_{s'\parallel}\right)\right]+\frac{\omega_p^2\beta_{s\parallel}}{c}\delta A_z\ , \qquad \text{(A.4)}$$

where $\beta_{s\parallel}=v_{s\parallel}/c$, $j_0=\sum_s q_s n_s v_{s\parallel}$ is the initial current density and $\rho_0=\rho_n-\sum_s q_s n_s$ is the initial free charge. Note that the Lorentz factors γ_s are absorbed into the definition of the plasma frequency $\omega_p^2=\sum_s\omega_{ps}^2=\sum_s q_s^2 n_s/\gamma_s m_s$. Taking the divergence of Eqn. A.2 and substituting for n_{s0} times Eqn. A.1, we obtain

$$\left(\frac{\partial^2}{\partial t^2}-\frac{1}{2}\gamma_s v_{th,s\perp}^2\nabla_\perp^2\right)\delta n_s=\frac{q_s n_s}{\gamma_s m_e}\nabla_\perp^2\psi_s\ ,$$

which may be Laplace transformed in time for conjugate variable ω and Fourier transformed in space for $\mathbf{k}_\perp$ and substituted for δn_s in Eqn. A.4, assuming that we neglect the transients arising from the Laplace transform (i.e. $\mathcal{L}(\partial\delta n/\partial t)=-i\omega\delta n(\omega)+\delta n(t=0)\approx -i\omega\delta n$), resulting in

$$-\left(\frac{\omega^2}{c^2}-k_\perp^2\right)\psi_s=\frac{\rho_0 c+j_0\beta_0}{\varepsilon_0 c}+\sum_{s'}\left(1-\beta_{s'\parallel}\beta_{s\parallel}\right)\frac{\omega_{ps'}^2}{\Omega_s^2}\nabla_\perp^2\psi_{s'}+\frac{\omega_p^2\beta_{s\parallel}}{c}\delta A_z\ , \qquad \text{(A.5)}$$

where $\Omega_s^2 = \omega^2 - \frac{1}{2}\gamma_s k_\perp^2 v_{th,s\perp}^2$. It is convenient to study the combinations of potentials $\psi_\pm = (\psi_1 \pm \psi_2)/2$, which leads to

$$\left(k_\perp^2 - \frac{\omega^2}{c^2}\right)\psi_+ = \frac{\rho_0 c + j_0\beta_0}{\varepsilon_0 c} + k_\perp^2\left(\sum_s \frac{\omega_{ps}^2}{\Omega_s^2}\psi_+ + \triangle_s \frac{\omega_{ps}^2}{\Omega_s^2}\psi_-\right) + \frac{\omega_p^2\beta_0}{c}\delta A_z \tag{A.6}$$

$$- \beta_0 k_\perp^2\left[\sum_s \frac{\omega_{ps}^2}{\Omega_s^2}\beta_{s\parallel}\psi_+ + \triangle_s \frac{\omega_{ps}^2}{\Omega_s^2}\beta_{s\parallel}\psi_-\right] \tag{A.7}$$

and

$$\left(k_\perp^2 - \frac{\omega^2}{c^2}\right)\psi_- = -\Delta\beta k_\perp^2\left[\sum_s \frac{\omega_{ps}^2}{\Omega_s^2}\beta_{s\parallel}\psi_+ + \triangle_s \frac{\omega_{ps}^2}{\Omega_s^2}\beta_{s\parallel}\psi_-\right] + \frac{\omega_p^2\Delta\beta}{c}\delta A_z\ , \tag{A.8}$$

where $\beta_0 = (\beta_1 + \beta_2)/2$ is the mean velocity of the species, $\Delta\beta = (\beta_1 - \beta_2)/2$ is the velocity difference and $\triangle_s$ is an operator that takes the difference, i.e. $\triangle_s x_s = x_1 - x_2$. Note that $\psi_+ = \phi - A_z c\beta_0$ is the pseudopotential associated with the average velocity and $\psi_- = -A_z c\Delta\beta$ means the ψ_- is a magnetic mode. In general, these present complicated mixed modes of ψ_+ and ψ_-, but we may study some special cases.

For two equal density ($\Delta\omega_p^2 = 0$, $\omega_{p1} = \omega_{p2} = \omega_b$), velocity ($\beta_0 = 0$, $\Delta\beta = \beta_b$) and transverse temperature ($\Omega_s^2 = \Omega^2 = \omega^2 - \frac{1}{2}\gamma_b k_\perp^2 v_{th\perp}^2$) colliding neutralized beams, with $A_{z0} = 0$, $j_0 = 0$ and $\rho_0 = 0$, these equations reduce to the independent modes

$$\left(k_\perp^2 - \frac{\omega^2}{c^2}\right)\psi_+ = \frac{\omega_p^2}{\Omega^2}k_\perp^2\psi_+ \tag{A.9}$$

and

$$\left(k_\perp^2 - \frac{\omega^2}{c^2}\right)\psi_- = -\beta_b^2\frac{\omega_b^2}{\Omega^2}k_\perp^2\psi_- - \frac{\omega_p^2}{c^2}\psi_-\ , \tag{A.10}$$

leading to the dispersion relations

$$1 - \frac{\omega_+^2}{k_\perp^2 c^2} = \frac{\omega_p^2}{\omega_+^2 - \frac{1}{2}\gamma_b k_\perp^2 v_{th\perp}^2}\ , \tag{A.11}$$

and

$$1 - \frac{(\omega_-^2 - \omega_p^2)}{k_\perp^2 c^2} = -\beta_b^2 \frac{\omega_b^2}{\omega_-^2 - \frac{1}{2}\gamma_b k_\perp^2 v_{th\perp}^2} \ . \tag{A.12}$$

For short wavelength perturbations $\omega_\pm^2 \ll k_\perp^2 c^2$ (recall that the Lorentz factor is absorbed in the plasma frequency so $k_\perp$ can still correspond to long wavelengths relative to the plasma skin depth), the dispersion relations reduce to

$$\omega_+^2 \simeq \omega_p^2 + \frac{1}{2}\gamma_b k_\perp^2 v_{th\perp}^2 \ , \tag{A.13}$$

and

$$\omega_- \simeq \pm i\beta_b \omega_b \sqrt{1 - \frac{\gamma_b k_\perp^2 v_{th\perp}^2}{2\beta_b^2 \omega_b^2}} \ , \tag{A.14}$$

i.e. for zero initial thermal spread the two modes are plasma oscillations at frequency ω_p and growth of waves with a rate $\Gamma = \beta_b \omega_b$, see also [70].

For a single electron beam with frequency ω_b propagating into a plasma with frequency $\omega_{p0} \approx \omega_p$, the initial charge and current densities are non-zero, which would cause issues with the analysis, including physically the fact that overall pinching of the whole beam can occur. As three dimensional simulations show, however, the background plasma response is on a much faster timescale than the beam responds to fields and it therefore acts to generate a return current and shield the bare charge of the beam to neutralize both the beam's current and charge, meaning $\rho \to 0$, $j_0 \to 0$. Hence, assuming that ρ_0 and j_0 are zero and further that $\sum_s \omega_{ps}^2/\Omega_s^2 \beta_{s\|} \approx 0$ and therefore $\bigtriangleup_s \omega_{ps}^2/\Omega_s^2 \beta_{s\|} \approx 2\omega_b^2/\Omega_b^2 \beta_b$, for a single electron beam the dispersion relation involving ψ_+ is still somewhat complex and coupled to ψ_-, but Eqn.A.8 for the (growing) mode ψ_- reduces to

$$k_\perp^2 - \frac{\omega_-^2}{c^2} = -\beta_b^2 k_\perp^2 \left[\frac{\omega_b^2}{\omega_-^2 - \frac{1}{2}\gamma_b k_\perp^2 v_{th\perp}^2}\right] - \frac{\omega_p^2}{c^2} \ , \tag{A.15}$$

which for $v_{th}^2 \to 0$ is similar to Eqn. 8 in Ref. [71] (note that the sign on the last term is incorrect). Again, in the limit that $\omega_-^2/k_\perp^2 c^2 \ll 1$ (but this time we should not neglect the term $\omega_p^2/k_\perp^2 c^2$ as the

contribution from the plasma is not suppressed by a factor γ), this reduces to

$$\Gamma \simeq \sqrt{\frac{\beta_b^2 \omega_b^2}{1 + \frac{\omega_p^2}{k_\perp^2 c^2}} - \frac{1}{2}\gamma_b k_\perp^2 v_{th\perp}^2} \; . \tag{A.16}$$

For $v_{th\perp}^2 \to 0$, this expression reduces to the growth rate for a cold, weak beam [72]. Eqn. A.16 shows that the current filamentation instability growth rate is suppressed for wavenumbers that are small compared with ω_p/c.

APPENDIX B

Current Filamentation Instability: Electron Transverse Profile Examples

This section provides examples of sequential on / off (concerning the filamentation gas cell's inlet gas supply) shots to qualitatively compare the structured filamented beams to their local reference shots that did not travel through the filamentation cell plasma. Figure B.1 displays sample shots for the shortest filamentation gas cell, Figure B.2 for the intermediate filamentation gas cell, and Figure B.3 for the longest filamentation gas cell. The length and density of the filamentation gas cell are displayed above each on / off pair. Given the large size of these images, they begin on the following page.

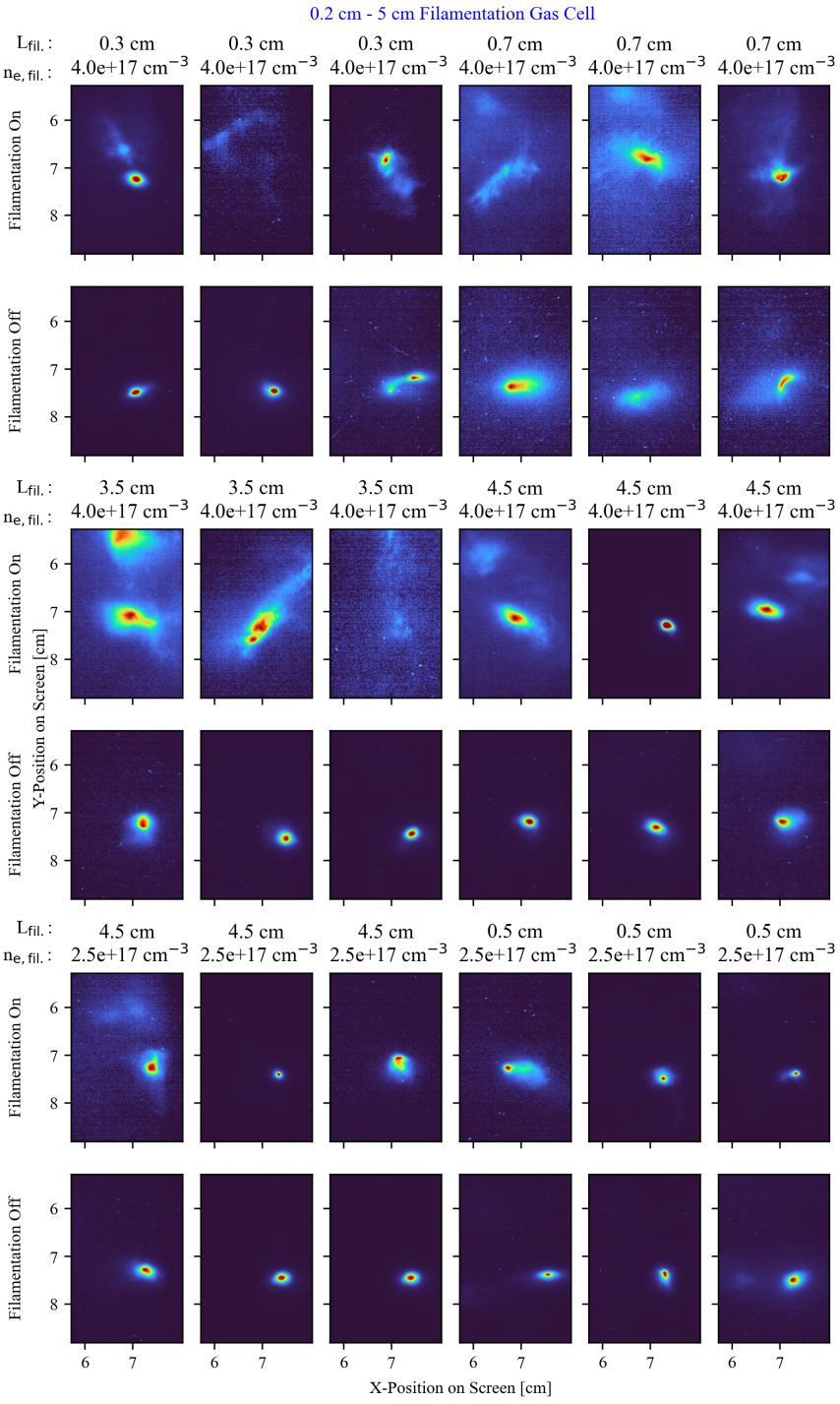


Figure B.1: Sequential filamentation gas cell on / off shots to compare the structured beams due to the filamentation cell compared to local reference shots for the shortest-length filamentation cell. Each image's color scale is normalized minimum and maximum range in pixel intensity values of that image.

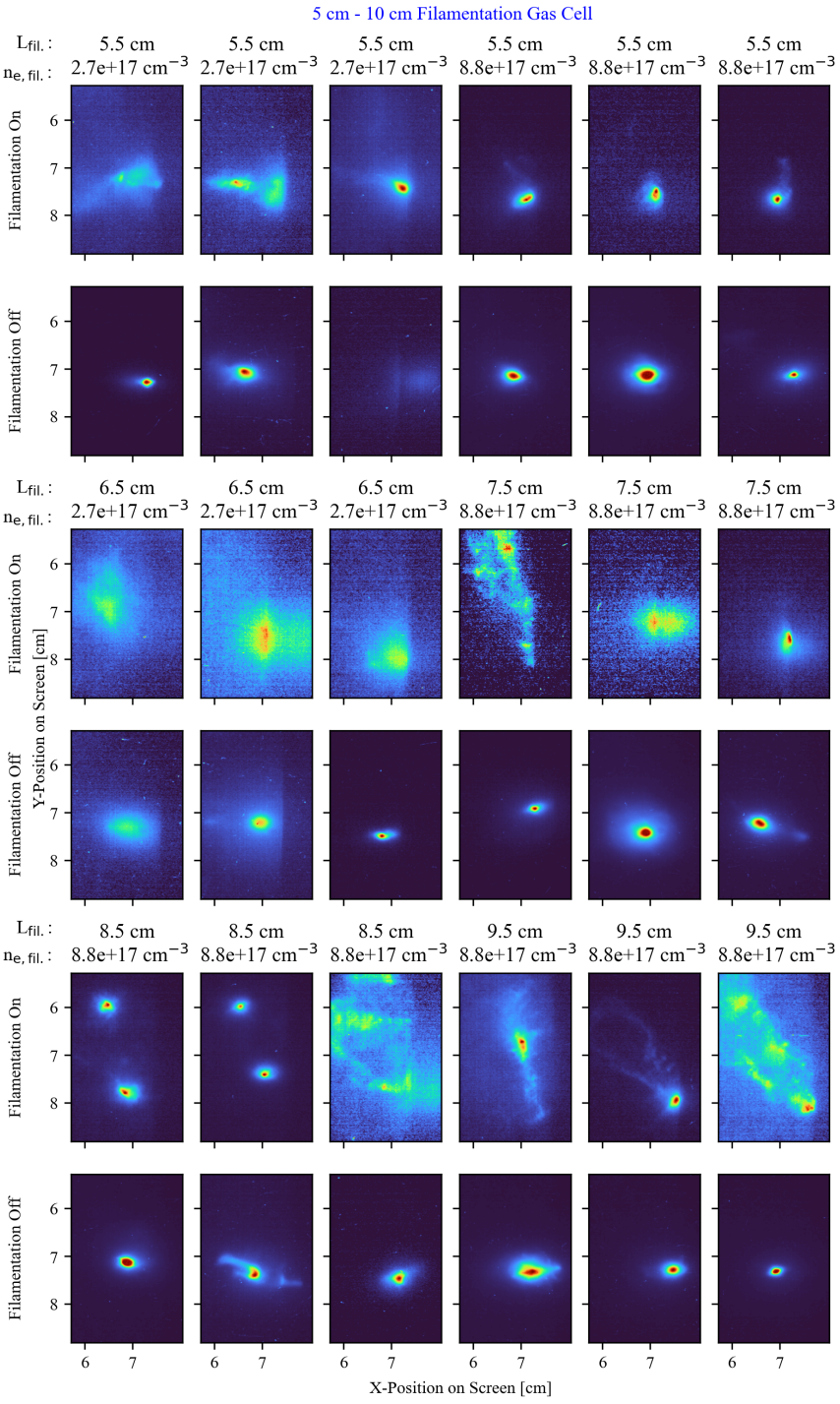


Figure B.2: Sequential filamentation gas cell on / off shots to compare the structured beams due to the filamentation cell compared to local reference shots for the intermediate-length filamentation cell. Each image's color scale is normalized minimum and maximum range in pixel intensity values of that image.

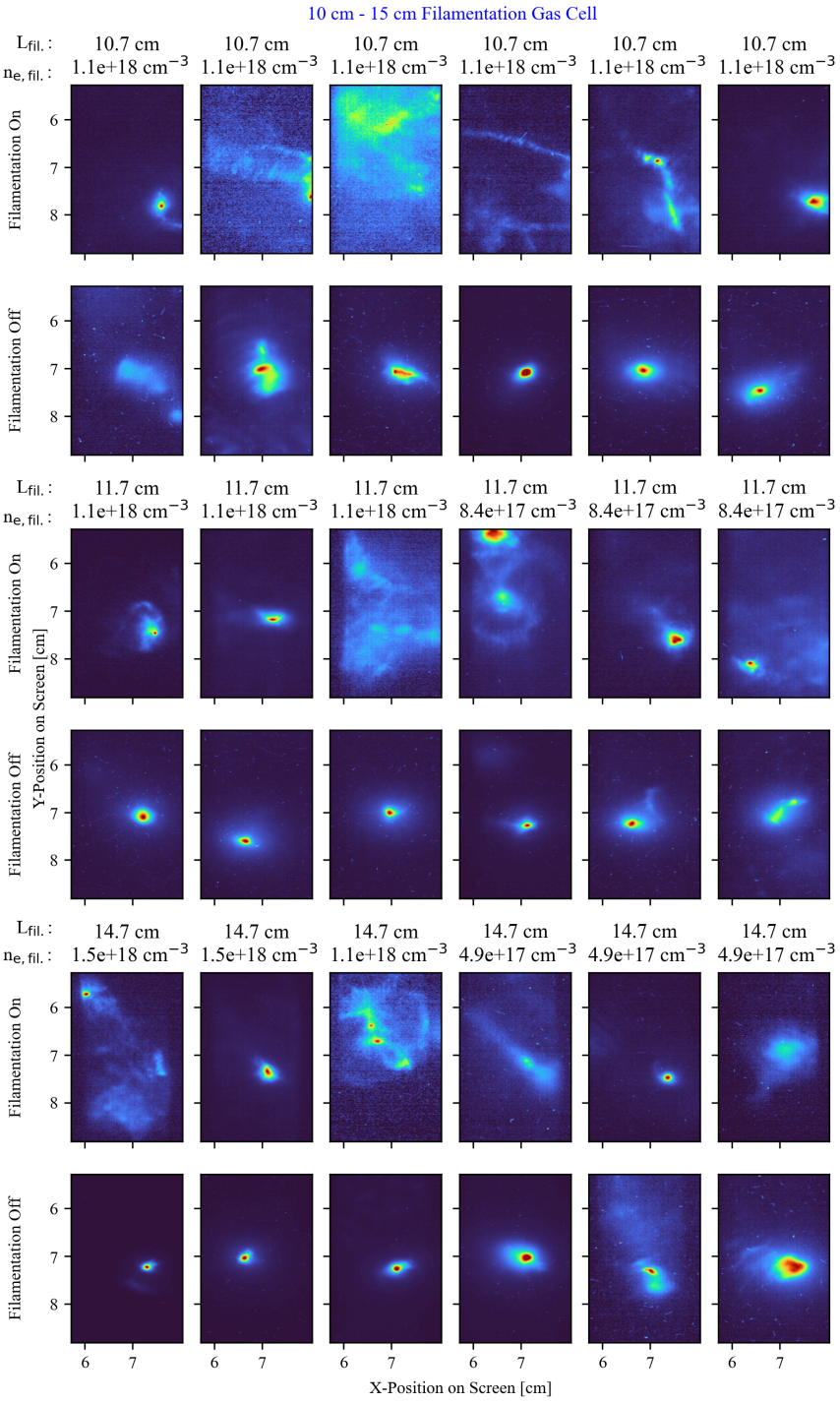


Figure B.3: Sequential filamentation gas cell on / off shots to compare the structured beams due to the filamentation cell compared to local reference shots for the longest-length filamentation cell. Each image's color scale is normalized minimum and maximum range in pixel intensity values of that image.

APPENDIX C

Characterization of Shock-Front Inducing Razor Blade

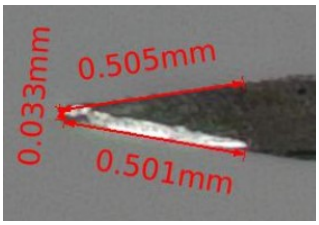


Figure C.1: Physical measurements of the beveled region of the blade that was utilized in the shock injection experiment which produced high-energy ($E > 1$ GeV), monoenergetic ($\Delta E < 10\%$) electron beams from a moderate-power ($P_L < 200$ TW) LWFA driver. The angles between the horizontal bulk blade body and the angled portion that leads to the knife edge are measured to be approximately 172° on the top surface of the blade and 168° on the bottom of the blade.

BIBLIOGRAPHY

[1] R. B. Neal. The Stanford Two-Mile Linear Electron Accelerator. Journal of Vacuum Science and Technology, 2(3):149–159, 5 1965.

[2] S. Döbert, C. Adolphsen, G. Bowden, D. Burke, J. Chan, V. Dolgashev, J. Frisch, K. Jobe, R. Jones, J. Lewandowski, R. Kirby, Z. Li, D. McCormick, R. Miller, C. Nantista, J. Nelson, C. Pearson, M. Ross, D. Schultz, T. Smith, S. Tantawi, J. Wang, T. Arkan, C. Boffo, H. Carter, I. Gonin, T. Khabiboulline, S. Mishra, G. Romanov, N. Solyak, Y. Funahashi, H. Hayano, N. Higashi, Y. Higashi, T. Higo, H. Kawamata, T. Kume, Y. Morozumi, K. Takata, T. Takatomi, N. Toge, K. Ueno, and Y. Watanabe. High gradient performance of NLC/GLC X-band accelerating structures. In Proceedings of the IEEE Particle Accelerator Conference, volume 2005, pages 372–374. IEEE, 2005.

[3] M Aicheler, P Burrows, M Draper, T Garvey, P Lebrun, K Peach, N Phinney, H Schmickler, D Schulte, and N Toge. A Multi-TeV Linear Collider Based on CLIC Technology. Technical report, SLAC National Accelerator Laboratory (SLAC), Menlo Park, CA (United States), 2 2012.

[4] G. Arduini, R. Assmann, R. Bailey, A. Butterworth, P. Collier, K. Cornelis, S. Fartoukh, M. Lamont, G. Morpurgo, G. Roy, J. Wenninger, and T. Wijnands. Electron-positron collisions at 209 GeV in LEP. In Proceedings of the IEEE Particle Accelerator Conference, volume 1, pages 356–358. IEEE, 2001.

[5] D. W. Kerst, G. D. Adams, H. W. Koch, and C. S. Robinson. Operation of a 300-Mev Betatron. Physical Review, 78(3):297–297, 5 1950.

[6] R W Aßmann. Lep Operation and Performance With Electron-Positron Collisions At 209 Gev. Proceedings of the LHC Workshop, Chamonix, July:323, 2001.

[7] J. B. Rosenzweig, D. B. Cline, B. Cole, H. Figueroa, W. Gai, R. Konecny, J. Norem, P. Schoessow, and J. Simpson. Experimental observation of plasma wake-field acceleration. Physical Review Letters, 61(1):98–101, 7 1988.

[8] A. Ting, C. I. Moore, K. Krushelnick, C. Manka, E. Esarey, P. Sprangle, R. Hubbard, H. R. Burris, R. Fischer, and M. Baine. Plasma wakefield generation and electron acceleration in a self-modulated laser wakefield accelerator experiment. Physics of Plasmas, 4(5 /2):1889–1899, 5 1997.

[9] E. Gschwendtner, M. Turner, E. Adli, A. Ahuja, O. Apsimon, R. Apsimon, A. M. Bachmann, F. Batsch, C. Bracco, F. Braunmüller, S. Burger, G. Burt, B. Buttenschön, A. Caldwell, J. Chappell, E. Chevallay, M. Chung, D. Cooke, H. Damerau, L. H. Deubner, A. Dexter, S. Doebert, J. Farmer, V. N. Fedosseev, R. Fiorito, R. A. Fonseca1, F. Friebel, L. Garolfi, S. Gessner, B. Goddard, I. Gorgisyan, A. A. Gorn, E. Granados, O. Grulke, A. Hartin, A. Helm, J. R. Henderson, M. Hüther, M. Ibison, S. Jolly, F. Keeble, M. D. Kelisani, S. Y. Kim, F. Kraus, M. Krupa, T. Lefevre, Y. Li, S. Liu, N. Lopes, K. V. Lotov, M. Martyanov, S. Mazzoni, V. A. Minakov, J. C. Molendijk, J. T. Moody, M. Moreira, P. Muggli, H. Panuganti, A. Pardons, F. Peña Asmus, A. Perera, A. Petrenko, A. Pukhov, S. Rey, P. Sherwood, L. O. Silva, A. P. Sosedkin, P. V. Tuev, F. Velotti, L. Verra, V. A. Verzilov, J. Vieira, C. P. Welsch, M. Wendt, B. Williamson, M. Wing, B. Woolley, and G. Xia. Proton-driven plasma wakefield acceleration in AWAKE. Philosophical Transactions of the Royal Society A: Mathematical, Physical and Engineering Sciences, 377(2151), 8 2019.

[10] T. Tajima and J. M. Dawson. Laser electron accelerator. Physical Review Letters, 43(4):267–270, 1979.

[11] Donna Strickland and Gerard Mourou. Compression of amplified chirped optical pulses. Optics Communications, 55(6):447–449, 10 1985.

[12] S. P.D. Mangles, C. D. Murphy, Z. Najmudin, A. G.R. Thomas, J. L. Collier, A. E. Dangor, E. J. Divall, P. S. Foster, J. G. Gallacher, C. J. Hooker, D. A. Jaroszynski, A. J. Langley, W. B. Mori, P. A. Norreys, F. S. Tsung, R. Viskup, B. R. Walton, and K. Krushelnick. Monoenergetic beams of relativistic electrons from intense laser-plasma interactions. Nature, 431(7008):535–538, 9 2004.

[13] J. Faure, Y. Glinec, A. Pukhov, S. Kiselev, S. Gordienko, E. Lefebvre, J.-P. Rousseau, F. Burgy, and V. Malka. A laser–plasma accelerator producing monoenergetic electron beams. Nature, 431(7008):541–544, 9 2004.

[14] C. G. R. Geddes, Cs. Toth, J. van Tilborg, E. Esarey, C. B. Schroeder, D. Bruhwiler, C. Nieter, J. Cary, and W. P. Leemans. High-quality electron beams from a laser wakefield accelerator using plasma-channel guiding. Nature, 431(7008):538–541, 9 2004.

[15] J Nees, A Maksimchuk, G Kalinchenko, B Hou, Y Ma, P Campbell, A McKelvey, L Willingale, I Jovanovic, C Kuranz, A Thomas, and K Krushelnick. ZEUS: A National Science Foundation Mid-Scale Facility for Laser-Driven Science in the QED Regime. In 2020 Conference on Lasers and Electro-Optics (CLEO). IEEE, 2020.

[16] L. Willingale, S. P. D. Mangles, P. M. Nilson, R. J. Clarke, A. E. Dangor, M. C. Kaluza, S. Karsch, K. L. Lancaster, W. B. Mori, Z. Najmudin, J. Schreiber, A. G. R. Thomas, M. S. Wei, and K. Krushelnick. Collimated Multi-MeV Ion Beams from High-Intensity Laser Interactions with Underdense Plasma. Physical Review Letters, 96(24):245002, 6 2006.

[17] A. Maksimchuk, S. Gu, K. Flippo, D. Umstadter, and V. Yu. Bychenkov. Forward Ion Acceleration in Thin Films Driven by a High-Intensity Laser. Physical Review Letters, 84(18):4108–4111, 5 2000.

[18] B. Dromey, M. Zepf, A. Gopal, K. Lancaster, M. S. Wei, K. Krushelnick, M. Tatarakis, N. Vakakis, S. Moustaizis, R. Kodama, M. Tampo, C. Stoeckl, R. Clarke, H. Habara, D. Neely, S. Karsch, and P. Norreys. High harmonic generation in the relativistic limit. Nature Physics, 2(7):456–459, 7 2006.

[19] F. Dollar, P. Cummings, V. Chvykov, L. Willingale, M. Vargas, V. Yanovsky, C. Zulick, A. Maksimchuk, A. G. R. Thomas, and K. Krushelnick. Scaling High-Order Harmonic Generation from Laser-Solid Interactions to Ultrahigh Intensity. Physical Review Letters, 110(17):175002, 4 2013.

[20] H Abu-Shawareb, R Acree, P Adams, J Adams, B Addis, R Aden, P Adrian, B B Afeyan, M Aggleton, and L Aghaian. Achievement of target gain larger than unity in an inertial fusion experiment. Physical Review Letters, 132(6):065102, 2024.

[21] J. P. Palastro, J. L. Shaw, P. Franke, D. Ramsey, T. T. Simpson, and D. H. Froula. Dephasingless Laser Wakefield Acceleration. Physical Review Letters, 124(13):134802, 4 2020.

[22] Alaleh Ghasemi, Saeed Mirzanejhad, and Taghi Mohsenpour. Flying focus laser Wakefield scheme for efficient acceleration. Optik, 287:171117, 9 2023.

[23] W. Lu, M. Tzoufras, C. Joshi, F. S. Tsung, W. B. Mori, J. Vieira, R. A. Fonseca, and L. O. Silva. Generating multi-GeV electron bunches using single stage laser wakefield acceleration in a 3D nonlinear regime. Physical Review Special Topics - Accelerators and Beams, 10(6), 2007.

[24] E. Esarey, C. B. Schroeder, and W. P. Leemans. Physics of laser-driven plasma-based electron accelerators. Reviews of Modern Physics, 81(3):1229–1285, 2009.

[25] B. Rus, F. Batysta, J. Čáp, M. Divoký, M. Fibrich, M. Griffiths, R. Haley, T. Havlíček, M. Hlavác, J. Hřebíček, P. Homer, P. Hříbek, J. Jand'ourek, L. Juha, G. Korn, P. Korouš, M. Košelja, M. Kozlová, D. Kramer, M. Krůs, J. C. Lagron, J. Limpouch, L. MacFarlane, M. Malý, D. Margarone, P. Matlas, L. Mindl, J. Moravec, T. Mocek, J. Nejdl, J. Novák, V. Olšovcová, M. Palatka, J. P. Perin, M. Pešlo, J. Polan, J. Prokůpek, J. Řídký, K. Rohlena, V. Růžička, M. Sawicka, L. Scholzová, D. Snopek, P. Strkula, and L. Švéda. Outline of the ELI-Beamlines facility. Diode-Pumped High Energy and High Power Lasers; ELI: Ultrarelativistic Laser-Matter Interactions and Petawatt Photonics; and HiPER: the European Pathway to Laser Energy, 8080:808010, 6 2011.

[26] J. E. Shrock, B. Miao, L. Feder, and H. M. Milchberg. Meter-scale plasma waveguides for multi-GeV laser wakefield acceleration. Physics of Plasmas, 29(7):073101, 7 2022.

[27] S. Kuschel, M. B. Schwab, M. Yeung, D. Hollatz, A. Seidel, W. Ziegler, A. Sävert, M. C. Kaluza, and M. Zepf. Controlling the Self-Injection Threshold in Laser Wakefield Accelerators. Physical Review Letters, 121(15), 2018.

[28] C. M. Huntington, A. G.R. Thomas, C. McGuffey, T. Matsuoka, V. Chvykov, G. Kalintchenko, S. Kneip, Z. Najmudin, C. Palmer, V. Yanovsky, A. Maksimchuk, R. P. Drake, T. Katsouleas, and K. Krushelnick. Current filamentation instability in laser wakefield accelerators. Physical Review Letters, 106(10):105001, 3 2011.

[29] J. M. Cole, K. T. Behm, E. Gerstmayr, T. G. Blackburn, J. C. Wood, C. D. Baird, M. J. Duff, C. Harvey, A. Ilderton, A. S. Joglekar, K. Krushelnick, S. Kuschel, M. Marklund, P. McKenna, C. D. Murphy, K. Poder, C. P. Ridgers, G. M. Samarin, G. Sarri, D. R. Symes, A. G.R. Thomas, J. Warwick, M. Zepf, Z. Najmudin, and S. P.D. Mangles. Experimental Evidence of Radiation Reaction in the Collision of a High-Intensity Laser Pulse with a Laser-Wakefield Accelerated Electron Beam. Physical Review X, 8(1):011020, 2 2018.

[30] C. McGuffey, A. G. R. Thomas, W. Schumaker, T. Matsuoka, V. Chvykov, F. J. Dollar, G. Kalintchenko, V. Yanovsky, A. Maksimchuk, K. Krushelnick, V. Yu. Bychenkov, I. V. Glazyrin, and A. V. Karpeev. Ionization Induced Trapping in a Laser Wakefield Accelerator. Physical Review Letters, 104(2):025004, 1 2010.

[31] M. Hansson, B. Aurand, X. Davoine, H. Ekerfelt, K. Svensson, A. Persson, C. G. Wahlström, and O. Lundh. Down-ramp injection and independently controlled acceleration of electrons in a tailored laser wakefield accelerator. Physical Review Special Topics - Accelerators and Beams, 18(7):071303, 7 2015.

[32] K. Schmid, A. Buck, C. M.S. Sears, J. M. Mikhailova, R. Tautz, D. Herrmann, M. Geissler, F. Krausz, and L. Veisz. Density-transition based electron injector for laser driven wakefield accelerators. Physical Review Special Topics - Accelerators and Beams, 13(9):091301, 9 2010.

[33] B. Allen, V. Yakimenko, M. Babzien, M. Fedurin, K. Kusche, and P. Muggli. Experimental Study of Current Filamentation Instability. Physical Review Letters, 109(18):185007, 11 2012.

[34] S. Corde, E. Adli, J. M. Allen, W. An, C. I. Clarke, C. E. Clayton, J. P. Delahaye, J. Frederico, S. Gessner, S. Z. Green, M. J. Hogan, C. Joshi, N. Lipkowitz, M. Litos, W. Lu, K. A. Marsh, W. B. Mori, M. Schmeltz, N. Vafaei-Najafabadi, D. Walz, V. Yakimenko, and G. Yocky. Multi-gigaelectronvolt acceleration of positrons in a self-loaded plasma wakefield. Nature, 524(7566):442–445, 8 2015.

[35] Spencer Gessner, Erik Adli, James M. Allen, Weiming An, Christine I. Clarke, Chris E. Clayton, Sebastien Corde, J. P. Delahaye, Joel Frederico, Selina Z. Green, Carsten Hast, Mark J. Hogan, Chan Joshi, Carl A. Lindstrøm, Nate Lipkowitz, Michael Litos, Wei Lu, Kenneth A. Marsh, Warren B. Mori, Brendan O'Shea, Navid Vafaei-Najafabadi, Dieter Walz, Vitaly Yakimenko, and Gerald Yocky. Demonstration of a positron beam-driven hollow channel plasma wakefield accelerator. Nature Communications, 7(1):11785, 6 2016.

[36] A. Doche, C. Beekman, S. Corde, J. M. Allen, C. I. Clarke, J. Frederico, S. J. Gessner, S. Z. Green, M. J. Hogan, B. O'Shea, V. Yakimenko, W. An, C. E. Clayton, C. Joshi, K. A. Marsh, W. B. Mori, N. Vafaei-Najafabadi, M. D. Litos, E. Adli, C. A. Lindstrøm, and W. Lu. Acceleration of a trailing positron bunch in a plasma wakefield accelerator. Scientific Reports, 7(1):14180, 10 2017.

[37] Erik Adli. Plasma wakefield linear colliders—opportunities and challenges. Philosophical Transactions of the Royal Society A: Mathematical, Physical and Engineering Sciences, 377(2151):20180419, 8 2019.

[38] Gevy J. Cao, Carl A. Lindstrøm, Erik Adli, Sébastien Corde, and Spencer Gessner. Positron acceleration in plasma wakefields. Physical Review Accelerators and Beams, 27(3):034801, 3 2024.

[39] G. Sarri, K. Poder, J. M. Cole, W. Schumaker, A. Di Piazza, B. Reville, T. Dzelzainis, D. Doria, L. A. Gizzi, G. Grittani, S. Kar, C. H. Keitel, K. Krushelnick, S. Kuschel, S. P. D. Mangles, Z. Najmudin, N. Shukla, L. O. Silva, D. Symes, A. G. R. Thomas, M. Vargas, J. Vieira, and M. Zepf. Generation of neutral and high-density electron–positron pair plasmas in the laboratory. Nature Communications, 6(1):6747, 4 2015.

[40] W.B. Mori. The physics of the nonlinear optics of plasmas at relativistic intensities for short-pulse lasers. IEEE Journal of Quantum Electronics, 33(11):1942–1953, 1997.

[41] E. A. Startsev and C. J. McKinstrie. Multiple scale derivation of the relativistic ponderomotive force. Physical Review E, 55(6):7527–7535, 6 1997.

[42] Vachaspati. Harmonics in the Scattering of Light by Free Electrons. Physical Review, 128(2):664–666, 10 1962.

[43] Lowell S. Brown and T. W. B. Kibble. Interaction of Intense Laser Beams with Electrons. Physical Review, 133(3A):A705–A719, 2 1964.

[44] P Gibbon. Short Pulse Laser Interactions With Matter: An Introduction. World Scientific, 2005.

[45] Anthony E Siegman. Lasers. University science books, 1986.

[46] A G Litvak. Finite-amplitude wave beams in a magnetoactive plasma. Sov. Phys. JETP, 30(344):166, 1970.

[47] Claire Ellen Max, Jonathan Arons, and A. Bruce Langdon. Self-Modulation and Self-Focusing of Electromagnetic Waves in Plasmas. Physical Review Letters, 33(4):209–212, 7 1974.

[48] A. G. R. Thomas, Z. Najmudin, S. P. D. Mangles, C. D. Murphy, A. E. Dangor, C. Kamperidis, K. L. Lancaster, W. B. Mori, P. A. Norreys, W. Rozmus, and K. Krushelnick. Effect of Laser-Focusing Conditions on Propagation and Monoenergetic Electron Production in Laser-Wakefield Accelerators. Physical Review Letters, 98(9):095004, 3 2007.

[49] J. Faure, Y. Glinec, J. J. Santos, F. Ewald, J.-P. Rousseau, S. Kiselev, A. Pukhov, T. Hosokai, and V. Malka. Observation of Laser-Pulse Shortening in Nonlinear Plasma Waves. Physical Review Letters, 95(20):205003, 11 2005.

[50] R.T. Sandberg and A.G.R. Thomas. Photon Acceleration from Optical to XUV. Physical Review Letters, 130(8):085001, 2 2023.

[51] A. G. R. Thomas. Acceleration of Electrons in Plasma. arXiv, 7 2020.

[52] Johannes Wenz and Stefan Karsch. Physics of laser-wakefield accelerators (LWFA). arXiv preprint arXiv:2007.04622, 2020.

[53] W. Lu, C. Huang, M. Zhou, W. B. Mori, and T. Katsouleas. Nonlinear Theory for Relativistic Plasma Wakefields in the Blowout Regime. Physical Review Letters, 96(16):165002, 4 2006.

[54] S. Wilks, T. Katsouleas, J. M. Dawson, and J. J. Su. Beam Loading Efficiency in Plasma Accelerators. pages 100–102, 1987.

[55] M. Tzoufras, W. Lu, F. S. Tsung, C. Huang, W. B. Mori, T. Katsouleas, J. Vieira, R. A. Fonseca, and L. O. Silva. Beam loading in the nonlinear regime of plasma-based acceleration. Physical Review Letters, 101(14), 2008.

[56] S. P. D. Mangles, G. Genoud, M. S. Bloom, M. Burza, Z. Najmudin, A. Persson, K. Svensson, A. G. R. Thomas, and C.-G. Wahlström. Self-injection threshold in self-guided laser wakefield accelerators. Physical Review Special Topics - Accelerators and Beams, 15(1):011302, 1 2012.

[57] I. Kostyukov, E. Nerush, A. Pukhov, and V. Seredov. Electron Self-Injection in Multidimensional Relativistic-Plasma Wake Fields. Physical Review Letters, 103(17):175003, 10 2009.

[58] C. E. Clayton, J. E. Ralph, F. Albert, R. A. Fonseca, S. H. Glenzer, C. Joshi, W. Lu, K. A. Marsh, S. F. Martins, W. B. Mori, A. Pak, F. S. Tsung, B. B. Pollock, J. S. Ross, L. O. Silva, and D. H. Froula. Self-Guided Laser Wakefield Acceleration beyond 1 GeV Using Ionization-Induced Injection. Physical Review Letters, 105(10):105003, 9 2010.

[59] Min Chen, Zheng-Ming Sheng, Yan-Yun Ma, and Jie Zhang. Electron injection and trapping in a laser wakefield by field ionization to high-charge states of gases. Journal of Applied Physics, 99(5), 3 2006.

[60] A. Pak, K. A. Marsh, S. F. Martins, W. Lu, W. B. Mori, and C. Joshi. Injection and Trapping of Tunnel-Ionized Electrons into Laser-Produced Wakes. Physical Review Letters, 104(2):025003, 1 2010.

[61] M. Vargas, W. Schumaker, Z.-H. He, Z. Zhao, K. Behm, V. Chvykov, B. Hou, K. Krushelnick, A. Maksimchuk, V. Yanovsky, and A. G. R. Thomas. Improvements to laser wakefield accelerated electron beam stability, divergence, and energy spread using three-dimensional printed two-stage gas cell targets. Applied Physics Letters, 104(17), 4 2014.

[62] H. Suk, N. Barov, J. B. Rosenzweig, and E. Esarey. Plasma electron trapping and acceleration in a plasma wake field using a density transition. Physical Review Letters, 86(6):1011–1014, 2 2001.

[63] P. Tomassini, M. Galimberti, A. Giulietti, D. Giulietti, L. A. Gizzi, L. Labate, and F. Pegoraro. Production of high-quality electron beams in numerical experiments of laser wakefield acceleration with longitudinal wave breaking. Physical Review Special Topics - Accelerators and Beams, 6(12):121301, 12 2003.

[64] S. Kalmykov, S. A. Yi, V. Khudik, and G. Shvets. Electron Self-Injection and Trapping into an Evolving Plasma Bubble. Physical Review Letters, 103(13):135004, 9 2009.

[65] A. Buck, J. Wenz, J. Xu, K. Khrennikov, K. Schmid, M. Heigoldt, J. M. Mikhailova, M. Geissler, B. Shen, F. Krausz, S. Karsch, and L. Veisz. Shock-front injector for high-quality laser-plasma acceleration. Physical Review Letters, 110(18):185006, 5 2013.

[66] S. Fourmaux, K. Ta Phuoc, P. Lassonde, S. Corde, G. Lebrun, V. Malka, A. Rousse, and J. C. Kieffer. Quasi-monoenergetic electron beams production in a sharp density transition. Applied Physics Letters, 101(11), 9 2012.

[67] S. Corde, K. Ta Phuoc, G. Lambert, R. Fitour, V. Malka, A. Rousse, A. Beck, and E. Lefebvre. Femtosecond x rays from laser-plasma accelerators. Reviews of Modern Physics, 85(1):1–48, 1 2013.

[68] D. A. G. Deacon, L. R. Elias, J. M. J. Madey, G. J. Ramian, H. A. Schwettman, and T. I. Smith. First Operation of a Free-Electron Laser. Physical Review Letters, 38(16):892–894, 4 1977.

[69] John David Jackson. Classical electrodynamics. John Wiley & Sons, 2021.

[70] F. Califano, R. Prandi, F. Pegoraro, and S. V. Bulanov. Nonlinear filamentation instability driven by an inhomogeneous current in a collisionless plasma. Physical Review E - Statistical Physics, Plasmas, Fluids, and Related Interdisciplinary Topics, 58(6):7837–7845, 12 1998.

[71] Burton D Fried. Mechanism for instability of transverse plasma waves. Physics of Fluids, 2(3):337, 1959.

[72] Roswell Lee and Martin Lampe. Electromagnetic Instabilities, Filamentation, and Focusing of Relativistic Electron Beams. Physical Review Letters, 31(23):1390–1393, 12 1973.

[73] William Alexander Schumaker. Pump-Probe Experiments & Radiation Generation using Laser Wakefield Accelerators. PhD thesis, University of Michigan, Ann Arbor, 2014.

[74] C. J. Hooker, J. L. Collier, O. Chekhlov, R. Clarke, E. Divall, K. Ertel, B. Fell, P. Foster, S. Hancock, A. Langley, D. Neely, J. Smith, and B. Wyborn. The Astra Gemini project – A dual-beam petawatt Ti:Sapphire laser system. Journal de Physique IV (Proceedings), 133:673–677, 6 2006.

[75] Yong Wang, Shoujun Wang, Alex Rockwood, Bradley M. Luther, Reed Hollinger, Alden Curtis, Chase Calvi, Carmen S. Menoni, and Jorge J. Rocca. 085 PW laser operation at 33 Hz and high-contrast ultrahigh-intensity $\lambda = 400$ nm second-harmonic beamline. Optics Letters, 42(19):3828, 10 2017.

[76] Advanced Laser Light Source (ALLS) — LaserNetUS.

[77] S. M. Saltiel, S. D. Savov, and I. V. Tomov. A simple technique for real time pulsewidth measurements of single ultrashort laser pulses. Optical and Quantum Electronics, 14(5):391–394, 9 1982.

[78] D.J. Kane and R. Trebino. Characterization of arbitrary femtosecond pulses using frequency-resolved optical gating. IEEE Journal of Quantum Electronics, 29(2):571–579, 1993.

[79] Rick Trebino, Kenneth W. DeLong, David N. Fittinghoff, John N. Sweetser, Marco A. Krumbügel, Bruce A. Richman, and Daniel J. Kane. Measuring ultrashort laser pulses in the time-frequency domain using frequency-resolved optical gating. Review of Scientific Instruments, 68(9):3277–3295, 9 1997.

[80] P. Tomassini and A. Giulietti. A generalization of Abel inversion to non-axisymmetric density distribution. Optics Communications, 199(1-4):143–148, 11 2001.

[81] J. P. Boris. Relativistic plasma simulation–optimization of a hybrid code. In Jay P. Boris and Ramy A. Shanny, editors, Proceedings of the Fourth Conference on Numerical Simulation of Plasmas, pages 3–67, Washington D.C., 11 1971. Naval Research Laboratory Department of the Navy.

[82] Z. J. Yang, T. H. Johansen, H. Bratsberg, G. Helgesen, and A. T. Skjeltorp. Potential and force between a magnet and a bulk Y1Ba 2Cu3O7-δ superconductor studied by a mechanical pendulum. Superconductor Science and Technology, 3(12):591–597, 12 1990.

[83] M. J. V. Streeter, C. Colgan, J.A. Carderelli, Y. Ma, N. Cavanagh, E. E. Los, H. Ahmed, A. F. Antoine, T. Audet, M. D. Balcazar, L. Calvin, B. Kettle, S. P. D. Mangles, Z. Najmudin, P. P. Rajeev, D. R. Symes, A. G. R. Thomas, and G. Sarri. Narrow bandwidth, low-emittance positron beams from a laser-wakefield accelerator. Scientific Reports, 14(1):6001, 3 2024.

[84] JC Wood. Betatron Radiation from Laser Wakefield Accelerators and its Applications. PhD thesis, Imperial College London, London, 3 2016.

[85] A. E. Hussein, N. Senabulya, Y. Ma, M. J.V. Streeter, B. Kettle, S. J.D. Dann, F. Albert, N. Bourgeois, S. Cipiccia, J. M. Cole, O. Finlay, E. Gerstmayr, I. Gallardo González, A. Higginbotham, D. A. Jaroszynski, K. Falk, K. Krushelnick, N. Lemos, N. C. Lopes, C. Lumsdon, O. Lundh, S. P.D. Mangles, Z. Najmudin, P. P. Rajeev, C. M. Schlepütz, M. Shahzad, M. Smid, R. Spesyvtsev, D. R. Symes, G. Vieux, L. Willingale, J. C. Wood, A. J. Shahani, and A. G.R. Thomas. Laser-wakefield accelerators for high-resolution X-ray imaging of complex microstructures. Scientific Reports, 9(1), 12 2019.

[86] G. Costa, M.P. Anania, A. Biagioni, F.G. Bisesto, M. Del Franco, M. Galletti, M. Ferrario, R. Pompili, S. Romeo, A.R. Rossi, A. Zigler, and A. Cianchi. Characterisation of supersonic gas jets for different nozzle geometries for laser-plasma acceleration experiments at SPARC_LAB. Journal of Instrumentation, 17(01):C01049, 1 2022.

[87] T Hosokai, K Kinoshita, T Watanabe, K Yoshii, T Ueda, A Zhidokov, M Uesaka, K Nakajima, M Kando, and H Kotaki. Supersonic gas jet target for generation of relativistic electrons with 12 TW-50 fs laser pulse. 8th European Particle Accelerator Conference, pages 981–983, 2002.

[88] C.K. Birdsall and A.B Langdon. Plasma Physics via Computer Simulation. CRC Press, 10 2018.

[89] J.L. Vay. Simulation of plasma accelerators with the Particle-In-Cell method. arXiv, 2020.

[90] D. Tskhakaya, K. Matyash, R. Schneider, and F. Taccogna. The Particle-In-Cell Method. Contributions to Plasma Physics, 47(8-9):563–594, 12 2007.

[91] T D Arber, K Bennett, C S Brady, A Lawrence-Douglas, M G Ramsay, N J Sircombe, P Gillies, R G Evans, H Schmitz, A R Bell, and C P Ridgers. Contemporary particle-in-cell approach to laser-plasma modelling. Plasma Physics and Controlled Fusion, 57(11):113001, 11 2015.

[92] Kane Yee. Numerical solution of initial boundary value problems involving maxwell's equations in isotropic media. IEEE Transactions on Antennas and Propagation, 14(3):302–307, 5 1966.

[93] Rémi Lehe, Manuel Kirchen, Igor A. Andriyash, Brendan B. Godfrey, and Jean-Luc Vay. A spectral, quasi-cylindrical and dispersion-free Particle-In-Cell algorithm. Computer Physics Communications, 203:66–82, 6 2016.

[94] R. Torres, T. Grismayer, F. Cruz, R.A. Fonseca, and L.O. Silva. OSIRIS-GR: General relativistic activation of the polar cap of a compact neutron star. arXiv, 2024.

[95] Qian Qian, Daniel Seipt, Marija Vranic, Thomas E. Grismayer, Thomas G. Blackburn, Christopher P. Ridgers, and Alexander G. R. Thomas. Parametric study of the polarization dependence of nonlinear Breit–Wheeler pair creation process using two laser pulses. Physics of Plasmas, 30(10), 10 2023.

[96] M. Kirchen, S. Jalas, J. Neuhaus-Steinmetz, and A.R. Maier. A spectral, quasi-3D, multi-GPU Particle-In-Cell code for plasma accelerators. Verhandlungen der Deutschen Physikalischen Gesellschaft, 2018.

[97] J.-L. Vay, A. Almgren, J. Bell, L. Ge, D.P. Grote, M. Hogan, O. Kononenko, R. Lehe, A. Myers, C. Ng, J. Park, R. Ryne, O. Shapoval, M. Thévenet, and W. Zhang. Warp-X: A new exascale computing platform for beam–plasma simulations. Nuclear Instruments and Methods in Physics Research Section A: Accelerators, Spectrometers, Detectors and Associated Equipment, 909:476–479, 11 2018.

[98] R. A. Fonseca, L. O. Silva, F. S. Tsung, V. K. Decyk, W. Lu, C. Ren, W. B. Mori, S. Deng, S. Lee, T. Katsouleas, and J. C. Adam. OSIRIS: A Three-Dimensional, Fully Relativistic Particle in Cell Code for Modeling Plasma Based Accelerators. pages 342–351, 2002.

[99] C Arran, J M Cole, E Gerstmayr, T G Blackburn, S P D Mangles, and C P Ridgers. Optimal parameters for radiation reaction experiments. Plasma Physics and Controlled Fusion, 61(7):074009, 7 2019.

[100] Xiaoming Wang, Rafal Zgadzaj, Neil Fazel, Zhengyan Li, S. A. Yi, Xi Zhang, Watson Henderson, Y.-Y. Chang, R. Korzekwa, H.-E. Tsai, C.-H. Pai, H. Quevedo, G. Dyer, E. Gaul, M. Martinez, A. C. Bernstein, T. Borger, M. Spinks, M. Donovan, V. Khudik, G. Shvets, T. Ditmire, and M. C. Downer. Quasi-monoenergetic laser-plasma acceleration of electrons to 2GeV. Nature Communications, 4(1):1988, 6 2013.

[101] L.T. Ke, K. Feng, W.T. Wang, Z.Y. Qin, C.H. Yu, Y. Wu, Y. Chen, R. Qi, Z.J. Zhang, Y. Xu, X.J. Yang, Y.X. Leng, J.S. Liu, R.X. Li, and Z.Z. Xu. Near-GeV Electron Beams at a Few Per-Mille Level from a Laser Wakefield Accelerator via Density-Tailored Plasma. Physical Review Letters, 126(21):214801, 5 2021.

[102] K. Poder, M. Tamburini, G. Sarri, A. Di Piazza, S. Kuschel, C.D. Baird, K. Behm, S. Bohlen, J.M. Cole, D.J. Corvan, M. Duff, E. Gerstmayr, C.H. Keitel, K. Krushelnick, S.P.D. Mangles, P. McKenna, C.D. Murphy, Z. Najmudin, C.P. Ridgers, G.M. Samarin, D.R. Symes, A.G.R. Thomas, J. Warwick, and M. Zepf. Experimental Signatures of the Quantum Nature of Radiation Reaction in the Field of an Ultraintense Laser. Physical Review X, 8(3):031004, 7 2018.

[103] B. Miao, J. E. Shrock, L. Feder, R. C. Hollinger, J. Morrison, R. Nedbailo, A. Picksley, H. Song, S. Wang, J. J. Rocca, and H. M. Milchberg. Multi-GeV Electron Bunches from an All-Optical Laser Wakefield Accelerator. Physical Review X, 12(3):031038, 7 2022.

[104] J. Faure, C. Rechatin, A. Norlin, A. Lifschitz, Y. Glinec, and V. Malka. Controlled injection and acceleration of electrons in plasma wakefields by colliding laser pulses. Nature, 444(7120):737–739, 12 2006.

[105] W. T. Wang, W. T. Li, J. S. Liu, Z. J. Zhang, R. Qi, C. H. Yu, J. Q. Liu, M. Fang, Z. Y. Qin, C. Wang, Y. Xu, F. X. Wu, Y. X. Leng, R. X. Li, and Z. Z. Xu. High-Brightness High-Energy Electron Beams from a Laser Wakefield Accelerator via Energy Chirp Control. Physical Review Letters, 117(12):124801, 9 2016.

[106] K. K. Swanson, H. E. Tsai, S. K. Barber, R. Lehe, H. S. Mao, S. Steinke, J. Van Tilborg, K. Nakamura, C. G.R. Geddes, C. B. Schroeder, E. Esarey, and W. P. Leemans. Control of tunable, monoenergetic laser-plasma-accelerated electron beams using a shock-induced density downramp injector. Physical Review Accelerators and Beams, 20(5):051301, 5 2017.

[107] D. E. Cardenas, S. Chou, E. Wallin, J. Xu, L. Hofmann, A. Buck, K. Schmid, D. E. Rivas, B. Shen, A. Gonoskov, M. Marklund, and L. Veisz. Electron bunch evolution in laser-wakefield acceleration. Physical Review Accelerators and Beams, 23(11):112803, 11 2020.

[108] S. Bohlen, T. Brümmer, F. Grüner, C. A. Lindstrøm, M. Meisel, T. Staufer, M. J.V. Streeter, M. C. Veale, J. C. Wood, R. D'Arcy, K. Põder, and J. Osterhoff. In Situ Measurement of Electron Energy Evolution in a Laser-Plasma Accelerator. Physical Review Letters, 129(24):244801, 12 2022.

[109] Y. Ma, D. Seipt, S. J.D. Dann, M. J.V. Streeter, C. A.J. Palmer, L. Willingale, and A. G.R. Thomas. Angular streaking of betatron X-rays in a transverse density gradient laser-wakefield accelerator. Physics of Plasmas, 25(11):113105, 11 2018.

[110] V. Malka, C. Coulaud, J. P. Geindre, V. Lopez, Z. Najmudin, D. Neely, and F. Amiranoff. Characterization of neutral density profile in a wide range of pressure of cylindrical pulsed gas jets. Review of Scientific Instruments, 71(6):2329–2333, 6 2000.

[111] S. V. Bulanov, V. A. Vshivkov, G. I. Dudnikova, F. Naumova, N. M. Pegoraro, and I. V. Pogorelsky. Laser acceleration of charged particles in inhomogeneous plasmas: i. Plasma Physics Reports, 23(4):259–269, 4 1997.

[112] P. Sprangle, B. Hafizi, J. R. Peñano, R. F. Hubbard, A. Ting, C. I. Moore, D. F. Gordon, A. Zigler, D. Kaganovich, and T. M. Antonsen. Wakefield generation and GeV acceleration in tapered plasma channels. Physical Review E, 63(5):056405, 4 2001.

[113] A. Pukhov and I. Kostyukov. Control of laser-wakefield acceleration by the plasma-density profile. Physical Review E, 77(2):025401, 2 2008.

[114] E. Guillaume, A. Döpp, C. Thaury, K. Ta Phuoc, A. Lifschitz, G. Grittani, J.-P. Goddet, A. Tafzi, S.W. Chou, L. Veisz, and V. Malka. Electron Rephasing in a Laser-Wakefield Accelerator. Physical Review Letters, 115(15):155002, 10 2015.

[115] Michaela Kozlova, Igor Andriyash, Julien Gautier, Stephane Sebban, Slava Smartsev, Noemie Jourdain, Uddhab Chaulagain, Yasmina Azamoum, Amar Tafzi, Jean-Philippe Goddet, Kosta Oubrerie, Cedric Thaury, Antoine Rousse, and Kim Ta Phuoc. Hard X Rays from Laser-Wakefield Accelerators in Density Tailored Plasmas. Physical Review X, 10(1):011061, 3 2020.

[116] Y. Ma, D. Seipt, K. Krushelnick, and A. G. R. Thomas. Generation of straight and curved hollow plasma channels by laser-generated nonlinear wakefields and studies of ultra-intense laser pulse guiding. Physics of Plasmas, 28(6), 6 2021.

[117] Xinzhe Zhu, Boyuan Li, Feng Liu, Jianlong Li, Zewu Bi, Xulei Ge, Hongyang Deng, Ziyang Zhang, Peilin Cui, Lin Lu, Wenchao Yan, Xiaohui Yuan, Liming Chen, Qiang Cao, Zhenyu Liu, Zhengming Sheng, Min Chen, and Jie Zhang. Experimental Demonstration of Laser Guiding and Wakefield Acceleration in a Curved Plasma Channel. Physical Review Letters, 130(21):215001, 5 2023.

[118] J. Luo, M. Chen, W.Y. Wu, S.M. Weng, Z.M. Sheng, C.B. Schroeder, D.A. Jaroszynski, E. Esarey, W.P. Leemans, W.B. Mori, and J. Zhang. Multistage Coupling of Laser-Wakefield Accelerators with Curved Plasma Channels. Physical Review Letters, 120(15):154801, 4 2018.

[119] Min Chen, Ji Luo, Fei-Yu Li, Feng Liu, Zheng-Ming Sheng, and Jie Zhang. Tunable synchrotron-like radiation from centimeter scale plasma channels. Light: Science & Applications, 5(1):e16015–e16015, 1 2016.

[120] Erich S. Weibel. Spontaneously growing transverse waves in a plasma due to an anisotropic velocity distribution. Physical Review Letters, 2(3):83–84, 2 1959.

[121] G Benford. Theory of filamentation in relativistic electron beams. Plasma Physics, 15(6):483–499, 6 1973.

[122] S. C. Wilks, W. L. Kruer, M. Tabak, and A. B. Langdon. Absorption of ultra-intense laser pulses. Physical Review Letters, 69(9):1383–1386, 8 1992.

[123] Max Tabak, James Hammer, Michael E. Glinsky, William L. Kruer, Scott C. Wilks, John Woodworth, E. Michael Campbell, Michael D. Perry, and Rodney J. Mason. Ignition and high gain with ultrapowerful lasers*. Physics of Plasmas, 1(5):1626–1634, 5 1994.

[124] Yuri Lyubarsky and David Eichler. Are Gamma-Ray Burst Shocks Mediated by the Weibel Instability? The Astrophysical Journal, 647(2):1250–1254, 8 2006.

[125] Mikhail V. Medvedev, Davide Lazzati, Brian C. Morsony, and Jared C. Workman. Jitter Radiation as a Possible Mechanism for Gamma-Ray Burst Afterglows: Spectra and Light Curves. The Astrophysical Journal, 666(1):339–345, 9 2007.

[126] Shuhua Zhai, Vladimir Tikhonchuk, Longqing Yi, Anabella Araudo, and Stefan Weber. Weibel instability mediated laser hole boring and ion acceleration in an electrostatic shock. Plasma Physics and Controlled Fusion, 63(8):085013, 8 2021.

[127] M Bornatici and Kai Fong Lee. Ordinary-mode electromagnetic instability in counter-streaming plasmas with anisotropic temperatures. Physics of Fluids, 13(3007), 1970.

[128] A. Bret, L. Gremillet, D. Bénisti, and E. Lefebvre. Exact Relativistic Kinetic Theory of an Electron-Beam–Plasma System: Hierarchy of the Competing Modes in the System-Parameter Space. Physical Review Letters, 100(20):205008, 5 2008.

[129] P. San Miguel Claveria, X. Davoine, J. R. Peterson, M. Gilljohann, I. Andriyash, R. Ariniello, C. Clarke, H. Ekerfelt, C. Emma, J. Faure, S. Gessner, M. J. Hogan, C. Joshi, C. H. Keitel, A. Knetsch, O. Kononenko, M. Litos, Y. Mankovska, K. Marsh, A. Matheron, Z. Nie, B. O'Shea, D. Storey, N. Vafaei-Najafabadi, Y. Wu, X. Xu, J. Yan, C. Zhang, M. Tamburini, F. Fiuza, L. Gremillet, and S. Corde. Spatiotemporal dynamics of ultrarelativistic beam-plasma instabilities. Physical Review Research, 4(2):023085, 5 2022.

[130] V B Pathak, T Grismayer, A Stockem, R A Fonseca, and L O Silva. Spatial-temporal evolution of the current filamentation instability. New Journal of Physics, 17(4):043049, 4 2015.

[131] J.R. Peterson, S. Glenzer, and F. Fiuza. Magnetic Field Amplification by a Nonlinear Electron Streaming Instability. Physical Review Letters, 126(21):215101, 5 2021.

[132] Zheng Gong, Karen Z. Hatsagortsyan, and Christoph H. Keitel. Electron Polarization in Ultrarelativistic Plasma Current Filamentation Instabilities. Physical Review Letters, 130(1):015101, 1 2023.

[133] Spencer Gessner, Erik Adli, James M. Allen, Weiming An, Christine I. Clarke, Chris E. Clayton, Sebastien Corde, Antoine Doche, Joel Frederico, Selina Z. Green, Mark J. Hogan, Chan Joshi, Carl A. Lindstrom, Michael Litos, Kenneth A. Marsh, Warren B. Mori, Brendan O'Shea, Navid Vafaei-Najafabadi, and Vitaly Yakimenko. Acceleration of a Positron Bunch in a Hollow Channel Plasma. 4 2023.

[134] C. B. Schroeder, E. Esarey, C. G. R. Geddes, C. Benedetti, and W. P. Leemans. Physics considerations for laser-plasma linear colliders. Physical Review Special Topics - Accelerators and Beams, 13(10):101301, 10 2010.

[135] B Foster, R D'Arcy, and C A Lindstrøm. A hybrid, asymmetric, linear Higgs factory based on plasma-wakefield and radio-frequency acceleration. New Journal of Physics, 25(9):093037, 9 2023.

[136] G Sarri, W Schumaker, A Di Piazza, K Poder, J M Cole, M Vargas, D Doria, S Kushel, B Dromey, G Grittani, L Gizzi, M E Dieckmann, A Green, V Chvykov, A Maksimchuk, V Yanovsky, Z H He, B X Hou, J A Nees, S Kar, Z Najmudin, A G R Thomas, C H Keitel, K Krushelnick, and M Zepf. Laser-driven generation of collimated ultra-relativistic positron beams. Plasma Physics and Controlled Fusion, 55(12):124017, 12 2013.

[137] Bruno Rossi. High Energy Particles. Prentice-Hall Inc, New York, 1952.

[138] VB Beresteskii, EM Lifshitz, and LP Pitaevskii. Quantum Electrodynamics. Butterworth-Heinemann, Oxford, 2008.

[139] William T. Scott. The Theory of Small-Angle Multiple Scattering of Fast Charged Particles. Reviews of Modern Physics, 35(2):231–313, 4 1963.

[140] R. Weingartner, S. Raith, A. Popp, S. Chou, J. Wenz, K. Khrennikov, M. Heigoldt, A. R. Maier, N. Kajumba, M. Fuchs, B. Zeitler, F. Krausz, S. Karsch, and F. Grüner. Ultralow emittance electron beams from a laser-wakefield accelerator. Physical Review Special Topics - Accelerators and Beams, 15(11):111302, 11 2012.

[141] Andreas R. Maier, Niels M. Delbos, Timo Eichner, Lars Hübner, Sören Jalas, Laurids Jeppe, Spencer W. Jolly, Manuel Kirchen, Vincent Leroux, Philipp Messner, Matthias Schnepp, Maximilian Trunk, Paul A. Walker, Christian Werle, and Paul Winkler. Decoding Sources of Energy Variability in a Laser-Plasma Accelerator. Physical Review X, 10(3):031039, 8 2020.

[142] A Alejo, G M Samarin, J Warwick, C McCluskey, G Cantono, T Ceccotti, S Dobosz Dufrénoy, P Monot, and G Sarri. Non-invasive characterisation of a laser-driven positron beam. Plasma Physics and Controlled Fusion, 62(5):055013, 5 2020.

[143] Song Li, Guangyu Li, Quratul Ain, Min Sup Hur, Antonio C. Ting, Victor V. Kulagin, Christos Kamperidis, and Nasr A. M. Hafz. A laser-plasma accelerator driven by two-color relativistic femtosecond laser pulses. Science Advances, 5(11), 11 2019.

[144] J. Warwick, T. Dzelzainis, M.E. Dieckmann, W. Schumaker, D. Doria, L. Romagnani, K. Poder, J.M. Cole, A. Alejo, M. Yeung, K. Krushelnick, S.P.D. Mangles, Z. Najmudin, B. Reville, G.M. Samarin, D.D. Symes, A.G.R. Thomas, M. Borghesi, and G. Sarri. Experimental Observation of a Current-Driven Instability in a Neutral Electron-Positron Beam. Physical Review Letters, 119(18):185002, 11 2017.

[145] Aaron Alejo, Roman Walczak, and Gianluca Sarri. Laser-driven high-quality positron sources as possible injectors for plasma-based accelerators. Scientific Reports, 9(1):5279, 3 2019.

[146] Gianluca Sarri, Luke Calvin, and Matthew Streeter. Plasma-based positron sources at EuPRAXIA. Plasma Physics and Controlled Fusion, 64(4):044001, 4 2022.

[147] A Ferrari, P.R. Sala, A Fasso, and J Ranft. FLUKA: A Multi-Particle Transport Code. CERN Technical Report (Stanford Linear Accelerator Center (SLAC)), 2005.

[148] S. Kneip, C. McGuffey, J. L. Martins, S. F. Martins, C. Bellei, V. Chvykov, F. Dollar, R. Fonseca, C. Huntington, G. Kalintchenko, A. Maksimchuk, S. P. D. Mangles, T. Matsuoka, S. R. Nagel, C. A. J. Palmer, J. Schreiber, K. Ta Phuoc, A. G. R. Thomas, V. Yanovsky, L. O. Silva, K. Krushelnick, and Z. Najmudin. Bright spatially coherent synchrotron X-rays from a table-top source. Nature Physics, 6(12):980–983, 12 2010.

[149] S. Corde, C. Thaury, K. Ta Phuoc, A. Lifschitz, G. Lambert, J. Faure, O. Lundh, E. Benveniste, A. Ben-Ismail, L. Arantchuk, A. Marciniak, A. Stordeur, P. Brijesh, A. Rousse, A. Specka, and V. Malka. Mapping the X-Ray Emission Region in a Laser-Plasma Accelerator. Physical Review Letters, 107(21):215004, 11 2011.

[150] J. Wenz, S. Schleede, K. Khrennikov, M. Bech, P. Thibault, M. Heigoldt, F. Pfeiffer, and S. Karsch. Quantitative X-ray phase-contrast microtomography from a compact laser-driven betatron source. Nature Communications, 6(1):7568, 7 2015.

[151] R. D'Arcy, S. Wesch, A. Aschikhin, S. Bohlen, C. Behrens, M.J. Garland, L. Goldberg, P. Gonzalez, A. Knetsch, V. Libov, A. Martinez de la Ossa, M. Meisel, T.J. Mehrling, P. Niknejadi, K. Poder, J.-H. Röckemann, L. Schaper, B. Schmidt, S. Schröder, C. Palmer, J.-P. Schwinkendorf, B. Sheeran, M.J.V. Streeter, G. Tauscher, V. Wacker, and J. Osterhoff. Tunable Plasma-Based Energy Dechirper. Physical Review Letters, 122(3):034801, 1 2019.

[152] R. W. Assmann, M. K. Weikum, T. Akhter, D. Alesini, A. S. Alexandrova, M. P. Anania, N. E. Andreev, I. Andriyash, M. Artioli, A. Aschikhin, T. Audet, A. Bacci, I. F. Barna, S. Bartocci, A. Bayramian, A. Beaton, A. Beck, M. Bellaveglia, A. Beluze, A. Bernhard, A. Biagioni, S. Bielawski, F. G. Bisesto, A. Bonatto, L. Boulton, F. Brandi, R. Brinkmann, F. Briquez, F. Brottier, E. Bründermann, M. Büscher, B. Buonomo, M. H. Bussmann, G. Bussolino, P. Campana, S. Cantarella, K. Cassou, A. Chancé, M. Chen, E. Chiadroni, A. Cianchi, F. Cioeta, J. A. Clarke, J. M. Cole, G. Costa, M. E. Couprie, J. Cowley, M. Croia, B. Cros, P. A. Crump, R. D'Arcy, G. Dattoli, A. Del Dotto, N. Delerue, M. Del Franco, P. Delinikolas, S. De Nicola, J. M. Dias, D. Di Giovenale, M. Diomede, E. Di Pasquale, G. Di Pirro, G. Di Raddo, U. Dorda, A. C. Erlandson, K. Ertel, A. Esposito, F. Falcoz,

A. Falone, R. Fedele, A. Ferran Pousa, M. Ferrario, F. Filippi, J. Fils, G. Fiore, R. Fiorito, R. A. Fonseca, G. Franzini, M. Galimberti, A. Gallo, T. C. Galvin, A. Ghaith, A. Ghigo, D. Giove, A. Giribono, L. A. Gizzi, F. J. Grüner, A. F. Habib, C. Haefner, T. Heinemann, A. Helm, B. Hidding, B. J. Holzer, S. M. Hooker, T. Hosokai, M. Hübner, M. Ibison, S. Incremona, A. Irman, F. Iungo, F. J. Jafarinia, O. Jakobsson, D. A. Jaroszynski, S. Jaster-Merz, C. Joshi, M. Kaluza, M. Kando, O. S. Karger, S. Karsch, E. Khazanov, D. Khikhlukha, M. Kirchen, G. Kirwan, C. Kitégi, A. Knetsch, D. Kocon, P. Koester, O. S. Kononenko, G. Korn, I. Kostyukov, K. O. Kruchinin, L. Labate, C. Le Blanc, C. Lechner, P. Lee, W. Leemans, A. Lehrach, X. Li, Y. Li, V. Libov, A. Lifschitz, C. A. Lindstrøm, V. Litvinenko, W. Lu, O. Lundh, A. R. Maier, V. Malka, G. G. Manahan, S. P. D. Mangles, A. Marcelli, B. Marchetti, O. Marcouillé, A. Marocchino, F. Marteau, A. Martinez de la Ossa, J. L. Martins, P. D. Mason, F. Massimo, F. Mathieu, G. Maynard, Z. Mazzotta, S. Mironov, A. Y. Molodozhentsev, S. Morante, A. Mosnier, A. Mostacci, A. S. Müller, C. D. Murphy, Z. Najmudin, P. A. P. Nghiem, F. Nguyen, P. Niknejadi, A. Nutter, J. Osterhoff, D. Oumbarek Espinos, J. L. Paillard, D. N. Papadopoulos, B. Patrizi, R. Pattathil, L. Pellegrino, A. Petralia, V. Petrillo, L. Piersanti, M. A. Pocsai, K. Poder, R. Pompili, L. Pribyl, D. Pugacheva, B. A. Reagan, J. Resta-Lopez, R. Ricci, S. Romeo, M. Rossetti Conti, A. R. Rossi, R. Rossmanith, U. Rotundo, E. Roussel, L. Sabbatini, P. Santangelo, G. Sarri, L. Schaper, P. Scherkl, U. Schramm, C. B. Schroeder, J. Scifo, L. Serafini, G. Sharma, Z. M. Sheng, V. Shpakov, C. W. Siders, L. O. Silva, T. Silva, C. Simon, C. Simon-Boisson, U. Sinha, E. Sistrunk, A. Specka, T. M. Spinka, A. Stecchi, A. Stella, F. Stellato, M. J. V. Streeter, A. Sutherland, E. N. Svystun, D. Symes, C. Szwaj, G. E. Tauscher, D. Terzani, G. Toci, P. Tomassini, R. Torres, D. Ullmann, C. Vaccarezza, M. Valléau, M. Vannini, A. Vannozzi, S. Vescovi, J. M. Vieira, F. Villa, C. G. Wahlström, R. Walczak, P. A. Walker, K. Wang, A. Welsch, C. P. Welsch, S. M. Weng, S. M. Wiggins, J. Wolfenden, G. Xia, M. Yabashi, H. Zhang, Y. Zhao, J. Zhu, and A. Zigler. EuPRAXIA Conceptual Design Report. The European Physical Journal Special Topics, 229(24):3675–4284, 12 2020.

[153] P. Muggli, B. E. Blue, C. E. Clayton, F. J. Decker, M. J. Hogan, C. Huang, C. Joshi, T. C. Katsouleas, W. Lu, W. B. Mori, C. L. O'Connell, R. H. Siemann, D. Walz, and M. Zhou. Halo Formation and Emittance Growth of Positron Beams in Plasmas. Physical Review Letters, 101(5):055001, 7 2008.

[154] C Joshi, E Adli, W An, C E Clayton, S Corde, S Gessner, M J Hogan, M Litos, W Lu, K A Marsh, W B Mori, N Vafaei-Najafabadi, B O'shea, Xinlu Xu, G White, and V Yakimenko. Plasma wakefield acceleration experiments at facet ii. Plasma Physics and Controlled Fusion, 60(3):034001, 3 2018.

[155] A.J. Gonsalves, K. Nakamura, J. Daniels, C. Benedetti, C. Pieronek, T.C.H. de Raadt, S. Steinke, J.H. Bin, S.S. Bulanov, J. van Tilborg, C.G.R. Geddes, C.B. Schroeder, Cs. Tóth, E. Esarey, K. Swanson, L. Fan-Chiang, G. Bagdasarov, N. Bobrova, V. Gasilov, G. Korn, P. Sasorov, and W.P. Leemans. Petawatt Laser Guiding and Electron Beam Acceleration to 8 GeV in a Laser-Heated Capillary Discharge Waveguide. Physical Review Letters, 122(8):084801, 2 2019.

[156] Steven J. Haney, Kurt W. Berger, Glenn D. Kubiak, Paul D. Rockett, and John Hunter. Pro-

totype high-speed tape target transport for a laser plasma soft-x-ray projection lithography source. Applied Optics, 32(34):6934, 12 1993.

[157] Colin N. Danson, Constantin Haefner, Jake Bromage, Thomas Butcher, Jean-Christophe F. Chanteloup, Enam A. Chowdhury, Almantas Galvanauskas, Leonida A. Gizzi, Joachim Hein, David I. Hillier, Nicholas W. Hopps, Yoshiaki Kato, Efim A. Khazanov, Ryosuke Kodama, Georg Korn, Ruxin Li, Yutong Li, Jens Limpert, Jingui Ma, Chang Hee Nam, David Neely, Dimitrios Papadopoulos, Rory R. Penman, Liejia Qian, Jorge J. Rocca, Andrey A. Shaykin, Craig W. Siders, Christopher Spindloe, Sándor Szatmári, Raoul M. G. M. Trines, Jianqiang Zhu, Ping Zhu, and Jonathan D. Zuegel. Petawatt and exawatt class lasers worldwide. High Power Laser Science and Engineering, 7:e54, 8 2019.

[158] D. L. Burke, R. C. Field, G. Horton-Smith, J. E. Spencer, D. Walz, S. C. Berridge, W. M. Bugg, K. Shmakov, A. W. Weidemann, C. Bula, K. T. McDonald, E. J. Prebys, C. Bamber, S. J. Boege, T. Koffas, T. Kotseroglou, A. C. Melissinos, D. D. Meyerhofer, D. A. Reis, and W. Ragg. Positron Production in Multiphoton Light-by-Light Scattering. Physical Review Letters, 79(9):1626–1629, 9 1997.

[159] Zhiyong Qin, Changhai Yu, Wentao Wang, Jiansheng Liu, Wentao Li, Rong Qi, Zhijun Zhang, Jiaqi Liu, Ming Fang, Ke Feng, Ying Wu, Lintong Ke, Yu Chen, Yi Xu, Yuxin Leng, Cheng Wang, Ruxin Li, and Zhizhan Xu. Ultralow-emittance measurement of high-quality electron beams from a laser wakefield accelerator. Physics of Plasmas, 25(2), 2 2018.

[160] R. J. Shalloo, S. J. D. Dann, J.-N. Gruse, C. I. D. Underwood, A. F. Antoine, C. Arran, M. Backhouse, C. D. Baird, M. D. Balcazar, N. Bourgeois, J. A. Cardarelli, P. Hatfield, J. Kang, K. Krushelnick, S. P. D. Mangles, C. D. Murphy, N. Lu, J. Osterhoff, K. Põder, P. P. Rajeev, C. P. Ridgers, S. Rozario, M. P. Selwood, A. J. Shahani, D. R. Symes, A. G. R. Thomas, C. Thornton, Z. Najmudin, and M. J. V. Streeter. Automation and control of laser wakefield accelerators using Bayesian optimization. Nature Communications, 11(1):6355, 12 2020.

[161] A Loulergue, M Labat, C Evain, C Benabderrahmane, V Malka, and M E Couprie. Beam manipulation for compact laser wakefield accelerator based free-electron lasers. New Journal of Physics, 17(2):023028, 2 2015.

[162] J P Couperus Cabadağ, S Bock, A Irman, A Koehler, M LaBerge, R Pausch, T Püschel, U Schramm, S Schöbel, and K Steiniger. Stable multi-day performance of a laser wakefield accelerator for FEL applications. Proc. Free-Elect. Laser, pages 196–200, 2022.

[163] Steffen Hillenbrand, Ralph Assmann, Anke-Susanne Müller, Oliver Jansen, Vitali Judin, and Alexander Pukhov. Study of Laser Wakefield Accelerators as injectors for Synchrotron light sources. Nuclear Instruments and Methods in Physics Research Section A: Accelerators, Spectrometers, Detectors and Associated Equipment, 740:153–157, 3 2014.

[164] K A Dewhurst, H L Owen, and Bruno Muratori. Use of Laser Wakefield Accelerators as Injectors for Compact Storage Rings. In 8th Int. Particle Accelerator Conf.(IPAC'17), Copenhagen, Denmark, 14â 19 May, 2017, pages 1760–1762. JACOW, Geneva, Switzerland, 2017.

[165] K Kranz, K Desch, D Elsner, and M Switka. Studies for a Laser Wakefield Driven Injector at ELSA. Proc. IPAC'22, pages 2686–2688, 2022.

[166] A. I. Titov, B. Kämpfer, and H. Takabe. Dimuon production by laser-wakefield accelerated electrons. Physical Review Special Topics - Accelerators and Beams, 12(11):111301, 11 2009.

[167] Bobbili Sanyasi Rao, Jong Ho Jeon, Hyung Taek Kim, and Chang Hee Nam. Bright muon source driven by GeV electron beams from a compact laser wakefield accelerator. Plasma Physics and Controlled Fusion, 60(9):095002, 9 2018.

[168] M Wei. Study of Nonlinear Evolution of the Weibel-like Instability of Relativistic Electron Beams Relevant to Fast Ignition and Astrophysics. Technical report, 2012.